Chemical Vapor Deposition and Physical Vapor Deposition of Wide Bandgap Metal Sulfides for Photovoltaic Devices

A dissertation submitted by

Jesse W. Cohan

In partial fulfillment of the requirements for the degree of

Doctor of Philosophy in Chemistry

Tufts University

May 2025

Advisor: Luke M. Davis

Abstract

Decarbonizing energy and electricity sources is critical to keeping anthropogenic global warming below 1.5 °C. Photovoltaics are a scalable technology that can meet global electricity demands without emissions of greenhouse gases while operating. Over the past decade, photovoltaics have benefited from a combination of significantly decreasing manufacturing costs and ca. 50% improvements to power conversion efficiencies, and are now less expensive sources of electricity than fossil fuels in many markets. As a result, most new installations of electricity generation capacity are solar.

As photovoltaic module efficiencies reach their practical limits, there is an opportunity for drastic improvements using tandem photovoltaics. By stacking a photo-absorber with a wider bandgap on top of existing modules, power conversion efficiencies greater than each module alone may be achieved, and experimentally this has demonstrated power conversion efficiencies above the Shockley-Queisser limit for single junction modules. This thesis explores binary metal sulfides as materials for top cells in tandem photovoltaics. Binary metal sulfides comprise several promising photo-absorbers with appropriate bandgaps and optoelectronic properties for use in top cells, and often benefit from close-space sublimation and chemical vapor deposition as inexpensive and scalable routes to fabrication. In this thesis, deposition and properties of zirconium(IV) sulfide and germanium(II) sulfide are described.

In chapter 2, zirconium(IV) sulfide (ZrS_2) thin films are deposited from the reaction of tetrakis(dimethylamido)zirconium(IV) ($Zr(NMe_2)_4$) and H_2S. This method allows for deposition of stoichiometric ZrS_2 films between 150-350 °C, the lowest reported range for CVD of crystalline films of this material. Deposition is demonstrated at rates of >100 nm/min, but films suffer ligand incorporation and low crystallinity. Films deposited at high growth rates also transition from

smooth and compact morphologies to loosely assembled plates at growth temperatures of ≥250 °C. Decreasing the $Zr(NMe_2)_4$ flux and growing in an excess of H_2S suppresses the growth of plates, increases crystallinity, and reduces ligand incorporation. The resulting films have morphologies suitable for photovoltaics and resistivities within 1-3 orders of magnitude of single crystals.

In chapter 3, chemical vapor deposition of ZrS_2 thin films is extended to polymer substrates. The low processing temperatures demonstrated in chapter 2 are taken advantage of to accommodate thermal budgets of <200 °C for many polymers typically used in flexible electronics. Growth of continuous and crystalline ZrS_2 films is demonstrated at 200 °C on Kapton and polyether ether ketone substrates. Growth on polydimethylsiloxane substrates at 200 °C is believed to be complicated by outgassing of the polymer and leads to non-uniform growth. Continuous but amorphous ZrS_2 films can be deposited at 150 °C on polyethylene terephthalate substrates.

Finally, in chapter 4 thermal evaporation and annealing of germanium(II) sulfide (GeS) thin films is explored. GeS is conveniently deposited with low source and substrate temperatures below 300 °C, but the resulting films are amorphous and highly resistive. Annealing films under vacuum was briefly explored but resulted in re-sublimation of GeS due to its high volatility. Annealing under H_2S atmospheres was then explored at 320-355 °C and may have initiated crystallization when dilute mixtures were used, but otherwise partially oxidized films to GeS_2. Annealing under Ar at 375-400 °C was explored last and was able to produce highly crystalline GeS films. Initially, the nucleation kinetics of GeS were poor, leading to discontinuous films. However, the number of defect sites on as-deposited films was increased using seed layers or substrate roughening, which afforded nearly continuous films of crystalline GeS from annealing.

Acknowledgements

There are a lot of people I would like to thank for helping me get to where I am today, and for being a special part of life:

First, are my parents. Thank you for always believing in me, pushing me forward, and supporting my dreams. I would not be the person I am today without you both. Mom, you are the the best science project partner I could have asked for – too bad we can't find our water cycle book from fifth grade. Dad, for being my skiing, golfing, and hiking partner – my favorite thing to do is whatever we are doing together. I love you both so much and am so grateful to have the best parents anyone could ask for.

Korey, my brother and best friend. I could not imagine growing up without you in my life. Thank you for being my golfing and skiing partner, but not hiking – I'll never get you out there. Our weekend rounds of golf with Alex and Andrew were the best part of my summers at Tufts and our weekly phone calls helped me keep my sanity.

Grammy and Papa, I'm so glad that you are close to home now and I get to see you so often. Grammy, for always being such a source of warmth and joy in my life. You have become a celebrity of sorts in the Davis lab – if only we could have happy hour as much as you do. Papa, for always being my main man, our phone calls always brighten my day. I love you both so much and am so grateful to have you in my life.

Grandma and Grandpa, I'm so lucky to have grown up with you both so close to home – I think that our scrabble matches were a big part of my training to be scientist. Grandma, I fondly remember you reading to me every time I came to visit when I was younger, thank you for all the memories on Glendale road. Grandpa, for being such a good scrabble partner and for all of the

pancakes at breakfast. I love you so much and I miss you every day. I know you are watching me and our family, and I hope I made you proud.

My wonderful aunts, uncles and cousins, for all your support through the years and for always encouraging me! Thank you to Leslie and David for the boat rides during the summer, it was always a great way to get my mind off work. Laurie (Lolly) and Steven, I'll promise I'll get down to Florida to visit eventually.

My advisor, Professor Luke M. Davis, for all his support, patience, and wisdom over the years. I don't know if I'll ever meet someone with as much breadth of knowledge as you have, spanning synthetic chemistry all the way to materials chemistry – you know how to make the precursors, how to deposit with them, and how to characterize the films – and more. It has been a privilege to work with you on so many interesting (and sometimes frustrating) projects, and to learn from you along the way. Funny enough, when I applied to Tufts, I did not see your name on the website because you had only started the previous semester. I was excited to learn that you planned to use a TGA for several projects, which I had used in undergraduate research, and this was one of the reasons I decided to join your lab. Of course, when I finally had a reason to use the TGA I delayed my experiments and then the instrument broke! Regardless, I am thankful to have learned to use several other cooler instruments.

My committee members Professor Charlie Sykes, Professor Art Utz, and Professor Raf Jaramillo. Thank you to Charlie and Art for serving on my committee these past several years, I appreciate all your encouragement and patience during my committee meetings. It was a privilege to learn from you during my time at Tufts. Thank you to Raf for agreeing to be my external committee member, I am so appreciative of your support. Coming to MIT to see your MBE system

was a real treat, although the giant gas cylinders of H_2S and H_2Se almost made me want to evacuate the building.

My exceptional lab mates and friends in the Davis lab. I don't think I would have made it this far without your support all of these years. Daniela (Dani) Chavez – we squabble all the time, probably for sport at this point – for her wonderful friendship and for working with me on several projects over the years. The Davis lab would not be the same without you, thanks for making it such a fun place for everyone. Lee Blackmer, for trying to teach me about synthetic chemistry even though I'm probably a lost cause at this point. I'll forgive you for laughing at my transition lens glasses because you drove me to the hospital when I cut my hand. Sanya Mittal, for her kindness and the baked goods – they have kept me going the past few years. Hopefully, I earned the latter when trying to fix your sunroof with duct tape. Abby Berube, for putting up with all my antics and help getting my last-minute experiments done. I'm sorry the polymer substrates outgas so much. To Katie Schrader, I'm so glad that someone in the lab has my sense of humor and I can talk about standup with. Eliza Spear, for all her help troubleshooting my CVD reactor and making group meetings more exciting with awesome CuI CVD project results. Remember, it is still not too late to be the Davis lab postdoc. Zhenhuan Zhao, for all his sage advice and letting me sneak in a few last-minute p-XRD experiments at Harvard. I also must mention Dr. Lauren Hartle and Susan Schmidt, who helped get me started in the Davis lab and were wonderful mentors. Of course, I need to acknowledge Ben Kass-Mullet, my only guy friend in the Davis lab. Thanks for helping balance things out for me!

My friends in (and out) of the Chemistry department at Tufts. Colin Lawler and Raj Prithviraj, who have always supported and encouraged me when things weren't going my way. Of course, they are also excellent bandmates, and it was so fun jamming out together and playing jazz

at department functions. Also, Daniel Voner and Mark Martirosian for being such great section mates in the Freshman 15 big band. I'm glad to be a part of this band and continue playing music through graduate school.

My professors and mentors at Muhlenberg College, for a wonderful education and for making the chemistry department feel like another home. Dr. Sparks, for giving me the push to pursue chemistry research. I don't think I would have been a chemistry major without your help. Dr. Fuller, for being an incredible research advisor, and for all the great conversations on chemistry and pretty much everything else. Dr. Gooch, for his mentorship and now friendship over the years. Muhlenberg would not have been the same without you, it's too bad I never got to have you as a professor. Dr. Ingersoll, for being such a great professor and for putting up with all my antics – I did get my lab reports in on time though. Don Hughes, for making my musical experience at Muhlenberg so much better. I am grateful for all your wisdom and patience in our trumpet lessons. Finally, Sam Chen for his mentorship and political knowledge. Playing trumpet on your tv show was so cool!

Finally, my friends from outside Tufts. Sean Bristow for checking in on me, encouraging me to keep up my studies, and then kicking my butt in Super Smash Bros. I'm looking forward to hanging out again, going on a hike, and then having a rematch. Brendan Trafford, for always hyping me up and giving me something to laugh about. Our panel conversations with Sean are my favorite place to talk about anything. Nick Stavinski, for his years of friendship and encouragement. I'm glad to have been a chemistry major with you and be a part of Dr. Sparks's lab. Jake Kramer, who I have known my whole life and is like a brother. Thanks for getting me out on to some awesome golf courses and fixing my golf swing when it inevitably goes bad.

Finally, to my other great friends at Muhlenberg, Brandon Eden, Troy Lovett, Tom Barrett, Patrick Sockler, James Dematteo and Candice Ziegler.

Table of Contents

List of Figures

List of Tables

Chapter 1. Introduction

1.1. Context: Decarbonization of Electricity through Photovoltaics

The world faces an existential crisis: energy and electricity sources must be decarbonized to prevent irreversible damages from climate change. Emissions of greenhouse gases, mainly CO_2, from the combustion of fossil fuels are the greatest contributor towards global warming. Production of electricity accounts for ca. 33% of these emissions.[1] The International Panel on Climate Change (IPCC) estimates that anthropogenic global warming has increased the average global surface temperature by 1.1 °C since the Industrial Revolution,[2] and with an estimated rate 0.1-0.3 °C warming per decade at the turn of the century, an increase in global temperature to ≥1.5 °C is projected between 2030-2052.[3] Decarbonization of existing and new electricity generation capacity will be critical to reducing emissions, as electricity demand is projected to increase from ca. 27,000 to 55,000 terawatt hours (TWh) between 2023-2050.[4, 5] If emissions are not curtailed, resulting damages from rising sea levels, drought and other natural disasters will be irreversible, even if goals of net zero emissions are achieved within the century.[3]

Harnessing solar energy is a viable and sustainable method to meet global electricity demands. Indeed, enough solar flux strikes the Earth's surface in one hour to meet the current global electricity consumption of ca. 30,000 TWh.[6, 7] While all incident light cannot be captured and converted to electricity, it is possible to estimate the fraction of global surface area required to meet current electricity demands. Assuming an average insolation of 1000 W/m^2, a capacity factor or 0.2, and that photovoltaics operate at 20% efficiency (currently available Si and CdTe modules operate at efficiencies of 20-22% and 19.7%, respectively[8, 9]) only 0.06% of available land area would be required (equations 1, 2 and 3).[10] For comparison, ca. 44% of all habitable global land

area is used for agriculture,[11] and the estimated surface area available on rooftops across the globe is as high as 2.86×10^{11} m^2.[12]

1) Installed capacity for 30,000 TWh = $(3 \times 10^{16}$ Wh$) \times \left(\frac{1}{0.2 \times 8760 \text{ h}}\right) = 17$ TW

2) Land area = $(3 \times 10^{16}$ Wh$) \times \left(\frac{1}{0.2 \times 8760 \text{ h}}\right) \times \frac{1}{1000\ Wm^{-2}} \times \frac{1}{20\%\ PCE} = 8.6 \times 10^{10}$ m^2

3) Percent of available land area = $100\% \times \frac{8.6 \times 10^{10} \text{ m}^2}{1.5 \times 10^{14} \text{ m}^2} = 0.06\%$

Decreasing costs of photovoltaic modules has enabled rapid deployment of these technologies, but solar energy only supplies a fraction of total electricity generation capacity. Between 2010 and 2023, the global average cost of electricity generated from solar (non-concentrated) photovoltaics decreased from 0.46 $/kWh to 0.04 $/kWh, and is now less expensive than electricity produced from fossil fuels, which cost between 0.05 $/kWh-0.2 $/kWh.[13] This decrease in price in is driven mostly by a combination of reductions in manufacturing costs and improvements in performance of silicon-based modules, which represent ca. 95% of new installations of photovoltaics in the world.[14] Indeed, from 2010 to 2024, the cost of Si module fabrication decreased 10-fold from 2.11$/ W_{dc} to 0.2 $/$W_{dc}$ while the PCE increased over 50% from 14.0 to 22.5%.[15] Such decreases in prices have afforded large increases in adoption of photovoltaics, which represented an impressive 93% of new global capacity installations in 2024.[16] In the United States newly installed electricity generation capacity increased from only <5 % solar between 2010-2014 to a projected 71% in 2025.[17] However, as of 2023 only 240 of 4300 terawatt hours (TWh), or 5.6% of electricity generated in the United States were produced by photovoltaics.[6] By comparison, 2510 TWh or 58% of this electricity was produced by burning of

fossil fuels. Thus, there remains a need to continue deployment of photovoltaic installations on the order of Terawatt hours to reduce reliance on fossil fuels. More efficient modules will expediate this monumental task.

1.2. Operating Principles of Photovoltaics

Thin film photovoltaic devices extract charge carriers using a potential difference arising from photoexcitation. The generic architecture of a thin film photovoltaic device includes a supporting substrate, a p-n heterojunction, and supporting metal electrode. The heterojunction is formed by a visible bandgap semiconductor, often a p-type material, and a wide band gap (ideally >3 eV to avoid parasitic absorption of visible light), n-type semiconductor as the electron transport layer. For devices utilizing n-type absorber layers, a p-type hole transport layer is used as the partner material. Some photovoltaic devices, such as those based on halide perovskite photo-absorbers, use a p-i-n junction, where the photo-absorber is intrinsic and surrounded by an n-type electron transport layer and p-type hole transport layer.[18] Figure 1.1 illustrates the working principles of photovoltaic based on a p-type photo-absorber. In the dark, the Fermi levels (E_F) of the devices equilibrate as charge carriers flow between the adjacent layers to establish electrochemical equilibrium (Figure 1.1b).[19] But, when the absorber layer is struck by incident photons with energies above its band gap, electrons are excited from the valence band to the conduction band. The electrons then flow downhill in energy and move from the absorber layer conduction band into the conduction band of the electron transport layer, and then to the Fermi level of the adjacent metal electrode (Figure 1.1c). Photoexcitation also leaves behind a charge carrying hole, a quasiparticle representing the absence of an electron, which moves uphill in energy from the valence band of the absorber layer into the second, adjacent metal electrode. Together,

these processes move the device out of electrochemical equilibrium and the Fermi-levels of the p and n-type materials junction return to energies near their positions out of electrical contact (Figure 1.1a). The difference in energy between these quasi-Fermi levels is open circuit voltage of the photovoltaic device.

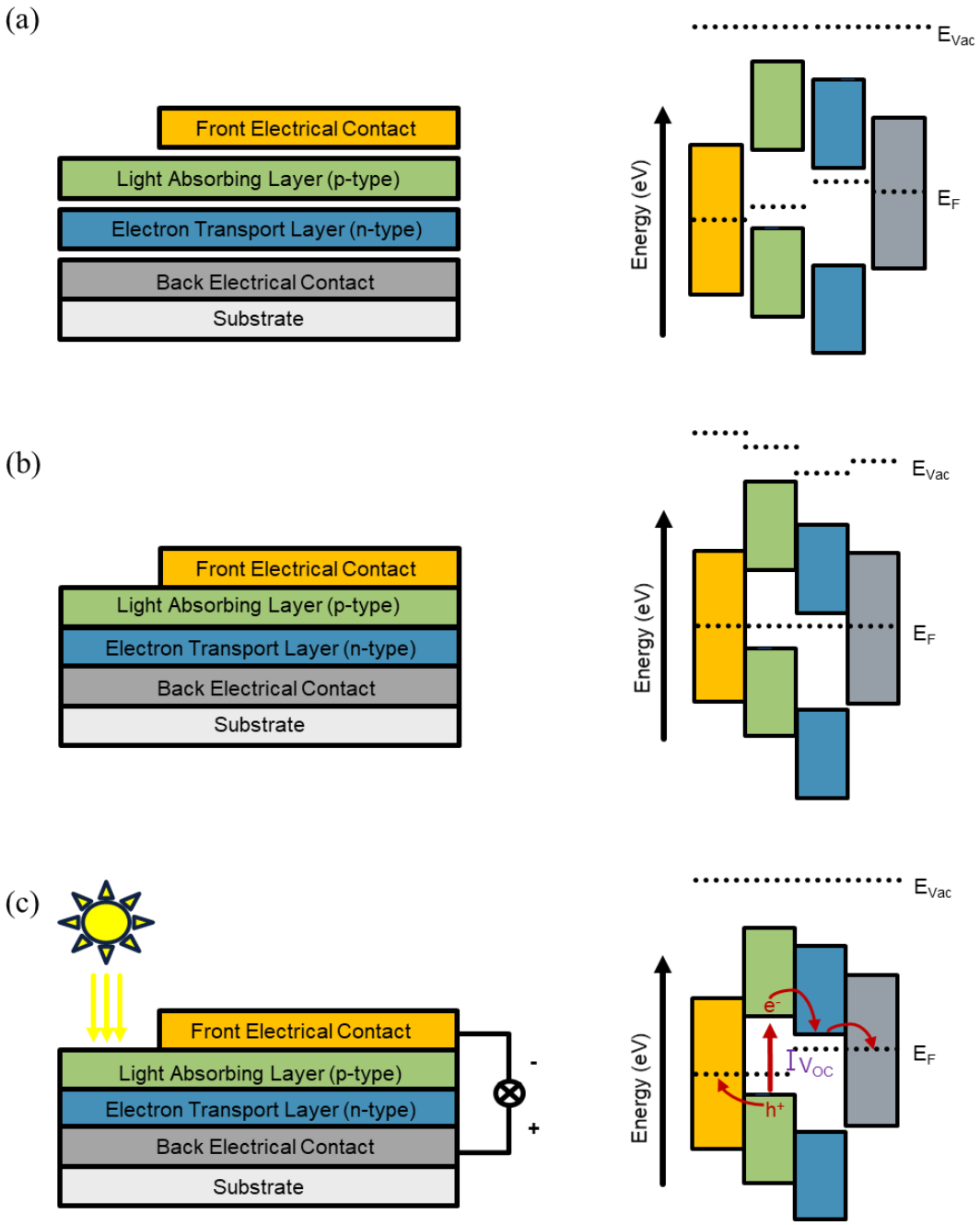

Figure 1.1. (a) Positions of the energy bands and Fermi-levels of the component layers of the device out of contact. (b) The layers of the device are electrically connected in the dark and electrochemical equilibrium is reached. (c) The device is exposed to light and driven out of electrochemical equilibrium. The Fermi-level and vacuum energy level are denoted E_F and E_{Vac}, respectively. Electrons, holes and the open circuit voltage are represented by e^-, h^+ and V_{OC}, respectively.

The Shockley-Queisser limit and kinetics of charge carrier propagation limit the power conversion efficiency (PCE) of single junction photovoltaics. The amount of solar flux that can be converted to electricity is fundamentally limited by the bandgap of the photo-absorber, as photons with energies below the bandgap are not absorbed, while thermalization of carriers prevents extraction of all electrical energy from photons with energies well above the gap.[20] The Schottky-Quiesser limit accounts for these losses, along with the distribution of solar irradiance to define the optimal band gap for terrestrial photovoltaics as 1.34 eV and the corresponding maximum PCE as 33.7% (although bandgaps of ca. 1.1-1.5 can afford maximum PCE's of >32%). Reductions in device efficiency also arise from kinetic processes controlling recombination of charge carriers before extraction to the electrodes.[20] Useful metrics for predicting the efficiency of charge carrier collection include the carrier lifetime, diffusion length and absorption coefficient.[21] Indeed, to extract all photoexcited charge carriers, the diffusion length must be greater than or equal to half of the absorber layer thickness. In this respect, thin film absorbers with high absorption coefficients (10^4-10^5 cm^{-1}) can be advantageous, as charge transport properties do not have to match those achieved for Si, with absorber thicknesses ca. 100× higher.[20]

1.3 Tandem Photovoltaics and Current Candidate Top Cells

The next generation of photovoltaics will be tandem modules. In these modules, two photovoltaic devices are stacked on top of one another, with the top device (or top cell) utilizing a wider bandgap photo-absorber than the bottom device (bottom cell).[22] In this configuration, high energy photons are more effectively converted to electricity by the top cell, while photons below the bandgap of the top cell are transmitted and absorbed by the bottom cell. Thus, with the use of two photo-absorber layers, efficiencies greater than either absorber alone can be achieved. With

proper matching of photo-absorber bandgaps and spectral efficiencies,[22] PCE's beyond the Shockley-Queisser limit can be accessed, with predicted PCE's as high as 45% for tandem modules.[22, 23] Importantly, tandem photovoltaics have already been shown experimentally to access PCE's beyond the Shockley-Quessier limit for single junction modules, with III-V on Si and perovskite on Si tandem modules achieving impressive record PCEs of 36.1% and 34.6%, respectively.[24] For comparison, the best research scale Si modules have reported PCEs of 26.8%[24], and the predicted maximum PCE of Si based modules is 29.5%.[20, 25] Thus, assembly of tandem photovoltaics from existing photo-absorber layers offers significant advantages in increasing PCE gains compared to just optimizing existing technologies. For this reason, there is significant research underway into candidate top cells for existing, lower bandgap modules such as Si and CdTe.[23]

Halide perovskites are of significant interest as top cells for tandem photovoltaics due their tunable bandgaps and potential for inexpensive and scalable processing. The perovskite structure is ABX_3, where A and B are either metallic or organic cations, and X is a halide. By tuning the composition of these components, the bandgap of halide perovskites can be varied from 1.2 to 2.3 eV.[22] Bandgaps of 1.7-1.8 eV provide the maximum theoretical PCE of 45% for top cells paired with Si.[22, 23] Typically, increasing the bromine to iodine ratio is used to tailor the bandgap of mixed halide perovskites to the desired range of 1.7-1.8,[23] however doing so often leads to lower carrier lifetimes and segregation into bromide and iodide rich phases under illumination.[22, 26] Efforts are underway to use surface passivation and cation substitution to prevent phase segregation in these materials.[27, 28] Regardless, mixed halide perovskites across several compositions benefit from potentially scalable solution processing methods with low thermal budgets, such as blade coating,

slot-die coating, spray coating, and ink jet coating.[23, 29] For this reason, several startups are working to commercialize tandem photovoltaics utilizing perovskite top cells.[30]

III-V semiconductors offer superior performance for tandem and multijunction photovoltaics, but deployment of these technologies is inhibited by high manufacturing costs. Of particular interest as a top cell from this family is GaInP, and with a bandgap of 1.8 eV,[31] can provided maximum theoretical PCE's of 45% and 42% for Si and CdTe bottom cells, respectively.[22] III-IV materials are often used to fabricate multi-junction modules, with GaInP/GaAs/Ge often used in space applications,[23] and GaInP/GaAs/GaInAs demonstrating a PCE of 39.5%, the highest of any non-concentrator module.[24] However, epitaxial growth of III-V films is required to obtain materials with crystallinity enabling the desired carrier transport properties.[32] Low throughput and high costs of wafers and equipment necessary for epitaxial growth have raised the cost of III-V modules as high as 150 $/W, which is ca. 400× higher than for commercially available Si and CdTe modules.[33] Direct deposition of III-V onto Si is possible and can lower manufacturing of tandem modules, but heteroepitaxial growth reduces device efficiency due to worse material quality.[34] To preserve material quality, III-V semiconductors can be deposited onto epitaxial substrates and lifted off to transfer to Si modules,[34] which adds complexity to manufacturing and lowers throughput.[33]

1.4. Metal Sulfides as Top Cells for Tandem Photovoltaics

1.4.1. Criteria for Selecting Top Cells

Binary, ternary, and complex metal chalcogenides span a multitude of promising and realized photo-absorbing materials. Most notable are cadmium telluride (CdTe), the transition metal dichalcogenides (such as molybdenum disulfide), chalcogenide perovskites, and quaternary

or complex chalcogenides such as copper indium gallium selenide (CIGS) and copper zin tin sulfide (CZTS). For brevity and relevance to materials focused on in later sections of the thesis, this review will focus on binary metal sulfide photo-absorbers. In selecting these materials as candidate top cells for existing technologies, the bandgap should be 1.6-2.1 eV to maximize the efficiency of existing Si and CdTe modules.[22] This lead to the selection of germanium(II) sulfide, cubic phase tin(II) sulfide, antimony(III) sulfide, zirconium(IV) sulfide, and hafnium(IV) sulfide for review, although several other binary metal sulfides exist with direct bandgaps between 1.6-2.1 eV, including but not limited to, copper(I) sulfide (ca. 1.8 eV),[35-37] mercury(II) sulfide (ca. 2 eV),[37, 38] and beta phase indium (III) sulfide (ca. 2.1 eV).[39-41] Finally, while this review will focus only on binary sulfides, a plethora of reviews are available on ternary[42-44] and quaternary[45-47] sulfide absorbers.

Vacuum deposition methods may enable rapid deployment of top cells for tandem photovoltaics and have been demonstrated at commercial scale for other metal chalcogenides. Of particular note is close-space sublimation, which is used to deposit CdTe absorber layers in photovoltaics at rates as high as 10 μm/min.[9, 48] Continued improvements to CdTe manufacturing has allowed these modules to account for almost half of the United States production capacity.[49] Chemical vapor deposition (CVD) has also been scaled industrially, and is used deposit fluorine doped tin(IV) oxide (FTO) on glass.[50] For many tandem module architectures, the top and bottom photovoltaic devices can be fabricated separately, which adds flexibility to manufacturing and loosens temperature constraints. To utilize 2T tandem architectures without wafer bonding (i.e., direct deposition of top cell layers onto the bottom cell),[23] close-space sublimation and CVD substrate temperatures should be minimized, ideally to <500 °C, which is the maximum temperature most Si modules can withstand.[22]

1.4.2. Germanium(II) sulfide

Germanium(II) sulfide (GeS) is a promising 2-D semiconductor with closely spaced direct and indirect bandgaps in the range of 1.6-1.8 eV and with a absorption coefficient of $>10^4$ cm^{-1}.[51, 52] The minority carrier mobility is reported as high as 86-90 $cm^2V^{-1}s^{-1}$ [53, 54] and photoexcited carrier lifetimes are 120-565 ps.[54-56] Some reports indicate that GeS has high resistivity, with single crystals showing values of either 10^2-10^3 or 10^6-10^7 Ω·cm.[57, 58] Establishing low resistance ohmic contact between GeS and metal contacts has been proven to be difficult due to Fermi-level pinning.[59]

GeS photovoltaics have recently been reported,[52, 60-62] with the first demonstration in 2021 still holding the record efficiency of 1.36%.[52] The champion GeS devices were fabricated using close-space sublimation of GeS at a temperature of 480 °C. Differences in thermal expansion coefficients of GeS and the underlying substrate resulted in film delamination, but this issue was resolved using a $MoSe_2$ interfacial layer.

GeS films can be deposited by thermal evaporation and close-space sublimation. Conveniently, GeS evaporates under vacuum between 300-400 °C as the molecular species,[63-65] allowing for congruent evaporation of films.[52] This sublimation mechanism enables close-space sublimation of stoichiometric films, with substrate temperatures of 200-390 °C[66] and 480 °C[52] reported. Vapor transport has also been used to deposit GeS films,[62, 67] as well as simple thermal evaporation.[68-70] When depositing GeS using physical vapor deposition, substrate temperatures of ≥350 °C are typically required to obtain crystalline films.[52, 66, 67]

There are limited reports of CVD and ALD of GeS films. CVD has been reported once using [Ge^{n}Bu$_3$(S^{n}Bu)] as a single source precursor at 600 °C and producing polycrystalline films of orthorhombic GeS.[71] The films were slightly Ge rich and micrographs show the films are

discontinuous. ALD using rac-1,3-Di-tert-butyl-4,5-dimethyl-1,3-diaza-2-germacyclopentane-2-ylidene and H_2S at 50-200 °C has been shown to deposit highly conformal and continuous GeS films,[72] but the material was amorphous. No other reports of either CVD or ALD of GeS are known, however, CVD and ALD of congeners GeSe[71, 73-75] and GeTe[71, 76, 77] have been explored.

1.4.3. Cubic Tin(II) sulfide

Tin(II) sulfide has received significant attention as photo-absorber layer for its earth abundant and non-toxic elements. Most efforts on this material have focused on the lower band gap, ca. 1.1-1.3 ev,[78, 79] orthorhombic phase of SnS, which has resulted in photovoltaics with PCEs of up to 4.4%[78, 80] However, the direct gap of orthorhombic SnS is too low for use as a top cell with either Si or CdTe.[22] Instead, the cubic phase of SnS is more appropriate, with a reported band gap of ca. 1.7 eV[81-83] and absorption coefficient of $>10^4$ cm^{-1}.[81] The electrical properties are also promising, with films fabricated with mobilities as high as 66 and 75 $cm^2V^{-1}s^{-1}$,[83, 84] and carrier concentrations on the order of 10^{15}-10^{16} cm^{-3},[83, 84] although lower values of 10^{12}-10^{13} are also reported.[85] Resistivities as low as 3.1 Ω·cm have been reported,[84] but films often suffer from high resistivities, typically on the order of 10^4-10^5 Ω·cm.[81, 83, 85, 86]

Although SnS can be deposited by close-space sublimation, there are no reports of purely cubic phase films obtained by this method. Instead, SnS films deposited by close-space sublimation are orthorhombic,[87-89] likely due to the high substrate temperatures of 450-500 °C. This is likely related to the metastable nature of cubic SnS,[90] with some studies showing conversion of the cubic phase to the orthorhombic phase with temperatures of >350 °C .[80, 84, 91] Indeed, lower temperature syntheses by chemical bath deposition[82, 83, 85] and ALD[80, 86, 92] have been shown to preferentially form cubic SnS.

Few ALD and CVD routes are known to deposit cubic SnS films. Of available methods for obtaining cubic SnS by ALD, the most common is by the reaction of tin(II) acetylacetonate and H_2S at 120 °C. In these studies, it was found that increasing H_2S purge times and use of substrates with strong interactions with the acetylacetonate ligand promote growth of cubic phase films.[86, 92, 93] Photovoltaics have been prepared from 35 nm thick films of cubic SnS deposited by this recipe and demonstrate a maximum PCE of 0.24%.[86] The reaction of bis(*N*,*N*′-diisopropylformamidinato)tin(II) and H_2S produces cubic SnS films at temperatures of 70 and 80 °C, but increasing film temperatures and thicknesses promote formation of the orthorhombic phase.[80, 94] Photovoltaics prepared from these cubic SnS layers have low short circuit current densities and a PCE was not reported. CVD of cubic SnS films is less common, with one report demonstrating growth at 300 °C using (dimethylamido)(*N*-phenyl-*N*′,*N*′-dimethylthiouriate)tin(II).[91]

1.4.4. Antimony(III) sulfide

Antimony(III) sulfide (Sb_2S_3) and congener antimony(III) selenide (Sb_2Se_3) show great promise as photo-absorbers. The record PCE's for Sb_2S_3 and Sb_2Se_3 photovoltaics are 8% and 10.1% respectively.[95, 96] Due a higher bandgap of ca. 1.7-1.8 eV,[97, 98] Sb_2S_3 is of particular interest as a top cell. The optoelectronic properties of Sb_2S_3 are highly favorable, with an absorption coefficient of 10^4-10^5 cm^{-1},[97, 98] carrier mobility of 10 $cm^2V^{-1}s^{-1}$,[99] diffusion length of ca. 1 μm,[100] and lifetime of 23 ns.[98]

Close-space sublimation can be used to deposit Sb_2S_3 at low growth temperatures. Typical parameters for these depositions are source temperatures of 500-580[101-103], and substrate temperatures of 300-400 °C.[101-103] Growth temperatures as low as 240 °C have been reported, but

produces films with significantly smaller crystallites than at 340-380 °C under the same conditions.[104] Film morphology can also be controlled by source temperatures, with faster growth rates encouraging larger grain growth in some instances.[101] Grain growth has also been demonstrated by deposition of an Sb_2S_3 seed layer prior to close-space sublimation, and enabled fabrication of photovoltaics with PCE's as high as 4.78%,[103] which remain the record for Sb_2S_3 cells processed using close-space sublimation.

Sb_2S_3 films can be deposited by both CVD and ALD, although the latter requires annealing to yield crystalline films. ALD of Sb_2S_3 has only been demonstrated using tris(dimethylamino)antimony(III) and H_2S, typically at temperatures of 120-130 °C,[105-107] although temperatures of 60-225 have been explored.[108] In all cases amorphous films were obtained, and required annealing at 300-330 °C to crystallize.[105-108] The highest reported PCE of Sb_2S_3 photovoltaics deposited using ALD is 5.77%.[105] More routes are available to Sb_2S_3 by CVD, notably with the reaction of $SbCl_3$ and H_2S producing continuous films at 300 °C and atmospheric pressure.[109] Several single source precursors for Sb_2S_3 are known, including *tris*(thiobenzoato)antimony(III),[110] antimony(III) tris(t-butylthiolate) and antimony(III) tris(2,2,2-trifluoroethanethiolate,[111] and several antimony dithiocarbamates.[112] However, films deposited by these precursors tend to have discontinuous morphologies due to the formation of either large platelets or rods.

1.4.5. Zirconium(IV) sulfide

Zirconium(IV) sulfide is an n-type photo absorber with attractive optoelectronic properties for use as a top cell. The indirect bandgap is typically reported between 1.7-1.8 eV[113, 114] although there is less certainty in the direct bandgap, with a range of 2.1-2.4 eV.[114-116] The absorption

coefficient is on the order of 10^3 cm^{-1} at the direct bandgap .[113, 114] Like for many transition metal dichalcogenides (TMDCs), most attention has been paid to monolayer and few layers variants of ZrS_2 for predicted carrier mobilities of >1200 $cm^2V^{-1}s^{-1}$.[117, 118] Recently, mobilities as high as 1250 $cm^2V^{-1}s^{-1}$ were demonstrated for 5 nm thick ZrS_2 films obtained by a combination of sputtering and sulfur annealing.[119] Carrier transport is also favorable in the bulk material, with mobilities of 1-5 $cm^2V^{-1}s^{-1}$ in films,[120-122] and as high as 61 $cm^2V^{-1}s^{-1}$ in single crystals.[123] The carrier concentration typically falls between 10^{17}–10^{18} cm^{-3},[122, 124, 125] but has been reported as high as 10^{19}–10^{20} cm^{-3}.[119] Only one demonstration of ZrS_2 photovoltaic device exists to date, which used drop-cast nanobelts to fabricate a Schottky solar cell with a PCE of 1.2%.[126]

High temperature CVD is typically used to deposit ZrS_2 films, although lower temperature methods have been reported. The most common precursor for ZrS_2 CVD are $ZrCl_4$ and sulfur, with temperatures of ≥800 °C promoting growth of highly crystalline films.[120-122, 127, 128] ZrS_2 films deposited under these conditions tend to have smooth grains with diameters on the order of 1 μm lying parallel to the substrate surface, particularly those grown epitaxially on sapphire substrates,[122, 127, 128] Flakey morphologies have been obtained on Si/SiO_2.[129] Lower temperature CVD of ZrS_2 has been achieved using alternative precursors, including $ZrOCl_2$ and thiourea at 430 °C,[130] and single-source zirconium dithiocarbamates at 400 °C.[131] Perhaps most notable is the CVD reaction of $ZrCl_4$ with H_2S instead of sulfur, which decreases the growth temperature as low as 450 °C.[132]

Reports of ALD of ZrS_2 films are limited compared to CVD. The first report of ALD of ZrS_2 films investigated growth using either $ZrCl_4$ or $Zr(NEtMe)_4$ and H_2S.[133] It was found that replacing $ZrCl_4$ with $Zr(NEtMe)_4$ lowered the minimum temperature for deposition of crystalline films from 350 to 200 °C. Films grown from $ZrCl_4$ and H_2S are moderately crystalline and have

compact grains under 100 nm in diameter. The only other report of ZrS_2 ALD explored growth using $Zr(NMe_2)_4$ and H_2S at 75-300 °C.[134] Films were amorphous at deposition temperatures of 75 °C and show diffractions associated with Zr_3S_4 or ZrS_3 as the temperature is increased to 200 and 300 °C.

Close-space sublimation has not been demonstrated for ZrS_2 films. References on the vapor pressure of ZrS_2 are scarce, with only one report suggesting ZrS_2 decomposes during evaporation and that sulfur constitutes the majority of the gas phase above ZrS_2.[135]

1.4.6. Hafnium(IV) sulfide

Hafnium(IV) sulfide may have appropriate optoelectronic properties for use as top cell. The indirect bandgap is typically reported as 1.9-2.1 eV,[113, 136, 137] with an absorption coefficient on the order of 10^3 at this energy. The direct gap is reported between 2.6-2.7 eV,[138-140] but as low as 2.1 eV.[141] Typical values of the direct gap of HfS_2 are outside the optimal bandgap of top cells for Si and CdTe.[22] There are few reports on the electrical properties of bulk HfS_2, with an early report offering a discouraging resistivity of 10^6-10^7 Ω·cm.[125] Instead, the electrical properties of monolayer and few layer HfS_2 are predicted to be far superior, with estimated carrier mobilities of >1500 $cm^2V^{-1}s^{-1}$.[117, 118]

Most reports of vapor deposition of HfS_2 use $HfCl_4$ and S_2 as CVD precursors at growth temperatures of 800-1000 °C.[139, 142-147] Films are typically highly crystalline and oriented in the (0001) plane, particularly on sapphire substrates, where epitaxial growth has been demonstrated.[139] CVD at 400-450 °C has been demonstrated using $Hf(S_2CNEt_2)_4$ as a single source precursor.[131] The growth temperature can be lowered even further using ALD, with growth by this method first reported from either $HfCl_4$, HfI_4, or $Hf(NEtMe)_4$ and H_2S.[133] The minimum temperatures required

for growth of crystalline films using $HfCl_4$, HfI_4, or $Hf(NEtMe)_4$ were 350, 300 and 200 °C, respectively. Plasma-assisted ALD has also been attempted using $Hf(NEtMe)_4$ and H_2S, but the crystallization threshold temperature was raised to 350 °C, possibly due to significant oxygen incorporation in films. Amorphous HfS_2 films can be deposited at temperatures as low as 60 °C from $Hf(NMe_2)_4$ and H_2S.[148, 149] Finally, like for ZrS_2, there are no reports of close-space sublimation of HfS_2. Photovoltaics have not been reported with HfS_2 absorber layers.

1.5 Conclusions

Anthropogenic global warming presents a fundamental threat to humanity and requires decarbonization of energy and electricity sources to prevent permanent damages. Photovoltaics are promising alternatives to fossil fuels, and through sustained efforts the cost of electricity from these technologies is now lower than fossil fuels in some markets.[13] Accordingly, photovoltaics represent the majority of new installations of electricity capacity in the United States,[17] however, the majority of electricity is still generated by fossil fuels.

Tandem photovoltaics can rapidly increase the power conversion efficiencies of available modules and can help generate a greater fraction of electricity from renewable sources. Although mixed halide perovskites and III-V semiconductors have seen success as top cells,[24] these technologies have not been deployed at scale terrestrially. Metal sulfides are an attractive class of materials with photo-absorbers exhibiting appropriate bandgaps for use as top cells with existing Si and CdTe moduless.[22] Of particular interest are the binary sulfides, due to available and scalable vacuum deposition techniques of close-space sublimation and chemical vapor deposition. This dissertation presents ZrS_2 and GeS as candidate photo-absorbers for top cells, and demonstrates

low temperature, vacuum assisted preparation of each. It is our hope that this work will inspire further investigations into binary sulfides as top cells for tandem photovoltaics.

1.6. References

1. Global CO_2 emissions from electricity generation, 2015-2027. https://www.iea.org/data-and-statistics/charts/global-co2-emissions-from-electricity-generation-2015-2027 (accessed April 28, 2025).
2. Lee, H.; Romero, J. *Climate Change 2023: Synthesis Report. Contribution of Working Groups I, II and III to the Sixth Assessment Report of the Intergovernmental Panel on Climate Change*; Intergovernmental Panel on Climate Change: Geneva, Switzerland, 2023.
3. IPCC *Global Warming of 1.5°C: IPCC Special Report on Impacts of Global Warming of 1.5°C above Pre-industrial Levels in Context of Strengthening Response to Climate Change, Sustainable Development, and Efforts to Eradicate Poverty*; 9781009157957; Cambridge University Press: Cambridge, 2022.
4. IEA; IREA; UNSD; World Bank; WHO *Tracking SDG7: The Energy Progress Report, 2023*; World Bank: Washington, DC, 2023.
5. IEA *Electricity 2025*; IEA: Paris, 2025.
6. International Energy Overview. https://www.eia.gov/international/overview/world (accessed April 28 ,2025).
7. Energy on a sphere. https://sos.noaa.gov/catalog/live-programs/energy-on-a-sphere/ (accessed April 28, 2025).
8. Crystalline Silicon Photovoltaics Research. *U.S. Department of Energy, Office of Energy Efficiency & Renewable Energy* **2023**.

9. Series 7. https://www.firstsolar.com/en/Products/Series-7 (accessed April 28, 2025).

10. Gordon, R. In *Why don't we have inexpensive PV systems made from Earth-abundant elements?*, ACS National Meeting, San Francisco, CA, August 12, 2014; San Francisco, CA, 2014.

11. Global land use for agriculture. https://ourworldindata.org/global-land-for-agriculture (accessed March 23, 2025).

12. Zhang, Z.; Qian, Z.; Chen, M.; Zhu, R.; Zhang, F.; Zhong, T.; Lin, J.; Ning, L.; Xie, W.; Creutzig, F.; Tang, W.; Liu, L.; Yang, J.; Pu, Y.; Cai, W.; Pu, Y.; Liu, D.; Yang, H.; Su, H.; Lu, M.; Li, F.; Cui, X.; Xie, Z.; Sheng, T.; Zhang, K.; Santi, P.; Tian, L.; Lü, G.; Yan, J., Worldwide rooftop photovoltaic electricity generation may mitigate global warming. *Nature Climate Change* **2025,** *15* (4), 393-402.

13. Levelized cost of energy by technology. https://ourworldindata.org/grapher/levelized-cost-of-energy (accessed March 23, 2025).

14. Feldman, D.; Dummit, K.; Zuboy, J.; Margolis, R. *Spring 2023 Solar Industry Update*; 2023. https://doi.org/10.2172/1974994

15. Solar Photovoltaic Manufacturing Cost Analysis. https://www.nrel.gov/solar/market-research-analysis/solar-manufacturing-cost.html (accessed March 23, 2025).

16. Renewables in 2024: 5 Key Facts Behind a Record-Breaking Year. https://www.irena.org/News/articles/2025/Apr/Renewables-in-2024-5-Key-Facts-Behind-a-Record-Breaking-Year (accessed April 28, 2025).

17. Feldman, D.; Zuboy, J.; Dummit, K.; Stright, D.; Heine, M.; Mirletz, H.; Margolis, R., Winter 2024 Solar Industry Update. 2024. https://doi.org/10.2172/2316015

18. Zhang, H.; Park, N.-G., Progress and issues in p-i-n type perovskite solar cells. *DeCarbon* **2024,** *3*, 100025.

19. Schlaf, R. Calibration of Photoemission Spectra and Work Function Determination. http://rsl.eng.usf.edu/Documents/Tutorials/PEScalibration.pdf (accessed May 1, 2025).

20. Polman, A.; Knight, M.; Garnett, E. C.; Ehrler, B.; Sinke, W. C., Photovoltaic materials: Present efficiencies and future challenges. *Science* **2016,** *352* (6283), aad4424.

21. Jaramillo, R.; Sher, M.-J.; Ofori-Okai, B. K.; Steinmann, V.; Yang, C.; Hartman, K.; Nelson, K. A.; Lindenberg, A. M.; Gordon, R. G.; Buonassisi, T., Transient terahertz photoconductivity measurements of minority-carrier lifetime in tin sulfide thin films: Advanced metrology for an early stage photovoltaic material. *Journal of Applied Physics* **2016,** *119* (3), 035101.

22. Leijtens, T.; Bush, K. A.; Prasanna, R.; McGehee, M. D., Opportunities and challenges for tandem solar cells using metal halide perovskite semiconductors. *Nature Energy* **2018,** *3* (10), 828-838.

23. Alberi, K.; Berry, J. J.; Cordell, J. J.; Friedman, D. J.; Geisz, J. F.; Kirmani, A. R.; Larson, B. W.; McMahon, W. E.; Mansfield, L. M.; Ndione, P. F.; Owen-Bellini, M.; Palmstrom, A. F.; Reese, M. O.; Reese, S. B.; Steiner, M. A.; Tamboli, A. C.; Theingi, S.; Warren, E. L., A roadmap for tandem photovoltaics. *Joule* **2024,** *8* (3), 658-692.

24. Best Research-Cell Efficiency Chart. https://www.nrel.gov/pv/cell-efficiency.html (accessed April 28, 2025).

25. Veith-Wolf, B. A.; Schäfer, S.; Brendel, R.; Schmidt, J., Reassessment of intrinsic lifetime limit in n-type crystalline silicon and implication on maximum solar cell efficiency. *Solar Energy Materials and Solar Cells* **2018,** *186*, 194-199.

26. Hoke, E. T.; Slotcavage, D. J.; Dohner, E. R.; Bowring, A. R.; Karunadasa, H. I.; McGehee, M. D., Reversible photo-induced trap formation in mixed-halide hybrid perovskites for photovoltaics. *Chemical Science* **2015,** *6* (1), 613-617.

27. Li, S.; Zheng, Z.; Ju, J.; Cheng, S.; Chen, F.; Xue, Z.; Ma, L.; Wang, Z., A Generic Strategy to Stabilize Wide Bandgap Perovskites for Efficient Tandem Solar Cells. *Advanced Materials* **2024,** *36* (9), 2307701.

28. Knight, A. J.; Herz, L. M., Preventing phase segregation in mixed-halide perovskites: a perspective. *Energy & Environmental Science* **2020,** *13* (7), 2024-2046.

29. Li, Z.; Klein, T. R.; Kim, D. H.; Yang, M.; Berry, J. J.; van Hest, M. F. A. M.; Zhu, K., Scalable fabrication of perovskite solar cells. *Nature Reviews Materials* **2018,** *3* (4), 18017.

30. Tandem PV Raises $50M to Take Back U.S. Leadership with New Perovskite Solar Manufacturing. https://www.tandempv.com/news/tandem-pv-raises-%2450m-to-take-back-u.s.-leadership-with-new-perovskite-solar-manufacturing (accessed April 28, 2025).

31. Essig, S.; Ward, S.; Steiner, M. A.; Friedman, D. J.; Geisz, J. F.; Stradins, P.; Young, D. L., Progress Towards a 30% Efficient GaInP/Si Tandem Solar Cell. *Energy Procedia* **2015,** *77*, 464-469.

32. Saif, O. M.; Zekry, A. H.; Abouelatta, M.; Shaker, A., A Comprehensive Review of Tandem Solar Cells Integrated on Silicon Substrate: III/V vs Perovskite. *Silicon* **2023,** *15* (15), 6329-6347.

33. Horowitz, K. A.; Remo, T. W.; Smith, B.; Ptak, A. J. *A Techno-Economic Analysis and Cost Reduction Roadmap for III-V Solar Cells*; National Renewable Energy Lab. (NREL), Golden, CO (United States): United States, 2018.

34. VanSant, K. T.; Tamboli, A. C.; Warren, E. L., III-V-on-Si Tandem Solar Cells. *Joule* **2021,** *5* (3), 514-518.

35. Yang, W.; Zhang, X.; Tilley, S. D., Emerging Binary Chalcogenide Light Absorbers: Material Specific Promises and Challenges. *Chemistry of Materials* **2021,** *33* (10), 3467-3489.

36. Martinson, A. B. F.; Elam, J. W.; Pellin, M. J., Atomic layer deposition of Cu2S for future application in photovoltaics. *Applied Physics Letters* **2009,** *94* (12).

37. Moon, D. G.; Rehan, S.; Yeon, D. H.; Lee, S. M.; Park, S. J.; Ahn, S.; Cho, Y. S., A review on binary metal sulfide heterojunction solar cells. *Solar Energy Materials and Solar Cells* **2019,** *200*, 109963.

38. Simpson, C. T.; Imaino, W.; Becker, W. M., Photoluminescence, optical absorption, and excitation spectra of cinnabar (α-HgS). *Physical Review B* **1980,** *22* (2), 911-920.

39. Rehwald, W.; Harbeke, G., On the conduction mechanism in single crystal β-indium sulfide In2S3. *Journal of Physics and Chemistry of Solids* **1965,** *26* (8), 1309-1324.

40. Bhira, L.; Essaidi, H.; Belgacem, S.; Couturier, G.; Salardenne, J.; Barreaux, N.; Bernede, J. C., Structural and Photoelectrical Properties of Sprayed β-In_2S_3 Thin Films. *physica status solidi (a)* **2000,** *181* (2), 427-435.

41. Gorai, S.; Guha, P.; Ganguli, D.; Chaudhuri, S., Chemical synthesis of β-In_2S_3 powder and its optical characterization. *Materials Chemistry and Physics* **2003,** *82* (3), 974-979.

42. Devika, R. S.; Vengatesh, P.; Shyju, T. S., Review on ternary chalcogenides: Potential photoabsorbers. *Materials Today: Proceedings* **2023**.

43. Tiwari, D.; Hutter, O. S.; Longo, G., Chalcogenide perovskites for photovoltaics: current status and prospects. *Journal of Physics: Energy* **2021,** *3* (3), 034010.

44. Sopiha, K. V.; Comparotto, C.; Márquez, J. A.; Scragg, J. J. S., Chalcogenide Perovskites: Tantalizing Prospects, Challenging Materials. *Advanced Optical Materials* **2022,** *10* (3), 2101704.

45. Ghorpade, U. V.; Suryawanshi, M. P.; Green, M. A.; Wu, T.; Hao, X.; Ryan, K. M., Emerging Chalcohalide Materials for Energy Applications. *Chemical Reviews* **2023,** *123* (1), 327-378.

46. Shah, U. A.; Wang, A.; Irfan Ullah, M.; Ishaq, M.; Shah, I. A.; Zeng, Y.; Abbasi, M. S.; Umair, M. A.; Farooq, U.; Liang, G.-X.; Sun, K., A Deep Dive into Cu_2ZnSnS_4 (CZTS) Solar Cells: A Review of Exploring Roadblocks, Breakthroughs, and Shaping the Future. *Small* **2024,** *20* (30), 2310584.

47. Hadke, S.; Huang, M.; Chen, C.; Tay, Y. F.; Chen, S.; Tang, J.; Wong, L., Emerging Chalcogenide Thin Films for Solar Energy Harvesting Devices. *Chemical Reviews* **2022,** *122* (11), 10170-10265.

48. Amin, N.; Rahman, K. S., Close-Spaced Sublimation (CSS): A Low-Cost, High-Yield Deposition System for Cadmium Telluride (CdTe) Thin Film Solar Cells. 2017; pp 361-379.

49. Feldman, D.; Margolis, R. *Q4 2019/Q1 2020 Solar Industry Update*; United States, 2020. https://www.nrel.gov/docs/fy20osti/77010.pdf

50. McCamy, J. Chemical Vapor Deposition of Coatings on Glass. https://www.lehigh.edu/imi/teched/GlassProcess/Lectures/Lecture11_McCamy_CVD%20Coatings%20On%20Glass.pdf (accessed May 1, 2025).

51. Malone, B. D.; Kaxiras, E., Quasiparticle band structures and interface physics of SnS and GeS. *Physical Review B* **2013,** *87* (24), 245312.

52. Feng, M.; Liu, S.; Hu, L.; Wu, J.; Liu, X.; Xue, D. J.; Hu, J.-S.; Wan, L.-J., Interfacial Strain Engineering in Wide-Bandgap GeS Thin Films for Photovoltaics. *Journal of the American Chemical Society* **2021,** *143*, 9664-9671.

53. Stanchev, A.; Vodenicharov, C., Photoconductivity kinetics of germanium monosulphide thin films. *Thin Solid Films* **1976,** *38* (1), 67-72.

54. Fan, X.; Su, L.; Zhang, F.; Huang, D.; Sang, D. K.; Chen, Y.; Li, Y.; Liu, F.; Li, J.; Zhang, H.; Xie, H., Layer-Dependent Properties of Ultrathin GeS Nanosheets and Application in UV–Vis Photodetectors. *ACS Applied Materials & Interfaces* **2019,** *11* (50), 47197-47206.

55. Khanmohammadi, S.; Tran, C.; Amini, H.; Colin-Ulloa, E.; Ekuma, C.; Koski, K. J.; Titova, L. V. In *Engineering ultrafast carrier dynamics in GeS: nanostructuring and small molecule intercalation*, 2022 47th International Conference on Infrared, Millimeter and Terahertz Waves (IRMMW-THz), 28 Aug.-2 Sept. 2022; 2022; pp 1-2.

56. Kushnir, K.; Shi, T.; Damian, L.; Anilao, A.; Koski, K. J.; Titova, L. V. In *Zero-Valent Au, Cu, and Sn Intercalation into GeS Nanoribbons: Tailoring Ultrafast Photoconductive Response*, Ultrafast Phenomena and Nanophotonics XXIV, 2020; p 17.

57. Bletskan, D.; Glukhov, K.; Kabatsii, V., Influence of cation vacancies and Bi impurity on the electronic structure and photoelectric properties of orthorhombic GeS. *Journal of Optoelectronics and Advanced Materials* **2019,** *21*, 629-640.

58. Solanki, G. K.; Patel, D. B.; Unadkat, S.; Agarwal, M. K., Synthesis and characterization of germanium monosulphide (GeS) single crystals grown using different transporting agents. *Pramana* **2010,** *74* (5), 813-825.

59. Sun, Y.; Jiao, Z.; Zandvliet, H. J. W.; Bampoulis, P., Strong Fermi-Level Pinning in GeS–Metal Nanocontacts. *The Journal of Physical Chemistry C* **2022,** *126* (27), 11400-11406.

60. Hu, L.; Feng, M.; Wang, X.; Liu, S.; Wu, J.; Yan, B.; Lu, W.; Wang, F.; Hu, J.-S.; Xue, D.-J., Solution-processed Ge(II)-based chalcogenide thin films with tunable bandgaps for photovoltaics. *Chemical Science* **2022**, *13*, 5944.

61. Hsueh, H.-C.; Li, J.-X.; Ho, C.-H., Polarization Photoelectric Conversion in Layered GeS. *Advanced Optical Materials* **2018,** *6* (4), 1701194.

62. Ribeiro, T. C. Science and technology of solar cells based on SnS, SnS_2 and GeS. Doctoral dissertation, Universidade Federal de Minas Gerais, 2023.

63. Lu, W.; Fang, Y.; Li, Z.; Li, S.; Liu, S.; Feng, M.; Xue, D.-J.; Hu, J.-S., Investigation of the sublimation mechanism of GeSe and GeS. *Chemical Communications* **2021,** *57* (87), 11461-11464.

64. Ross, L.; Bourgon, M., Thermal analysis of germanium(II) sulfide. *Canadian Journal of Chemistry* **2011,** *46*, 2464-2468.

65. Sutter, E.; Sutter, P., 1D Wires of 2D Layered Materials: Germanium Sulfide Nanowires as Efficient Light Emitters. *ACS Applied Nano Materials* **2018,** *1* (3), 1042-1049.

66. Drabavičius, A.; Pakštas, V.; Jasiūnas, R.; Koltsov, M.; Talaikis, M.; Naujokaitis, A.; Spalatu, N.; Kondrotas, R.; Gulbinas, V.; Franckevičius, M., Synthesis and characterization of polycrystalline GeS thin films for optoelectronic applications. *Materials Science in Semiconductor Processing* **2025,** *188*, 109193.

67. Zhang, Q.; Matsumura, R.; Fukata, N., Synthesis of Large-Area GeS Thin Films with the Assistance of Pre-deposited Amorphous Nanostructured GeS Films: Implications for Electronic and Optoelectronic Applications. *ACS Applied Nano Materials* **2023,** *6* (8), 6920-6928.

68. Stanchev, A.; Vodenicharov, C., Kinetics of Vacuum Deposition of GeS Films. *physica status solidi (a)* **1975,** *27* (2), 615-619.

69. Naik, R.; Aparimita, A.; Alagarasan, D.; Varadharajaperumal, S.; Ganesan, R., Linear and nonlinear optical properties change in Ag/GeS heterostructure thin films by thermal annealing and laser irradiation. *Optical and Quantum Electronics* **2020,** *52* (3), 136.

70. Munira, M. J. A.-H.; Raad, Compositional, Structural and Morphological Analyses of Bulk GeS Alloy and its Thin Films. **2021,** *1039*, 398-405.

71. Robinson, F.; Sethi, V.; de Groot, C. H. K.; Hector, A. L.; Huang, R.; Reid, G., Low-Pressure CVD of GeE (E = Te, Se, S) Thin Films from Alkylgermanium Chalcogenolate Precursors and Effect of Deposition Temperature on the Thermoelectric Performance of GeTe. *ACS Applied Materials & Interfaces* **2021,** *13* (40), 47773-47783.

72. Kim, S. B.; Sinsermsuksakul, P.; Hock, A. S.; Pike, R. D.; Gordon, R. G., Synthesis of N-Heterocyclic Stannylene (Sn(II)) and Germylene (Ge(II)) and a Sn(II) Amidinate and Their Application as Precursors for Atomic Layer Deposition. *Chemistry of Materials* **2014,** *26* (10), 3065-3073.

73. Kim, W.; Yoo, S.; Yoo, C.; Park, E.-S.; Jeon, J.; Kwon, Y. J.; Woo, K. S.; Kim, H. J.; Lee, Y. K.; Hwang, C. S., Atomic layer deposition of GeSe films using $HGeCl_3$ and $[(CH3)_3Si]_2Se$ with the discrete feeding method for the ovonic threshold switch. *Nanotechnology* **2018,** *29* (36), 365202.

74. Haider, A.; Deng, S.; Devulder, W.; Maes, J. W.; Girard, J.-M.; Khalil El Hajjam, G.; Kar, G. S.; Opsomer, K.; Detavernier, C.; Givens, M.; Goux, L.; Van Elshocht, S.; Delhougne, R.; Delabie, A.; Caymax, M.; Swerts, J., Pulsed chemical vapor deposition of conformal GeSe for application as an OTS selector. *Materials Advances* **2021,** *2* (5), 1635-1643.

75. Yumigeta, K.; Brayfield, C.; Cai, H.; Hajra, D.; Blei, M.; Yang, S.; Shen, Y.; Tongay, S., The synthesis of competing phase GeSe and $GeSe_2$ 2D layered materials. *RSC Advances* **2020,** *10* (63), 38227-38232.

76. Gwon, T.; Eom, T.; Yoo, S.; Lee, H.-K.; Cho, D.-Y.; Kim, M.-S.; Buchanan, I.; Xiao, M.; Ivanov, S.; Hwang, C. S., Atomic Layer Deposition of GeTe Films Using $Ge\{N[Si(CH3)_3]_2\}_2$, $\{(CH3)_3Si\}_2Te$, and Methanol. *Chemistry of Materials* **2016,** *28* (19), 7158-7166.

77. Pore, V.; Hatanpää, T.; Ritala, M.; Leskelä, M., Atomic Layer Deposition of Metal Tellurides and Selenides Using Alkylsilyl Compounds of Tellurium and Selenium. *Journal of the American Chemical Society* **2009,** *131* (10), 3478-3480.

78. Sinsermsuksakul, P.; Sun, L.; Lee, S. W.; Park, H. H.; Kim, S. B.; Yang, C.; Gordon, R. G., Overcoming Efficiency Limitations of SnS-Based Solar Cells. *Advanced Energy Materials* **2014,** *4* (15), 1400496.

79. Sinsermsuksakul, P.; Heo, J.; Noh, W.; Hock, A. S.; Gordon, R. G., Atomic Layer Deposition of Tin Monosulfide Thin Films. *Advanced Energy Materials* **2011,** *1* (6), 1116-1125.

80. Kim, S. B.; Zhao, X.; Davis, L. M.; Jayaraman, A.; Yang, C.; Gordon, R. G., Atomic Layer Deposition of Tin Monosulfide Using Vapor from Liquid Bis(*N*,*N*′-diisopropylformamidinato)tin(II) and H_2S. *ACS Applied Materials & Interfaces* **2019,** *11* (49), 45892-45902.

81. Javed, A.; Khan, N.; Bashir, S.; Ahmad, M.; Bashir, M., Thickness dependent structural, electrical and optical properties of cubic SnS thin films. *Materials Chemistry and Physics* **2020,** *246*, 122831.

82. Nair, P. K.; Garcia-Angelmo, A. R.; Nair, M. T. S., Cubic and orthorhombic SnS thin-film absorbers for tin sulfide solar cells. *physica status solidi (a)* **2016,** *213* (1), 170-177.

83. Chalapathi, U.; Poornaprakash, B.; Park, S.-H., Chemically deposited cubic SnS thin films for solar cell applications. *Solar Energy* **2016,** *139*, 238-248.

84. Kishore Bhat, T. R.; Jeganath, K.; George, S. D.; Raviprakash, Y., Annealing-induced phase conversion on spray pyrolyzed cubic-SnS thin films. *Journal of Materials Science: Materials in Electronics* **2023,** *34* (8), 747.

85. Chalapathi, U.; Poornaprakash, B.; Park, S.-H., Growth and properties of cubic SnS films prepared by chemical bath deposition using EDTA as the complexing agent. *Journal of Alloys and Compounds* **2016,** *689*, 938-944.

86. Voznyi, A. A.; Bilousov, O. V.; Landeke-Wilsmark, B.; Keller, J.; Ren, J.; Zhang, S.-L.; Hägglund, C., Ultrathin Solar Cells Based on Atomic Layer Deposition of Cubic versus Orthorhombic Tin Monosulfide. *ACS Applied Energy Materials* **2021,** *4* (8), 8085-8097.

87. Andrade-Arvizu, J. A.; García-Sánchez, M. F.; Courel-Piedrahita, M.; Santoyo-Morales, J.; Jiménez-Olarte, D.; Albor-Aguilera, M.; Vigil-Galán, O., Pressure induced directional transformations on close spaced vapor transport deposited SnS thin films. *Materials & Design* **2016,** *110*, 878-887.

88. Voznyi, A.; Kosyak, V.; Yeromenko, Y.; Keller, J.; Bērziņa, A.; Shamardin, A.; Iatsunskyi, I.; Shpetnyi, I.; Plotnikov, S.; Opanasyuk, A., Close-spaced sublimation of SnS absorber layers and SnS/CdS heterojunction solar cells with Mo and Ti back metal contacts. *Thin Solid Films* **2020,** *709*, 138153.

89. Spalatu, N.; Hiie, J.; Kaupmees, R.; Volobujeva, O.; Krustok, J.; Oja Acik, I.; Krunks, M., Postdeposition Processing of SnS Thin Films and Solar Cells: Prospective Strategy To Obtain Large, Sintered, and Doped SnS Grains by Recrystallization in the Presence of a Metal Halide Flux. *ACS Applied Materials & Interfaces* **2019,** *11* (19), 17539-17554.

90. Skelton, J. M.; Burton, L. A.; Oba, F.; Walsh, A., Metastable cubic tin sulfide: A novel phonon-stable chiral semiconductor. *APL Materials* **2017,** *5* (3).

91. Ahmet, I. Y.; Hill, M. S.; Johnson, A. L.; Peter, L. M., Polymorph-Selective Deposition of High Purity SnS Thin Films from a Single Source Precursor. *Chemistry of Materials* **2015,** *27* (22), 7680-7688.

92. Bilousov, O. V.; Voznyi, A.; Landeke-Wilsmark, B.; Villamayor, M. M. S.; Nyberg, T.; Hägglund, C., Substrate Effects on Crystal Phase in Atomic Layer Deposition of Tin Monosulfide. *Chemistry of Materials* **2021,** *33* (8), 2901-2912.

93. Bilousov, O. V.; Ren, Y.; Törndahl, T.; Donzel-Gargand, O.; Ericson, T.; Platzer-Björkman, C.; Edoff, M.; Hägglund, C., Atomic Layer Deposition of Cubic and Orthorhombic Phase Tin Monosulfide. *Chemistry of Materials* **2017,** *29* (7), 2969-2978.

94. Zhao, X.; Davis, L. M.; Lou, X.; Kim, S. B.; Uličná, S.; Jayaraman, A.; Yang, C.; Schelhas, L. T.; Gordon, R., Study of the crystal structure of SnS thin films by atomic layer deposition. *AIP Advances* **2021,** *11* (3).

95. Wang, S.; Zhao, Y.; Che, B.; Li, C.; Chen, X.; Tang, R.; Gong, J.; Wang, X.; Chen, G.; Chen, T.; Li, J.; Xiao, X., A Novel Multi-Sulfur Source Collaborative Chemical Bath Deposition Technology Enables 8%-Efficiency Sb_2S_3 Planar Solar Cells. *Advanced Materials* **2022,** *34* (41), 2206242.

96. Duan, Z.; Liang, X.; Feng, Y.; Ma, H.; Liang, B.; Wang, Y.; Luo, S.; Wang, S.; Schropp, R. E. I.; Mai, Y.; Li, Z., Sb_2Se_3 Thin-Film Solar Cells Exceeding 10% Power Conversion Efficiency Enabled by Injection Vapor Deposition Technology. *Advanced Materials* **2022,** *34* (30), 2202969.

97. Kondrotas, R.; Chen, C.; Tang, J., Sb_2S_3 Solar Cells. *Joule* **2018,** *2* (5), 857-878.

98. Barthwal, S.; Kumar, R.; Pathak, S., Present Status and Future Perspective of Antimony Chalcogenide (Sb_2X_3) Photovoltaics. *ACS Applied Energy Materials* **2022,** *5* (6), 6545-6585.

99. Savadogo, O.; Mandal, K. C., Studies on new chemically deposited photoconducting antimony trisulphide thin films. *Solar Energy Materials and Solar Cells* **1992,** *26* (1), 117-136.

100. Darga, A.; Mencaraglia, D.; Longeaud, C.; Savenije, T. J.; O'Regan, B.; Bourdais, S.; Muto, T.; Delatouche, B.; Dennler, G., On Charge Carrier Recombination in Sb2S3 and Its Implication for the Performance of Solar Cells. *The Journal of Physical Chemistry C* **2013,** *117* (40), 20525-20530.

101. Zhou, R.; Tang, B.; Xie, Q.; Wu, W.; Wan, L.; Zelewski, S. J.; Zhu, J., Orientation control of close-spaced sublimation processed Sb_2S_3 thin films for efficient and stable planar solar cells. *Applied Physics Letters* **2024,** *124* (23), 233903.

102. Guo, L.; Zhang, B.; Li, S.; Zhang, Q.; Buettner, M.; Li, L.; Qian, X.; Yan, F., Scalable and efficient Sb_2S_3 thin-film solar cells fabricated by close space sublimation. *APL Materials* **2019,** *7* (4), 041105.

103. Wu, W.; Tang, B.; Wan, L.; Mao, X.; Wang, H.; Tong, G.; Chen, T.; Zhou, R., Enhanced Performance of Close-Spaced Sublimation Processed Antimony Sulfide Solar Cells via Seed-Mediated Growth. *Advanced Science* **2024,** *11* (46), 2409312.

104. Krautmann, R.; Spalatu, N.; Josepson, R.; Nedzinskas, R.; Kondrotas, R.; Gržibovskis, R.; Vembris, A.; Krunks, M.; Oja Acik, I., Low processing temperatures explored in Sb_2S_3 solar cells by close-spaced sublimation and analysis of bulk and interface related defects. *Solar Energy Materials and Solar Cells* **2023,** *251*, 112139.

105. Kim, D.-H.; Lee, S.-J.; Park, M. S.; Kang, J.-K.; Heo, J. H.; Im, S. H.; Sung, S.-J., Highly reproducible planar Sb_2S_3-sensitized solar cells based on atomic layer deposition. *Nanoscale* **2014,** *6* (23), 14549-14554.

106. Büttner, P.; Scheler, F.; Pointer, C.; Döhler, D.; Barr, M. K. S.; Koroleva, A.; Pankin, D.; Hatada, R.; Flege, S.; Manshina, A.; Young, E. R.; Mínguez-Bacho, I.; Bachmann, J., Adjusting Interfacial Chemistry and Electronic Properties of Photovoltaics Based on a Highly Pure Sb_2S_3 Absorber by Atomic Layer Deposition. *ACS Applied Energy Materials* **2019,** *2* (12), 8747-8756.

107. Lee, S.-J.; Sung, S.-J.; Yang, K.-J.; Kang, J.-K.; Kim, J. Y.; Do, Y. S.; Kim, D.-H., Approach to Transparent Photovoltaics Based on Wide Band Gap Sb_2S_3 Absorber Layers and Optics-Based Device Optimization. *ACS Applied Energy Materials* **2020,** *3* (12), 12644-12651.

108. Mahuli, N.; Halder, D.; Paul, A.; Sarkar, S. K., Atomic layer deposition of amorphous antimony sulfide (a-Sb_2S_3) as semiconductor sensitizer in extremely thin absorber solar cell. *Journal of Vacuum Science & Technology A* **2020,** *38* (3).

109. Kalangestani, F. C., Dependence of physical and chemical properties of Sb_2S_3 thin film prepared by APCVD method on deposition time. *Journal of Materials Science: Materials in Electronics* **2023,** *34* (1), 22.

110. Murtaza, G.; Akhtar, M.; Azad Malik, M.; O'Brien, P.; Revaprasadu, N., Aerosol assisted chemical vapor deposition of Sb_2S_3 thin films: Environmentally benign solar energy material. *Materials Science in Semiconductor Processing* **2015,** *40*, 643-649.

111. Castro, J. R.; Dale, P.; Mahon, M. F.; Molloy, K. C.; Peter, L. M., Deposition of Antimony Sulfide Thin Films from Single-Source Antimony Thiolate Precursors. *Chemistry of Materials* **2007,** *19* (13), 3219-3226.

112. Rodriguez-Castro, J.; Mahon, M. F.; Molloy, K. C., Aerosol-Assisted CVD of Antimony Sulfide from Antimony Dithiocarbamates. *Chemical Vapor Deposition* **2006,** *12* (10), 601-607.

113. Greenaway, D. L.; Nitsche, R., Preparation and optical properties of group IV–VI2 chalcogenides having the CdI_2 structure. *Journal of Physics and Chemistry of Solids* **1965,** *26* (9), 1445-1458.

114. Moustafa, M.; Zandt, T.; Janowitz, C.; Manzke, R., Growth and band gap determination of the ZrS_xSe_{2-x} single crystal series. *Physical Review B* **2009,** *80* (3), 035206.

115. Borghesi, A.; Chen-jia, C.; Guizzetti, G.; Nosenzo, L.; Reguzzoni, E.; Stella, A.; Lévy, F., Thermoreflectance studies of transition-metal dichalcogenides between 1 and 9 eV. *Physical Review B* **1986,** *33* (4), 2422-2428.

116. Peloquin, G.; Provencher, R.; Jandl, S.; Aubin, M., Optical transitions in ZrS_2 and $ZrSe_2$ from thermoreflectance measurements. *Journal of Physics C: Solid State Physics* **1986,** *19*, 3141.

117. Zhang, W.; Huang, Z.; Zhang, W.; Li, Y., Two-dimensional semiconductors with possible high room temperature mobility. *Nano Research* **2014,** *7* (12), 1731-1737.

118. Afzalian, A., Ab initio perspective of ultra-scaled CMOS from 2D-material fundamentals to dynamically doped transistors. *npj 2D Materials and Applications* **2021,** *5* (1), 5.

119. Hamada, M.; Matsuura, K.; Sakamoto, T.; Muneta, I.; Hoshii, T.; Kakushima, K.; Tsutsui, K.; Wakabayashi, H., High Hall-Effect Mobility of Large-Area Atomic-Layered Polycrystalline ZrS_2 Film Using UHV RF Magnetron Sputtering and Sulfurization. *IEEE Journal of the Electron Devices Society* **2019,** *7*, 1258-1263.

120. Zhang, M.; Zhu, Y.; Wang, X.; Feng, Q.; Qiao, S.; Wen, W.; Chen, Y.; Cui, M.; Zhang, J.; Cai, C.; Xie, L., Controlled Synthesis of ZrS_2 Monolayer and Few Layers on Hexagonal Boron Nitride. *Journal of the American Chemical Society* **2015,** *137* (22), 7051-7054.

121. Zhu, Y.; Wang, X.; Zhang, M.; Cai, C.; Xie, L., Thickness and temperature dependent electrical properties of ZrS_2 thin films directly grown on hexagonal boron nitride. *Nano Research* **2016,** *9* (10), 2931-2937.

122. Tian, Y.; Cheng, Y.; Huang, J.; Zhang, S.; Dong, H.; Wang, G.; Chen, J.; Wu, J.; Yin, Z.; Zhang, X., Epitaxial growth of large area ZrS_2 2D semiconductor films on sapphire for optoelectronics. *Nano Research* **2022,** *15* (7), 6628-6635.

123. Herninda, T. M.; Ho, C.-H., Optical and Thermoelectric Properties of Surface-Oxidation Sensitive Layered Zirconium Dichalcogenides $ZrS_{2-x}Se_x$ (x = 0, 1, 2) Crystals Grown by Chemical Vapor Transport. *Crystals* **2020,** *10* (4), 327.

124. Li, L.; Fang, X.; Zhai, T.; Liao, M.; Gautam, U. K.; Wu, X.; Koide, Y.; Bando, Y.; Golberg, D., Electrical Transport and High-Performance Photoconductivity in Individual ZrS_2 Nanobelts. *Advanced Materials* **2010,** *22* (37), 4151-4156.

125. Conroy, L. E.; Park, K. C., Electrical properties of the Group IV disulfides, titanium disulfide, zirconium disulfide, hafnium disulfide and tin disulfide. *Inorganic Chemistry* **1968,** *7* (3), 459-463.

126. Li, L.; Wang, H.; Fang, X.; Zhai, T.; Bando, Y.; Golberg, D., High-performance Schottky solar cells using ZrS_2 nanobelt networks. *Energy & Environmental Science* **2011,** *4* (7), 2586-2590.

127. Lu, C.; Ge, Y.; Luo, M.; Xu, X., Optical Nonlinearity of Emerging ZrS_2 and HfS_2 Semiconductors. *Annalen der Physik* **2023,** *535* (1), 2200309.

128. Huang, J.; Tian, Y.; Cheng, Y.; Li, X.; Zhang, S.; Jiang, J.; Chen, J.; Wang, G.; Li, J.; Yin, Z.; Zhang, X., Large-area epitaxial growth of 2D $ZrS_{2(1-x)}Se_{2x}$ semiconductor alloys with fully

tunable compositions and bandgaps for optoelectronics. *Science China Materials* **2023,** *66* (5), 1870-1878.

129. Jin, Y.; Sun, J.; Zhang, L.; Yang, J.; Wu, Y.; You, B.; Liu, X.; Leng, K.; Liu, S., Controllable Oxidation of ZrS_2 to Prepare High-κ, Single-Crystal m-ZrO_2 for 2D Electronics. *Advanced Materials* **2023,** *35* (18), 2212079.

130. Thiyagarajan, R.; Beevi, M. M.; Anusuya, M., Nano structural characteristics of zirconium sulphide thin films. *J Am Sci* **2009,** *5* (3), 26.

131. Thompson, J. Development of Single-Source CVD Precursors for Group IV, V and VI Metal Disulfides. Doctoral Dissertation, University of Bath, 2017.

132. Motojima, S.; Takahashi, Y.; Sugiyama, K., Anomalous pillar-shaped crystal growth of zirconium disulfide. *Journal of Crystal Growth* **1976,** *33* (1), 116-124.

133. Mattinen, M.; Popov, G.; Vehkamäki, M.; King, P. J.; Mizohata, K.; Jalkanen, P.; Räisänen, J.; Leskelä, M.; Ritala, M., Atomic Layer Deposition of Emerging 2D Semiconductors, HfS_2 and ZrS_2, for Optoelectronics. *Chemistry of Materials* **2019,** *31* (15), 5713-5724.

134. Meng, X.; Liu, Y.; Watanabe, F.; Velasquez Carballo, K.; Cai, J.; Chen, Z.; Zhou, H., Atomic layer deposition of two-dimensional layered zirconium sulfide. *Materials Today Chemistry* **2024,** *37*, 102013.

135. Dubrovskaya, G. N., Thermal stability of Group IV transition metal sulfides. *Ukr. Khim. Zh. (Russ. Ed.)* **1967,** *33* (10), 997-1003.

136. Lin, D.-Y.; Hsu, H.-P.; Wang, C.-W.; Chen, S.-W.; Shih, Y.-T.; Hwang, S.-B.; Sitarek, P., Temperature-Dependent Absorption of Ternary $HfS_{2-x}Se_x$ 2D Layered Semiconductors. *Materials* **2022,** *15* (18).

137. Gaiser, C.; Zandt, T.; Krapf, A.; Serverin, R.; Janowitz, C.; Manzke, R., Band-Gap Engineering with HfS_xSe_{2-x}. *Physical Review B* **2004,** *69* (7).

138. Wang, D.; Zhang, X.; Guo, G.; Gao, S.; Li, X.; Meng, J.; Yin, Z.; Liu, H.; Gao, M.; Cheng, L.; You, J.; Wang, R., Large-Area Synthesis of Layered $HfS_{2(1-x)}Se_{2x}$ Alloys with Fully Tunable Chemical Compositions and Bandgaps. *Advanced Materials* **2018,** *30* (44), 1803285.

139. Wang, D.; Zhang, X.; Liu, H.; Meng, J.; Xia, J.; Yin, Z.; Wang, Y.; You, J.; Meng, X.-M., Epitaxial growth of HfS_2 on sapphire by chemical vapor deposition and application for photodetectors. *2D Materials* **2017,** *4* (3), 031012.

140. Roubi, L.; Carlone, C., Resonance Raman spectrum of HfS_2 and ZrS_2. *Physical Review B* **1988,** *37* (12), 6808-6812.

141. Zelewski, S. J.; Kudrawiec, R., Photoacoustic and modulated reflectance studies of indirect and direct band gap in van der Waals crystals. *Scientific Reports* **2017,** *7* (1), 15365.

142. Zheng, B.; Chen, Y.; Wang, Z.; Qi, F.; Huang, Z.; Hao, X.; Li, P.; Zhang, W.; Li, Y., Vertically oriented few-layered HfS_2 nanosheets: growth mechanism and optical properties. *2D Materials* **2016,** *3* (3), 035024.

143. Zheng, B.; Wang, Z.; Qi, F.; Wang, X.; Yu, B.; Zhang, W.; Chen, Y., CVD growth of large-area and high-quality HfS_2 nanoforest on diverse substrates. *Applied Surface Science* **2018,** *435*, 563-567.

144. Wang, D.; Zhang, X.; Guo, G.; Gao, S.; Li, X.; Meng, J.; Yin, Z.; Liu, H.; Gao, M.; Cheng, L.; You, J.; Wang, R., Large-Area Synthesis of Layered $HfS_{2(1-x)}Se2_x$ Alloys with Fully Tunable Chemical Compositions and Bandgaps. *Advanced Materials* **2018,** *30* (44), 1803285.

145. Leem, M.; Lee, H.; Park, T.; Ahn, W.; Kim, H.; Lee, E.; Kim, H., Intriguing morphological evolution during chemical vapor deposition of HfS_2 using $HfCl_4$ and S on sapphire substrate. *Applied Surface Science* **2020,** *509*, 144701.

146. Singh, J.; Shao, J.-H.; Chen, G.-T.; Wu, H.-S.; Tsai, M.-L., The growth mechanism and intriguing optical and electronic properties of few-layered HfS_2. *Nanoscale Advances* **2023,** *5* (1), 171-178.

147. Yan, C.; Gan, L.; Zhou, X.; Guo, J.; Huang, W.; Huang, J.; Jin, B.; Xiong, J.; Zhai, T.; Li, Y., Space-Confined Chemical Vapor Deposition Synthesis of Ultrathin HfS_2 Flakes for Optoelectronic Application. *Advanced Functional Materials* **2017,** *27* (39), 1702918.

148. Baji, Z.; Fogarassy, Z.; Sulyok, A.; Petrik, P., Investigation of the Tetrakis(dimethylamino)hafnium and H_2S ALD Process: Effects of Deposition Temperature and Annealing. *Solids* **2022,** *3* (2), 258-270.

149. Cao, Y.; Wähler, T.; Park, H.; Will, J.; Prihoda, A.; Moses Badlyan, N.; Fromm, L.; Yokosawa, T.; Wang, B.; Guldi, D. M.; Görling, A.; Maultzsch, J.; Unruh, T.; Spiecker, E.; Halik, M.; Libuda, J.; Bachmann, J., Area-Selective Growth of HfS_2 Thin Films via Atomic Layer Deposition at Low Temperature. *Advanced Materials Interfaces* **2020,** *7* (23), 2001493.

Chapter 2: Low-Temperature Chemical Vapor Deposition of Zirconium(IV) Sulfide Thin Films

2.1. Contributions

The work presented below is derived from a manuscript in progress. I deposited ZrS_2 thin films and characterized them using scanning electron microscopy, energy dispersive X-ray spectroscopy, X-ray diffraction, and four-point probe. Daniela Chavez and Abigail D. Berube measured the composition of ZrS_2 films using XPS and fit the spectra. Professor Luke M. Davis supervised the project and assisted in writing and editing the manuscript. I also wrote and edited the manuscript, along with Daniela Chavez and Abigail D. Berube. The authors thank Shao-Liang Zheng for assistance with pXRD measurements. This project is funded by Tufts University and the National Science Foundation (DMR-2224949).

2.1. Abstract

Transition metal dichalcogenides like zirconium disulfide absorb visible light, and monolayers can have exceptionally large carrier mobilities. Integrating these materials into wafer-based devices will likely require deposition methods operating below 400 °C. Chemical vapor deposition (CVD) may offer one such route, because it is suitable for large substrate areas and complex substrate geometries. However, current CVD methods deposit ZrS_2 above 400 °C, typically from $ZrCl_4$ and sulfur. Guided by thermochemical calculations that suggested the reaction between hydrogen sulfide and tetrakis(dimethylamido)zirconium(IV) would be more favorable, we demonstrate low-temperature CVD using these compounds. Film deposition proceeds rapidly at 150-350 °C, producing stoichiometric, polycrystalline ZrS_2 films. Films can grow at rates >100

nm/min, although slower growth increases the film crystallinity and decreases C and N impurities. At substrate temperatures above 250 °C, the film morphology transitions from densely packed small grains to larger, more loosely packed vertical sheets. In an excess of H_2S, decreasing the $Zr(NMe_2)_4$ partial pressure can suppress the growth of these plates. Resistivities of product films are within 1-3 orders of magnitude of single crystal data. Optical properties are consistent with previously reported films of ZrS_2, suggesting this route may offer a method for integrating ZrS_2 into thermally sensitive devices.

2.2. Introduction

Chalcogenide semiconductors represent some of the earliest known and most useful semiconducting materials. From Faraday's first report of the characteristic decreasing resistance with increasing temperature in silver sulfide,[1] through Smith's discovery of photoconductivity in selenium,[2] to Braun's observation of rectification in lead sulfide,[3] elements and compounds of group 16 critically enabled the development of the semiconductor field. The utility of this family of compounds continues in the modern day, with zinc sulfide serving as an important inorganic phosphor, especially when activated by silver or copper.[4] Tin selenide and related chalcogenides represent the best thermoelectric materials.[5, 6] Cadmium telluride remains the most important thin-film photovoltaic material, retaining a 5% share of the fast-growing solar market.[7]

Two exemplar classes of the next generation of chalcogenide semiconductors are transition metal dichalcogenides (TMDCs) and perovskite-structured complex chalcogenides. The transition metal dichalcogenides are layered materials that have computed or measured monolayer mobilities exceeding 1200 $cm^2V^{-1}s^{-1}$.[8-10] These superior carrier transport properties have made TMSC's attractive candidates for optoelectronic devices,[11, 12] gas sensors,[13] supercapacitors,[14] and piezoelectrics.[15, 16] Chalcogenide perovskites have garnered substantial interest in the last decade

as optoelectronic materials.[17-21] Barium zirconium sulfide ($BaZrS_3$), for example, has charge carrier lifetimes of 50-100 ns,[22, 23] and charge carrier diffusion lengths near 5 μm.[23] Simulations predict single-junction photovoltaics based on $BaZrS_3$ could reach efficiencies as high as 28%.[24]

Zirconium(IV) sulfide is an n-type TMDC with favorable optoelectronic properties. The bulk material absorbs visible light, with an indirect bandgap of 1.7–1.8 eV[25, 26] and a direct bandgap in the range 2.1–2.4 eV.[26-28] The absorption coefficient is on the order of 10^3 cm^{-1} at the direct bandgap.[25, 26] Majority carrier transport properties are also promising, with a carrier concentration on the order of 10^{17}–10^{18} cm^{-3},[29-31] and a carrier mobility of up to 61 $cm^2V^{-1}s^{-1}$ in single crystals,[32] and 1–5 $cm^2V^{-1}s^{-1}$ in films.[29, 33, 34] As a monolayer and few-layer material, ZrS_2 has drawn interest for predicted[8, 9] and realized[10] carrier mobilities in excess of 1200 $cm^2V^{-1}s^{-1}$. Combined, these properties have enabled fabrication of photodetectors,[29, 30, 35, 36] field effect transistors,[30, 34, 37] and photovoltaics[38] based on ZrS_2 films or exfoliated crystals.

New approaches are needed for depositing ZrS_2 films because current methods preclude integration with thermally sensitive substrates and devices, or lack scalability. Chemical vapor deposition (CVD) from $ZrCl_4$ and sulfur is the most utilized method for preparing ZrS_2 films; although high-quality films can be obtained from this chemistry, growth temperatures ≥800 °C are typical.[29, 33, 34, 39, 40] Earlier reports of CVD of ZrS_2 demonstrate that replacing sulfur with hydrogen sulfide allows film growth as low as 450 °C,[41] and CVD from $ZrOCl_2$ and thiourea has been demonstrated at 430 °C.[42] CVD of ZrS_2 films from single-source zirconium dithiocarbamates occurs as low 425 °C.[43] Although temperatures as low as 50 °C have been utilized for synthesis of ZrS_2 quantum dots,[44, 45] and ZrS_2 nanostructures prepared at higher temperatures can be transferred to other substrates through methods such as drop casting,[30, 46] these methods may not scale as well as all-vapor methods. Because the synthesis of chalcogenide perovskites like $BaZrS_3$ often

proceeds via reaction of BaS (or a relative like BaS_3[47]) with ZrS_2, new methods to prepare ZrS_2 films may ultimately also enable the synthesis of chalcogenide perovskite films.

The use of more reactive precursors may lower the CVD growth temperature of ZrS_2. Beyond replacing sulfur with H_2S, replacing $ZrCl_4$ in the typical ZrS_2 reaction should also be beneficial, as significant precedent exists for lowering growth temperatures by replacing metal halides with metal amides in CVD of other materials, including in closely related TiS_2.[48-50] Although the mechanisms of CVD and atomic layer deposition (ALD) can be different, owing to different precursor dosing strategies, it is relevant that in ALD of ZrS_2, substituting $ZrCl_4$ with tetrakis(ethylmethyl)zirconium(IV), $Zr(NEtMe)_4$, decreased the minimum growth temperature for crystalline films from 350 to 200 °C.[36] ALD of amorphous ZrS_2 has been reported at temperatures as low as 75 °C using tetrakis(dimethylamido)zirconium(IV), $Zr(NMe_2)_4$, and H_2S.[51] Replacing the reaction of $ZrCl_4$ and sulfur with the reaction of a zirconium dialkylamide and H_2S changes the mechanism of CVD from reduction-oxidation chemistry to acid-base chemistry. The nitrogen of the dialkylamide should be protonated readily by H_2S, as similar chemistry is known to occur on surfaces for weaker acids such as H_2O or H_3N.[50, 52]

We now report CVD of ZrS_2 from $Zr(NMe_2)_4$ and H_2S at temperatures below 400 °C. Reactions of these precursors deposit stoichiometric, polycrystalline films at temperatures as low as 150 °C, the lowest reported temperature for CVD of ZrS_2. Growth rates exceeding 100 nm/min are possible, although very rapid depositions afford amorphous films. Above 250 °C, fast growth leads to sheets of ZrS_2 arrayed vertically out of the substrate. Slower growth in an H_2S-rich environment allows control over the morphology of ZrS_2 films, suppressing the formation of flakes at 250–300 °C. The optical properties of the product films are consistent with typical values for films of ZrS_2. The electrical resistivity of the best films lies within 1 order of magnitude of single

crystals and high-temperature CVD films; enhancing the crystallinity and grain size of low-temperature CVD films may be a direction for future improvement.

2.3. Experimental

2.3.1 Deposition of ZrS_2 Thin Films

Materials. Tetrakis(dimethylamido)zirconium(IV), 99%, was purchased from Strem Chemical Co., stored in an Ar-filled glovebox, and used without further purification. Hydrogen sulfide (99.5%) was purchased from Matheson Tri-Gas and purified to ≤1 ppb H_2O using an ARM acid gas purifier (AG-301-150330-V04-F). Argon gas was purified (nominally to ≤0.1 ppb H_2O, O_2, CO, CO_2) using an Entegris GateKeeper gas purifier (GPUS35FHX04R00CA). Quartz substrates were purchased from Chemglass Life Sciences (CGQ-0640-01). c-Plane sapphire substrates were purchased from SPI Supplies (502SS25-4-AB). Glass slides coated with indium tin oxide (ITO) were purchased from MTI Corporation (ITO252507R15HFT115nm). SEMI-grade acetone and isopropanol were purchased from VWR and used as received. For instrument calibration,[53] single crystals of ZrS_2 (>99.9995%, flux zone grown) were purchased from 2D Semiconductors.

Vapor pressure measurements. We constructed a simple apparatus to measure the vapor pressure of $Zr(NMe_2)_4$, in a similar environment to our deposition chamber (Figure 2.1). The measurement apparatus is built around a VCR cross, connected to two VCR bellows valves and two pressure gauges. Vapor pressure measurements were recorded using a Baratron pressure gauge (range of 0.01–10 Torr) and the base pressure of the system was measured with a Pirani gauge (0.1–760 Torr). One VCR bellows valve isolates the $Zr(NMe_2)_4$ precursor, contained in a vapor-draw style bubbler, from the pressure gauges. The second bellows valve isolates the cross—and

thus the gauges and bubbler—from vacuum. All metal connections on the apparatus are ¼″ VCR, made using 316L stainless steel gaskets. The glass bubbler bottom (Kurt J. Lesker) is identical to that used on the CVD reactor and heated using the same custom heated jacket, although the bubbler top is of the vapor draw style (one feedthrough) rather than the carrier gas style (two feedthroughs). The rest of the apparatus was heated using heating tape controlled with PID temperature controllers (HTS/Amptek Company). Vacuum is provided by a roughing pump (Agilent TriScroll 300 dry vacuum pump), through a leak valve and a turbomolecular pump (Leybold TurboVac 50) connected to a residual gas analyzer (Inficon Transpector 2.0, TSPTT200, 0-200 amu); only the dry scroll pump was in use during these measurements.

To measure the absolute vapor pressure of $(ZrNMe_2)_4$, we first loaded 1 g of this compound into the glass bubbler in an Ar-filled glovebox, with the bellows valve (BV2) attached. With this valve closed, the bubbler was connected to the VCR cross, and the apparatus evacuated. The valve on the bubbler was then opened, and the bubbler evacuated to remove Ar. After evacuation at room temperature, the bellows valve on the bubbler (BV2) was closed, and the system was ready for measurements. A similar sequence of evacuating atmosphere and residual gases was followed on each new day of measurements.

Individual vapor pressure measurements were collected by heating the apparatus under vacuum. To make each individual measurement, after the room-temperature evacuation sequence described above, the bubbler and the measurement system were heated to the set temperature. The apparatus was pumped down to a base pressure of ≤3 mTorr. Then, the bellows valve isolating the apparatus from vacuum (BV1) was closed, and the bellows valve isolating the bubbler from the apparatus (BV2) was opened. The vapor pressure of $(ZrNMe_2)_4$ was allowed to stabilize over 2 minutes and then measured using either the Baratron or the Pirani pressure gauge. Trials were

repeated 3-5× at temperatures between 35 and 65 °C, with the bubbler and body of the apparatus heated to the same temperature.

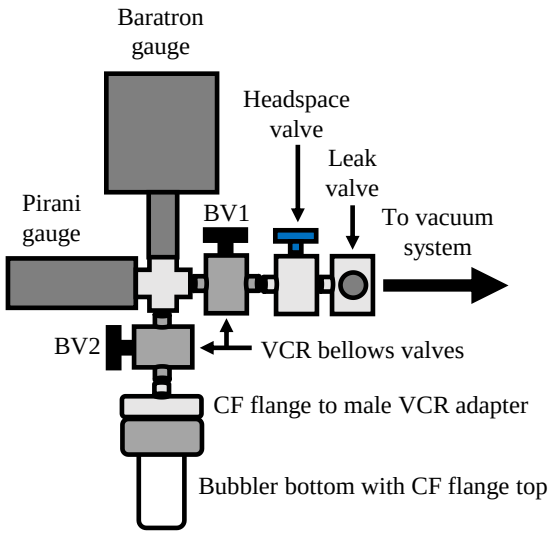

Figure 2.1. Schematic diagram of the apparatus used to measure the vapor pressure of $Zr(NMe_2)_4$.

CVD reactor. All ZrS_2 films were deposited in a custom-built, hot walled CVD reactor. A piping and instrumentation diagram is shown in Figure 2.2, a reactor schematic is shown in Figure 2.3, and a photograph of the reactor is provided in Figure 2.4. The CVD reactor was assembled and operated inside of a walk-in fume hood as a safety precaution in the event of an H_2S leak. As an additional precaution in working with H_2S, all components in the reactor are constructed of stainless steel (304, 316, or 321) or quartz, and elastomer seals are EPDM, EPR, or Buna-N.[54]

The CVD reactions are conducted in a quartz tube (25 mm OD, 20.5 mm ID, 450 mm length; MTI Corp). heated by a Lindberg Blue M Mini-Mite tube furnace (TF55035A-1). The quartz tube is connected on either side to 316 stainless-steel quick connect to KF25 adapters (High Vac Depot, AD-QC-KF25X100) which are supported by laboratory jacks. The internal and external O-rings on the adapter are EPDM (with dash sizes of -214 and -320, respectively). A 316

stainless-steel tray is used as a substrate holder (12″ length, 0.625″ width, 0.075″ thick) and is used to insert or retrieve samples from the reaction zone. Precursors are delivered to the reaction zone through a 304 stainless steel KF25 blank with two 0.25″ OD 304 stainless-steel feedthrough tubes (Ideal Vacuum Products, LLC; P104211). The vacuum side of the feedthrough tubes are cut to 3.5″ long so that they extend to 1″ past the start of the heated coils in the tube furnace. On the air side, the feedthrough tubes are cut (one each) to 1″ and 3″ and adapted to 0.25″ VCR fittings using 316 stainless steel ferrule to VCR adapters (Swagelok, SS-4-VCR-6-400).

Precursors are delivered to the reaction zone through separate delivery lines. To deliver $Zr(NMe_2)_4$, Ar carrier gas is supplied to the bubbler via an MFC. The bubbler is assembled from two pieces: the bottom is domed 7052 borosilicate glass, 4.75″ long and 1.5″ in diameter, adapted to a Kovar 2.75″ CF flange (Kurt J. Lesker). The bubbler top is a 304 stainless-steel 2.75″ CF flange with two ¼″ tube feedthroughs, with male VCR connections on the air side. The feedthroughs are each bent 90° on the air side, 180 ° to each other, and offset by 1.5″. Upstream of the bubbler is a 12″ 321 stainless-steel bellows tubing with VCR fittings, and downstream of the bubbler is a braided 36″ 321 stainless-steel bellows tubing with VCR fittings. The braided tubing is connected to the air side one of the 304 stainless-steel feedthrough tubes on the reactor. H_2S gas is supplied to the reaction zone through the second feedthrough tube using another braided, 36″ 321 stainless-steel hose with VCR fittings. A VCR tee is installed on the upstream side of this braided hose; this tee is connected via two 6″ lengths of 321 stainless-steel flexible bellows tubing with VCR fittings to the H_2S MFC and a second Ar MFC, allowing for H_2S to be diluted before reaching the reaction zone.

Ar gas is purified before delivery to a manifold supplying the two Ar mass flow controllers, one used for the bubbler carrier gas and the other for purging and for diluting H_2S with Ar. Ar is

supplied from a size 300 cylinder via a two-stage regulator through 304 stainless steel tubing (0.25″ OD) bent and fed over the top of the walk-in fume hood. A ferrule to VCR adapter is used to connect the tubing to an Entegris GateKeeper GPU HX series gas purifier (GPUS35FHX04R00CA) that is protected on either side by VCR bellows valves (Swagelok, SS-4BG-V51). The purifier is rated to remove H_2O, O_2, CO_2, and CO impurities to <0.1 ppb. The purifier is connected to a manifold constructed from a VCR cross. One arm of the cross is capped, and occasionally used during He leak checking of the reactor. The other two arms of the cross connect to the two Ar MFCs using 6″ 321 stainless-steel flexible bellows tubing with VCR fittings. MFCs were purchased from Aalborg with 304 stainless-steel bodies, Buna-N internal O-rings and VCR fittings (GFCS-011796).

H_2S is supplied from a lecture bottle and purified before delivery to a mass flow controller. Chemically pure grade H_2S was purchased from Matheson Tri-Gas (CP, 99.5% purity, G1540275), with a specified H_2O content of ≤0.01%. A two-stage lecture bottle regulator and 0.25″ OD stainless-steel tubing connects the H_2S gas to an ARM acid gas purifier (AG-301-150330-V04-F) intended to reduce the H_2O concentration to <1 ppb. The H_2S purifier has two VCR connections and is protected on either side by 316 stainless-steel bellows valves (SS-4BG-V51). The upstream side of the purifier is connected to the tubing from the lecture bottle with a ferrule to VCR adapter, and the downstream side of the purifier is connected to the MFC. The H_2S MFC was acquired from Aalborg and is made of 304 stainless steel with EPR internal seals (GFCS-021183). A VCR bellows valve is placed immediately downstream of the H_2S MFC to prevent trace amounts of gas from breaking through; when the valve is open 1–2 ppm of H_2S can be detected in the reactor, even when the MFC is unplugged.

Downstream of the reactor, a KF25 cross connects the reactor to the sample access port, a pressure gauge, and the vacuum system. The KF25 cross is made of 304 stainless steel and is connected directly to the quick connect adapter on the outlet of the reaction zone. All O-rings installed on the KF25 cross are EPDM. Directly across the cross from the reaction zone, samples can be accessed by removing a 304 stainless steel KF25 blank. On a second arm of the KF25 cross, a thermocouple gauge with an NPT connection (Kurt J. Lesker, KJL-5311) provides pressure readout, with a range of 1.0×10^{-3}–7.6×10^{2} Torr. The pressure gauge is attached to an NPT to KF25 adapter, and the connection is covered with epoxy to enhance the seal. A 304 stainless steel, manual butterfly valve with KF25 connections (Kurt J. Lesker, KBV010MSQF25) separates the KF25 cross and the pressure gauge. The remaining arm of the KF25 cross connects to a 304 stainless steel KF25 elbow, itself connected to a manual butterfly valve providing isolation from and access to the roughing vacuum pump.

The pressure in the CVD reactor is maintained by a roughing pump that is protected from H_2S by a foreline trap. A reactor base pressure of 30 mTorr is achieved using an Edwards RV8 direct-drive rotary vane pump (A65401906). Immediately upstream of the vacuum pump is a 304 stainless steel foreline trap (Ancorp, VSHE-L-QF25) with KF25 connections and sealed in the middle with a Buna-N gasket. To improve the seal, the Buna-N gasket is coated in Krytox grease. To remove H_2S from the gas stream, the foreline trap is filled with SULFURTRAP EX media (Chemical Product Industries, ST-EX-50-10). Upstream of the scrubbing media in the same foreline trap, 3A molecular sieves are added to prevent back-streaming of water and pump oil into the reaction zone. The molecular sieves were added during a troubleshooting phase, but low-oxygen films were deposited both with and without the sieves. A 20″ long and 1″ ID 304 stainless-

steel flexible bellows tube with KF25 fittings connects the foreline trap to the KF25 butterfly valve isolating the reactor from vacuum.

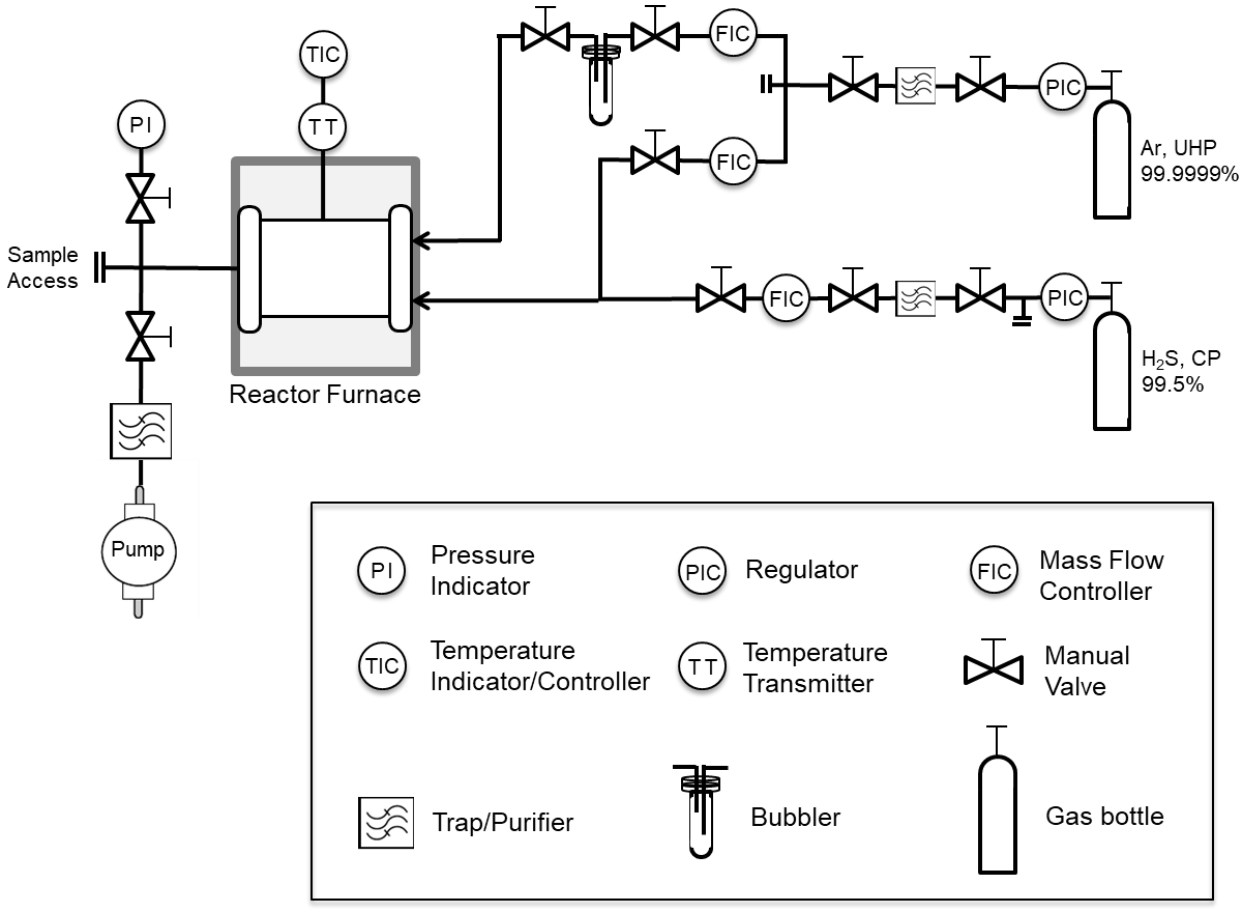

Figure 2.2 Piping and instrumentation diagram for the custom-built chemical vapor deposition reactor used in this work. The entire reactor resides in a walk-in fume hood, supported by a table constructed of T-slot aluminum framing and 0.25″ aluminum sheet.

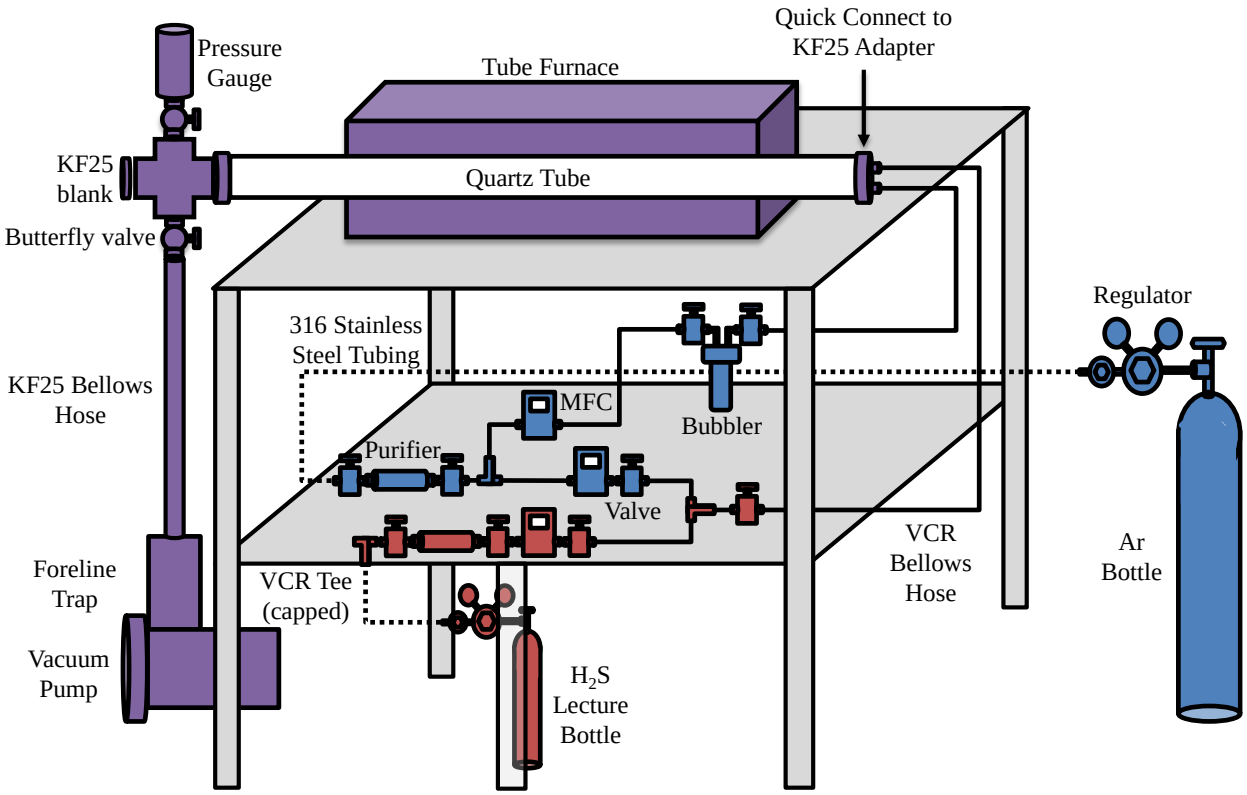

Figure 2.3. Schematic of the custom-built chemical vapor deposition reactor used in this work.

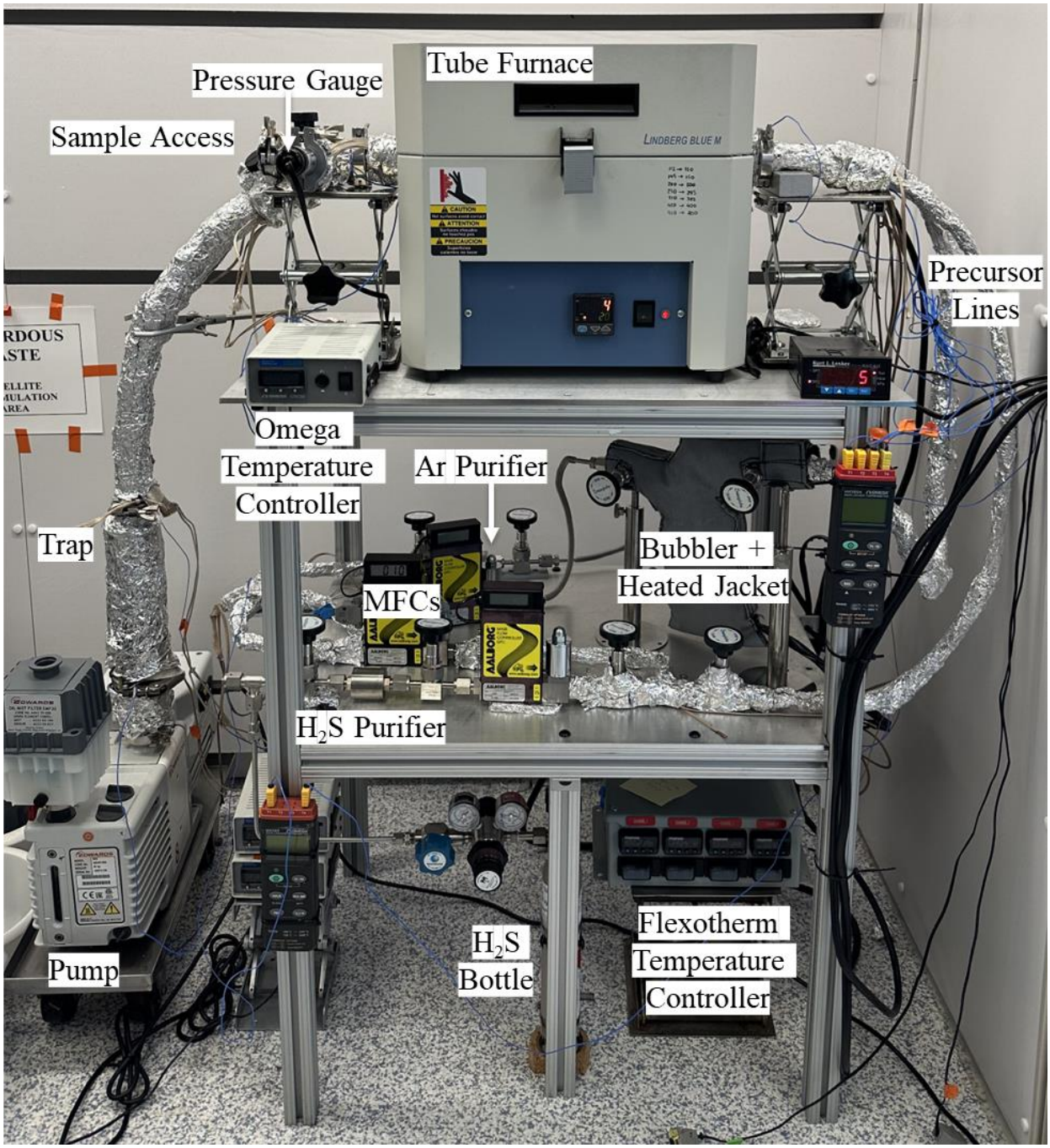

Figure 2.4. Photograph of the custom-built chemical vapor deposition reactor used in this work.

Substrate cleaning. ZrS_2 films were deposited primarily onto quartz substrates, with additional studies on indium tin oxide (ITO) and c-plane sapphire. Substrates were initially cleaned by hand-scrubbing with a slurry of Alconox detergent, and rinsed with deionized water. Substrates were then rinsed with SEMI grade acetone, SEMI grade isopropanol, and blown dry with nitrogen gas. To remove any remaining organic contaminants, the substrates were exposed to UV/ozone (Ossila) for 10 min before loading into the CVD reactor.

Substrate positions and analysis. ZrS_2 films were deposited onto substrates cleaved to 1″ long × 0.5″ wide, unless otherwise noted, and placed either 0.5″ or 1.5″ from the precursor inlets. For depositions of ZrS_2 using recipes 1-3 (Table 1), substrates were placed 1.5″ from the precursor inlets. For recipe 1, all substrates were quartz; for recipe 2, quartz was placed closest to the inlets, followed by ITO, quartz, and ITO. For recipe 3, quartz was again placed closest to the inlets, followed now by ITO, sapphire, and a second quartz substrate. Depositions using recipes 4–6 (Table 1) used only quartz substrates, with the frontmost sample 0.5″ from the precursor inlets. In all cases, these substrates were placed back-to-back with the 1″ side in the direction of precursor flow. Film samples are identified in the text by the location of the front of the substrate during deposition, even when data are collected from the middle of the sample.

Because films of ZrS_2 are air- and moisture-sensitive, separate samples were typically prepared for each measurement. 1″ × 0.5″ substrates were scored on the underside, normal to the precursor flow, into three regions, each 0.33″ long × 0.5″ wide (Figure 2.5). Starting closest to the precursor inlets, the scored regions were used for analysis by SEM/EDS, four-point probe, and pXRD (Figure 2.5). These analysis positions can be combined with the nominal distances to find exact locations for each measurement; for simplicity, we refer to all samples by the nominal distance. Reported film compositions from EDS are from the frontmost sample of each deposition.

For analysis by XPS, a 1 cm^2 piece of quartz or ITO was placed 3″ from the precursor inlets between the standard 1″ long × 0.5″ wide substrates. In some cases, 0.5″ × 0.5″ quartz substrates for UV-vis measurements were placed at the rear of the reactor, 4″ from the precursor inlets. Care was taken to minimize air exposure; samples were stored under vacuum in the reactor until analysis.

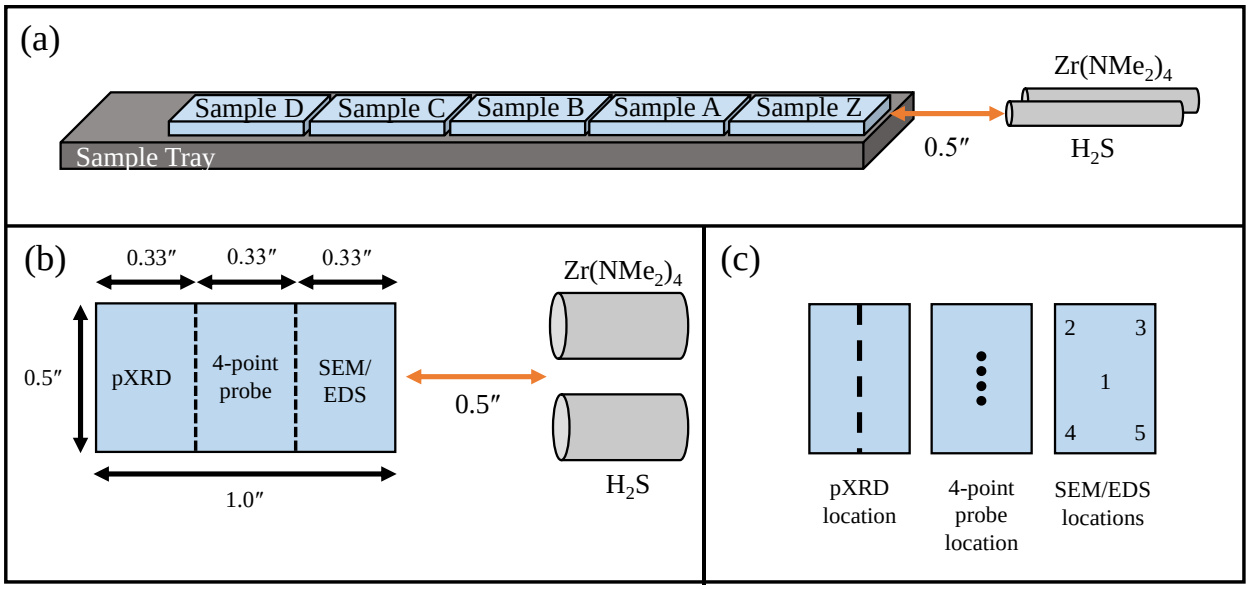

Figure 2.5. (a) Arrangement of 1″ × 0.5″ substrates in a typical ZrS_2 depositions. Samples A–D are laid back-to-back, with the 1″ side in the direction of precursor flow. Sample A is placed 1.5″ from the precursor inlets; an additional sample, Z, is sometimes placed upstream of A, 0.5″ from the precursor inlets. (b) Schematic showing sample Z placed in front of the precursor inlets, with zones for each characterization method marked. The underside of the substrate is scored normal to the precursor flow (dashed lines) and cleaved with wafer clippers after deposition. (c) Schematic of the sample after cleavage, showing the locations analyzed on ZrS_2 samples. EDS data are collected in 5 locations, and 4-point probe and pXRD data are collected in the center of the sample.

Baking out the CVD reactor. To remove H_2O adsorbed to surfaces within the CVD reactor, bakeouts were routinely performed before depositing ZrS_2. After loading cleaned substrates into the CVD reactor, the quartz tube reaction zone was heated to 400 °C for 2 hours

under active vacuum with 100 sccm Ar flowing (~815 mTorr). Except for the tubing upstream of the $Zr(NMe_2)_4$ precursor bubbler, all precursor-carrying tubing downstream of an MFC was heated to 110 °C during this time. The KF25 cross, quick flange adapters, and vacuum bellows hose were heated to 45 °C; the temperature was limited to prevent compression-set failure of the EPDM O-rings.

General deposition procedure. To start a deposition, the flow set points of the MFCs were adjusted to implement a recipe, and the precursors were introduced to the reaction zone. First, the flow rate of the Ar dilution MFC was increased from the bakeout setpoint of 100 sccm to either 109 or 200 sccm, depending on the reaction conditions utilized (Table 1). Next, a butterfly valve isolating the pressure gauge was closed to protect the gauge from exposure to H_2S. To introduce H_2S to the reaction zone, valves were opened sequentially, starting at the lecture bottle main valve, followed by the valve on the H_2S lecture bottle regulator, and then the VCR bellows valves on either side of the H_2S purifier. Before each valve was opened, all connections upstream were checked for leaks using a portable H_2S monitoring device purchased from RAE Systems (range of 0.1–100 ppm, G01-0102-000). The H_2S MFC was then turned on and the flow rate was adjusted for the deposition. Next, $Zr(NMe_2)_4$ was introduced into the reaction zone by plugging in the MFC controlling the bubbler carrier gas, adjusting the flow rate, and then simultaneously opening the valves immediately upstream and downstream of the bubbler.

To stop a deposition, the sequence used to start the reaction was run in reverse. First, the valves installed on the $Zr(NMe_2)_4$ bubbler were simultaneously closed and the MFC providing the bubbler carrier gas was turned off. Next, the H_2S MFC was turned off, followed by closing valves sequentially from downstream to upstream. Breakthrough of H_2S at the vacuum pump was checked by sampling the exhaust; using 800 g of SULFURTRAP EX in our foreline trap geometry, we

found breakthrough (≥0.1 ppm H_2S) occurs after delivering a total of 3 L of H_2S. We therefore replace the scrubbing media after flowing 2.5 L, to operate with a safety margin. Note that for SULFURTRAP EX to work effectively for pure H_2S in our flow rate range (up to 100 sccm), the manufacturer suggests a residence time of ≥90 s and trap length-to-diameter ratio of ≥4. The bubbler heater and heated lines were then turned off and the furnace was set to 20 °C, and propped open with an aluminum block to speed the cooling process. Once the temperature of the furnace reached ≤30 °C, the Ar purge gas flow rate was decreased to 10 sccm.

To vent the reactor, the reaction zone was isolated from vacuum and filled with Ar gas. Before venting, the Ar purge gas flow rate was increased to 100 sccm and the VCR bellows valve downstream of the H_2S MFC was closed; when open, we find the MFC can let through enough H_2S for us to measure 1–2 ppm of H_2S in the reactor. The butterfly valve isolating the vacuum pump is closed and the clamp securing the KF25 blank access door to the reactor is removed.

When not in use, the reactor is kept at room temperature under active vacuum with 10 sccm Ar flowing from the purging MFC to act as a protecting gas. These conditions are also used to store samples in the reactor prior to or between analyses. Additional details on operating the CVD reactor, changing the scrubbing agent, and other general maintenance guidance can be found in **Appendix 1**.

Specific deposition conditions. We explored several deposition settings during the course of this work, particularly flow rates and precursor heating temperatures. These settings are summarized in Table 1.

Table 2.1 Precursor delivery conditions used for CVD of ZrS_2 films.

Deposition Recipe	1	2	3	4	5	6
Bubbler Temperature (°C)	65	55	45	35	35	35
Bubbler Carrier Gas Flow Rate (sccm)	40	20	10	5	5	2
H_2S Flow Rate (sccm)	10	5	1	1	5	1
Purge Gas Flow Rate (sccm)	0	95	109	200	200	200

2.3.2. Characterization of ZrS_2 Thin Films

Morphology and thickness. The morphology and thickness of ZrS_2 films were examined using field-emission scanning electron microscopy (FE-SEM), in plan view and cross-section. This imaging was performed with an AMRAY 1845 FE-SEM with SEMView8000, refurbished and installed by SEMTech Solutions (North Billerica, MA). Select samples were characterized at the Harvard University Center for Nanoscale Systems (CNS) using a Zeiss Gemini 360.

Crystallinity. The crystallinity of ZrS_2 films was assessed using powder X-ray diffraction (p-XRD) at the Harvard University Department of Chemistry and Chemical Biology Center for Crystallographic Studies. X-ray diffractograms were recorded using a Bruker D2 PHASER X-ray diffractometer using Cu Kα radiation ($\lambda = 1.542$ Å) and a $\theta-2\theta$ scan. Unless otherwise indicated, scans were performed in the 2θ range of 10°–60° with an increment of 0.05° and a dwell time of 1 s. XRD data are plotted with standard reference patterns, generated from CIF files using Match.[55] The following reference patterns from the Crystallography Open Database[56] were used: ZrS_2, 5910006; Zr_3S_4, 1530167; ZrOS, 9009070; and ZrN, 1539259.

Composition. Energy dispersive X-ray spectroscopy (EDS) and X-ray photoelectron spectroscopy (XPS) were calibrated with ZrS_2 single crystals, and then used to determine the composition of ZrS_2 thin films deposited by CVD.

EDS data were collected using a Thermo Scientific Noran System 6 with UltraDry silicon drift detector. The EDS detector is mounted normal to the imaging beam, so the sample stage was

tilted 20° toward the detector during analysis to increase the X-ray counts arriving at the detector. Samples were analyzed with a 10 kV imaging voltage, and a working distance of 20–28 mm. EDS maps were collected for at least two locations from each film sample. Single crystal samples were placed on a carbon sticky and exfoliated using Scotch tape before loading into the SEM, and thin films were loaded into the SEM without further modification.

During the course of experiments, the UltraDry detector was damaged; subsequent EDS experiments were conducted at Harvard CNS. At Harvard, EDS was performed using a Zeiss Gemini 360 with Oxford Instruments Ultim Max EDS. Samples were analyzed with a 10 kV imaging voltage and a working distance of 8–10 mm.

Purity. X-ray Photoelectron Spectroscopy (XPS) data were collected in a mu-metal SPECS Ultrahigh Vacuum (UHV) chamber equipped with a PHOIBOS 100 MCD-5 hemispherical analyzer, a non-monochromated dual Al and Mg X-ray source, and SPECS IQE 12/38 ion gun for sputter-cleaning samples. This instrument was refurbished and installed by 3E8 Scientific (Tewksbury, MA). The system contains a custom-built, turbo-pumped load-lock for fast sample introduction and removal. The sample stage can be biased ±30 V, and can be heated to ca. 500 °C.

Samples were mounted in a standard SPECS sample holder and loaded for XPS analysis. Immediately after deposition, samples on pre-measured 10 mm × 10 mm substrates (ITO for recipe 2 and 3 depositions at ≤300°C, quartz for all others) were placed into a sample holder and secured with titanium clips to electrically ground the sample. The sample was then placed in the loadlock of the UHV system, typically with under 8 min of exposure to atmosphere. The samples were introduced into the main analysis chamber after ca. 40 min of pump-down time.

Films were characterized by XPS to determine the composition, including both the stoichiometry and incorporation of impurities from air, moisture, or ligand decomposition. We

have recently reported calibration data and experimental parameters for XPS of a ZrS_2 single crystal in our UHV chamber.[53] Data were collected using our non-monochromated Al K_α X-ray source. Samples were cleaned with Ar ion etching, with the ion sputter current monitored using a picoammeter connected to the sample stage. Samples were characterized first on the as-deposited, air-exposed surface (dp 0), and then a compositional depth profile consisting of three etch levels was collected. The first etch was 30 min at 1500 V with 30 nA sputter current (dp 1). This first etch aims to remove carbonaceous contaminants from exposure to ambient air. The next two etch etches aim to access the bulk of the film; the subsequent scans were collected after etching at 3000 V for 30 min with 500 nA sputter current (dp 2), and then for 2 h at same conditions (dp3). Different settings were used for survey scans (5 to 1300 eV binding energy; 50 eV pass energy; 100 ms dwell time; 0.5 eV step size; 2 scans/sample) and high-resolution scans of characteristic regions (50 eV pass energy; 100 ms dwell time; 0.1 eV step size; 10 scans/sample). Spectra were collected in the following order: full spectrum survey, C 1*s*, O 1*s*, Zr 3*d*, S 2*p*, and N 1*s*.

Fitting and Interpretation of XPS Data. Our spectrometer was calibrated to a clean silver foil. A silver foil was cleaned by sputtering with Ar^+ until no C or O appeared in the high-resolution C 1s and O 1s spectra. The foil was heated to 100 °C over 30 min to remove implanted Ar. Then, the separation between the Ag $3d_{5/2}$ and Ag M_4NN peaks was used to perform a gain calibration of our energy scale. Finally, the $3d_{5/2}$ peak location was used to reference our spectra. After gain correction, a shift of −4.69 eV brings the Ag $3d_{5/2}$ peak binding energy into alignment with the literature value of 368.21 eV.[57] In our system, the FWHM of the Ag $3d_{5/2}$ peak is 1.41 eV.

Appropriate fitting parameters for Zr 3*d* and S 2*p* were determined by measuring and fitting a single crystal of ZrS_2 in our instrument.[53] All fitting was performed using CasaXPS version 2.3.22PR1.0.[58] Spectra were referenced to measurements of the sputter-cleaned silver foil collected

under identical instrument settings. Then, the peak positions for stoichiometric ZrS_2 were confirmed by high-resolution scans of the appropriate binding energy regions for zirconium and sulfur. Our measurements were close to, but not identical with, previously reported high-resolution spectra using a monochromated X-ray source, but without a detailed description of the instrument calibration or sample oxygen content.[59] Peak positions are detailed in our recent paper,[53] with binding energies of 181.5 eV for the Zr $3d_{5/2}$ peak with spin-orbit splitting of 2.4 eV to the Zr $3d_{3/2}$ peak, and 161.5 eV for the S $2p_{3/2}$ peak with spin-orbit splitting of 1.16 eV to the S $2p_{1/2}$.

With the peak positions determined, iterative fitting was performed to derive appropriate fitting parameters for the Zr 3*d* and S 2*p* spectra of the single crystal. On the freshly exfoliated single crystal, the Zr 3*d* peaks of ZrS_2 were best fit with a pseudo-Voigt line shape generated as a sum of 55% Gaussian and 45% Lorentzian functions, sGL(45), with an exponential tail modifier 1.5. During this fitting, a Shirly background was applied, and the FWHM was restrained to 1.4-1.8 eV for both of the spin-orbit split Zr 3*d* peaks, which were constrained to be separated by 2.4 eV. The exponential tail modifier was necessary to obtain satisfactory fits for the Zr 3*d* region, and is well precedented for conductive Zr-containing samples.[60] A similar procedure for the S 2*p* peaks provided satisfactory fits with an sGL(30) line shape with no tailing. A Shirley background was used, and the spin-orbit components were constrained to be separated by 1.16 eV, while the FWHM of each peak was restrained to be 1.5-1.9 eV.

To assist in fitting oxide present in ZrS_2 films, we also collected data on the oxidized surface of a zirconium foil. A coupon of zirconium foil was cleaned with SEMI-grade solvents and introduced into the UHV chamber; we intended to clean the foil with Ar^+ sputtering and use the Zr metal as a reference for the Zr 3*d* line shape and fitting parameters. However, a very thick oxide layer on the foil was difficult to remove entirely, and we were able to obtain good fitting

parameters from a single crystal of ZrS_2. Nonetheless, the sputter-cleaned surface provided a good reference set for deriving fitting parameters for the Zr 3*d* lines of ZrO_2. Drawing on this experience, the zirconium oxide components present in the Zr 3*d* region of ZrS_2 films with surface or bulk oxide were fit with an sGL(45) line shape without a tail modifier, and with the same FWHM and spin-orbit splitting constraints as the sulfur-associated Zr 3*d* peaks.[60, 61] In more heavily oxidized films, the oxygen-associated Zr 3*d* peak forms a well-defined shoulder on the high binding energy side of the Zr 3*d* envelope; this shoulder was used to assign the peak position of the Zr 3*d* oxide at ~183.3 eV. This position agrees well with our foil data and with the literature.[62]

Carbon, nitrogen, and oxygen were fit in a similar fashion. The adventitious carbon was fit with two peaks in the C 1*s* region, one for C-C species at 285.3 eV and C-O constituents at 288.5 eV; the FWHM of each was constrained to 1.5-2.5 eV. When present, the N 1*s* peak was fit with a single component, with FWHM of 1.5-2.0eV. The O 1*s* peak was fit with two components corresponding to zirconium(IV) oxide and surface hydroxyls. All components were constrained to a FWHM of 1.5-1.9 eV. For all three 1*s* regions, sGL(30) line shapes provided good fits, although the spectra were often noisy because these contaminants were typically present in low concentrations.

Electrical properties. The sheet resistance of select ZrS_2 films was measured using a Signatone S-302-4 four-point probe, with a probe spacing of 1 mm. Measurements were collected on samples exposed to atmosphere for no more than 20 minutes.

Optical properties. The optical properties of ZrS_2 films were measured using UV-Vis spectroscopy. Reflectance and transmittance were measured from 250–850 nm on a Jasco V-570 UV/VIS/NIR Spectrophotometer equipped with an integrating sphere. Measurements were collected on regions of ZrS_2 exposed to atmosphere for no more than 20 min. The reflectance and

transmittance of a duplicate quartz substrate were measured to correct for substrate reflection using the method of Cesaria,[63] and the resulting absorption coefficients were plotted in the Tauc fashion.

2.4. Results and Discussion

2.4.1 Precursor Selection

We designed the ZrS_2 deposition to proceed rapidly at temperatures below 400 °C. Because the heats of formation of zirconium disulfide[64] and several volatile zirconium(IV) compounds[65] have been measured, we used thermochemical calculations to select suitable precursors. Based on our experience with low-temperature CVD, we considered the acid-base reactions:

$$ZrL_4 + 2\ H_2S \longrightarrow ZrS_2 + 4\ HL \qquad (1)$$

where L is a ligand chosen from Cl^-, $iPrO^-$, Me_2N^-, Et_2N^-, and the alkyls $PhCH_2^-$, $tBuCH_2^-$, and $Me_3SiCH_2^-$. As shown in Figure 2.6, these reactions are enthalpically favorable at room temperature for the amido and alkyl compounds, but not for the chloride and alkoxide compounds. Because all of the reactions are entropically favorable, they can be induced to proceed through heating. Given our goal of lowering the substrate temperature, selecting chemistry favorable at room temperature offered the best chance of low-temperature CVD. Although the thermodynamic driving force is largest for the alkyls, the amido compounds are generally less thermally sensitive than the alkyl compounds of group 4. Considered alongside the literature precedent for ALD of ZrO_2[52] and ZrS_2[36] and CVD of TiS_2,[49] ZrO_2,[66] and Zr_3N_4,[50] these thermochemical data suggested using zirconium(IV) amido compounds as the zirconium source for low-temperature CVD.

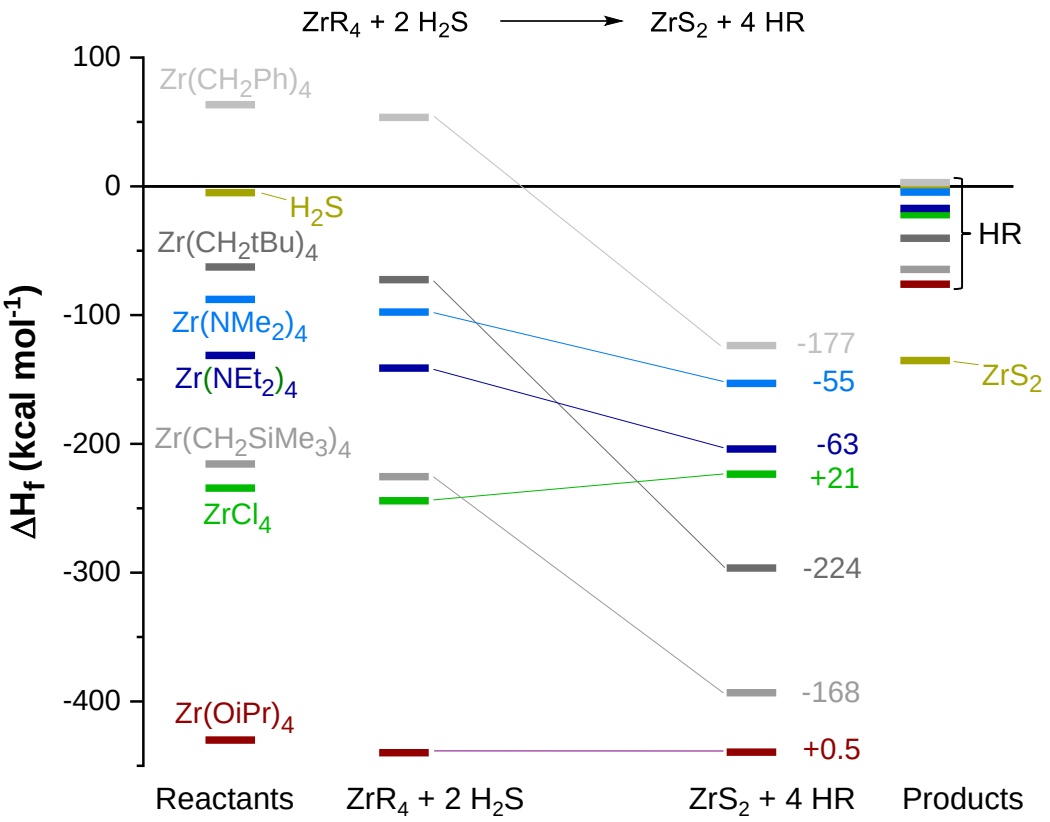

Figure 2.6. Plot of the enthalpies of the reactions of zirconium(IV) compounds with hydrogen sulfide to form ZrS_2. The data are shown in four columns; the outer columns are the standard heats of formation of the individual reactants and products, and the inner two columns are the sums of the heats of formation of the reactants and products. ΔH_{rxn} is favorable (-) for the alkyl and amido compounds, but not the alkoxide or chloride compounds.

To select delivery conditions, we performed simultaneous thermogravimetric analysis/differential scanning calorimetry (TGA/DSC) studies on $Zr(NMe_2)_4$ and measured its vapor pressure at up to 65 °C. We first sought to identify the thermal stability of $Zr(NMe_2)_4$ using TGA/DSC, and found that when heated using a linear ramp mode with a rate of 10 °C/min, $Zr(NMe_2)_4$ shows evaporation behavior typical of a single mass-loss event (presumably evaporation) but 20 wt.% residue suggests precursor decomposition. Differential scanning calorimetry (DSC) obtained concurrently shows an endothermic peak at 60 °C, an exothermic peak

that appears by 76 °C and persists to at least 100 °C, and a second exothermic peak present above 160 °C (Figure 2.7). We attribute the first two features to the melting point and decomposition of $Zr(NMe_2)_4$, which aligns well with values previously identified as 60 and 80 °C, respectively, from TGA.[52] Together, our data suggest decomposition of $Zr(NMe_2)_4$ may occur as early as just above the melting point, which should limit our delivery temperature to ca. 65 °C. Vapor pressure measurements indicate that at 65 °C the vapor pressure of $Zr(NMe_2)_4$ is ca. 1 Torr (Figure 2.7), and we selected this temperature for our first experiment.

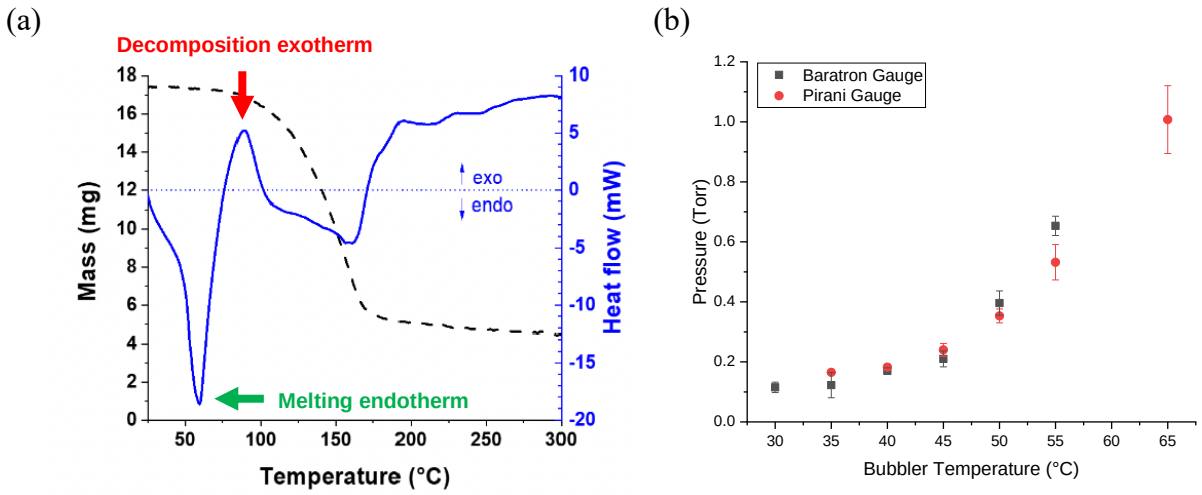

Figure 2.7. (a) Simultaneous TGA/DSC of $Zr(NMe_2)_4$ acquired when heating with a linear ramp rate of 10 °C/min ramp rate. The black dashed lines represent the sample mass in mg and the solid blue line represent the heat flow in mW. (b) Vapor pressure of $Zr(NMe_2)_4$ as a function of bubbler temperature at 30–65 °C. Data points represent the average pressure over 3–5 replicate measurements and error bars represent the standard deviation of these measurements. Black squares represent measurements made with a Baratron absolute pressure gauge, and red circles represent measurements made with a Pirani gauge.

2.4.3 Screen of Deposition Conditions

We constructed a CVD reactor to test our hypothesis that judicious precursor selection could allow lower deposition temperatures in CVD of ZrS_2. This reactor is described in section **2.3.1**. We designed the reactor to safely handle H_2S,[54] by constructing it of H_2S-compatible

materials and placing it inside a fume hood. Having selected a highly reactive zirconium amido precursor, $Zr(NMe_2)_4$, we then sought to identify the conditions necessary to deposit stoichiometric, impurity-free, crystalline films of ZrS_2.

Preliminary depositions were conducted at 200 °C to identify suitable precursor delivery parameters. We selected an initial reactor temperature of 200 °C, drawing on ALD of ZrO_2 and ZrS_2 using $Zr(NMe_2)_4$ and H_2O and H_2S at this temperature.[36, 51, 52] Although the simultaneous presence of both precursors may enable additional reactions in CVD compared with ALD, the ALD precedent at this temperature suggested both that $Zr(NMe_2)_4$ could be used despite being above its decomposition temperature, and that the surface reactions of $Zr(NMe_2)_4$ and H_2S, and their chemisorbed fragments, could proceed rapidly. We used 40 sccm of Ar as a carrier gas to transport the amido precursor vapor. We delivered H_2S at 10 sccm, without a carrier gas. Under these conditions, the H_2S should be in at least 5-fold excess of the stoichiometry required for Reaction 1.

These precursor delivery parameters (recipe 1) afforded extremely high growth rates. Under reaction conditions, dark films appeared in under 5 min. The bubbler was completely exhausted during this deposition, and ultimately films grew thick enough to delaminate from the quartz substrates.

To slow the growth of ZrS_2 films, we decreased the delivery rates of $Zr(NMe_2)_4$ and H_2S. The details of delivery conditions 2 and 3 are listed in Table 1; we adjusted the deposition parameters in steps. In each step, we lowered the flux of $Zr(NMe_2)_4$ by decreasing the bubbler temperature by 10 °C and halving the Ar carrier gas flow rate. The vapor pressures of $Zr(NMe_2)_4$ were then 0.65 Torr (55 °C, recipe 2) and 0.2 Torr (45 °C, recipe 3). We also lowered the H_2S flow rate from 10 sccm to 5 sccm and then 1 sccm, keeping the H_2S in at least 2-fold excess. Finally,

we added argon to dilute the H_2S, seeking to achieve more uniform deposition down the length of the reactor. Cross-sectional microscopy of the films placed 1.5″ downstream from the precursor inlets revealed growth rates of 180 nm/min (recipe 2, Figure 2.8) and 35 nm/min (recipe 3, Figure 2.9). The $Zr(NMe_2)_4$ bubbler was refilled between recipe 2 and recipe 3.

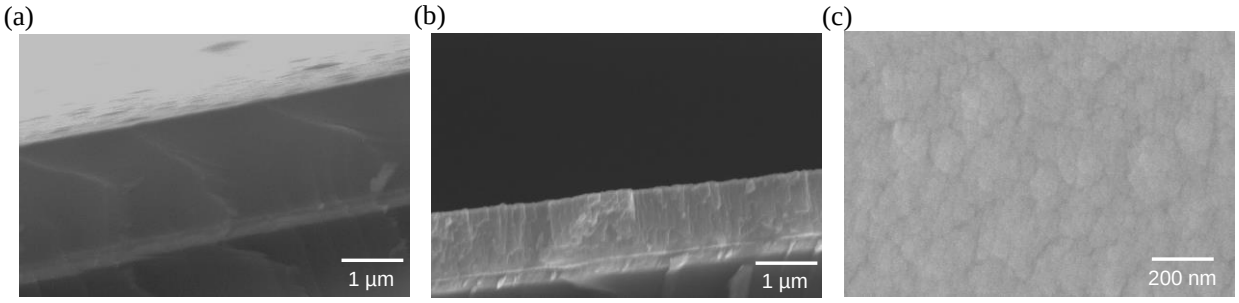

Figure 2.8. Micrographs of samples deposited on quartz for 10 min at 200 °C using recipe 2. Samples were placed (a) 1.5″, (b) 3.5″, and (c) 3.5″ from the precursor inlets. The scale bars in the cross-sections are 1 µm, and the plan-view scale bare is 200 nm.

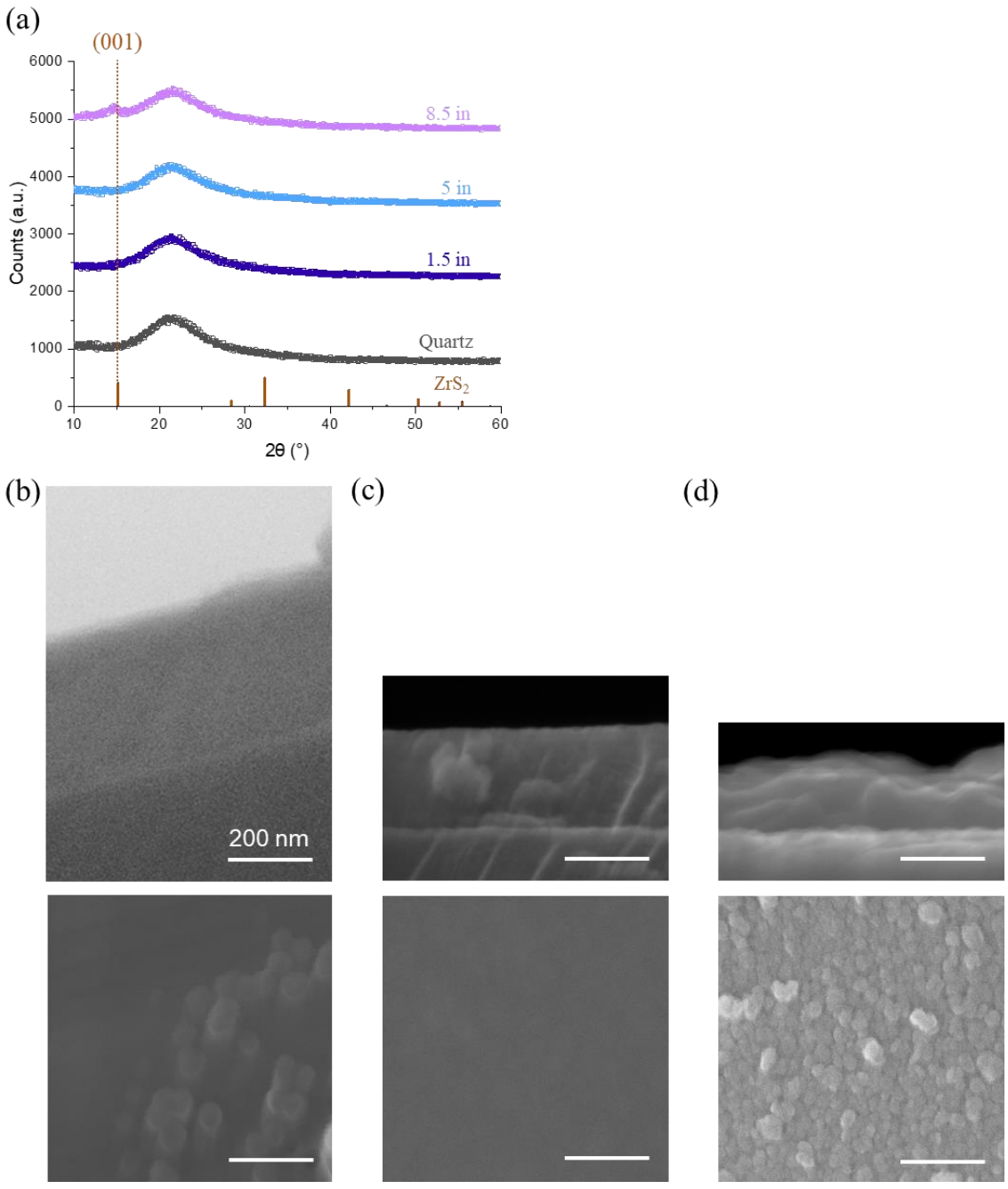

Figure 2.9. (a) X-ray diffractograms of ZrS_2 films deposited on quartz for 10 min at 200 °C using fast growth recipe 3. Films at the front of the reactor are amorphous and the film at the rear is weakly crystalline. Plan-view and cross section micrographs of samples placed (b) 1.5″, (c) 5″, and (d) 8.5″ from the precursor inlets. The scale bar in each micrograph is 200 nm.

2.4.4. Initial Study of Deposition Temperature—Fast Growth Recipe 3

Having obtained some control over the deposition by decreasing the flux of each precursor, we explored the impact of temperature on the CVD reaction. We tested substrate temperatures from 200–350 °C using recipe 3. The growth rate increases with temperature, with the largest apparent increase occurring between 200 and 250 °C, as film morphology transitions from dense with small, compact grains to porous, with vertically aligned sheets (Figure 2.10). ZrS_2 films with flakes are fragile and scratch off easily when handled with forceps. For all deposition temperatures, the growth rate is highest at the front of the reaction zone, where the partial pressure of each precursor is highest.

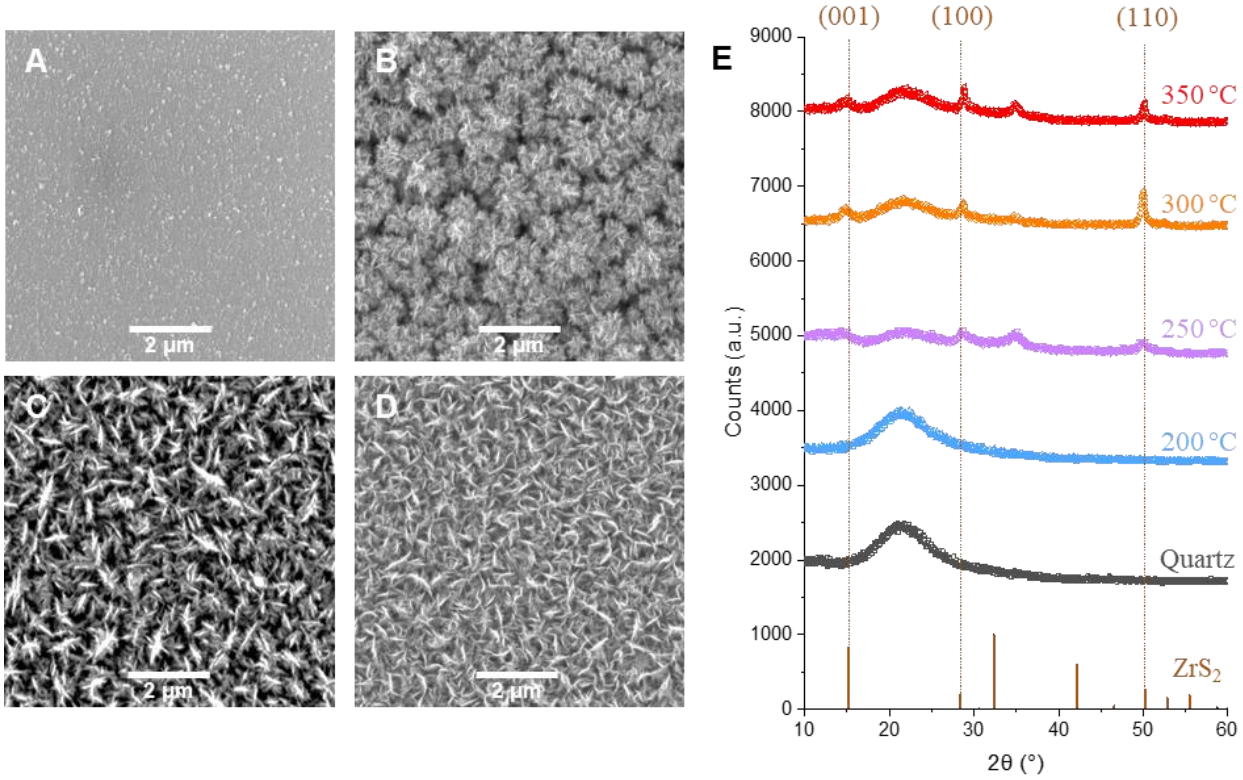

Figure 2.10. Plan-view micrographs of ZrS_2 films deposited 1.5″ from precursor inlets using fast growth recipe 3 at (a) 200 °C, (b) 250 °C, (c) 300 °C, and (d) 350 °C; scale bars represent 2 µm. (e) Diffractograms for these films and a bare quartz substrate, plotted above the reference pattern for ZrS_2 (COD 5910006).

ZrS_2 films deposited at 200 °C in 10 min using recipe 3 comprise continuous, small-grained films that increase in crystallinity down the length of the reaction zone. Figure 2.9 shows films of tightly packed, approximately spherical grains with diameters of ~50 nm. Down the length of the reactor, film roughness increases slightly and film thickness decreases from 400 nm (implied growth rate: 40 nm/min) at 1.5″ from the precursor inlets to 130 nm at 8.5″. These films also transition from amorphous near the front of the deposition zone to weakly crystalline near the rear, with a single broad peak emerging in powder diffractograms that corresponds to the (001) plane of ZrS_2 in the 1T phase. The films appear to grow preferentially with ZrS_2 layers parallel to the substrate surface. The domain size calculated by the Scherrer equation is ca. 10 nm, smaller than the grain size observed by SEM. By EDS, the films appear approximately stoichiometric, with compositions (neglecting the 8-10 at.% Si detected from the substrate): 36-37 at.% Zr, 60-63 at.% S, and 1-3 at.% O. For comparison, EDS of a freshly exfoliated single crystal of ZrS_2 provided: 37-40 at.% Zr, 59-62 at.% S, and 0-1.5 at.% O (Figure 2.11, Table 2). Along with 50.1 at.% Zr, 36.0 at.% S, 4.7 at.% O, XPS detects 6.5 at.% C and 2.8 at.% N, suggesting the growth incorporates some ligand fragments (see section **2.4.8**). The composition of a freshly exfoliated single crystal measured by XPS in our UHV chamber is 33.4 at.% Zr, 63.4 at.% S, 0.0 at.% O, and 3.2 at.% C.[53]

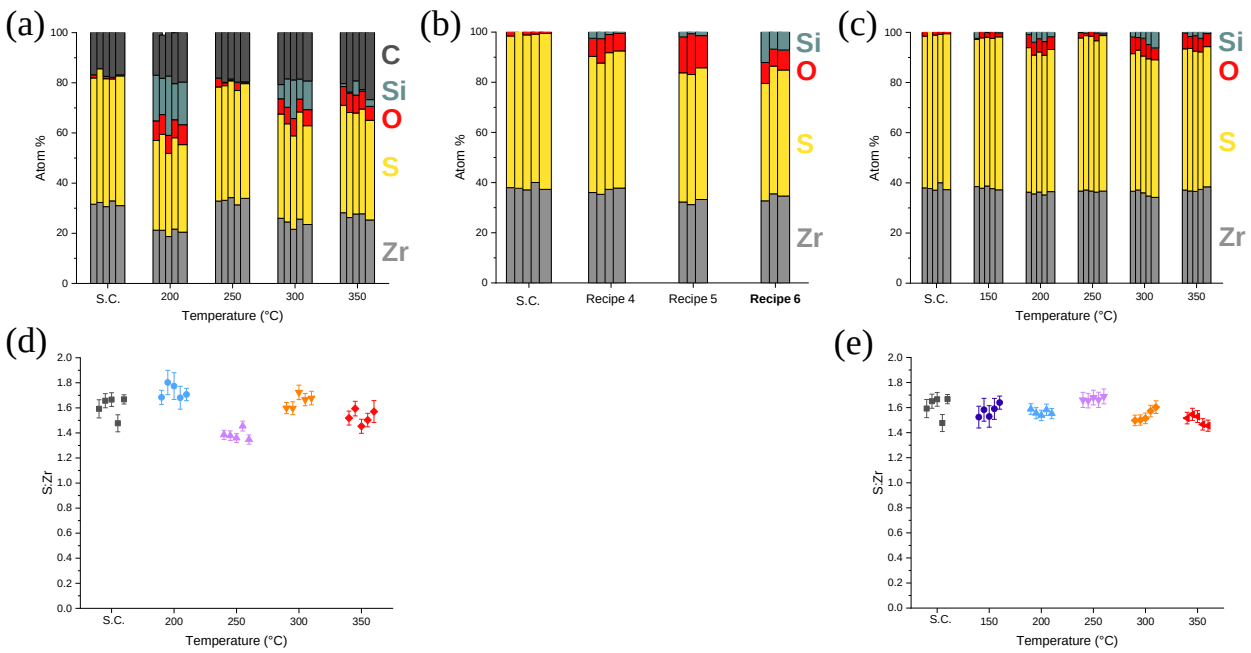

Figure 2.11. Composition of a ZrS_2 single crystal (S.C). and films deposited at various temperatures using (a) fast growth recipe 3, (b) recipes 4-6, and (c) slow growth recipe 6. Scatter plots show the S:Zr ratio of a ZrS_2 single crystal and films deposited at various temperatures using (d) fast growth recipe 3, and (e) slow growth recipe 6. Films used for EDS were deposited 1.5″ and 0.5″ from the precursor inlets for fast and slow growth recipes, respectively.

Table 2.2 EDS compositions of ZrS_2 films deposited with the fast growth recipe 3 at 200-350 °C. Averages of five locations are listed, ± 1 standard deviation.

Sample	%Zr	%S	% O	% Si	S:Zr
S.C	31.7 ± 0.9	51.0 ± 1.7	0.7 ± 0.5	0.0 ± 0.0	1.61 ± 0.08
200 °C	25.4 ± 1.7	43.8 ± 2.6	9.3 ± 0.5	21.5 ± 4.4	1.73 ± 0.05
250 °C	40.9 ± 1.3	56.7 ± 0.6	2.1 ± 1.8	0.3 ± 0.1	1.39 ± 0.04
300 °C	30.0 ± 2.3	49.5 ± 2.9	7.7 ± 0.8	12.8 ± 4.5	1.65 ± 0.05
350 °C	34.9 ± 0.7	53.5 ± 2.0	9.1 ± 0.9	2.7 ± 2.7	1.53 ± 0.06

Table 2.3. EDS compositions of ZrS_2 films deposited at 300 °C using recipes 4-6. Averages of five locations are listed, ± 1 standard deviation.

Recipe	%Zr	%S	% O	% Si	S:Zr
S.C.	31.7 ± 0.9	51.0 ± 1.7	0.6 ± 0.5	0.0 ± 0.0	1.61 ± 0.08
4	36.6 ± 1.1	53.9 ± 1.1	7.8 ± 1.3	1.6 ± 1.1	1.47± 0.03
5	32.2 ± 1.0	52.0 ± 0.5	14.5 ± 1.7	1.3 ± 0.6	1.61 ± 0.04
6	34.3 ± 1.4	49.3 ± 2.2	7.7 ± 0.8	8.7 ± 3.0	1.44 ± 0.01

Table 2.4. EDS compositions of ZrS_2 films deposited with the slow growth recipe 6 at 150-350 °C. Averages of five locations are listed, ± 1 standard deviation.

Sample	%Zr	%S	% O	% Si	S:Zr
S.C.	31.7 ± 0.9	51.0 ± 1.7	0.6 ± 0.5	0.0 ± 0.0	1.61 ± 0.08
150 °C	38.0 ± 0.6	59.8 ± 0.9	1.7 ± 0.8	0.5 ± 1.0	1.57 ± 0.05
200 °C	36.0 ± 0.6	56.2 ± 0.9	5.2 ± 0.1	2.5 ± 1.3	1.56 ± 0.02
250 °C	36.7 ± 0.3	61.3 ± 0.7	1.7 ± 1.0	0.3 ± 0.2	1.67 ± 0.01
300 °C	35.8 ± 1.2	55.0 ± 0.5	5.8 ± 1.0	3.5 ± 1.9	1.54 ± 0.05
350 °C	37.3 ± 0.7	56.0 ± 0.7	5.6 ± 0.6	1.2 ± 0.9	1.50 ± 0.04

ZrS_2 films deposited using recipe 3 at 250 °C in 16 min are weakly crystalline, and largely made up of sheets of ZrS_2 growing perpendicular to the substrate. Micrographs of ZrS_2 films deposited 1.5″ from the precursor inlets show clumps of platelets (Figure 2.10); down the reactor, the plates appear less aggregated into clusters, until they disappear at rear of the deposition zone (Figure 2.12). Films decrease in thickness down the reactor, from 6000 nm (implied growth rate: 375 nm/min—but note that these plate-like films are not fully dense) at 1.5″ from the precursor inlets to 200 nm (12.5 nm/min) at 4.5″. Diffractograms of the front films show low intensity peaks corresponding to the (001), (100), and (110) planes of ZrS_2 (Figure 2.10), indicating less preferential orientation than at 200°C. The 100 and 110 reflections arise from flakes of ZrS_2 growing vertically out of the substrate. The intensity of these diffractions decreases down the length of the reactor (Figure 2.13), reversing the trend observed at 200 °C, but consistent with the decrease in areal density of flakes. An impurity phase with a broad diffraction peak at $2\theta = 35.1°$

appears in films deposited at the front of the reaction zone (Figure 2.13). Unambiguously identifying this phase from a single broad diffraction peak is not possible, although phases like ZrOS, Zr_3S_4, and ZrN all have diffraction peaks near $2\theta = 35°$. The composition data do not fully resolve this question, with EDS measuring: 39-42 at.% Zr, 56-57 at.% S, and 0.5-4 at.% O (Figure 2.11, Table 2.2). XPS detects 38 at.% Zr, 53 at.% S, 6.3 at.% O, and 2.8 at.% C (see section **2.4.8**).

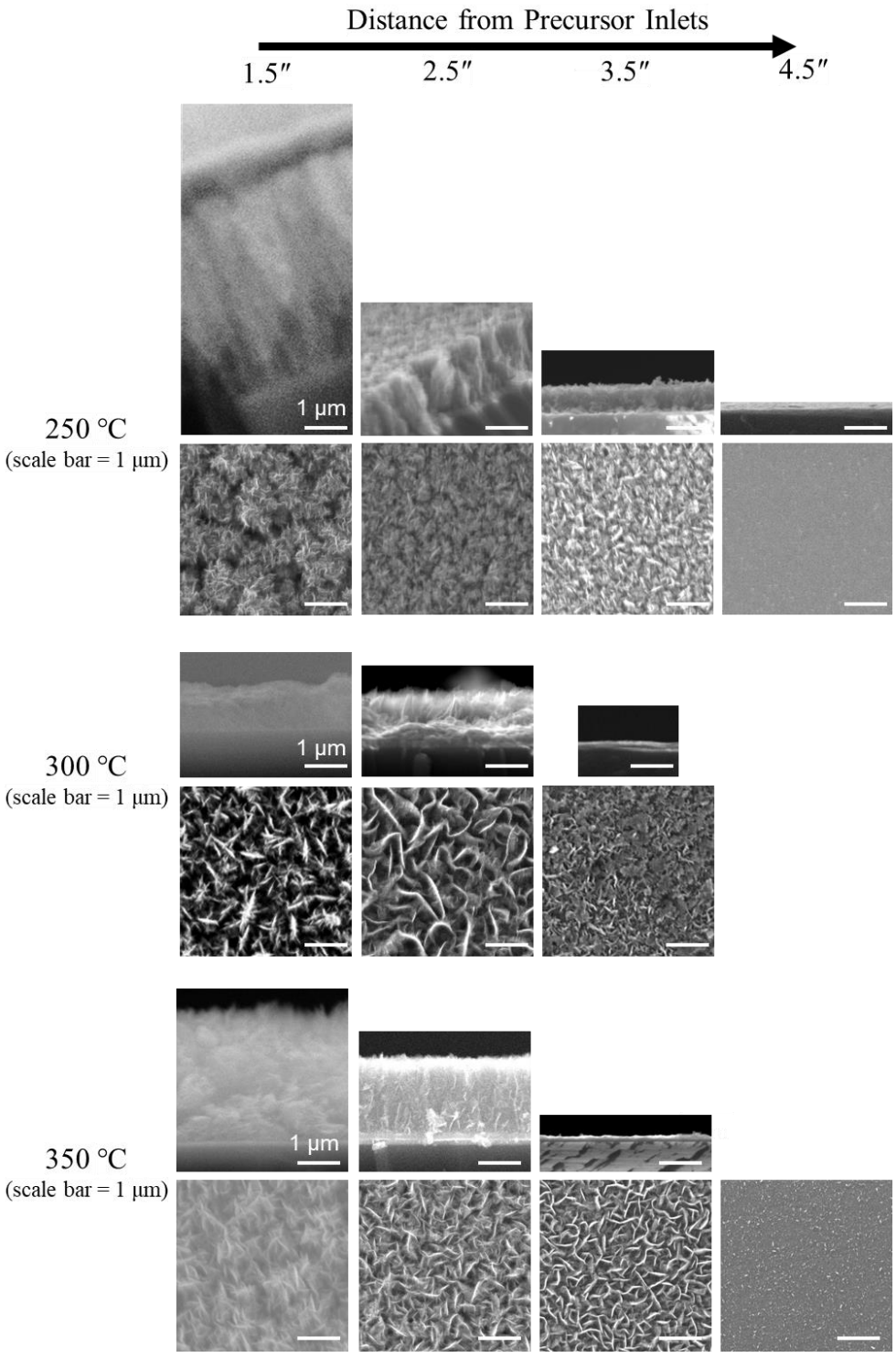

Figure 2.12. Plan-view and cross-sectional micrographs of ZrS_2 films in locations 1.5″–4.5″ from the precursor inlets in depositions at 250–350 °C using fast growth recipe 3. Scale bars are 1 μm.

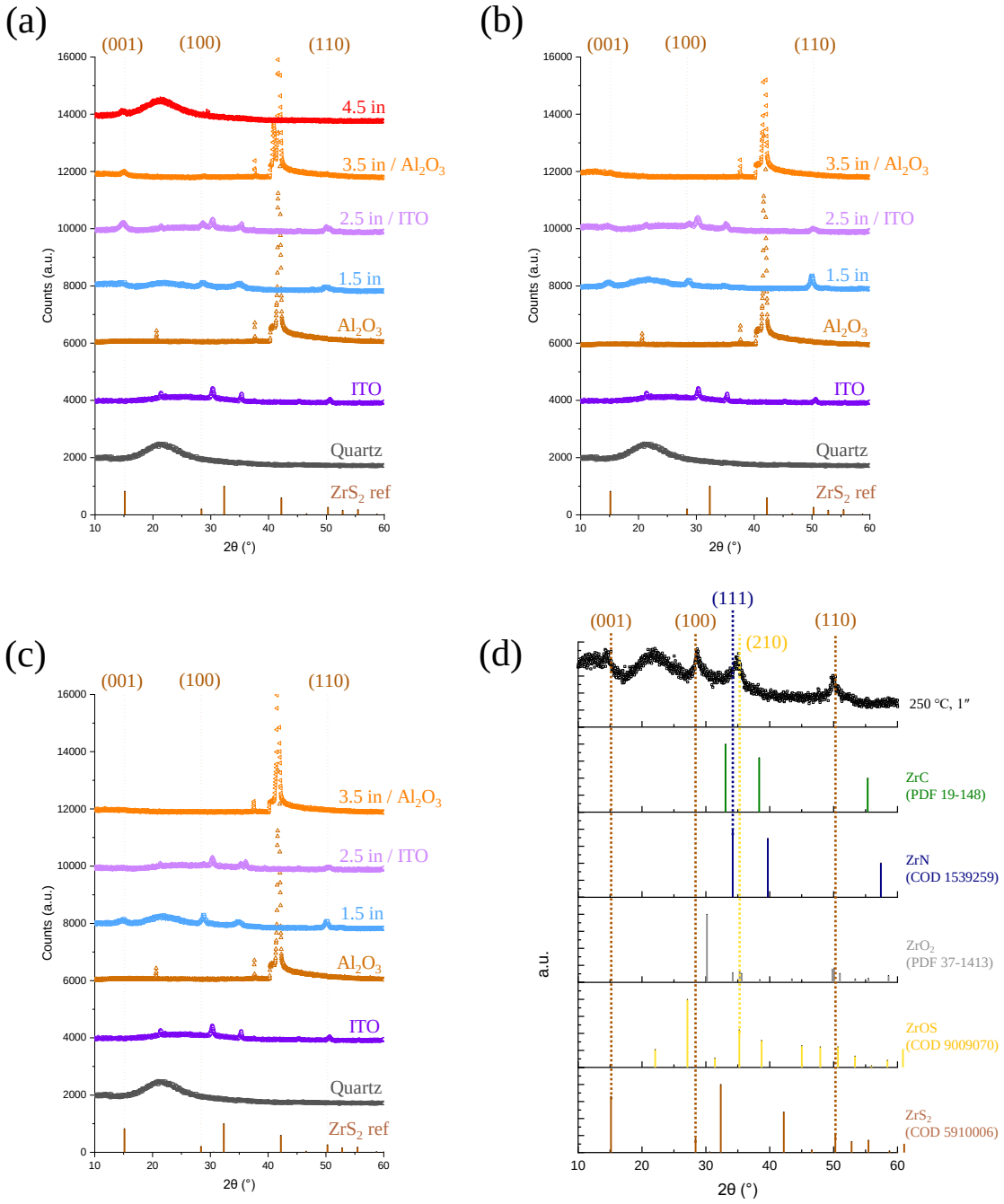

Figure 2.13. Powder X-ray diffractograms of ZrS_2 films deposited 1.5″–4.5″ from the precursor inlets using fast growth recipe 3. The substrates were quartz (1.5″), ITO (2.5″), Al_2O_3 (3.5″), and quartz (4.5″). Films were deposited at (a) 250 °C, (b) 300 °C, and (c) 350 °C. (d) Comparison of known diffraction patterns of several reference compounds to a sample located 1.5″ for the precursor inlets in a deposition at 250 °C.

ZrS_2 films deposited using recipe 3 at 300 °C in 15 min comprise larger, better separated flakes, with similar crystallinity as at 250 °C. The flakes are largest at 2.5″ down the reactor; they are clustered more near the front of the reactor, and smaller and more uniformly distributed near the rear of the reactor (Figure 2.12). Films decrease in thickness down the reactor, from 1000 nm (ca. 66 nm/min) at 1.5″ to 240 nm at 3.5″. Diffractograms of the front films show similar texturing to the films at 250 °C, but with enhanced 110 reflections near the inlet (Figures 2.10, 2.13). The impurity phase at $2\theta = 35.1°$ appears in the front film, but more weakly than at 250 °C. Films appear to contain more oxygen, with compositions by EDS (neglecting 7-19 at.% Si): 33-35 at.% Zr, 56-58 at.% S, and 7-11 at.% O (Figure 2.11, Table 2.2). The oxygen incorporation may result from a small oxygen source during deposition (e.g., residual adsorbed water), or air exposure of the porous, high surface area film before analysis. XPS detects 5.9 at.% O, suggesting the measured oxygen is present in the films (not solely from the quartz substrate). No C or N is detected, while the composition of the film is 38.9 at.% Zr, 55.2 at.% S, and 5.9 at.% O (see section **2.4.8**).

ZrS_2 films grown using recipe 3 at 350 °C in 15 min contain a thick, porous network of flakes, with similar crystallinity to 250-300 °C. Films rapidly decrease in thickness down the reactor, from 3000 nm (ca. 200 nm/min) at 1.5″ to 275 nm at 3.5″ (Figure 2.12). Diffractograms of the front films show similar texturing to the films at 250 °C (Figures 2.10, 2.13). The impurity phase at $2\theta = 35.1°$ appears in the front film, similar to 250 °C. Like at 300 °C, films contain up to 10 at.% oxygen, with EDS providing: 34.3-35.9 at.% Zr, 49.8-54.9 at.% S, and 7.6-10.1 at.% O. Here, the Si signal is 0.6-7.0 at.%, suggesting the oxygen is within the film (Figure 2.11, Table 2.2). Consistent with this view, XPS detects 12.6 at.% O. No N is detected, but 2.4 at.% C is present along with 37.4 at.% Zr and 47.7 at.% S (see section **2.4.8**). XPS studies on samples

deposited on ITO substrates show 9.1% In, possibly indicating a reaction with the substrate, and prompted us to pursue all further XPS studies on quartz substrates.

Overall, these results show rapid deposition of the layered TMDC ZrS_2. At 200 °C, this recipe deposits material at the front of the reactor faster than ZrS_2 can crystallize. The crystalline material grows initially with ZrS_2 sheets parallel to the substrate surface, as revealed by pXRD patterns textured in the [001] direction. As deposition temperature increases, nucleation appears to randomize, allowing fast growth in the in-plane directions for ZrS_2 to produce sheets or flakes of ZrS_2 growing perpendicular to the substrate surface. Although this type of high surface area growth can be useful for devices like supercapacitors,[14, 67] we sought to suppress this growth and maintain smooth, compact film growth more typically used for optoelectronic devices.

2.4.5. Experiments to Suppress Flake Growth and Enhance Crystallinity

We next explored new precursor delivery conditions, seeking to improve the crystallinity and control the morphology of ZrS_2 films deposited at higher temperatures. We explored whether slower growth rates and higher partial pressures of H_2S might encourage compact film growth throughout the reactor. We investigated an additional 3 precursor delivery conditions, recipes 4–6 (Table 1), which lowered the vapor pressure to 0.1 Torr (35 °C, recipes 4–6) and halved the flow of Ar carrier gas for $Zr(NMe_2)_4$ twice (recipes 4 and 6) to the reduce the growth rate of ZrS_2 at 300 °C. We also studied the effects of adding 5× more H_2S (recipe 5). Due to differences in film growth rates, deposition times were set to 1 h for recipes 4 and 5, and to 4 h for recipe 6.

Decreasing the flux of $Zr(NMe_2)_4$ using recipe 4 increased the crystallinity of ZrS_2 films, with divergent morphologies based on local precursor partial pressures. In samples deposited at the front of the reaction zone, recipe 4 affords films with more intense diffractions, textured

somewhat towards the (001) plane compared with recipe 3 (Figure 2.14). Down the length of the reaction zone, the intensity of the 001 diffraction remains relatively constant despite film thickness decreasing from 3500 nm (60 min deposition, growth rate of ca. 58 nm/min) at 1.5″ to 300 nm at 4.5″, again suggesting increasing film crystallinity (Figure 2.15). The impurity phase at $2\theta = 35.1°$ is no longer present. Film morphology is comparable to recipe 3, with clustered flakes at the front of the reaction zone; larger, more uniformly distributed flakes 2.5″–3.5″ from the precursor inlets; and a compact morphology with scattered platelets at the rear (Figures 2.14 and 2.16). Films grown via recipe 4 have similar compositions to recipe 3 films, 36-38 at.% Zr, 53-55 at.% S, and 7-9 at.% O (Figure 2.11, Table 2.3).

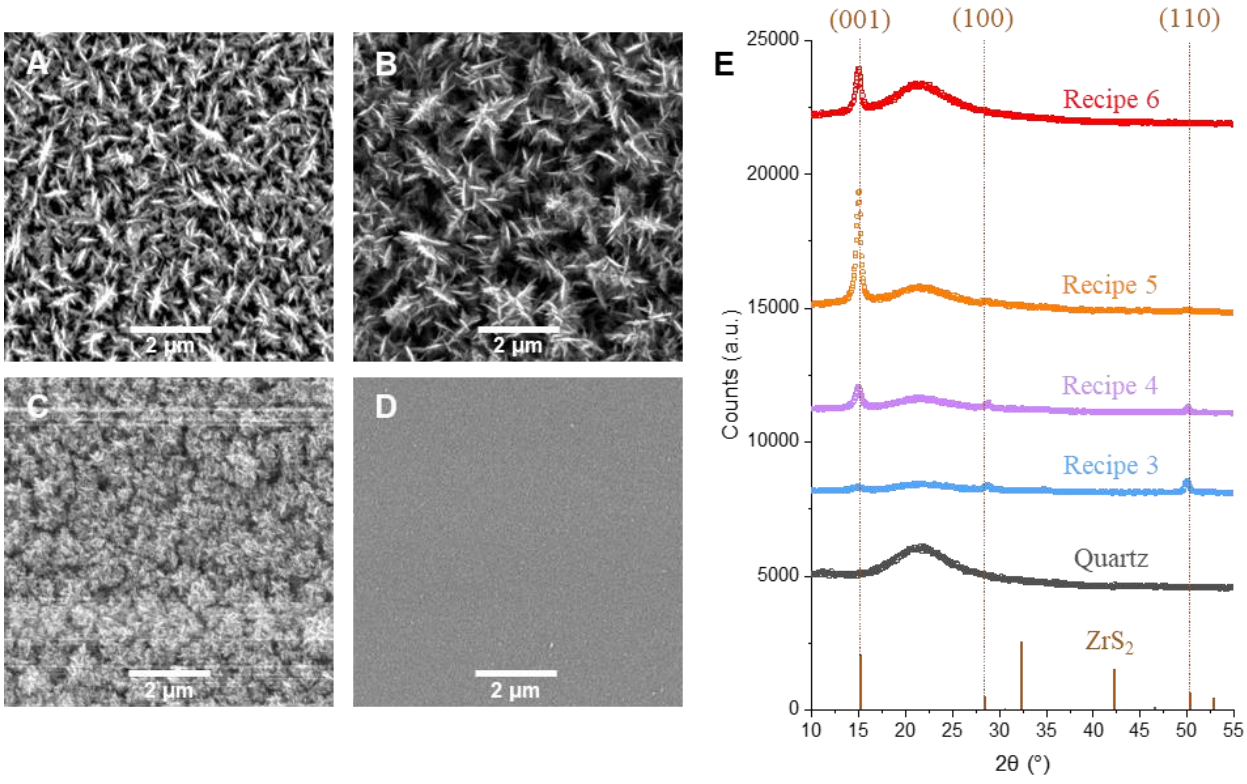

Figure 2.14. Plan-view micrographs of ZrS_2 films deposited 1.5″ from precursor inlets at 300 °C using (a) recipe 3, (b) recipe 4, (c) recipe 5, and (d) recipe 6; scale bars represent 2 µm. (e) Diffractograms for these films and a bare quartz substrate, plotted above the reference pattern for ZrS_2 (COD 5910006).

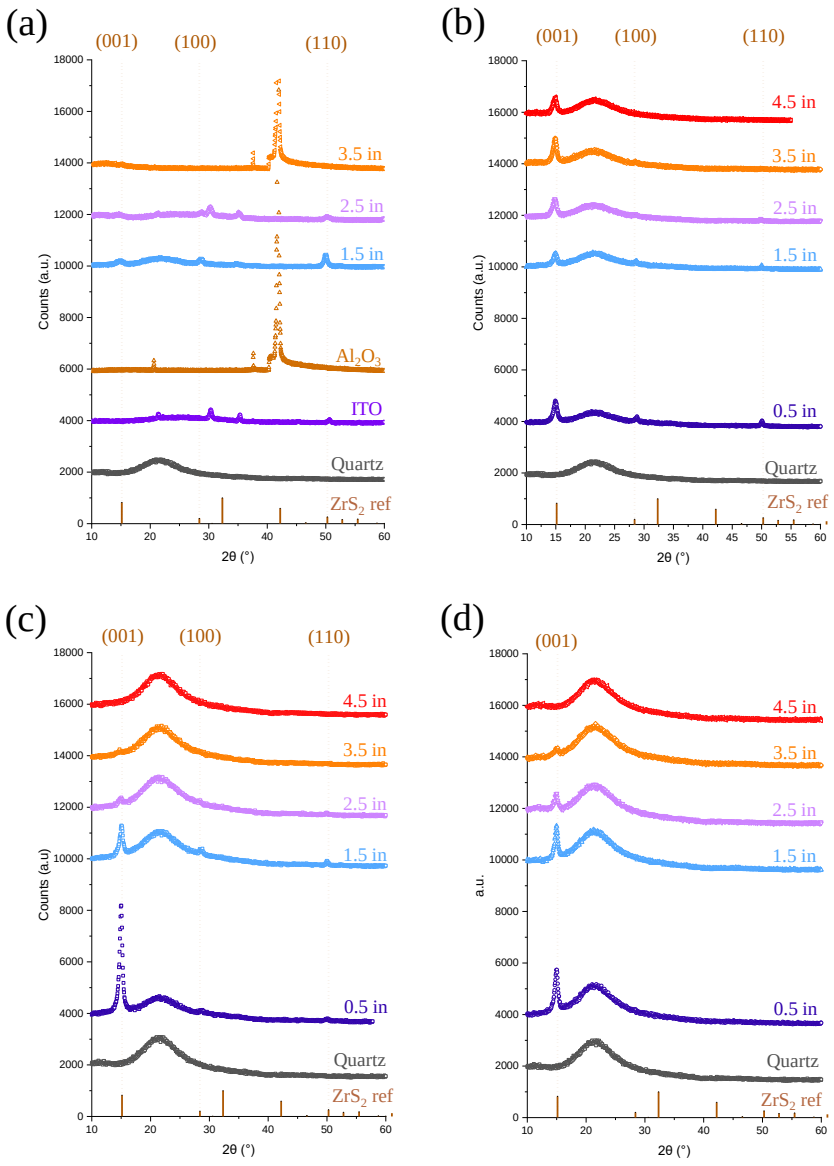

Figure 2.15. Powder X-ray diffractograms of ZrS_2 films deposited 1.5″–4.5″ from the precursor inlets at 300 °C using (a) recipe 3, (b) recipe 4, (c) recipe 5, and (d) recipe 6. These depositions were performed sequentially, and the bubbler was not refilled between depositions. Substrates for samples deposited using recipe 3 are quartz (1.5″ and 4.5″), ITO (2.5″) and c-plane sapphire (3.5″). All substrates for recipes 4–6 are quartz. The ZrS_2 reference diffraction pattern is COD 5910006.

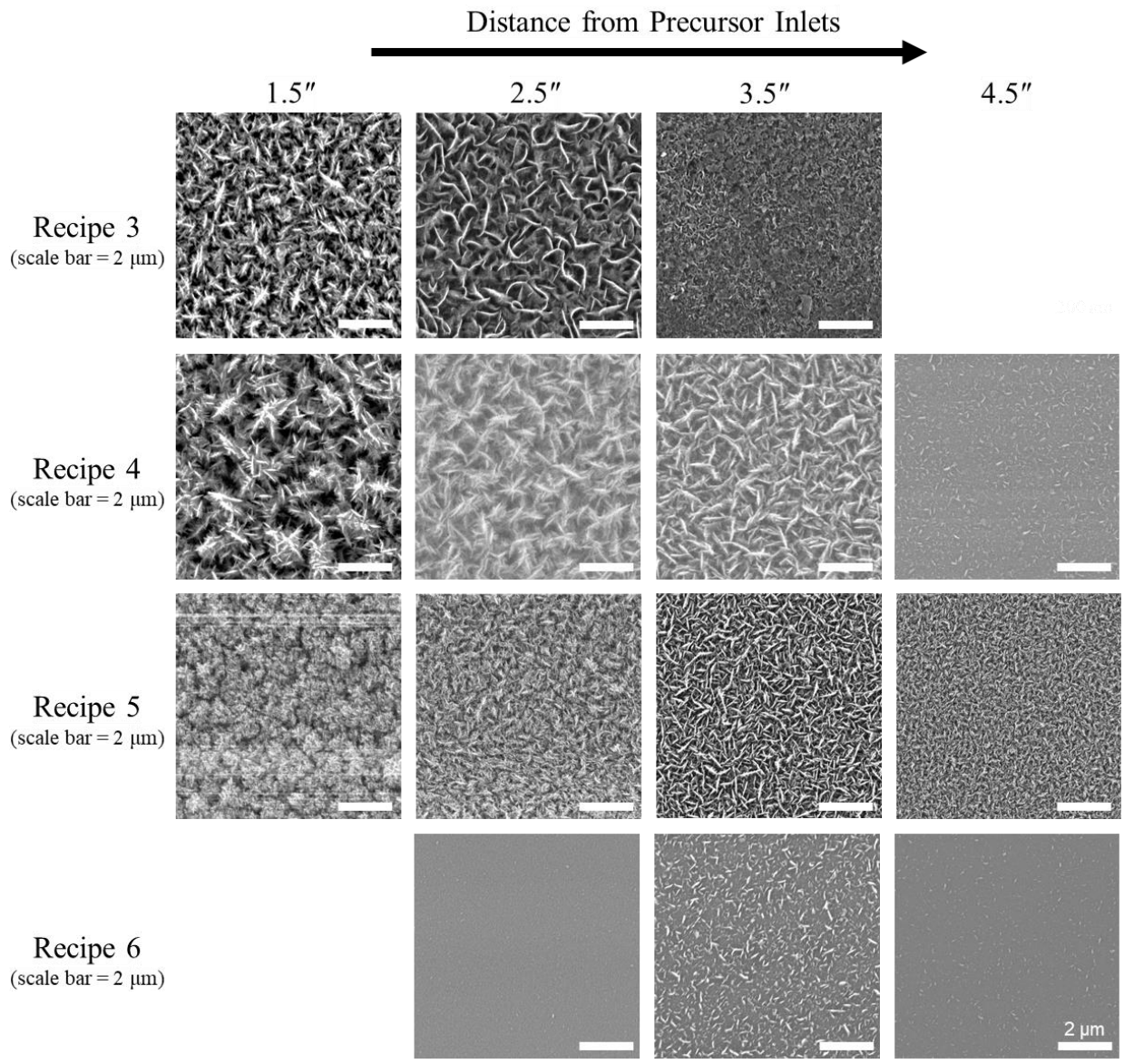

Figure 2.16. Plan-view micrographs of ZrS_2 films deposited 1.5″–4.5″ from the precursor inlets using recipes 3, 4, 5, and 6 at 300 °C. Substrates for samples deposited using recipe 3 are quartz (1.5″ and 4.5″), ITO (2.5″) and c-plane sapphire (3.5″). All substrates for recipes 4–6 are quartz. The scale bar in each micrograph is 2 μm.

Importantly for our understanding of the plate growth, we also found a gradient of morphologies normal to precursor flow on the front substrates. As shown in Figure 2.17, a dense forest of plates grows in front of the $Zr(NMe_2)_4$ inlet, transitioning to smooth and compact films

in front of the H_2S inlet. Cross-sectional micrographs across this morphology gradient reveal a layer of ZrS_2 flakes that decreases in height towards the H_2S inlet, atop a dense layer of nearly constant thickness until flakes are absent. This gradient suggests fast growth of plates is stimulated by high partial pressures of $Zr(NMe_2)_4$, although it leaves open whether the *absolute* partial pressure or the partial pressure *relative* to the partial pressure of H_2S (or both) controls flake growth.

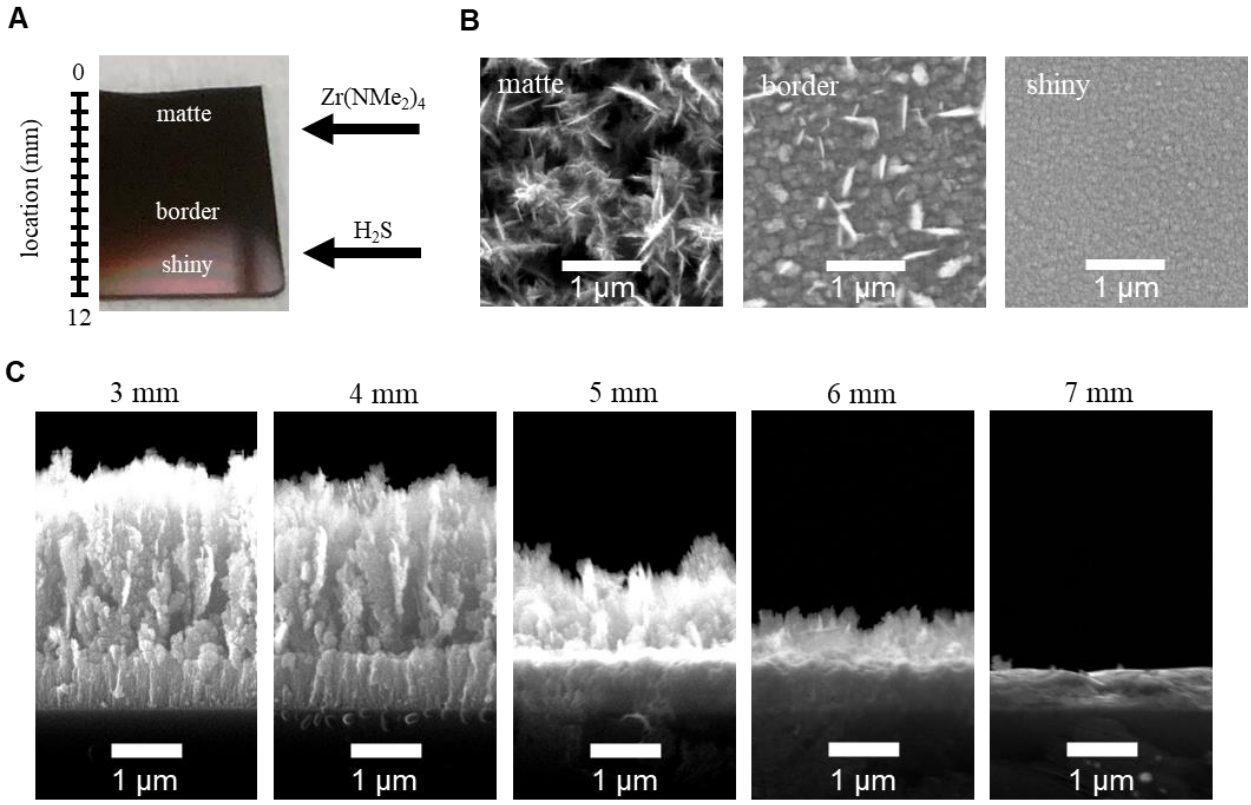

Figure 2.17. Changes in morphology across the sample in a film deposited 0.5″ from the precursor inlets at 300 °C. (a) Photograph of the sample showing the transition from matte to shiny appearance. (b) Plan-view micrographs corresponding to the matte, border, and shiny regions labeled in (a). (c) Microscopic cross-sections of the film taken with increasing distance from the left edge of the substrate; the matte region in front of the $Zr(NMe_2)_4$ inlet corresponds to the vertical plates, whereas the shiny region in front of the H_2S inlet corresponds to the compact film. All scale bars represent 1 μm.

Growing ZrS_2 in a larger excess of H_2S (recipe 5) did not suppress the formation of flakes but did improve crystallinity at the front of the reaction zone. To test whether higher H_2S partial pressure can suppress the formation of flakes, we increased the H_2S delivery rate from 1 sccm to 5 sccm while keeping all other parameters the same (Table 2.1). In Figure 2.14, microscopy reveals clumps of small flakes at the front of the reaction zone, which are similar in appearance to those on films deposited at 250 °C using recipe 3 (Figure 2.12). Films deposited farther downstream have comparable morphologies to the front of the reaction zone, with smaller flake sizes compared to recipes 3 and 4 (Figure 2.16). Interestingly, we found that the intensity of the 001 reflection in the frontmost sample increases relative to recipe 4 despite films being thinner, but down the reaction zone the intensity of all diffractions decreases sharply (Figure 2.15). This decrease in intensity down the reactor matches the change in thickness, from 1700 nm (60 min growth, growth rate ca. 28 nm/min) at 1.5″ to 400 nm at 3.5″. Films grown via recipe 5 suffered from oxygen incorporation, containing, 31-33 at.% Zr, 51-53 at.% S, and 12-16 at.% O (Figure 2.11, Table 2.3).

In contrast, further lowering the flux of $Zr(NMe_2)_4$ eliminated the formation of flakes at the front of the reaction zone. For these depositions, our slow growth recipe 6, we returned the H_2S flow to recipe 4, and lowered the Ar carrier gas flowrate from 5 to 2 sccm to decrease the flux of $Zr(NMe_2)_4$ (Table 2.1). Plan view microscopy of films deposited 1.5″–2.5″ from the precursor inlets show the absence of flakes, with films comprising small, compact grains similar in appearance to those obtained at 200 °C (Figure 2.14). Farther downstream in the reaction zone a sparse overlayer of flakes is present (Figure 2.16). The intensity of the 001 reflection in the frontmost film is intermediate to that obtained using recipes 4 and 5, and the (100) and (110) planes of ZrS_2 are not detected (Figure 2.14). Like recipe 5, the intensity of the (001) diffraction decreases down the length of the reactor (Figure 2.15), suggesting the crystallization rate now matches or

exceeds the deposition rate. Film thickness decreases from 900 nm (growth duration: 240 min, implied growth rate: 3.8 nm/min) at 1.5″ to 180 nm at 3.5″.

2.4.6. Study of Deposition Temperature—Slow Growth Recipe 6

We then utilized this slow-growth recipe, 6, for a second study of the impact of temperature on ZrS_2 film deposition. We first refilled the $Zr(NMe_2)_4$ bubbler, having used ~90% of the precursor charge in depositions using recipe 3 at 200–350 °C and recipes 4–6 at 300 °C. Films were deposited on quartz substrates at 150–350 °C, with an additional substrate 0.5″ from the precursor inlets to obtain more information on morphology gradients that might be present. Due to the (intentionally) low growth rates, the deposition time was increased to 4 hours, until films 0.5″–1.5″ from the precursor inlets were dark brown in color. Morphology, thickness, and crystallinity of films were characterized down the reactor in each deposition as was the sheet resistance using four-point probe measurements. All films are more crystalline than their counterparts deposited with recipe 3. Samples deposited at all temperatures were analyzed by XPS, and no C or N were detected in the film bulk; the films were stoichiometric ZrS_2 with ≤6 at.% O (Figure 2.11, Table 2.4). Films decrease in thickness down the reactor, and are generally thickest in front of the $Zr(NMe_2)_4$ inlet (Figures 2.18 and 2.19).

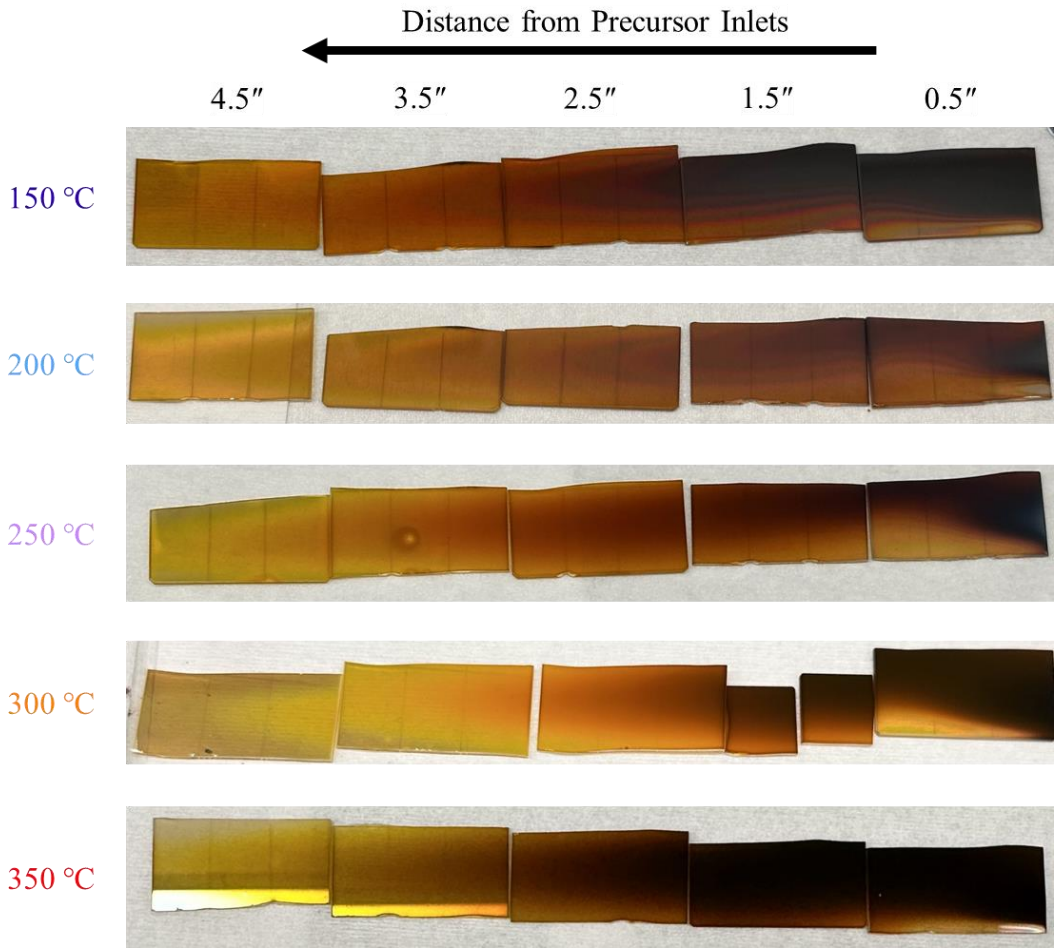

Figure 2.18 Photographs of ZrS_2 films deposited at 150-350 °C using slow growth recipe 6. Some spatial variation in the film thickness can be observed both down the reactor and perpendicular to the gas flow.

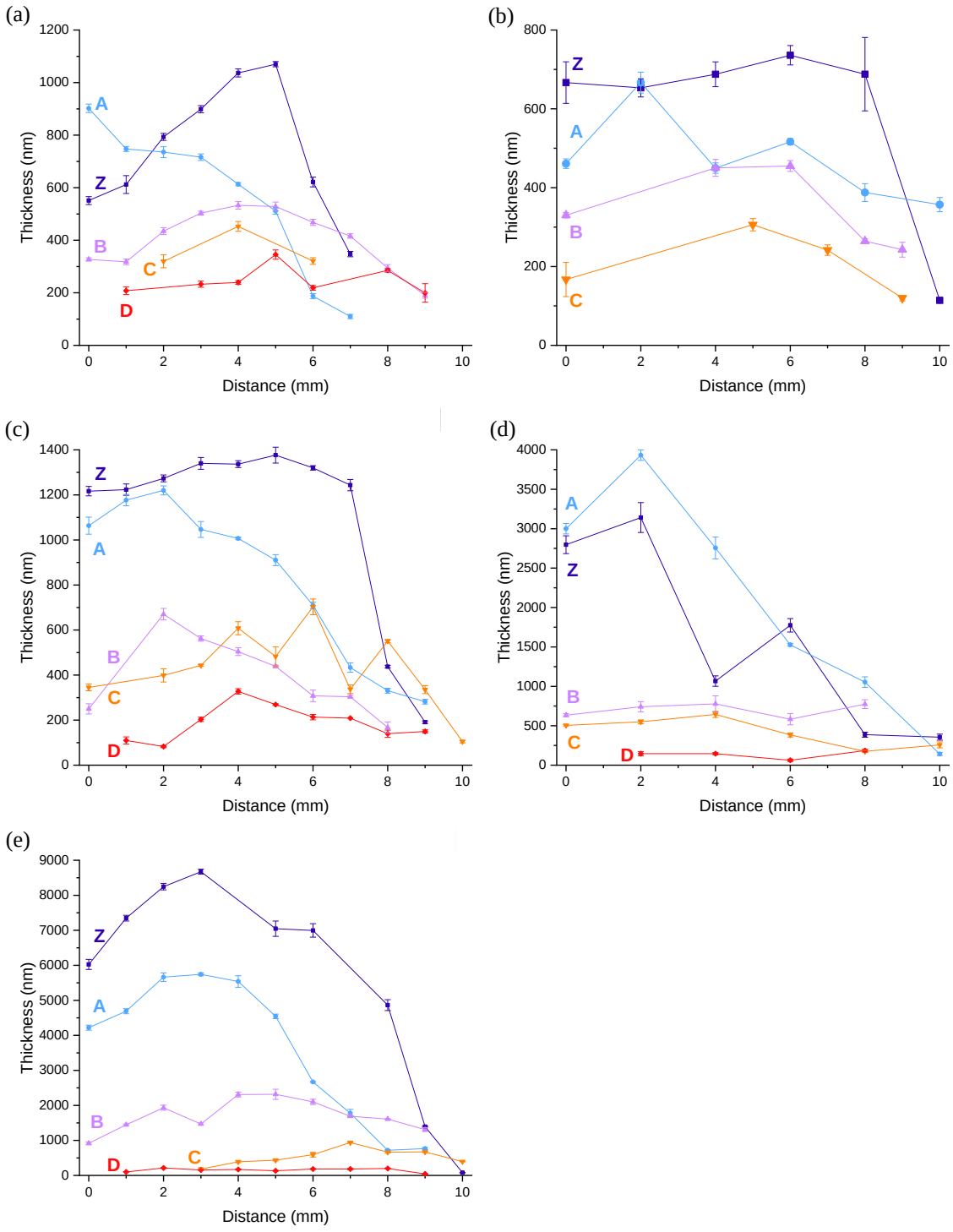

Figure 2.19 Thickness profiles of ZrS_2 films normal to the precursor flow at deposition temperatures of (a) 150 °C, (b) 200 °C, (c) 250 °C, (d) 300 °C, and (e) 350 °C. Thicknesses are obtained from SEM cross-sections, collected at positions Z (0.5″ from the precursor inlets), A (1.5″), B (2.5″), C (3.5″), and D (4.5″). The $Zr(NMe_2)_4$ inlet is on the left, and the H_2S inlet on the right, along the distance (x) axis.

Depositing ZrS_2 at 150 and 200 °C using our slow growth recipe affords films with smooth, compact morphologies and enhanced crystallinity relative to recipe 3. Down the length of the reactor, films deposited at 150 °C roughen in appearance, while at 200 °C films maintain similar morphologies throughout the length of the reaction zone (Figure 2.20). Figure 4 shows we are now able to obtain crystalline films at the front of the reactor at 200 °C, displaying a single intense diffraction from the (001) plane of ZrS_2. Down the length of the reactor, the intensity of this diffraction peak is mostly constant despite film thickness deceasing from 1400 nm at 0.5″ (5.8 nm/min) to 500 nm at 4.5″ (Figure 2.21), which suggests increasing crystallinity similar to that observed using recipe 3.

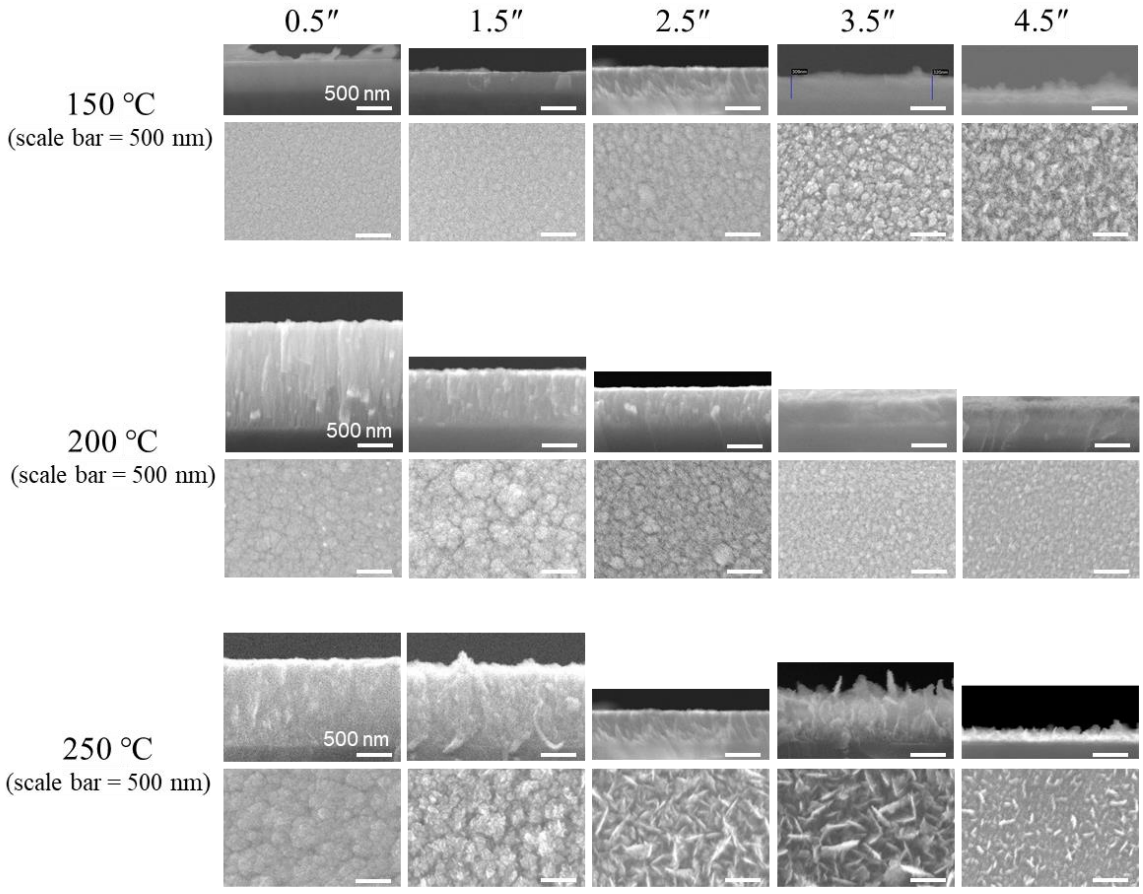

Figure 2.20. Plan-view and cross-sectional micrographs of ZrS_2 films deposited 0.5″–4.5″ from the precursor inlets using recipe 6 at 150–250 °C. The scale bar is 500 nm in all images.

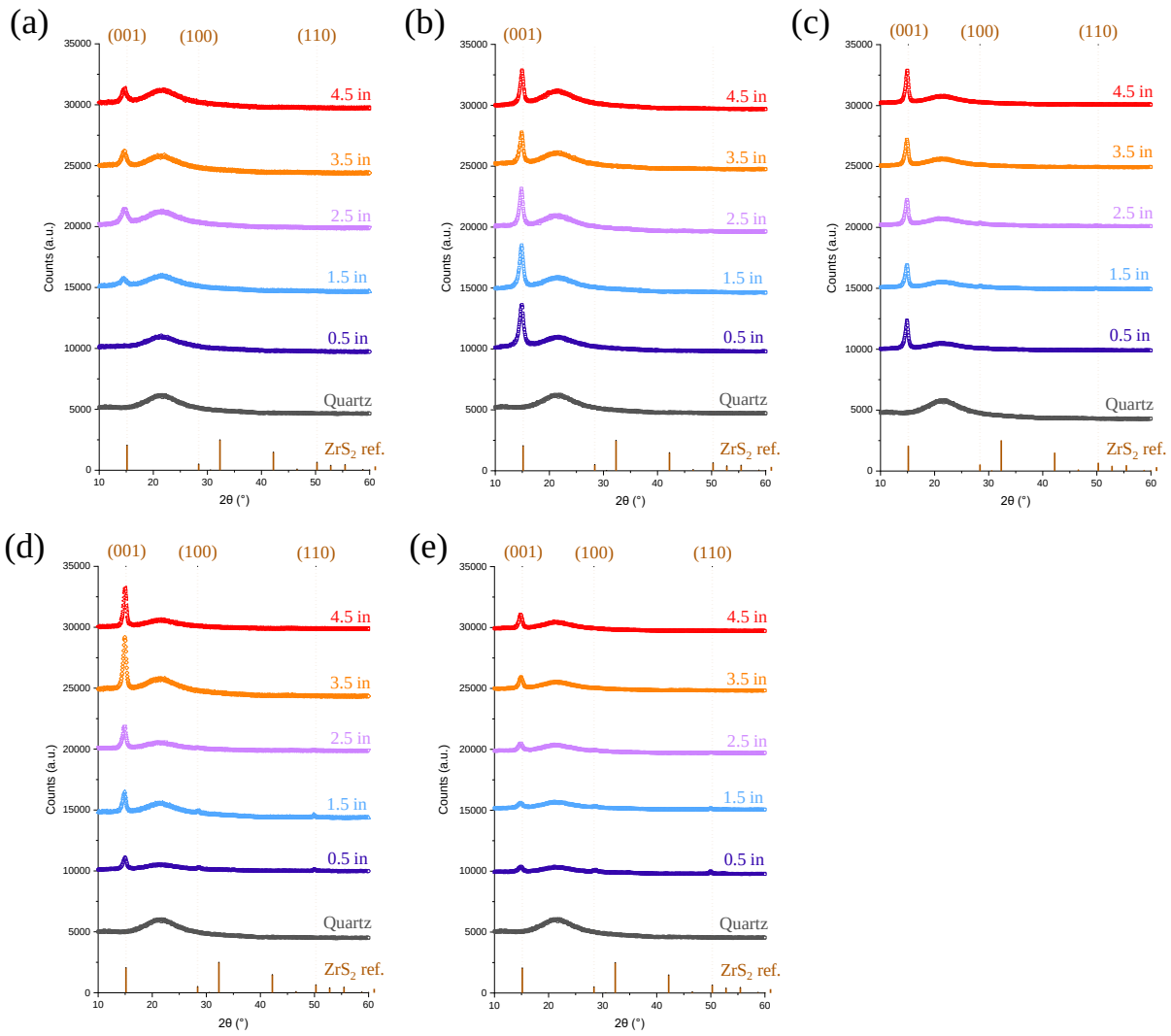

Figure 2.21. Powder diffractograms of ZrS_2 film deposited 0.5″–4.5″ from the precursor inlets using slow growth recipe 6 at (a) 150 °C, (b) 200 °C, (c) 250 °C, (d) 300 °C, and (e) 350 °C. The ZrS_2 reference diffraction pattern (abbreviated ZrS_2 ref). is COD 5910006.

The crystallinity of films deposited at 200 °C using our slow growth recipe is significantly higher than for films deposited using recipe 3, and, surprisingly, the highest among all temperatures using recipe 6. At 150 °C, we also observe an increase in crystallinity down the length of the reaction zone, but with amorphous films at the front of the reactor and weakly crystalline films at the rear. The 150 °C films are 900 nm thick at 0.5″ (growth rate of ca. 3.8 nm/min), decreasing to 175 nm at 4.5″. Films deposited at both temperatures are stoichiometric ZrS_2, with

EDS providing compositions of 37-39 at.% Zr, 59-61 at. % S, and 0.4-2.4 at.% O at 150 °C, and 35-37 at.% Zr, 55-58 at. % S, and 5 at.% O at 200 °C (Figure 2.11, Table 2.4). Repeated depositions of films at 200 °C for 4 h with varying precursor charge levels in the bubbler show that the film growth rate decreases as the charge of solid $Zr(NMe_2)_4$ precursor is depleted (Figure 2.22). The thickness of the frontmost film decreases from ca. 1500 nm to ca. 900 nm as the precursor fill level decreases from 1 g to 0.4 g. This result is typical for a solid precursor,[68, 69] where the evaporation rate is generally proportional to the precursor surface area, which decreases as material evaporates.

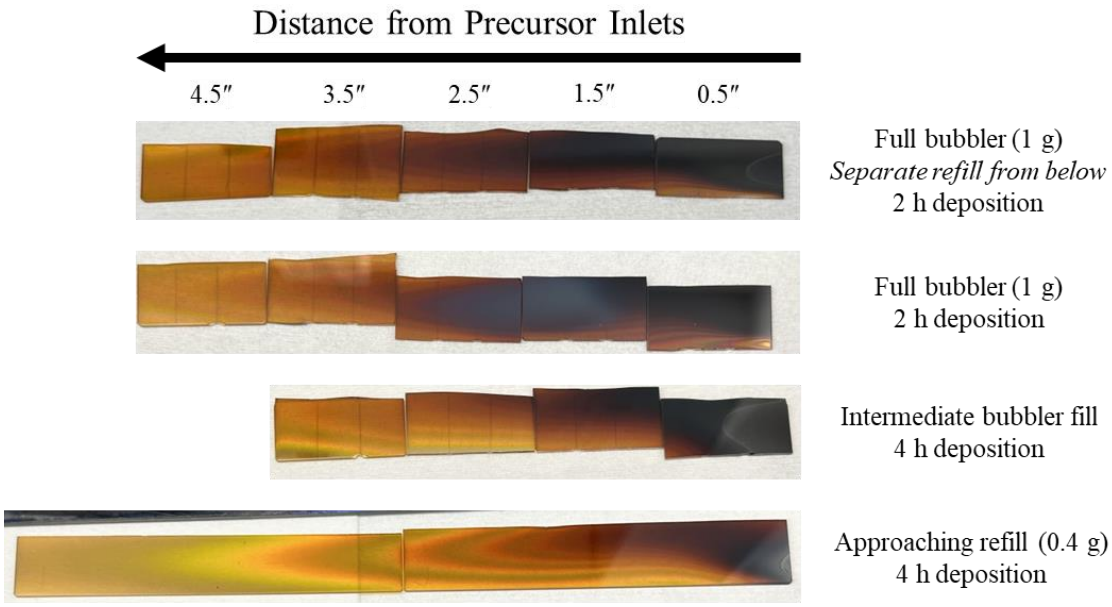

Figure 2.22. Photographs of ZrS_2 deposited at 200 °C using recipe 6 at different fill levels of the $Zr(NMe_2)_4$ bubbler. At comparable fill levels (top two) the deposition rate and film thickness gradient locations are comparable. As the precursor is depleted (bottom two), film growth rate decreases, and the spatial pattern of thickness varies as well.

Increasing the deposition temperature to 250 °C leads to a gradient of morphologies down the reaction zone but with increasing preference for the (001) plane. Figure 2.20 demonstrates that films comprising smooth and compact grains can now be obtained at the front of the reaction zone.

However, this morphology transitions to clumps of small flakes 1.5″ from the precursor inlets, larger and sparser flakes at 2.5″–3.5″, and smaller disperse flakes at the rear of the growth zone. This transition to sparse coverage of flakes mirrors film growth observed in recipe 3 at this temperature. Owing to the emergence of the flakes, the thickness profile down the reactor is more complicated, with films at 3.5″ appearing thicker than those at 2.5″; overall, films decrease from 1300 nm at 0.5″ (growth rate of ca. 5.4 nm/min) to 200 at 4.5″. Like at 200 °C, the intensity of the 001 reflection is relatively constant down the length of the reaction zone, suggesting increasing crystallinity down the reactor, and is more intense than in films deposited at the same temperature using recipe 3 (Figures 2.13 and 2.21), but slightly less intense than in films of similar thicknesses deposited at 200 °C via recipe 6. Low intensity 100 and 110 diffraction peaks are visible on films 1.5″–3.5″ from the precursor inlets, consistent with the emergence of nanosheets in this region of the reactor. The film at the front of the reactor is stoichiometric ZrS_2, with EDS measuring 36-37 at.% Zr, 60-62 at. % S, and 1-3 at.% O (Figure 2.11, Table 2.4)

Increasing the growth temperature to 300–350 °C leads to the return of films with flaky morphologies at the front of the reaction zone. Plan-view microscopy of a ZrS_2 film deposited at the front of the reactor at 300 °C reveals small clumps of flakes, rather than smooth and compact grains originally seen using these deposition conditions (Figures 2.14, 2.23 and 2.24). This difference in morphology is likely due to the different fill levels of the $Zr(NMe_2)_4$ bubbler, and corroborates the sensitivity of film growth to the flux of $Zr(NMe_2)_4$. Like at 250 °C, down the length of the reactor flake size increases and areal density decreases until 3.5″ from the precursor inlets, before rapidly dropping off to afford films with scattered flakes at the rear (Figure 2.23). Films are 3500 nm thick at 0.5″ (growth rate of ca. 14.6 nm/min), decreasing to 250 nm at 4.5″. At 350 °C, films at the front of the reactor start out with large flakes (Figure 2.23), which decrease

in size down the length of the reactor. Similar to depositions at 300 °C using recipe 4, at 350 °C we also observe a gradient of flaky to compact morphologies normal precursor flow at the front of the reaction zone (Figure 2.25). Considering the steep drop-off in film thickness down the reaction zone, from 8500 nm at 0.5″ (growth rate of ca. 35.4 nm/min) to 250 nm at 4.5″, the reduction in density of flake coverage at films in the rear of the reaction zone is likely correlated with exhaustion of $Zr(NMe_2)_4$ vapor. Films deposited at both temperatures are stoichiometric ZrS_2, with EDS providing compositions of 34-37 at.% Zr, 55-56 at. % S, and 5-7 at.% O at 300 °C, and 37-38 at.% Zr, 55-57 at. % S, and 5-6 at.% O at 350 °C (Figure 2.11, Table 2.4).

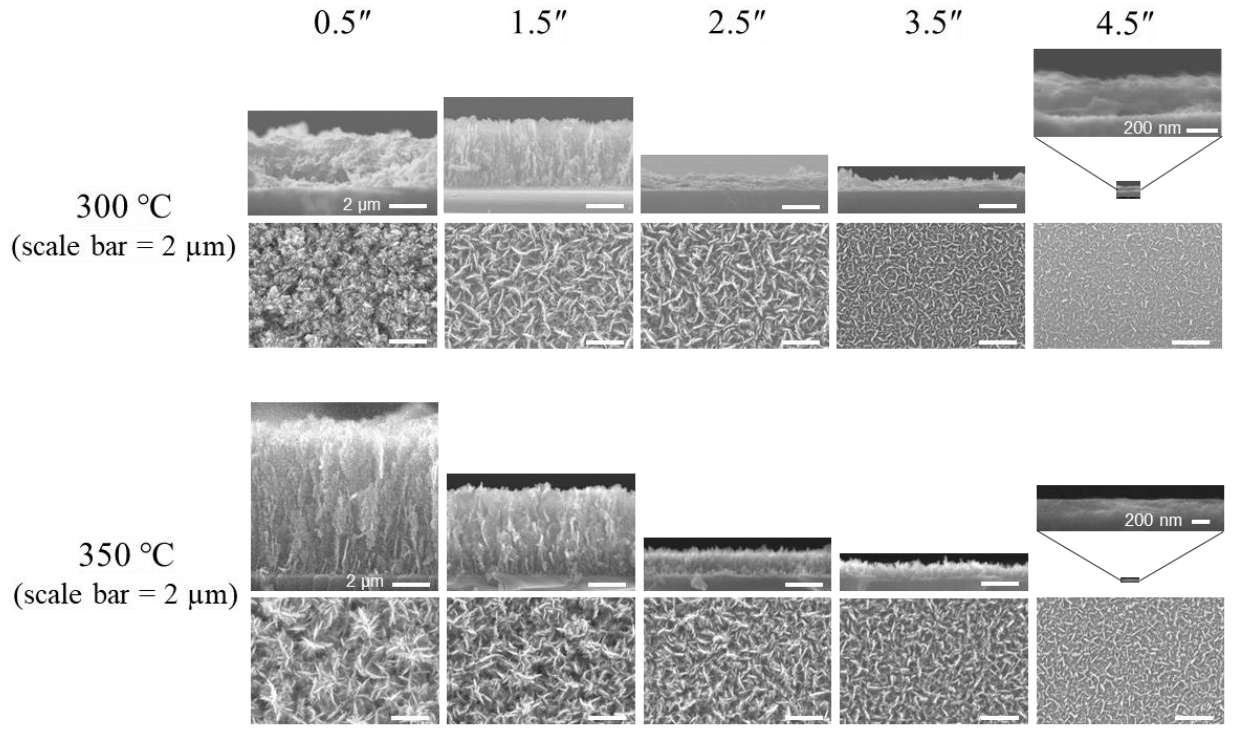

Figure 2.23. Plan-view and cross-sectional micrographs of ZrS_2 films deposited 0.5″–4.5″ from the precursor inlets using recipe 6 at 300 and 350 °C. The scale bar is 2 μm, except in the insets, where it is 200 nm.

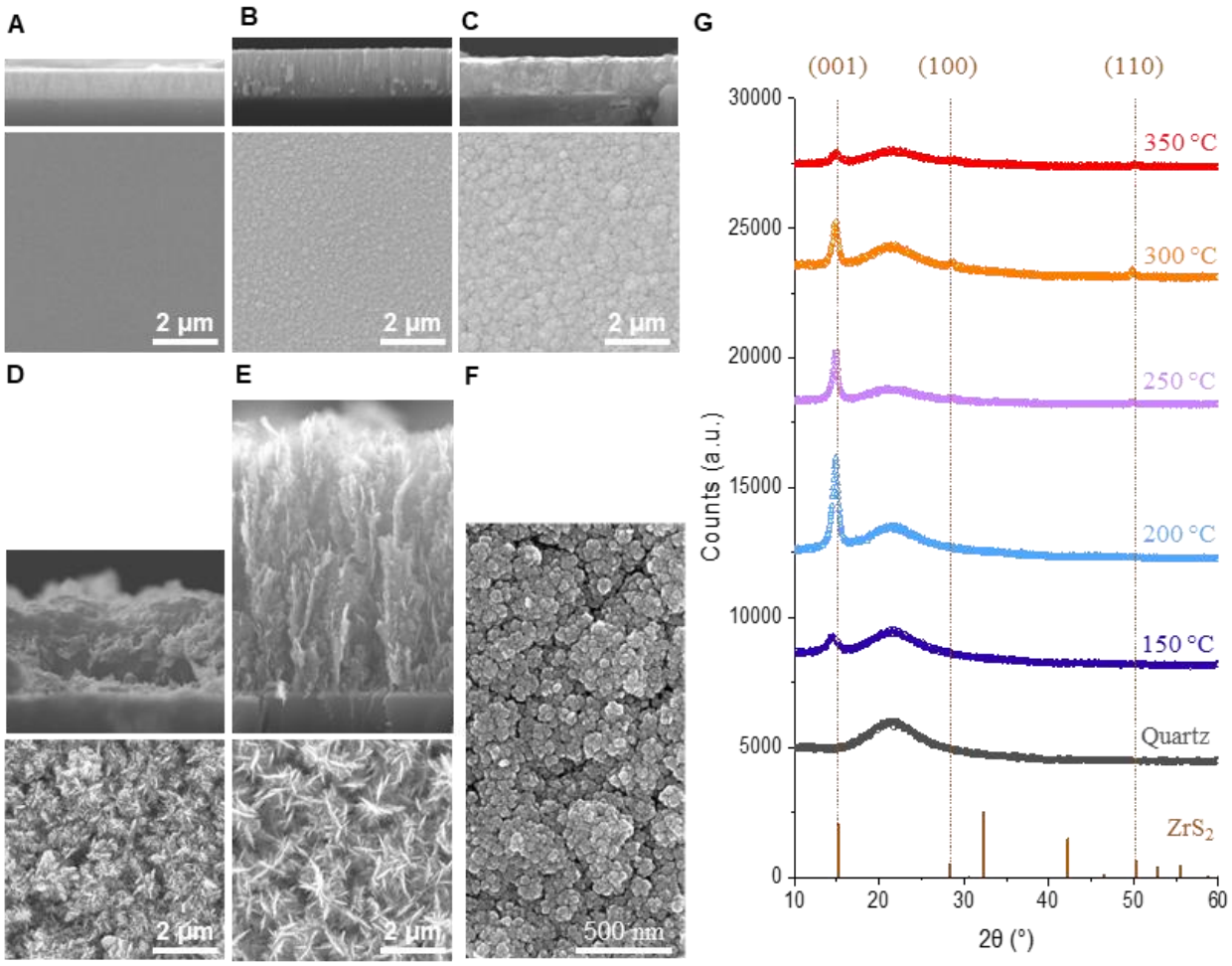

Figure 2.24. Plan-view and cross-section micrographs of ZrS_2 films deposited on quartz substrates 0.5″ from the precursor inlets using recipe 6 at (a) 150 °C, (b) 200 °C, (c) 250 °C, (d) 300 °C, and (e) 350 °C; scale bars represent 2 µm. (f) A high-magnification micrograph a film deposited at 200 °C, with scale bar 500 nm. (g) Diffractograms of films (a)–(e) and a bare quartz substrate, plotted with the ZrS_2 reference pattern (COD 5910006).

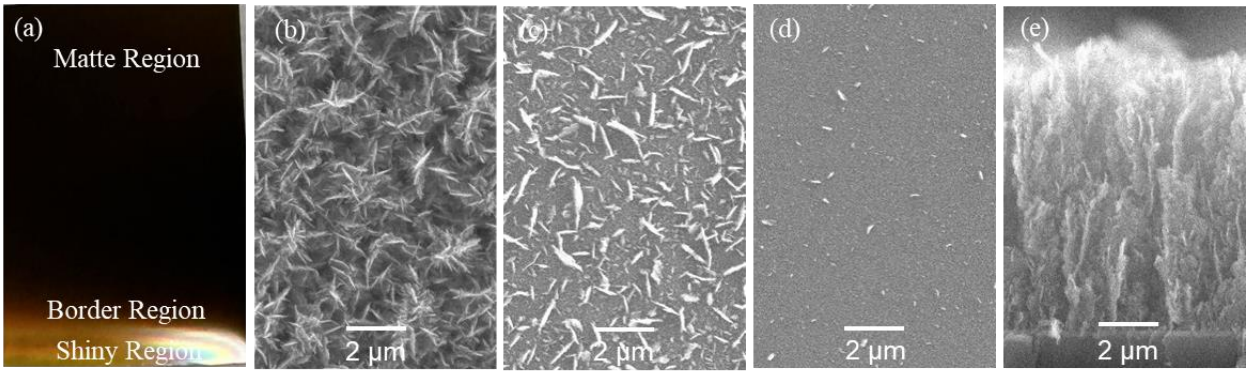

Figure 2.25. (a) Photograph of a ZrS_2 film deposited at the front of the reaction zone at 350 °C using slow growth recipe 6. The matte region is in front of the $Zr(NMe_2)_4$ precursor inlet and the shiny region is in front of the H_2S precursor inlet. Plan-view micrographs are obtained from the (b) matte, (c) border, and (d) shiny regions of the photograph. (e) A cross-sectional micrograph of the flaky morphology in the matte region.

Films deposited at 300 and 350 °C are less oriented in the [001] direction than at 200 and 250 °C but increase in this orientation down the reaction zone. Like for recipe 3, Figure 2.24 shows that the intensity of the 001 reflection decreases as temperature increases from 200–350 °C, despite increasing film thicknesses (in equivalent positions). Like films grown at 150 °C, the intensity of the 001 reflection increases down the length of the reaction zone despite film thickness decreasing, again indicating enhanced crystallinity towards the rear (Figure 2.21). Concurrently, the intensity of 100 and 110 reflections decreases down the reaction zone, suggesting texturing in the [001] direction.

Overall, these results show that slowing the deposition of the layered TMDC ZrS_2 can alter the film morphology, improving crystallinity and in some cases suppressing growth of plates vertically out of the substrate surface. At 200 °C, films can crystallize during deposition, even at the front of the reactor. The films maintain the crystallographic orientation observed in faster growth at this temperature, with ZrS_2 sheets parallel to the substrate surface. As deposition

temperature increases, flakes do still grow out of the films surface, especially when the $Zr(NMe_2)_4$ bubbler has been recently filled. The combined results suggest that—at least in the H_2S-rich conditions we deposited under—morphological control is provided primarily by the rate of $Zr(NMe_2)_4$ delivery. With smooth, compact films available, we measured the electrical and optical properties of several films.

2.4.7. Reducing Oxygen Incorporation

When growing compact films of ZrS_2 using recipe 6, oxygen incorporation primarily resulted from reactor leaks, real or virtual. Certainly air exposure does oxygenate the film surface; we can detect up to 1 ppm H_2S evolving from films (presumably by hydrolysis) freshly removed from the reactor. Nonetheless, the film bulk (either probed by EDS, or accessed by sputtering during XPS) typically contains ≤5 at.% O if the reactor is leak-free and properly baked out. Over the course of these depositions, we identified several external leaks (i.e., of air into the reactor) through helium-based leak detection with a mass spectrometer. Leaks were found in flexible stainless steel bellows tubing; where possible, we replaced sections of this tubing with thick-walled ¼″ stainless steel tubing with butt-welded VCR fittings. In one case, we identified a leak in the H_2S MFC that resulted from failure of a corroded O-ring. We also developed a bakeout procedure to remove virtual leaks (e.g., water desorbing from the reactor walls) enabling reliably low-oxygen film deposition.

Effective bakeouts of the reactor relied on three principles: high temperatures for quartz tubes, low temperatures around O-rings, and separate baking of traps. Removal of water from the reactor walls was especially important for the longer growth times of recipe 6. We found that short exposures to high temperatures were superior to long exposures to lower temperatures for baking freshly installed quartz tubes. For example, when baking the quartz tube at 150 °C for up to 72 h,

ZrS_2 films contained ≥10 at.% oxygen. In contrast, baking the quartz tube at 400 °C for just 2 h reliably produced films with ≤5% oxygen. We monitored the efficacy of the bakeout in real time by measuring the rate of rise; values below 1 mTorr/min at the deposition temperature were adequate for low-oxygen films. The several KF flanges in our reactor have elastomeric O-rings that require more gentle baking; when heated at higher temperatures (90 °C) or for longer times (10s of h), we observed compression-set failure, leading to reactor rates of rise of several Torr/min. Finally, isolating the foreline trap during trap bakeouts was also necessary to keep the CVD reactor dry. Besides the quartz tube, the only other component regularly removed for maintenance is the foreline trap, to replace the H_2S-scrubbing media. We learned through experience that this trap must be baked separately from the reactor when reinstalled, or adsorbed water baked out of the trap will distribute throughout the reactor and condense, especially on the low-temperature areas with elastomeric seals.

2.4.8. X-ray Photoelectron Spectroscopy

We used XPS to analyze films for impurities like C, N, and O, and to study the chemical speciation of Zr and S in the films. We collected survey scans, as well as high-resolutions scans of the Zr 3*d*, S 2*p*, O 1*s*, N 1*s*, and C 1*s* regions. After initial measurements of ZrS_2 with a few at.% O proved challenging to fit unambiguously, especially in the Zr 3*d* region, we collected a reference data set shown in Figure 2.26 using a single crystal of ZrS_2.[53] The resulting fitting procedure is described in section **2.3.2**, and we used the crystal-derived fitting procedure for all film data.

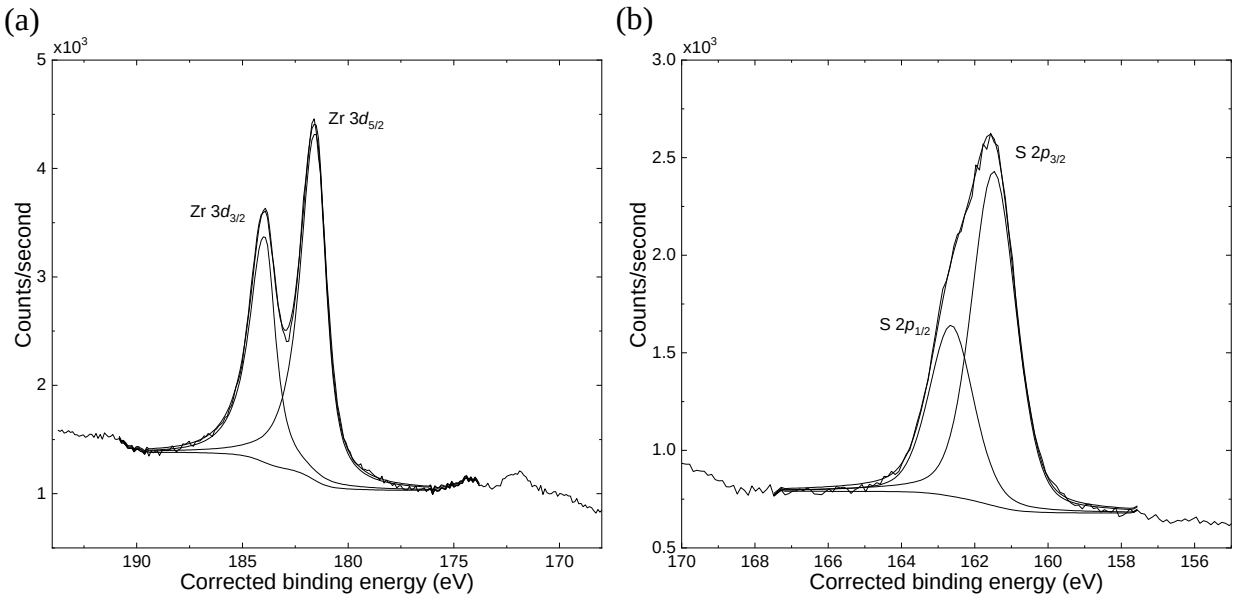

Figure 2.26. High-resolution XPS spectra of (a) Zr 3*d* and (b) S 2*p* regions for a single crystal of ZrS_2. Zr $3d_{5/2}$ and $3d_{3/2}$ peaks are fit with a line shape of sGL(45) with an exponential tail modifier of 1.5. S $2p_{3/2}$ and $2p_{1/2}$ peaks are fit with a line shape of sGL 30.

As described above, XPS identifies C and N in recipe 3 depositions at 200 °C (Figure 2.27), but not in depositions using recipe 6 (Figure 2.28). The presence of C and N likely result from ligand decomposition under recipe 3 conditions. The N contamination can be suppressed by increasing the growth temperature, although some C remains at most temperatures in recipe 3 (Figure 2.29, Table 2.5). The high surface area of these films—many vertically arrayed plates of ZrS_2—makes the origin of the C harder to establish, as sputter-cleaning the surface cannot eliminate all of the air-exposed material, unlike in a compact film. In contrast, films deposited via recipe 6 have C and N impurities below the ~1 at.% limit of detection of high-resolution XPS at most temperatures (Figure 2.30, Table 2.6). These films also typically have oxygen incorporation below 5 at. %.

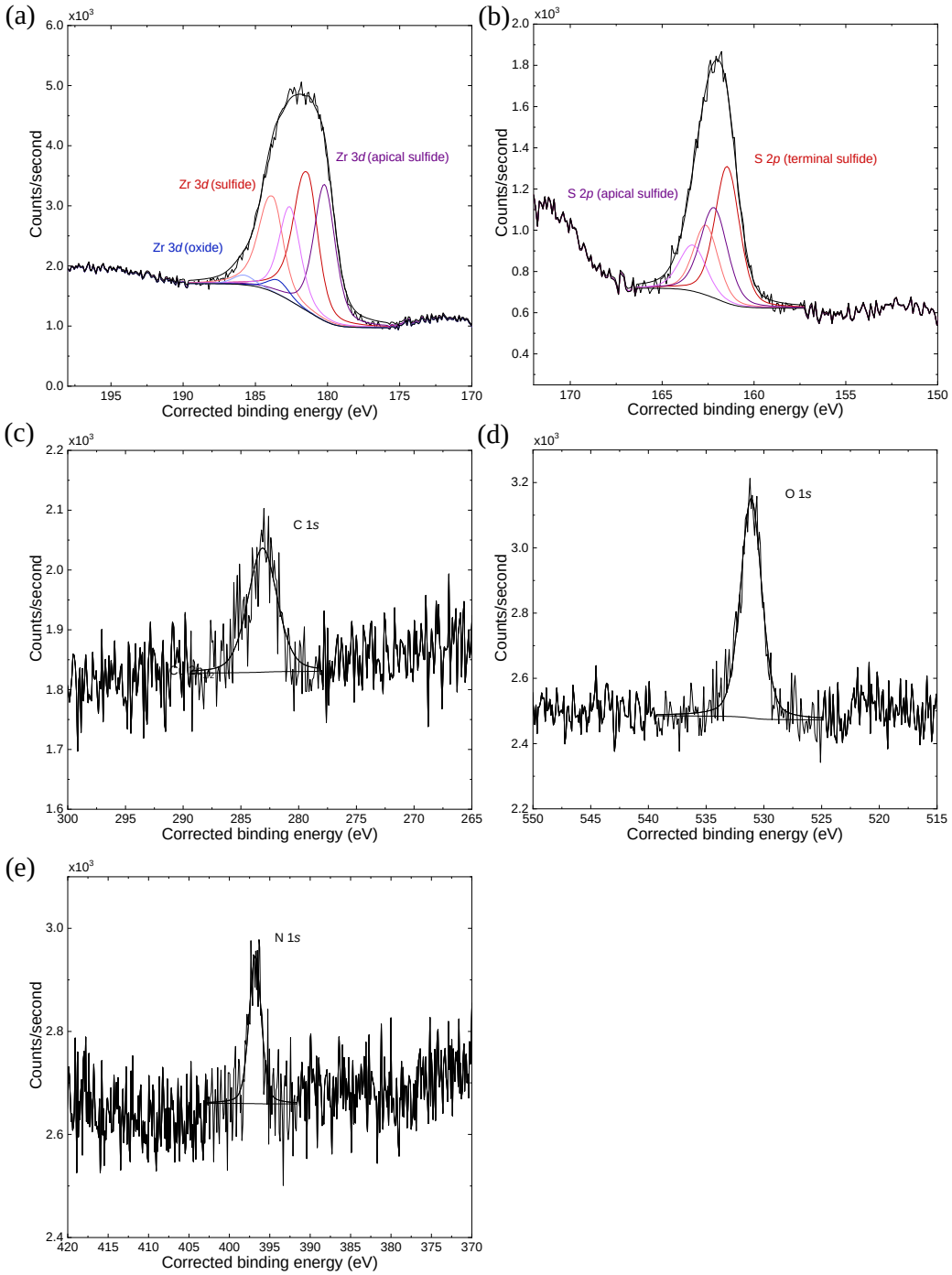

Figure 2.27 . High-resolution XPS spectra of the (a) Zr 3*d*, (b) S 2*p*, (c) C 1*s*, (d) O 1*s*, and (e) N 1*s* regions for a ZrS_2 film grown with recipe 3 at 200 °C. The presence of a nitride peak in the N 1*s* region suggests incorporation of amido ligand fragments into the film during its growth. The film was etched at 3 kV and 500 nA for 300 min. N appears at all etch levels.

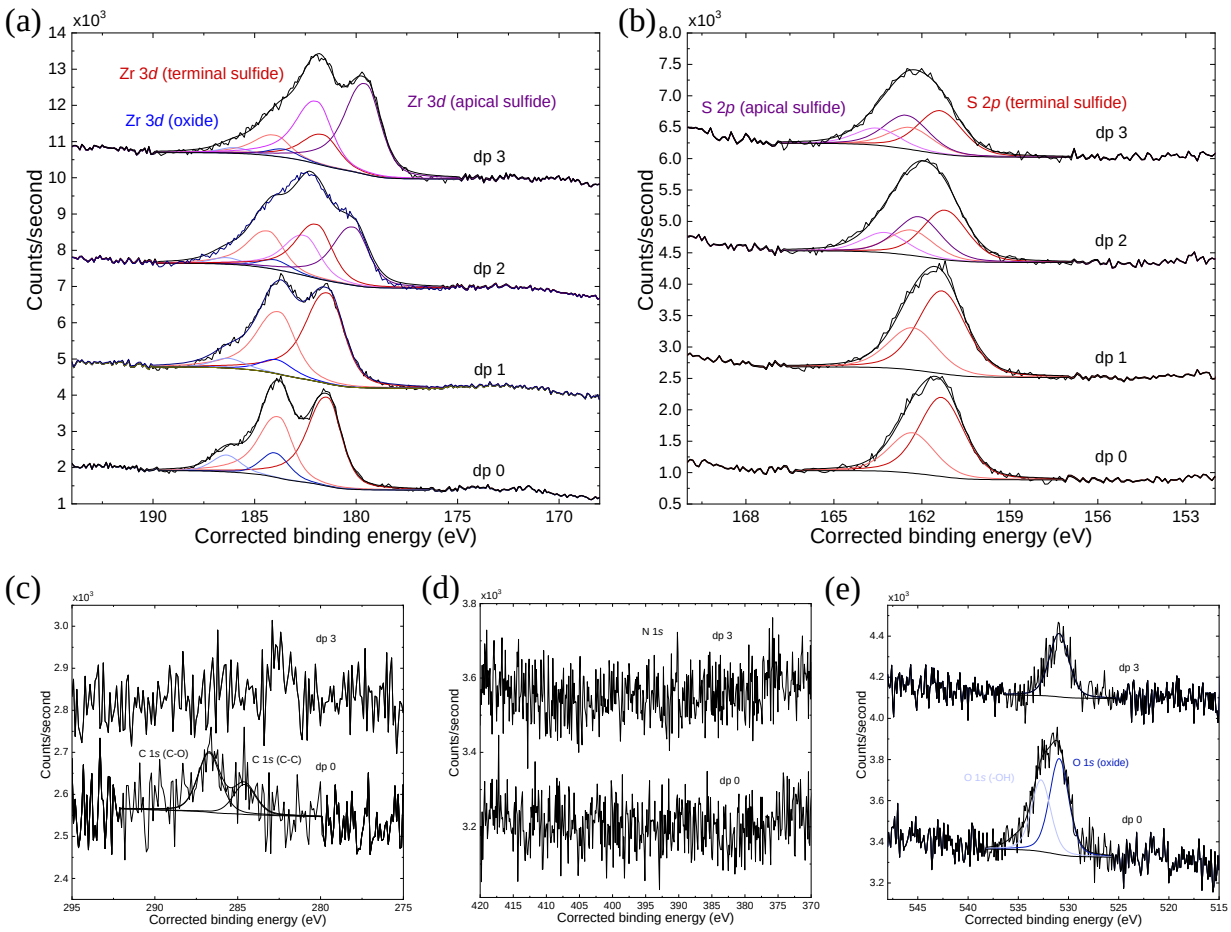

Figure 2.28 High-resolution XPS spectra of a ZrS_2 film grown using recipe 6 at 200 °C. The spectrum of the air-exposed surface (dp 0) is compared with the spectrum after the first etch with gentle sputter conditions (1.5 kV, 30-50 nA, 30 min; dp 1), the second etch with harsh sputter conditions (3 kV, 500 nA, 30 min; dp 2), and the final etch with harsh sputter conditions (3 kV, 500 nA, 120 min; dp 3), for (a) the Zr 3*d* region, and (b) the S 2*p* region. The apical sulfide signal, with fit components depicted in purple, grows in on the higher binding energy side for S 2*p*, and the lower binding energy side for Zr 3*d*. The spectrum of the air-exposed surface (dp 0) is compared with the spectrum after the final etch with harsh sputter conditions (dp 3) for (c) the C 1*s* region, (d) the N 1*s* region, (e) the O 1*s* region.

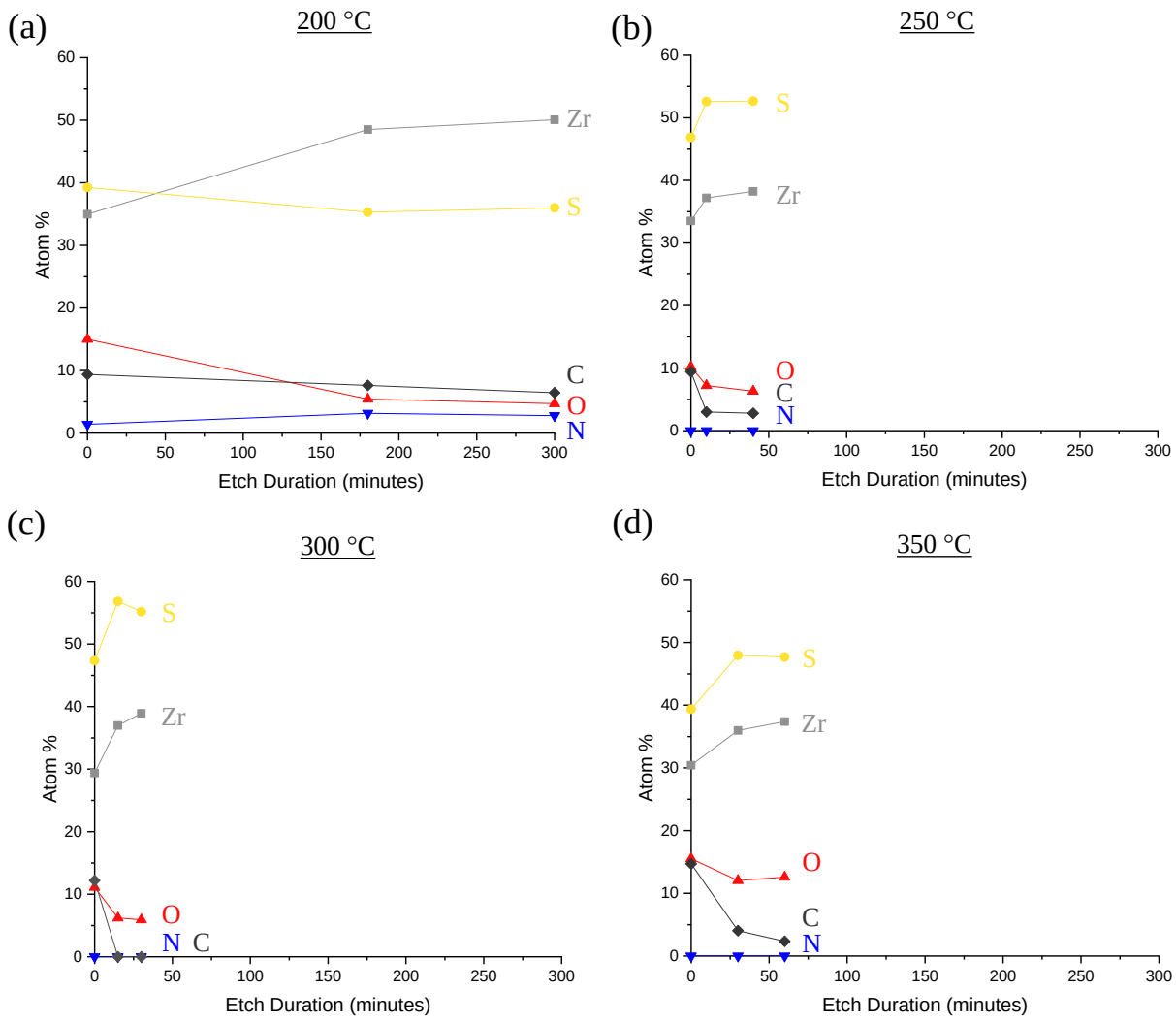

Figure 2.29. Composition as a function of sputter time for ZrS_2 films deposited using fast growth recipe 3 at (a) 200 °C, (b) 250 °C, (c) 300 °C, and (d) 350 °C. The films were etched by Ar^+ sputtering at 3 kV and 500 nA.

Table 2.5. XPS compositions of a ZrS_2 single crystal and ZrS_2 films deposited with the fast growth recipe 3 at 200-350 °C. Quantification is shown for fits to spectra collected after the final etch level. The films were etched by Ar^+ sputtering at 3 kV and 500 nA.

Temperature (°C)	Etch Duration (minutes)	Atom %					S:Zr
		Zr 3d	S 2p	O 1s	C 1s	N 1s	
S.C.	0	33.4	63.4	0.0	3.2	0.0	1.9
200	300	50.1	36.0	4.7	6.5	2.8	0.72
250	40	38.2	52.7	6.3	2.8	0.0	1.38
300	30	38.9	55.2	5.9	0.0	0.0	1.42
350	60	37.4	47.7	12.6	2.4	0.0	1.28

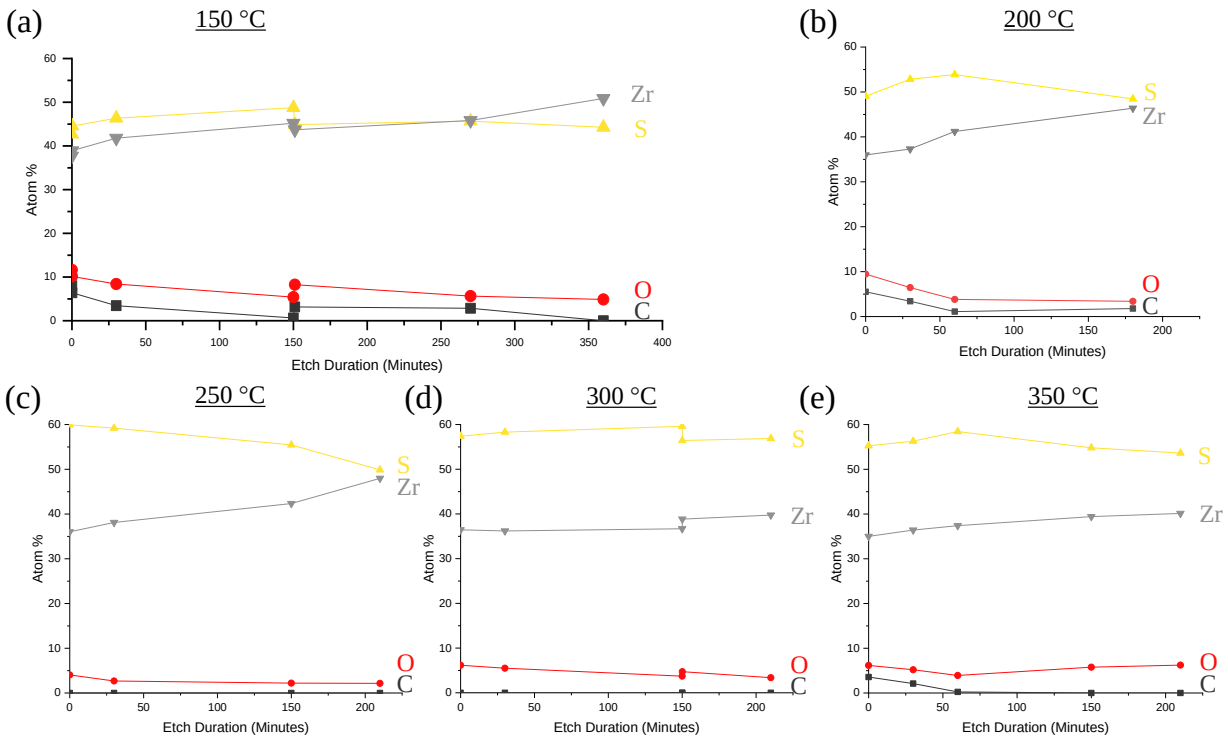

Figure 2.30. Composition as a function of sputter time for ZrS_2 films deposited using slow growth recipe 6 at (a) 150 °C, (b) 200 °C, (c) 250 °C, (d) 300 °C, and (e) 350 °C. The films were etched by Ar^+ sputtering at 1.5 kV and 50-100 nA for 30 minutes for the first etch and then 3 kV and 500 nA for the following etches.

Table 2.6. XPS compositions of a ZrS_2 single crystal and ZrS_2 films deposited with the slow growth recipe 6 at 150-350 °C. Quantification is shown for fits to spectra collected after the first, gentle etch level. The films were etched by Ar^+ sputtering at 1.5 kV and 50-100 nA.

Temperature (°C)	Etch Duration (minutes)	Atom %					S:Zr
		Zr 3d	S 2p	O 1s	C 1s	N 1s	
S.C.	0	33.4	63.4	0.0	3.2	0.0	1.9
150	30	38.9	44.6	10.1	5.4	0.0	1.15
200	20	35.2	54.5	4.3	6.0	0.0	1.55
250	30	38.1	59.2	2.7	0.0	0.0	1.55
300	30	36.2	58.3	5.5	0.0	0.0	1.61
350	30	36.4	56.3	5.2	2.1	0.0	1.55

Sputtering into ZrS_2 films can alter the stoichiometry and induce formation of new sulfur and zirconium signals. During sputter-etch experiments on single crystals (Figure 2.31) and on CVD films (Figure 2.28), we found that the at.% S decreases with Ar^+ sputter duration under high-power etch conditions (3 kV, 500 nA). Low-power sputtering can be used to remove the carbonaceous species from air exposure (1.5 kV, 50-100 nA), or to mill into the film with less chemical damage (1.5 kV, 100 nA). In long-duration, high-power etch experiments, new features grow in on the high binding energy side of the S 2*p* region, and the low binding energy side of the Zr 3*d* region. These features appear together, and we tentatively assign them to the generation of apical sulfides[70, 71] at the film surface by sputtering. This new species appears in both single crystal and film systems (Figure 2.31 and Figure 2.28). The decrease in at.% S relative to Zr rules against an alternative interpretation of the new signals as arising from persulfides (S_2^{2-}, as in ZrS_3), because such species would require an increase in the S:Zr ratio.

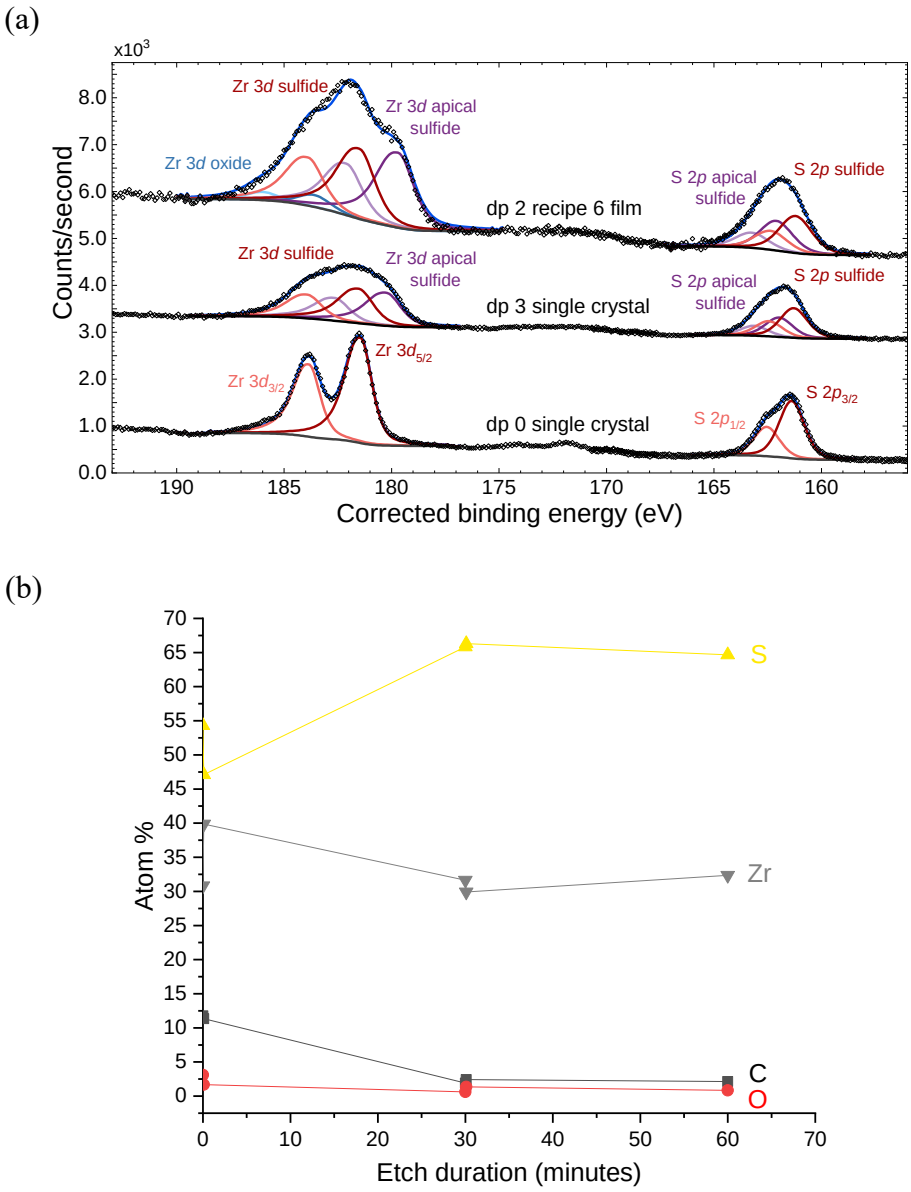

Figure 2.31. (a) Comparison of etch profiles for a single crystal and a film deposited at 200 °C using recipe 6, highlighting the formation of a second ZrS_2 species ("apical sulfide"[66, 67]). The bottom spectrum shows a freshly exfoliated single crystal, containing only ZrS_2; the two spectra above it show a single crystal and a film after 1 h of sputter-etching, showing the growth of a new Zr- and S-containing species. (b) Measured elemental composition of the ZrS_2 single crystal vs. etch time.

2.4.9. Electrical and Optical Properties

ZrS_2 films deposited with recipe 6 typically have resistivities in the broad range of 3 to 1000 Ω·cm, depending on temperature and location in the reactor. Sheet resistance data measured by four-point probe are shown in Figure 2.31. The sheet resistance does not appear to be strongly impacted by oxygen content, at least below ca. 10 at.% O (Figure 2.32). Owing to spatial variation in the thickness (Figure 2.18), individual resistivities are somewhat difficult to calculate reliably, although we are confident in this range of values (Figure 2.31). Film crystallinity and deposition temperature appear to impact the resistivity, with higher crystallinity and higher deposition temperature generally providing lower resistivity. Indeed, films deposited at 350 °C at 3.5″ and 4.5″ from the precursor inlets have resistivities as low as 7 and 3 Ω·cm, respectively. These values approach resistivities of 0.5 Ω·cm reported for ZrS_2 films deposited by CVD at 1000 °C with grain sizes on the order of several microns across.[29] The resistivity of ZrS_2 single crystals is comparable to high temperature CVD films, with values of 0.1-0.75 Ω·cm.[31, 32, 41] The small grain size of our films likely contributes to the relatively high resistivity at low deposition temperatures, although the lower resistivity at higher temperatures on small grained films suggests other material properties may be contributing to carrier transport.

CVD films of ZrS_2 absorb light as expected, although interference fringes make fitting the optical data difficult. UV-vis absorption data and Tauc plots for a film grown at 200 °C using recipe 6 are shown in Figure 5c,d. Data for select other films grown by recipes 3 and 6 are shown in Figure 2.33. Absorption turns on in the range of 1.7-1.8 eV, consistent with the indirect bandgap for this material, and saturates in the range of 2.2-2.6 eV, consistent with strong absorption near the direct bandgap. Films of ZrS_2 deposited by other methods also show interference fringes in the

reflectance or transmittance data.[36] We thus view these films as having typical optical properties for polycrystalline films of ZrS_2.

Despite the promising optoelectronic properties of our ZrS_2 films, we failed to fabricate photovoltaic devices with PCE's above 0.01%. We utilized two devices stacks, either ITO/ZrS_2/Au:Ti as (Schottky cells) or FTO/ZrS_2/CuBr/Au:Ti (p/n junction), with the latter using thermal evaporation or vapor transport deposition to deposit CuBr as the hole transport layer. In all cases, devices were assembled from ZrS_2 deposited using recipe 6 at 200 °C, since these conditions afford compact morphologies and good crystallinity down the entire length of the reaction zone. Details on device fabrication, testing and troubleshooting may be found at the end of the thesis in **Appendix 2**.

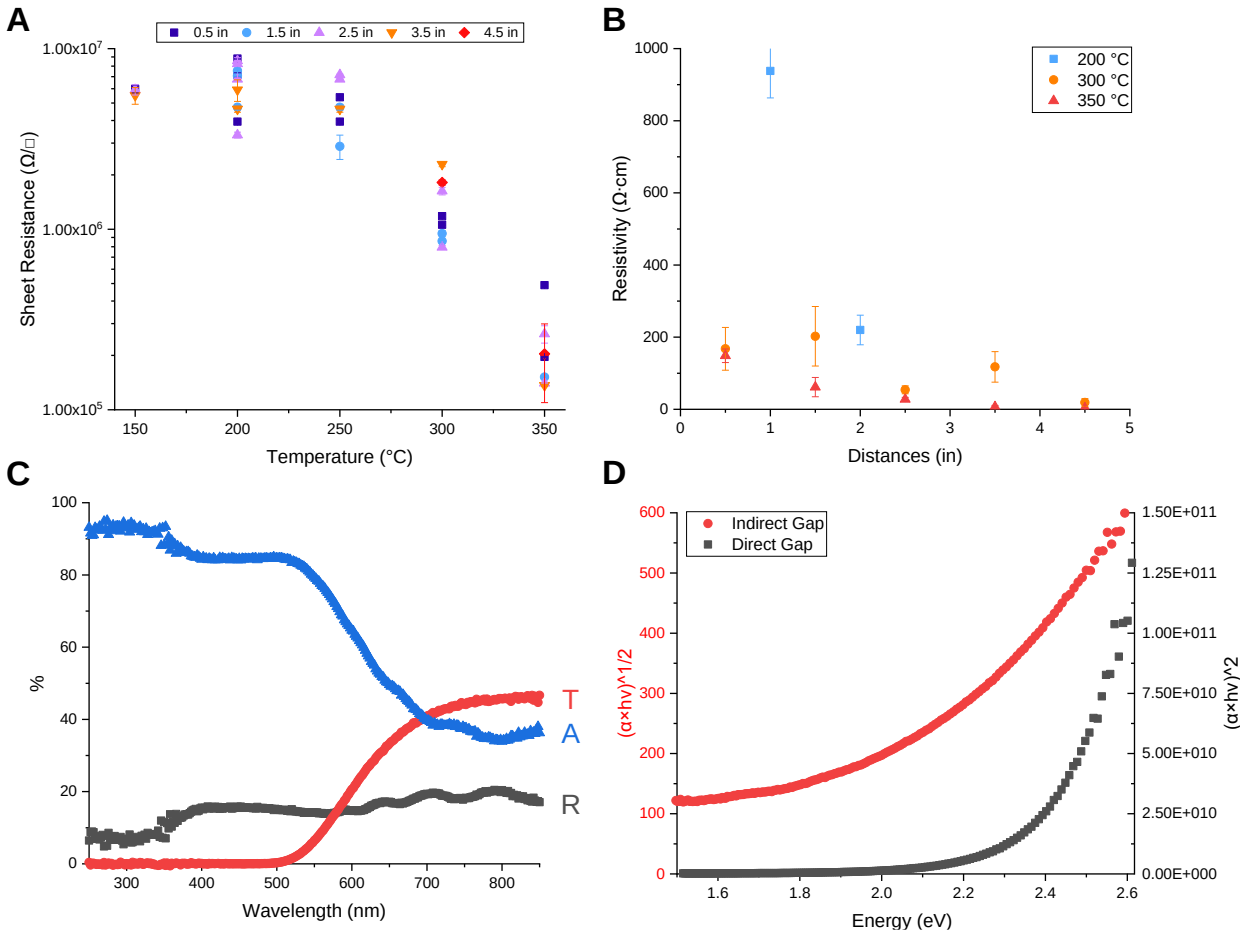

Figure 2.32. Electrical and optical properties of films deposited using recipe 6: (a) the sheet resistance at different substrate temperatures and reactor locations, and (b) the resistivity down the reaction zone at 200–350 °C. (c) The reflectance, transmittance, and absorption of a 1500-nm thick ZrS_2 film deposited at 200 °C. (d) Tauc plots for the direct and indirect gap of the ZrS_2 film shown in figure (c).

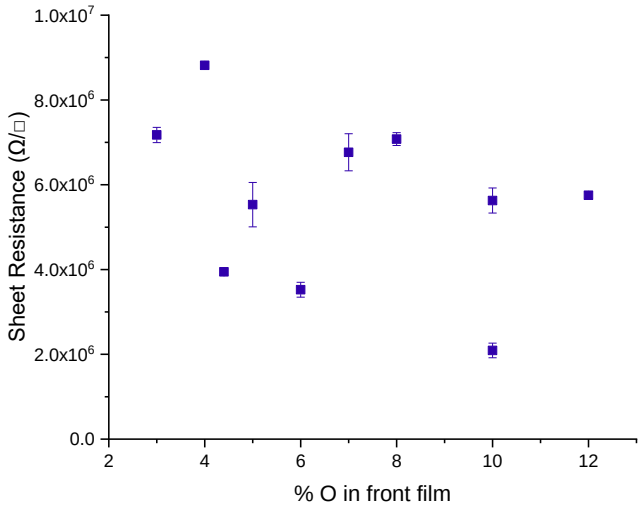

Figure 2.33. Sheet resistance of ZrS_2 vs. oxygen content (by EDS) for samples deposited at the front of the reaction zone using a growth temperature of 200 °C and slow growth recipe 6.

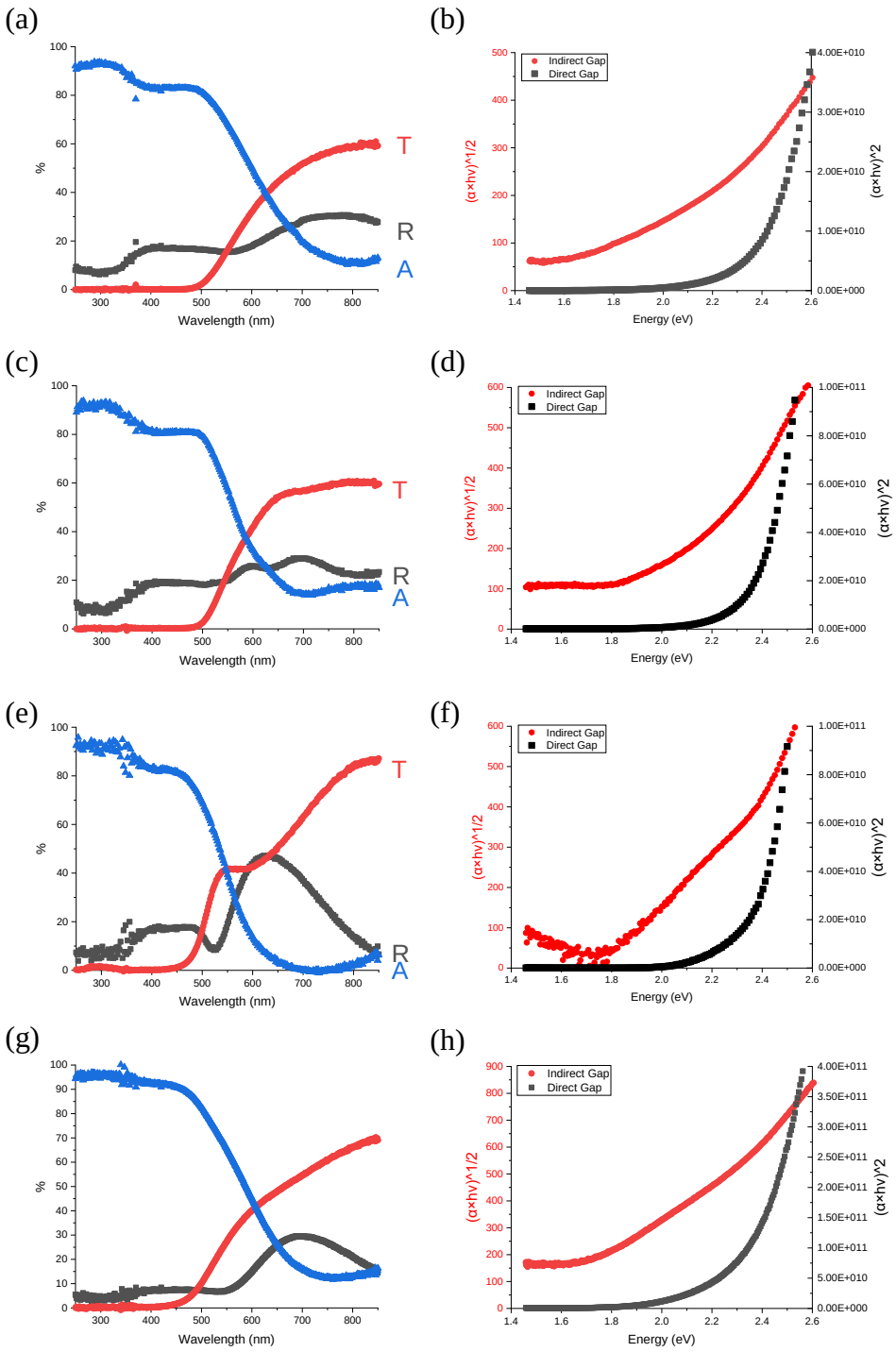

Figure 2.34. Plots of the raw UV-vis data for the % transmission (T), % reflection (R), and % absorption (A), combined with Tauc plots constructed from the absorption coefficient for ZrS_2 films (a, b) 700 nm thick, deposited using recipe 6 at 200 °C; (c, d) 450 nm thick, deposited using recipe 6 at 200 °C; (e, f) 375 nm thick, deposited under the same conditions; (g, h) 110 nm thick, deposited at 200 °C using recipe 3.

2.5. Conclusion

We have demonstrated that using the reaction between hydrogen sulfide and tetrakis(dimethylamido)zirconium(IV) amide allows low-temperature, rapid growth of ZrS_2 films. Under many conditions, films are stoichiometric, crystalline, and contain little or no contamination with C and N. Growth rates can be very high, exceeding 100 nm/min, although the film quality generally improves with slower growth. CVD of crystalline ZrS_2 is possible at 150 °C, the lowest temperature yet reported for this material. At substrate temperatures above 250 °C, the film morphology transitions from densely packed small grains to larger, loosely packed plates growing perpendicular to the substrate. In all cases, rapid growth appears to proceed in the plane of the ZrS_2 layers, with changes in morphology resulting from changes in the orientation of nuclei. In an excess of H_2S, decreasing the $Zr(NMe_2)_4$ partial pressure can suppress the growth of the vertical plates. Growth proceeds similarly on SiO_2, Al_2O_3, and ITO substrates; the maximum temperature of growth on ITO is limited to 350 °C. Optical properties of the product films are consistent with expectation and with previously reported films of ZrS_2. Electrical resistivities of the most conductive films are within an order of magnitude of bulk ZrS_2; however, many films have higher resistivities, and the small grain sizes typical of this deposition process may need enhancement for implementation in electronic devices.

2.6. References

1. Faraday, M., XX. Experimental researches in electricity.— fourth series. *Philosophical Transactions of the Royal Society of London* **1833,** *123*, 507-522.

2. Smith, W., Effect of Light on Selenium During the Passage of An Electric Current. *Nature* **1873,** *7*, 303.

3. Braun, F., Uber die Stromleitung durch Schwefelmetalle. *Annalen der Physik* **1875,** *229* (12), 556-563.

4. Franz, K. A.; Kehr, W. G.; Siggel, A.; Wieczoreck, J.; Adam, W., Luminescent Materials. In *Ullmann's Encyclopedia of Industrial Chemistry*, Wiley-VCH Verlag GmbH & Co. : Weinham, DE, 2012; Vol. 21, pp 591-630.

5. Zhou, C.; Lee, Y. K.; Yu, Y.; Byun, S.; Luo, Z.-Z.; Lee, H.; Ge, B.; Lee, Y.-L.; Chen, X.; Lee, J. Y.; Cojocaru-Mirédin, O.; Chang, H.; Im, J.; Cho, S.-P.; Wuttig, M.; Dravid, V. P.; Kanatzidis, M. G.; Chung, I., Polycrystalline SnSe with a thermoelectric figure of merit greater than the single crystal. *Nature Materials* **2021,** *20*, 1378-1384.

6. Yan, Q.; Kanatzidis, M. G., High-performance thermoelectrics and challenges for practical devices. *Nature Materials* **2022,** *21*, 503-513.

7. Scarpulla, M. A.; McCandless, B.; Phillips, A. B.; Yan, Y.; Heben, M. J.; Wolden, C.; Xiong, G.; Metzger, W. K.; Mao, D.; Krasikov, D.; Sankin, I.; Grover, S.; Munshi, A.; Sampath, W.; Sites, J. R.; Bothwell, A.; Albin, D.; Reese, M. O.; Romeo, A.; Nardone, M.; Klie, R.; Walls, J. M.; Fiducia, T.; Abbas, A.; Hayes, S. M., CdTe-based thin film photovoltaics: Recent advances, current challenges and future prospects. *Solar Energy Materials and Solar Cells* **2023,** *255*, 112289.

8. Zhang, W.; Huang, Z.; Zhang, W.; Li, Y., Two-dimensional semiconductors with possible high room temperature mobility. *Nano Research* **2014,** *7* (12), 1731-1737.

9. Afzalian, A., Ab initio perspective of ultra-scaled CMOS from 2D-material fundamentals to dynamically doped transistors. *npj 2D Materials and Applications* **2021,** *5* (1), 5.

10. Hamada, M.; Matsuura, K.; Sakamoto, T.; Muneta, I.; Hoshii, T.; Kakushima, K.; Tsutsui, K.; Wakabayashi, H., High Hall-Effect Mobility of Large-Area Atomic-Layered Polycrystalline ZrS_2 Film Using UHV RF Magnetron Sputtering and Sulfurization. *IEEE Journal of the Electron Devices Society* **2019,** *7*, 1258-1263.

11. Wang, Q. H.; Kalantar-Zadeh, K.; Kis, A.; Coleman, J. N.; Strano, M. S., Electronics and optoelectronics of two-dimensional transition metal dichalcogenides. *Nature Nanotechnology* **2012,** *7* (11), 699-712.

12. Mak, K. F.; Shan, J., Photonics and optoelectronics of 2D semiconductor transition metal dichalcogenides. *Nature Photonics* **2016,** *10* (4), 216-226.

13. Lee, E.; Yoon, Y. S.; Kim, D.-J., Two-Dimensional Transition Metal Dichalcogenides and Metal Oxide Hybrids for Gas Sensing. *ACS Sensors* **2018,** *3* (10), 2045-2060.

14. Cherusseri, J.; Choudhary, N.; Sambath Kumar, K.; Jung, Y.; Thomas, J., Recent trends in transition metal dichalcogenide based supercapacitor electrodes. *Nanoscale Horizons* **2019,** *4* (4), 840-858.

15. Choi, W.; Choudhary, N.; Han, G. H.; Park, J.; Akinwande, D.; Lee, Y. H., Recent development of two-dimensional transition metal dichalcogenides and their applications. *Materials Today* **2017,** *20* (3), 116-130.

16. Dong, L.; Lou, J.; Shenoy, V. B., Large In-Plane and Vertical Piezoelectricity in Janus Transition Metal Dichalchogenides. *ACS Nano* **2017,** *11* (8), 8242-8248.

17. Sadeghi, I.; Ye, K.; Xu, M.; Li, Y.; LeBeau, J. M.; Jaramillo, R., Making $BaZrS_3$ Chalcogenide Perovskite Thin Films by Molecular Beam Epitaxy. *Advanced Functional Materials* **2021,** *31* (45), 2105563.

18. Abir, S. S. H.; Sharma, S.; Sharma, P.; Karla, S.; Balasubramanian, G.; Samuel, J.; Koratkar, N., Piezoelectricity in chalcogenide perovskites. *Nature Communications* **2024,** *15* (1), 5768.

19. Meng, W.; Saparov, B.; Hong, F.; Wang, J.; Mitzi, D. B.; Yan, Y., Alloying and Defect Control within Chalcogenide Perovskites for Optimized Photovoltaic Application. *Chemistry of Materials* **2016,** *28* (3), 821-829.

20. Njema, G. G.; Kibet, J. K., A review of chalcogenide-based perovskites as the next novel materials: Solar cell and optoelectronic applications, catalysis and future perspectives. *Next Nanotechnology* **2025,** *7*, 100102.

21. Swarnkar, A.; Mir, W. J.; Chakraborty, R.; Jagadeeswararao, M.; Sheikh, T.; Nag, A., Are Chalcogenide Perovskites an Emerging Class of Semiconductors for Optoelectronic Properties and Solar Cell? *Chemistry of Materials* **2019,** *31* (3), 565-575.

22. Wei, X.; Hui, H.; Zhao, C.; Deng, C.; Han, M.; Yu, Z.; Sheng, A.; Roy, P.; Chen, A.; Lin, J.; Watson, D. F.; Sun, Y.-Y.; Thomay, T.; Yang, S.; Jia, Q.; Zhang, S.; Zeng, H., Realization of $BaZrS_3$ chalcogenide perovskite thin films for optoelectronics. *Nano Energy* **2020,** *68*, 104317.

23. Ye, K.; Zhao, B.; Diroll, B. T.; Ravichandran, J.; Jaramillo, R., Time-resolved photoluminescence studies of perovskite chalcogenides. *Faraday Discussions* **2022,** *239* (0), 146-159.

24. Vincent Mercy, E. N.; Srinivasan, D.; Marasamy, L., Emerging $BaZrS_3$ and $Ba(Zr,Ti)S_3$ Chalcogenide Perovskite Solar Cells: A Numerical Approach Toward Device Engineering and Unlocking Efficiency. *ACS Omega* **2024,** *9* (4), 4359-4376.

25. Greenaway, D. L.; Nitsche, R., Preparation and optical properties of group IV–VI2 chalcogenides having the CdI_2 structure. *Journal of Physics and Chemistry of Solids* **1965,** *26* (9), 1445-1458.

26. Moustafa, M.; Zandt, T.; Janowitz, C.; Manzke, R., Growth and band gap determination of the ZrS_xSe_{2-x} single crystal series. *Physical Review B* **2009,** *80* (3), 035206.

27. Borghesi, A.; Chen-jia, C.; Guizzetti, G.; Nosenzo, L.; Reguzzoni, E.; Stella, A.; Lévy, F., Thermoreflectance studies of transition-metal dichalcogenides between 1 and 9 eV. *Physical Review B* **1986,** *33* (4), 2422-2428.

28. Peloquin, G.; Provencher, R.; Jandl, S.; Aubin, M., Optical transitions in ZrS_2 and $ZrSe_2$ from thermoreflectance measurements. *Journal of Physics C: Solid State Physics* **1986,** *19*, 3141.

29. Tian, Y.; Cheng, Y.; Huang, J.; Zhang, S.; Dong, H.; Wang, G.; Chen, J.; Wu, J.; Yin, Z.; Zhang, X., Epitaxial growth of large area ZrS_2 2D semiconductor films on sapphire for optoelectronics. *Nano Research* **2022,** *15* (7), 6628-6635.

30. Li, L.; Fang, X.; Zhai, T.; Liao, M.; Gautam, U. K.; Wu, X.; Koide, Y.; Bando, Y.; Golberg, D., Electrical Transport and High-Performance Photoconductivity in Individual ZrS_2 Nanobelts. *Advanced Materials* **2010,** *22* (37), 4151-4156.

31. Conroy, L. E.; Park, K. C., Electrical properties of the Group IV disulfides, titanium disulfide, zirconium disulfide, hafnium disulfide and tin disulfide. *Inorganic Chemistry* **1968,** *7* (3), 459-463.

32. Herninda, T. M.; Ho, C.-H., Optical and Thermoelectric Properties of Surface-Oxidation Sensitive Layered Zirconium Dichalcogenides $ZrS_{2-x}Se_x$ (x = 0, 1, 2) Crystals Grown by Chemical Vapor Transport. *Crystals* **2020,** *10* (4), 327.

33. Zhang, M.; Zhu, Y.; Wang, X.; Feng, Q.; Qiao, S.; Wen, W.; Chen, Y.; Cui, M.; Zhang, J.; Cai, C.; Xie, L., Controlled Synthesis of ZrS_2 Monolayer and Few Layers on Hexagonal Boron Nitride. *Journal of the American Chemical Society* **2015,** *137* (22), 7051-7054.

34. Zhu, Y.; Wang, X.; Zhang, M.; Cai, C.; Xie, L., Thickness and temperature dependent electrical properties of ZrS_2 thin films directly grown on hexagonal boron nitride. *Nano Research* **2016,** *9* (10), 2931-2937.

35. Wang, X.; Huang, L.; Jiang, X.-W.; Li, Y.; Wei, Z.; Li, J., Large scale ZrS_2 atomically thin layers. *Journal of Materials Chemistry C* **2016,** *4* (15), 3143-3148.

36. Mattinen, M.; Popov, G.; Vehkamäki, M.; King, P. J.; Mizohata, K.; Jalkanen, P.; Räisänen, J.; Leskelä, M.; Ritala, M., Atomic Layer Deposition of Emerging 2D Semiconductors, HfS_2 and ZrS_2, for Optoelectronics. *Chemistry of Materials* **2019,** *31* (15), 5713-5724.

37. Hamada, M.; Matsuura, K.; Hamada, T.; Muneta, I.; Kakushima, K.; Tsutsui, K.; Wakabayashi, H., ZrS_2 symmetrical-ambipolar FETs with near-midgap TiN film for both top-gate electrode and Schottky-barrier contact. *Japanese Journal of Applied Physics* **2021,** *60* (SB), SBBH05.

38. Li, L.; Wang, H.; Fang, X.; Zhai, T.; Bando, Y.; Golberg, D., High-performance Schottky solar cells using ZrS_2 nanobelt networks. *Energy & Environmental Science* **2011,** *4* (7), 2586-2590.

39. Lu, C.; Ge, Y.; Luo, M.; Xu, X., Optical Nonlinearity of Emerging ZrS_2 and HfS_2 Semiconductors. *Annalen der Physik* **2023,** *535* (1), 2200309.

40. Huang, J.; Tian, Y.; Cheng, Y.; Li, X.; Zhang, S.; Jiang, J.; Chen, J.; Wang, G.; Li, J.; Yin, Z.; Zhang, X., Large-area epitaxial growth of 2D $ZrS_{2(1-x)}Se_{2x}$ semiconductor alloys with fully tunable compositions and bandgaps for optoelectronics. *Science China Materials* **2023,** *66* (5), 1870-1878.

41. Motojima, S.; Takahashi, Y.; Sugiyama, K., Anomalous pillar-shaped crystal growth of zirconium disulfide. *Journal of Crystal Growth* **1976,** *33* (1), 116-124.

42. Thiyagarajan, R.; Beevi, M. M.; Anusuya, M., Nano structural characteristics of zirconium sulphide thin films. *J Am Sci* **2009,** *5* (3), 26.

43. Thompson, J. Development of Single-Source CVD Precursors for Group IV, V and VI Metal Disulfides. Doctoral Dissertation, University of Bath, 2017.

44. Wang, Z.; Gu, Y.; Liu, F.; Wu, W., Facile synthesis of wide bandgap ZrS_2 colloidal quantum dots for solution processed solar-blind UV photodetectors. *Chemical Communications* **2023,** *59* (92), 13771-13774.

45. Gokulsaswath, V.; Suganya, G.; Monika, S.; Kalpana, G., Investigation of Zirconium Disulphide Quantum Dots for Supercapacitor Applications. *Crystal Research and Technology* **2023,** *59* (5), 2300111.

46. Zhang, Y.-L.; Wu, X.-C.; Tao, Y.-R.; Mao, C.-J.; Zhu, J.-J., Fabrication and field-emission performance of zirconium disulfide nanobelt arrays. *Chemical Communications* **2008,** (23), 2683-2685.

47. Yang, R.; Nelson, J.; Fai, C.; Yetkin, H. A.; Werner, C.; Tervil, M.; Jess, A. D.; Dale, P. J.; Hages, C. J., A Low-Temperature Growth Mechanism for Chalcogenide Perovskites. *Chemistry of Materials* **2023,** *35* (12), 4743-4750.

48. Motojima, S.; Itoh, K.; Takahashi, Y.; Sugiyama, K., Chemical vapor deposition of titanium disulfide. *Bulletin of the Chemical Society of Japan* **1978,** *51*, 3240-3244.

49. Peters, E. S.; Carmalt, C. J.; Parkin, I. P., Dual-source chemical vapour deposition of titanium sulfide thin films from tetrakisdimethylamidotitanium and sulfur precursors. *Journal of Materials Chemistry* **2004,** *14* (23), 3474-3477.

50. Fix, R.; Gordon, R. G.; Hoffman, D. M., Chemical vapor deposition of titanium, zirconium, and hafnium nitride thin films. *Chemistry of Materials* **1991,** *3* (6), 1138-1148.

51. Meng, X.; Liu, Y.; Watanabe, F.; Velasquez Carballo, K.; Cai, J.; Chen, Z.; Zhou, H., Atomic layer deposition of two-dimensional layered zirconium sulfide. *Materials Today Chemistry* **2024,** *37*, 102013.

52. Hausmann, D. M.; Kim, E.; Becker, J.; Gordon, R. G., Atomic Layer Deposition of Hafnium and Zirconium Oxides Using Metal Amide Precursors. *Chemistry of Materials* **2002,** *14* (10), 4350-4358.

53. Chavez, D.; Berube, A. D.; Davis, L. M., Zirconium disulfide single crystal, ZrS_2(0001), characterized by X-ray photoelectron spectroscopy. *Surface Science Spectra* **2025,** *32*, 014004.

54. Dasgupta, N. P.; Mack, J. F.; Langston, M. C.; Bousetta, A.; Prinz, F. B., Design of an atomic layer deposition reactor for hydrogen sulfide compatibility. *Review of Scientific Instruments* **2010,** *81* (4), 044102.

55. Putz, H.; Brandenburg, K. *Match! - Phase Analysis using Powder Diffraction*, Crystal Impact: Kreuzherrenstr. 102, 53227 Bonn, Germany.

56. Gražulis, S.; Chateigner, D.; Downs, R. T.; Yokochi, A. F. T.; Quirós, M.; Lutterotti, L.; Manakova, E.; Butkus, J.; Moeckg, P.; Bail, A. L., Crystallography Open Database – an open-access collection of crystal structures. *Journal of Applied Crystallography* **2009,** *42* (4), 726-729.

57. Seah, M. P.; Gilmore, I. S.; Beamson, G., XPS: binding energy calibration of electron spectrometers 5—re-evaluation of the reference energies. *Surf. Interface Anal.* **1998,** *26* (9), 642-649.

58. Fairley, N.; Fernandez, V.; Richard-Plouet, M.; Guillot-Deudon, C.; Walton, J.; Smith, E.; Flahaut, D.; Greiner, M.; Biesinger, M.; Tougaard, S.; Morgan, D.; Baltrusaitis, J., Systematic and collaborative approach to problem solving using X-ray photoelectron spectroscopy. *Applied Surface Science Advances* **2021,** *5*, 100112.

59. Jellinek, F.; Pollak, R. A.; Shafer, M. W., X-ray photoelectron spectra and electronic structure of zirconium trisulfide and triselenide. *Mater. Res. Bull.* **1974,** *9* (6), 845-856.

60. Gadzuk, J. W.; Šunjić, M., Excitation energy dependence of core-level x-ray-photoemission-spectra line shapes in metals. *Physical Review B* **1975,** *12* (2), 524-530.

61. Sacher, E., Asymmetries in Transition Metal XPS Spectra: Metal Nanoparticle Structure, and Interaction with the Graphene-Structured Substrate Surface. *Langmuir* **2010,** *26* (6), 3807-3814.

62. Baba, Y.; Sasaki, T. A., Application of X-ray-induced Auger electron spectroscopy to state analyses of hydrogen implanted in Y, Zr and Nb metals. *Surface and Interface Analysis* **1984,** *6* (4), 171-173.

63. Cesaria, M.; Caricato, A. P.; Martino, M., Realistic absorption coefficient of ultrathin films. *Journal of Optics* **2012,** *14* (10), 105701.

64. Wagman, D. D.; Evans, W. H.; Parker, V. B.; Schumm, R. H.; Halow, I.; Bailey, S. M.; Churney, K. L.; Nuttall, R. L., The NBS tables of chemical thermodynamic properties. Selected values for inorganic and C_1 and C_2 organic substances in SI units. *Journal of Physical and Chemical Reference Data* **1982,** *11*, 1-392.

65. Lappert, M. F.; Patil, D. S.; Pedley, J. B., Standard Heats of Formation and M-C Bond Energy Terms for Some Homoleptic Transition Metal Alkyls MR_n. *J. Chem. Soc., Chem. Commun.* **1975**, 830-831.

66. Bastianini, A.; Battiston, G., A.; Gerbasi, R.; Porchia, M.; Daolio, S., Chemical Vapor Deposition of ZrO_2 Thin Films Using $Zr(NEt_2)_4$ as Precursor. *J. Phys. IV France* **1995,** *05* (C5), C5-525-C5-531.

67. Velasco, A.; Ryu, Y. K.; Boscá, A.; Ladrón-de-Guevara, A.; Hunt, E.; Zuo, J.; Pedrós, J.; Calle, F.; Martinez, J., Recent trends in graphene supercapacitors: from large area to microsupercapacitors. *Sustainable Energy & Fuels* **2021,** *5* (5), 1235-1254.

68. Broomhall-Dillard, R. N. R.; Gordon, R. G.; Wagner, V. A., Volatile Liquid Precursors for the Chemical Vapor Deposition (CVD) of Thin Films Containing Alkali Metals. *Materials Research Symposium Proceedings* **2000,** *606*, 139.

69. Andre, C. L.; El-Zein, N.; Tran, N., Bubbler for constant vapor delivery of a solid chemical. *Journal of Crystal Growth* **2007,** *298*, 168-171.

70. Weber, T.; Muijsers, J. C.; Niemantsverdriet, J. W., Structure of Amorphous MoS_3. *Journal of Physical Chemistry* **1995,** *99*, 9194-9200.

71. Mattinen, M.; Gity, F.; Coleman, E.; Vonk, J. F. A.; Verheijen, M. A.; Duffy, R.; Kessels, W. M. M.; Bo, A. A., Atomic Layer Deposition of Large-Area Polycrystalline Transition Metal Dichalcogenides from 100 °C through Control of Plasma Chemistry. *Chemistry of Materials* **2022,** *34*, 7280-7292.

Chapter 3. Exploring Low Temperature Chemical Vapor Deposition of Zirconium(IV) Sulfide on Polymer Substrates

3.1. Contributions

The work presented below is derived from a manuscript in progress. I deposited ZrS_2 thin films and characterized them using scanning electron microscopy, energy dispersive X-ray spectroscopy, X-ray diffraction, and four-point probe. Abigail D. Berube measured the composition of ZrS_2 films using XPS and analyzed the data with supervision from Daniela Chavez. Professor Luke M. Davis supervised the project and assisted in writing and editing the manuscript. This project is funded by Tufts University and the National Science Foundation (DMR-2224949).

3.2. Abstract

Transition metal dichalcogenides (TMDCs) have carrier mobilities of >1000 $cm^2V^{-1}s^{-1}$ that are desirable in optoelectronic and sensing devices. Flexible electronics using TMDCs have been demonstrated, but high processing temperatures preclude direct deposition of high quality crystalline films onto polymers, which often have upper working temperatures of 80-200 °C. Using $Zr(NMe_2)_4$ and H_2S as precursors, low temperature chemical vapor deposition (CVD) of zirconium(IV) sulfide (ZrS_2) is demonstrated on a variety of polymer substrates. Stoichiometric and crystalline ZrS_2 films can be deposited on polyimide (Kapton) and polyether ether ketone (PEEK) substrates at 200 °C, with resistivities of the latter comparable to ZrS_2 films deposited at 800-1000 °C from $ZrCl_4$ and sulfur. Depositions of ZrS_2 on polydimethylsiloxane (PDMS) at 200 °C and polyethylene terephthalate (PET) at 150 °C produce partially oxidized films that are either

weakly crystalline or amorphous. All substrates withstand exposure to H_2S and temperature, as assessed by the crease test.

3.1. Introduction

Flexible electronics offer unique opportunities to expand the utility of conventional, planar devices. These devices have seen applications in photovoltaics, photodetectors, field-effect transistors, displays, and sensors.[72-75] Of particular relevance and importance are flexible photovoltaics, which can be prepared using scalable and inexpensive roll-to-roll manufacturing methods.[76, 77] These lightweight devices can be deployed onto curves surfaces and can be delivered inexpensively and safely to remote settings off-grid.[78, 79] Flexible photovoltaics can also be used to power portable electronics, including vehicles.[77, 80] The most common polymers for flexible photovoltaics are polyethylene terephthalate (PET) and polyethylene napthalate (PEN),[75, 81] although polycarbonate (PC) and polyimides (like Kapton) have been used as well.[76]

Common polymers used in flexible electronics typically have temperature ceilings below 200 °C. While there are is some discrepancy in reporting between manufactures, temperature ceilings for popular polymers such as PET, high density polyethylene (HDPE), polymethyl methacrylate (PMMA) and PC are 120-150, 80-90, 60-80, and 130-150 °C, respectively. Exceptions to this trend include polydimethylsiloxane (PDMS) and Kapton, with upper working temperatures typically reported between 200-300 and 350-400 °C, respectively.

The properties of TMDCs make them attractive candidates for use in flexible electronics, but high processing temperatures often preclude direct deposition onto polymer substrates. Since CVD routes to TMDCs are typically >250 °C and as high as 1000 °C,[82] these process are incompatible with direct deposition onto most polymer substrates, which typically have

temperature ceilings of 80-210 °C.[82] Instead, TMDCs are often deposited first onto thermally robust substrates and then transferred onto the desired polymer.[82-84] Transfer processes can often result in contamination and or damage to the substrate.[83, 85] While sputtering may be used to deposit TMDCs directly onto polymer substrates, the resulting films are often amorphous,[86] and thermal annealing often cannot be used to crystallized films without damage to the substrate. To the best of our knowledge, only direct deposition of crystalline TMDCs onto polymers (Kapton and Parylene) by CVD has been demonstrated for MoS_2,[85, 87, 88] which can be prepared at temperatures as low as 150 °C using molybdenum hexacarbonyl and dimethyl sulfide.[85]

We now report direct CVD of ZrS_2 films on a variety of polymer substrates at temperatures of 150 and 200 °C. Using our slow growth recipe (6) developed in chapter 2, we use $Zr(NMe_2)_4$ and H_2S to deposit stoichiometric and crystalline ZrS_2 films on Kapton and PEEK at 200 °C, and partially oxidized ZrS_2 films on PDMS and PET at 200 and 150 °C, respectively. All polymers withstand exposure to H_2S and temperature, as suggested by the crease test. The sheet resistance and resistivity of ZrS_2 films deposited on PEEK is comparable to films deposited on quartz substrates under the same conditions. Current and or voltage measurements were below the limit of detection on ZrS_2 films deposited on Kapton, PDMS and PET substrates. Shortening of deposition times and careful selection of additional polymers may expand the library of available substrates for low temperature ZrS_2 CVD.

3.3. Experimental

3.3.1. Deposition of ZrS_2 Thin Films

Materials. Tetrakis(dimethylamido)zirconium(IV) with a purity of 99% was purchased from Strem Chemical Co. (Newburyport, MA, USA), and used without further purification.

Hydrogen sulfide with a purity 99.5% (H_2O content of ≤0.01%) was purchased from Matheson Gas (p/n, G1540275) and purified further to ≤1 ppb H_2O using an ARM acid gas purifier (p/n, AG-301-150330-V04-F). Argon was purified (≤0.1 ppb H_2O, O_2, CO, CO_2) with an Entegris GateKeeper gas purifier (GPUS35FHX04R00CA). Electrical grade Kapton substrates with a thickness of 0.005″ were purchased from McMaster-Carr (p/n, 2271k3). PEEK substrates of the same thickness were also purchased from McMaster-Carr (p/n, 8504k12). Polydimethylsiloxane (PDMS) substrates 80 and 800 μm thick were purchased from SiMPore (p/n, GASKET-80PK and GASKET-800PK, respectively). Substrates believed to be polyethylene terephthalate (PET) substrates were acquired with the PDMS substrates purchased from SiMPore. Quartz substrates were purchased from ChemGlass (p/n, CGQ-0640-01). For instrument calibration,[53] single crystals of ZrS_2 (>99.9995%, flux zone grown) were purchased from 2D Semiconductors (Scottsdale, AZ, USA).

CVD Reactor. Chemical vapor deposition was performed in a custom-built, hot-walled CVD reactor described in chapter 2. For all depositions, the foreline trap was loaded with 600 g of SULFURTRAP EX media and an additional 200 mL of activated 3A molecular sieves upstream of the scrubber.

Substrate Cleaning. ZrS_2 films were deposited on Kapton, PEEK, PDMS and PET polymer substrates, as well as quartz substrates. All polymer substrates were cleaned by sonicating for 10 minutes in SEMI-grade acetone, followed by sonicating for another 10 minutes in SEMI-grade isopropanol. After sonication, samples were rinsed off with SEMI-grade isopropanol and blown dry with nitrogen. Quartz substrates were cleaned by first hand-scrubbing in a slurry of Alconox detergent and rinsing with deionized water. The substrates were then rinsed with SEMI-grade acetone, SEMI-grade isopropanol, and blown dry with nitrogen gas. Finally, the substrates

were exposed to UV/ozone (Ossila) for 10 min to remove any remaining organic contaminants. Polymer substrates were not treated using UV/ozone.

Substrate Positions and Analysis. ZrS_2 films were primarily deposited onto polymer substrates cut to 1″ long × 0.5″ wide. In each deposition, three polymer substrates are placed back-to-back placed, starting 0.5″ from the precursor inlets inside the CVD reactor. A quartz substrate also cleaved to 1″ long × 0.5″ wide was placed immediately downstream of the polymer substrates. In some instances, a 1 cm^2 polymer substrate was added directly downstream of the second polymer substrate to collect XPS data on. Otherwise, XPS samples were acquired by cutting a small piece from the downstream end of the polymer substrate 1.5″ from the precursor inlets.

Each ZrS_2 film deposited onto 1″ long × 0.5″ wide substrates was cut into three pieces for analysis. A razor blade was used to cut ZrS_2 films deposited on polymer samples, while films deposited on quartz were scored with a diamond scribe and cleaved using wafer cutters. Note that to avoid damage to the ZrS_2 film while cutting polymers to obtain cross sections for microscopy, the substrate was bent at ca. 30-45° (with the film facing the opposite direction of bending) to allow the razor blade to glide more easily through the substrate. On each sample, and in increasing distance from the precursor inlets, the cut regions were used for SEM/EDS, four-point probe, and p-XRD. Due to convolution of peaks from the underlying substrate, EDS data is typically only reported from the front-most sample.

Baking Out the CVD Reactor. To remove H_2O adsorbed to surfaces within the CVD reactor, bakeouts were routinely performed before deposition of ZrS_2. After installing a new quartz tube onto the reactor, this zone was heated to 400 °C for 2 hours under active vacuum with 100 sccm Ar flowing (~860 mTorr). Except for the Swagelok tubing upstream of the $Zr(NMe_2)_4$ precursor bubbler, all precursor-carrying Swagelok tubing downstream of an MFC were heated to

110 °C during this time. The KF25 cross, quick flange adapters, and vacuum bellows hose were heated to 45 °C; the temperature was limited to prevent compression-set failure of the EPDM O-rings.

Degassing of Polymer Substrates. After completing bakeouts of the CVD reactor, polymer substrates were added to degas overnight. Substrates were loaded after the quartz tube in the CVD reaction zone had cooled to 50 °C to avoid thermal degradation. The reaction zone was then maintained at 50 °C for 12-15 hours while flowing 10 sccm of Ar to sweep out any gases originating from the polymer substrates. Without this step, we found that all polymers outgassed significantly, as indicated by rate of rise tests. Indeed, after the CVD reactor was loaded with polymer substrates, brought to the set reaction temperature, and isolated from vacuum, the pressure increased at a rate on the order of 10 mTorr/min, and as high as 100 mTorr/min for substrates with thickness of ca. 1 mm. In the absence of polymers and after the degassing step, the rate of rise under these conditions is typically 0.5-1.0 mTorr/min.

Deposition Conditions. ZrS_2 films were deposited at 200 °C onto Kapton, PEEK and PDMS substrates, and at 150 °C on PET substrates. All depositions were carried out using recipe 6 developed in chapter 2, which was optimized for enhancing crystallinity on quartz substrates. Precursor delivery conditions used in this work are summarized in Table 3.1.

Table 3.1. Precursor delivery conditions used to deposit ZrS_2 films at 150 and 200 °C.

Deposition Recipe	6
Bubbler Temperature (°C)	35
Bubbler Carrier Gas Flowrate (sccm)	2
H_2S Flowrate (sccm)	1
Purge Gas Flowrate	200

3.3.2 Characterization of ZrS_2 Thin Films

Morphology and thickness. The morphology and thickness of ZrS_2 films was examined using field-emission scanning electron microscopy (FESEM), in plan-view and cross-section, respectively. This imaging was performed using a Zeiss Gemini 360 SEM at the Harvard University Center for Nanoscale Systems (CNS).

Crystallinity. The crystallinity of ZrS_2 films was assessed using powder X-ray diffraction (p-XRD) at the Harvard University Department of Chemistry and Chemical Biology Center for Crystallographic Studies. X-ray diffractograms were recorded using a Bruker D2 PHASER X-ray diffractometer using Cu Kα radiation ($\lambda = 1.542$ Å) and a $\theta-2\theta$ scan. Scans were performed in the 2θ range of 10°–60° with an increment of 0.05° and a dwell time of 1 s. Either a glass or c-plane sapphire substrate was used to mount polymer substrates on the p-XRD sample.

Composition. Energy dispersive X-ray spectroscopy (EDS) and X-ray photoelectron spectroscopy (XPS) were calibrated with ZrS_2 single crystals, and then used to determine the composition of ZrS_2 thin films deposited by CVD. EDS data were collected using an Oxford Instruments Ultim Max EDS installed on the Zeiss Gemini 360 used for microscopy at CNS. Samples were analyzed with a 10 kV imaging voltage and a working distance of 8 – 10 mm. Single crystals were exfoliated three times using Scotch tape to remove surface oxides before EDS analysis.

Purity. XPS data were collected in a mu-metal SPECS Ultrahigh Vacuum (UHV) chamber described in the experimental section of chapter 2. Additional details on XPS fitting procedures are also available in the experimental section of chapter 2. XPS spectra were collected and fit by Abigail Berube with supervision from Daniela Chavez.

Electrical properties. The sheet resistance of ZrS_2 films was measured using a Signatone S-302-4 four-point probe. Measurements were collected on samples exposed to atmosphere for no more than 20 minutes.

3.4. Results and Discussion

3.4.1. Selecting Compatible Substrates

Deposition of ZrS_2 onto polymer substrates is constrained by limitations to both temperature and H_2S exposure. Although ZrS_2 films can be deposited at temperatures of up to 350 °C using recipes described in chapter 2, for deposition of crystalline films with compact morphologies down the length of the reactor a substrate temperature of 200 °C is most appropriate. However, most polymers utilized in flexible electronics have temperature ceilings below 200 °C and degrade or become brittle with prolonged exposure to H_2S. Therefore, we identified Kapton and PEEK as more appropriate candidate substrates for ZrS_2 depositions, as these materials have reported maximum operating temperatures of ca. 400 and ca. 250 °C, respectively, and have resistance to H_2S.[89] Kapton is the preferred substrate for flexible electronics in space applications,[90] due to its resistance to vacuum, radiation and energetic particles.[91] PEEK substrates are not used as often in flexible electronics as polymers such as Kapton and PET, although there are several reports of its use in these applications.[92-94] While PDMS is typically used as a transfer substrate,[95] it has a temperature ceiling as high as 200 °C and moderate resistance to H_2S,[96] and is the third candidate for depositions at 200 °C. Although the deposition temperature must be lowered to 150 °C to deposit on PET, we also select this polymer due to high resistance to H_2S,[97] and since it is a popular substrate for flexible electronics.[98]

3.4.2. Deposition Uniformity and Substrate Performance

Uniform ZrS_2 films can be deposited on Kapton and PEEK at 200 °C without damage to the underlying substrates. ZrS_2 films deposited on Kapton and PEEK appear shiny by eye, and transition from black or dark brown at the front of the reaction zone to orange and yellow as film thickness decreases down the length of the reactor (Figure 3.1). Both substrates remain intact upon exposure to CVD conditions and pass the crease test. Additionally, films are well adhered to the substrate and do not delaminate when attempting a Scotch tape test.

Deposition of ZrS_2 on PDMS at 200 °C affords films with surface coverage dependent on substrate thickness and location. As shown in Figure 3.1, on 800 μm thick PDMS the majority of deposition occurs in front of the $Zr(NMe_2)_4$ inlet and drops off significantly at a distance of 1.5″. Since deposition occurs as expected on a quartz witness sample placed 3.5″ from the precursor inlets, the lack of deposition on PDMS substrates 1.5-2.5″ from the precursor inlets is presumably related to the substrate. It is hypothesized that deposition uniformity is partially associated with outgassing of PDMS (the reactor rate of rise immediately before deposition was ca. 8 mTorr/min), as reducing the substrate thickness to 80 μm reduced outgassing (rate of rise of 0.5 mTorr/min) and improved surface coverage. Regardless, deposition on thinner PDMS still results in splotchy films 2.5″ from the precursor inlets. Interestingly, film uniformity is also highest directly in front of the $(ZrNMe_2)_4$ precursor inlet on thin PDMS (Figure 3.1), which may suggest gas phase speciation or growth rate is also an important growth parameter on this substrate. On both thick and thin PDMS substrates it was also found that ZrS_2 films were not well adhered and failed the Scotch tape test. This is perhaps not unsurprising for PDMS, considering it is often used to transfer materials between substrates.[95] Adhesion of ZrS_2 to PDMS is not negligible though, as placement

of PDMS directly on the CVD reactor sample holder pulls off film accumulated over several depositions.

Uniform ZrS_2 films are deposited on PET at 150 °C, but with some damage to the underlying substrates. Like on Kapton and PEEK, ZrS_2 films deposited on PET are shiny and appear continuous by eye, with no obvious splotches like on PDMS (Figure 3.1). The films are also well adhered and pass Scotch tape tests. However, some damage to the underlying substrates was observed under CVD conditions, as the PET slightly contracted and bent, presumably due to overshooting of the furnace temperature to 170 °C when ramping to the set temperature. Regardless, the substrates pass the crease test before and after exposure to deposition conditions, suggesting minimal damage.

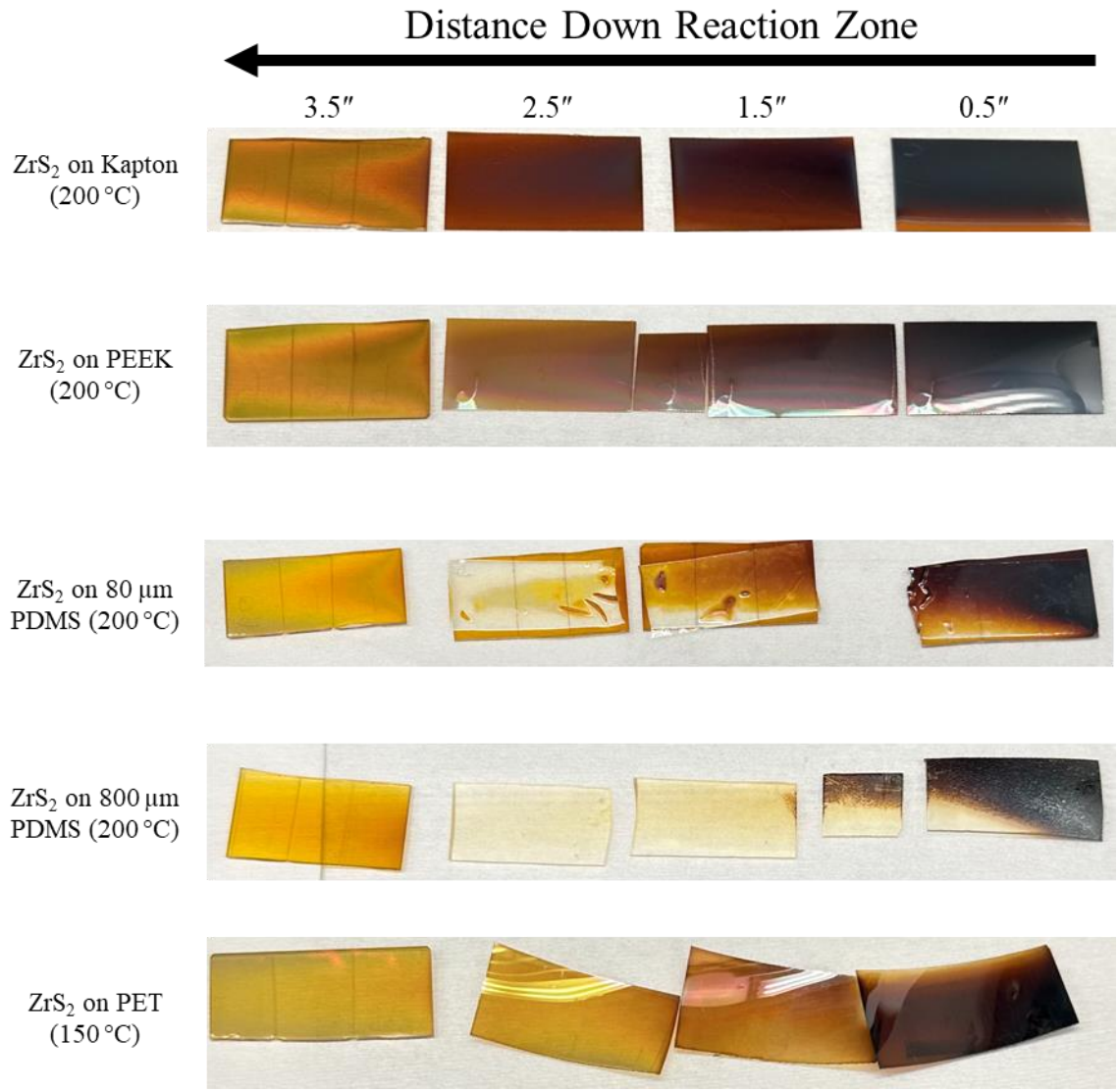

Figure 3.1. Photographs of ZrS_2 films deposited on various polymer substrates at either 150 or 200 °C. Polymer substrates are placed 0.5 – 2.5″ from the precursor inlets, while a quartz substrate witness is placed 3.5″ from the precursor inlets. Thin PDMS substrates are mounted on pieces of glass to prevent them from sticking to the stainless-steel sample tray and from bending while handling (which leads to cracking of films).

3.4.3. Film Morphology

Planview microscopy of ZrS_2 films deposited on Kapton and PEEK reveals clusters of roughly spherical grains with diameters of ca. 20-30 nm. Film morphology is relatively constant down the length of the reaction zone (0.5-2.5″ from the precursor inlets), although some smoothing of films is observed as clusters become slightly smaller (Figures 3.2 and 3.3). There is no significant difference in morphology between ZrS_2 films deposited on Kapton and PEEK substrates and quartz witness substrates placed at the end of the reaction zone for each deposition (3.5″ from the precursor inlets). Cross section micrographs reveal films have a columnar structure on both substrates (Figure 3.4).

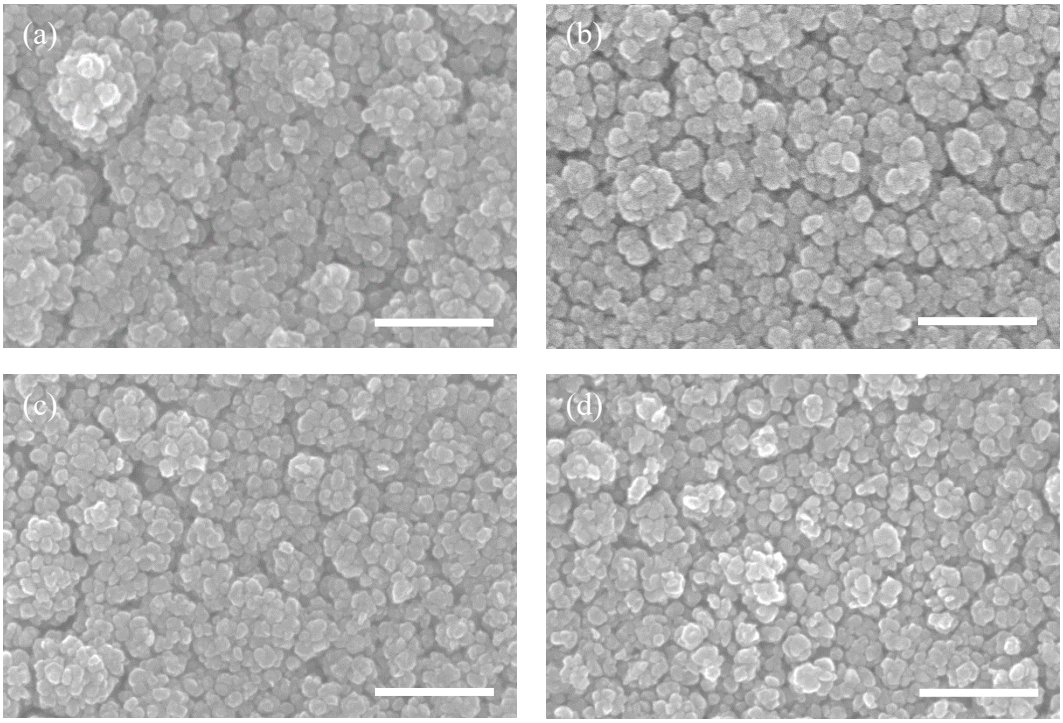

Figure 3.2. Plan-view micrographs of ZrS_2 films deposited at 200 °C at distances of 0.5″ (a), 1.5″ (b) and 2.5″ (c) from the precursor inlets on Kapton substrates, and 3.5″ from the precursor inlets on a quartz substrate (d). Scale bars are 250 nm.

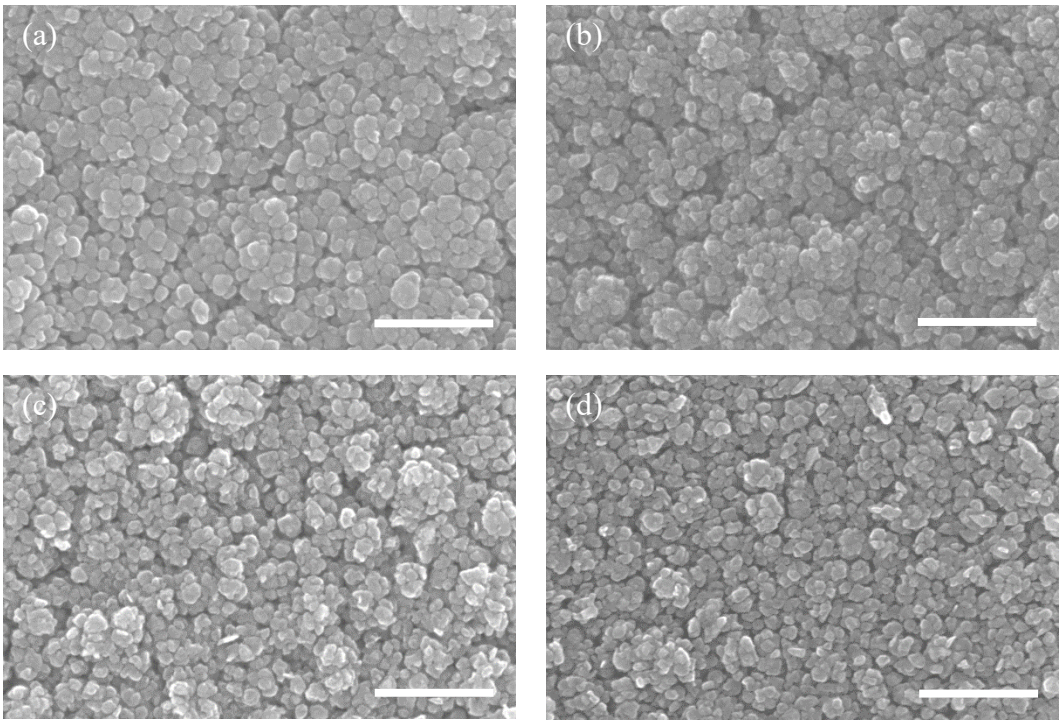

Figure 3.3. Plan-view micrographs of ZrS_2 films deposited at 200 °C at distances of 0.5″ (a), 1.5″ (b) and 2.5″ (c) from the precursor inlets on PEEK substrates, and 3.5″ from the precursor inlets on a quartz substrate (d). Scale bars are 250 nm.

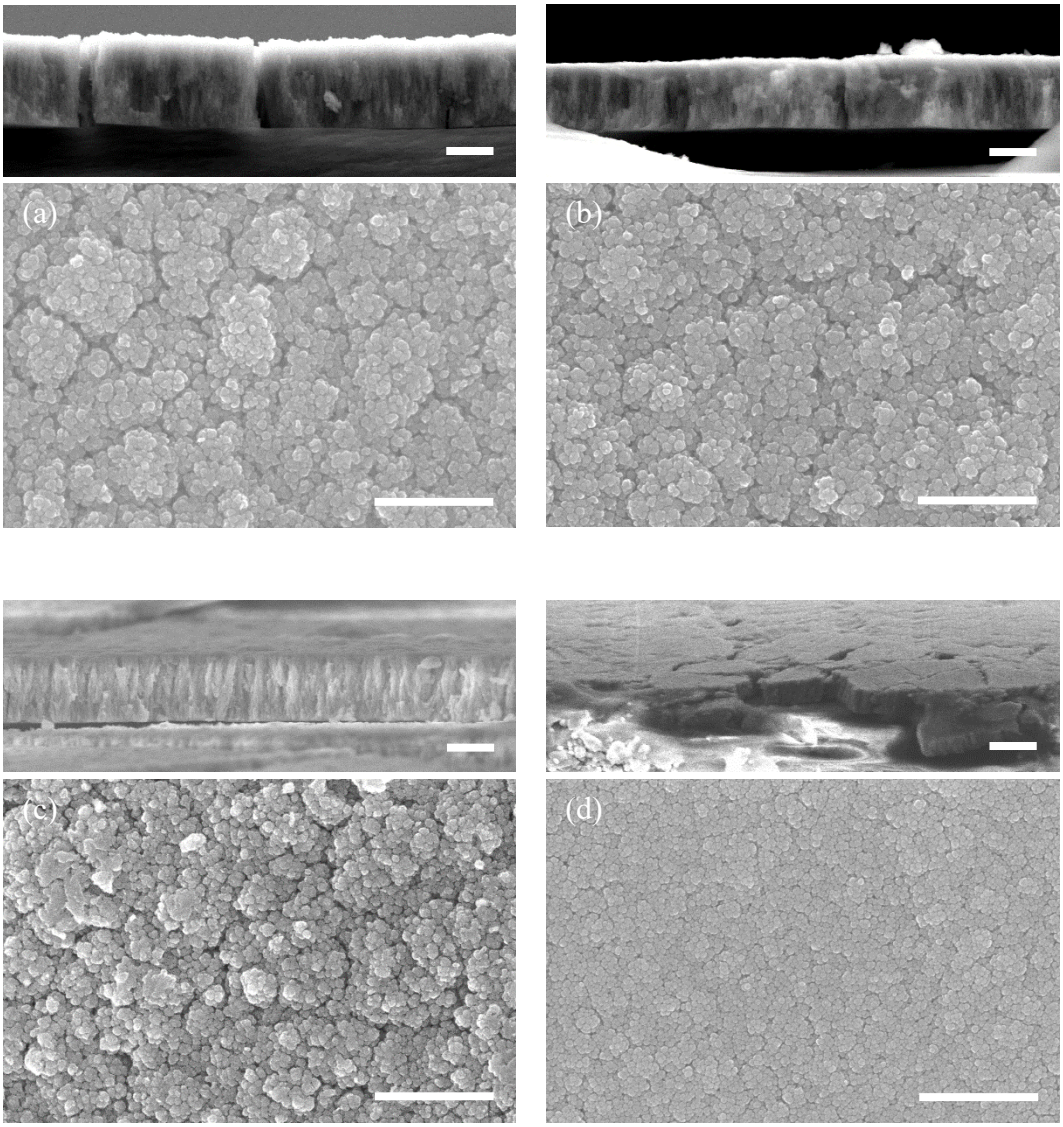

Figure 3.4. Plan-view and cross-section micrographs of ZrS_2 films deposited at the front of the reaction zone on (a) Kapton, (b) PEEK, (c) PDMS, and (d) PET substrates. Scale bars on plan-view micrographs are 500 nm and scale bars on cross-section micrographs are 1 μm.

The morphology of ZrS_2 films deposited on thin PDMS substrates at the front of the reaction zone is comparable to morphologies observed on Kapton and PEEK substrates. As shown in micrographs in Figures 3.4 and 3.5, the morphology of the frontmost film on thin PDMS has clusters of roughly spherical grains with diameters of ca. 20-30 nm. Without the use of a glass supporting substrate, the thin PDMS substates would bend easily while handling, which fractured ZrS_2 films and complicated analysis by XPS (Figure 3.6). At a distance of 1.5″ from the precursor inlets, grains shapes are similar to those at the front of the reaction zone, but with slightly smaller diameters (Figure 3.5). Features were not observable on the PDMS substrate 2.5″ from the precursor inlets (due to excessive charging under the microscope) and the morphology on the quartz substrate 3.5″ from the precursor inlets is comparable to quartz witness samples from depositions containing Kapton and PEEK substrates (Figures 3.2, 3.3 and 3.5). There were no observable features on ZrS_2 films deposited on thick PDMS substrates.

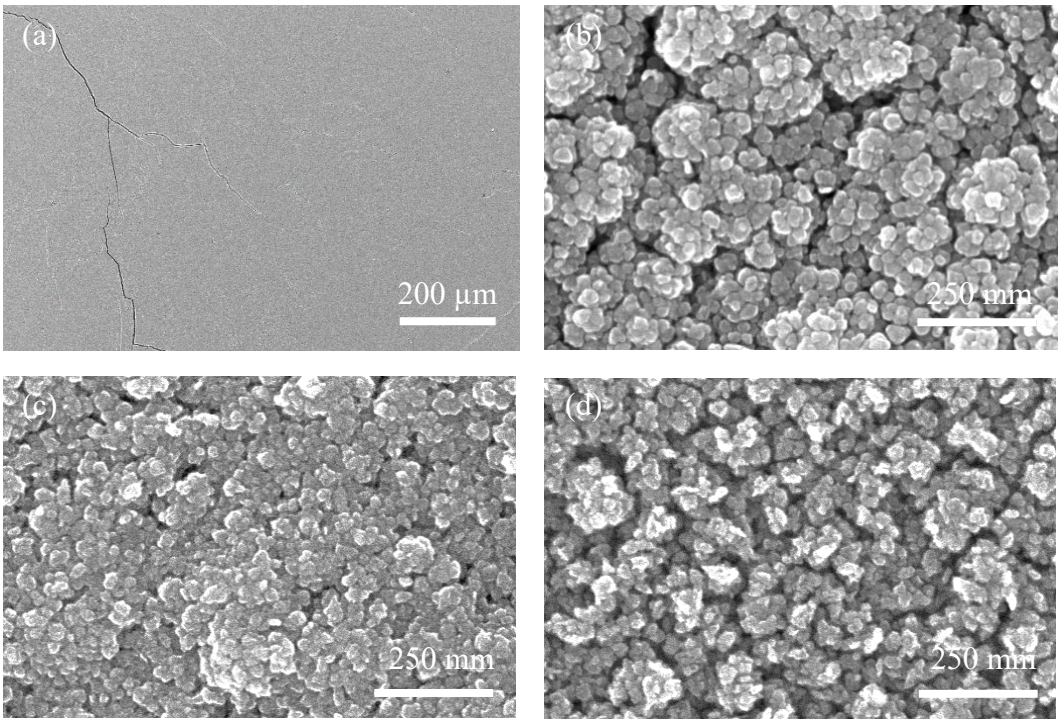

Figure 3.5. Plan-view micrographs of ZrS_2 films deposited at 200 °C at distances of 0.5″ (a and b) and 1.5″ (c) from the precursor inlets on 80 µm thick PDMS substrates, and 3.5″ from the precursor inlets on a quartz substrate (d). The absence or significant cracking in films is shown in (a) and representative film microscopies are shown in (b), (c) and (d).

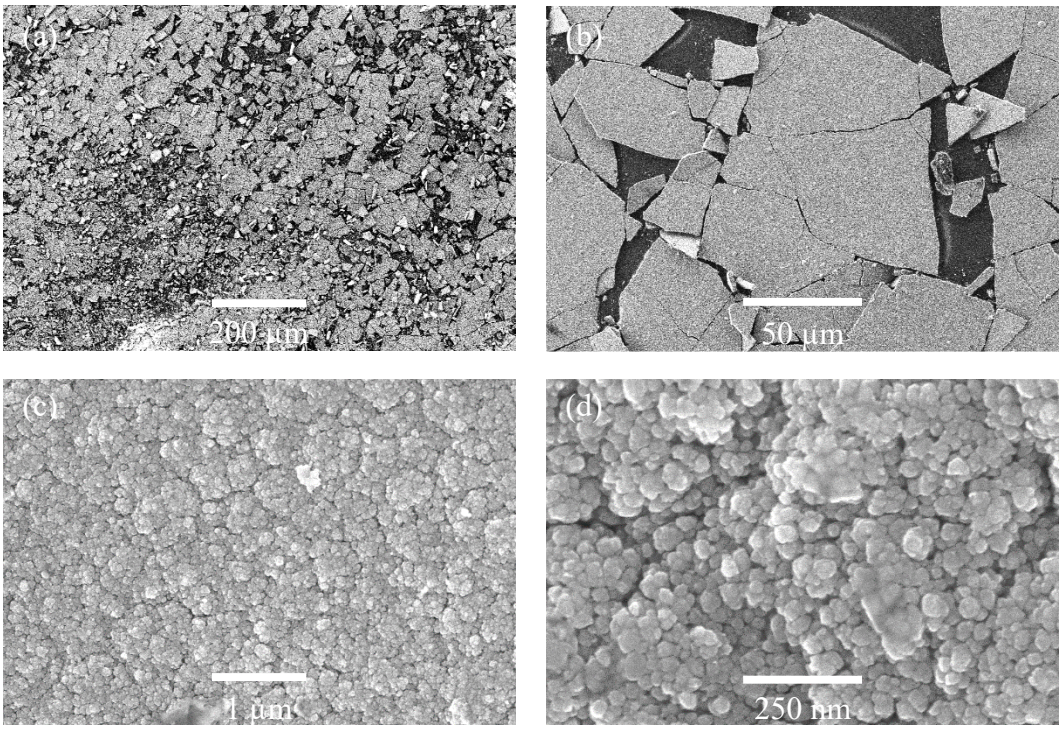

Figure 3.6. Plan-view micrographs of ZrS_2 films deposited at 200 °C on a 80 µm thick PDMS substrate placed at the front of the reaction zone without a supporting glass substrate. Figure (a) provides an overview of the sample, showing that the film is fractured. Figure (b) shows islands of film separated by cracks and figures (c) and (d) show the morphology of the ZrS_2 film.

The morphology of ZrS_2 films deposited on PET varies with location down the length of the reaction zone. As shown in figure 3.7, films deposited at the front of the reaction zone (0.5″ from the precursor inlets) have smoother morphologies and slightly larger grains than films deposited 1.5 and 2.5″ from the precursor inlets, which have comparable morphologies to films deposited at 200 °C on Kapton, PEEK and quartz. The quartz witness substrate has the same morphology as films deposited 1.5 and 2.5″ from the precursor inlets, but with the addition of small flakes 20-30 nm across scattered on the surface. This gradient of morphologies down the reaction zone has been observed on depositions on all quartz substrates under these conditions.

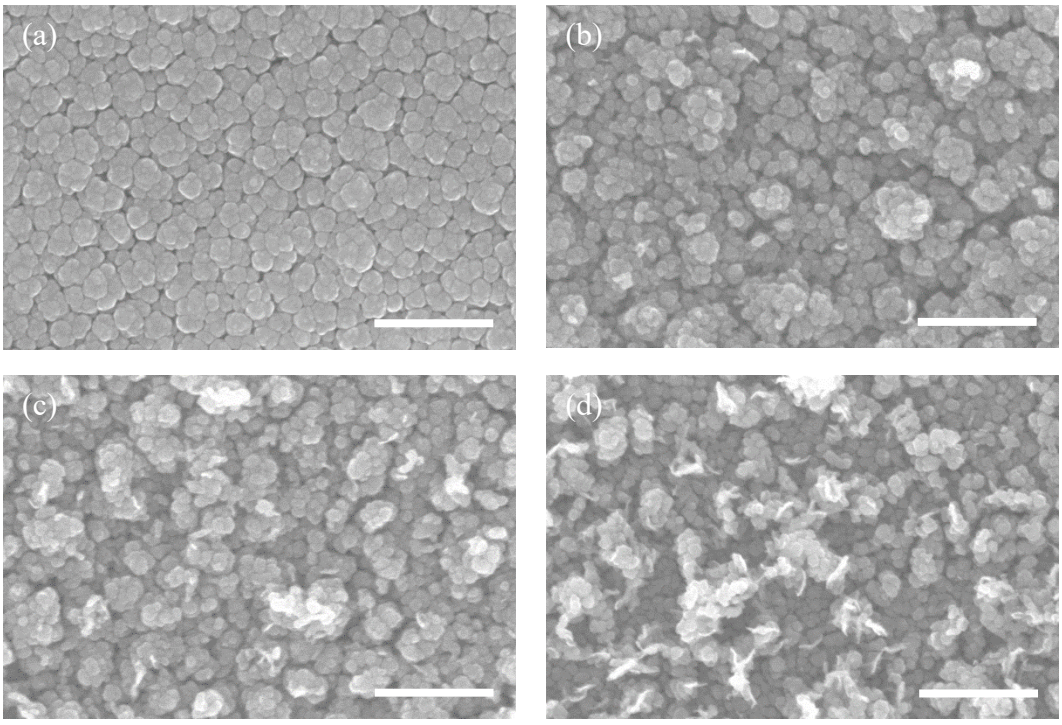

Figure 3.7. Plan-view micrographs of ZrS_2 films deposited at 150 °C at distances of 0.5″ (a), 1.5″ (b) and 2.5″ (c) from the precursor inlets on PET substrates, and 3.5″ from the precursor inlets on a quartz substrate (d). Scale bars are 250 nm.

3.4.4. Film Crystallinity

Deposition of ZrS_2 at yields crystalline films on PEEK and thin (80 μm) PDMS substrates. Films deposited on both polymers are phase pure ZrS_2, and exhibit only the 001 reflection for ZrS_2 (COD 5910006), the same as for depositions on only quartz substrates. Down the length of the reaction zone films become less crystalline, with weakly crystalline films at the rear having reflections that are nearly discernable on diffractograms (Figure 3.8). Films deposited on PEEK are more crystalline than on PDMS, with films of similar thicknesses having more intense 001 reflections (Figures 3.1 and 3.8) Compared to ZrS_2 films from depositions only containing quartz substrates, films deposited on PEEK, PDMS and quartz (witness) substrates are less crystalline (Figure 2.21). While lower ZrS_2 crystallinity on polymer substrates may reflect differences in

surface chemistry compared to quartz substrates, lower crystallinity on the quartz witness substrates suggests the effect is related to the presence of polymers during the CVD reaction. It is possible that outgassing of polymer substrates or by products from attack of polymers by H_2S releases species inhibiting crystallization of ZrS_2, but there is no data available to substantiate these claims.

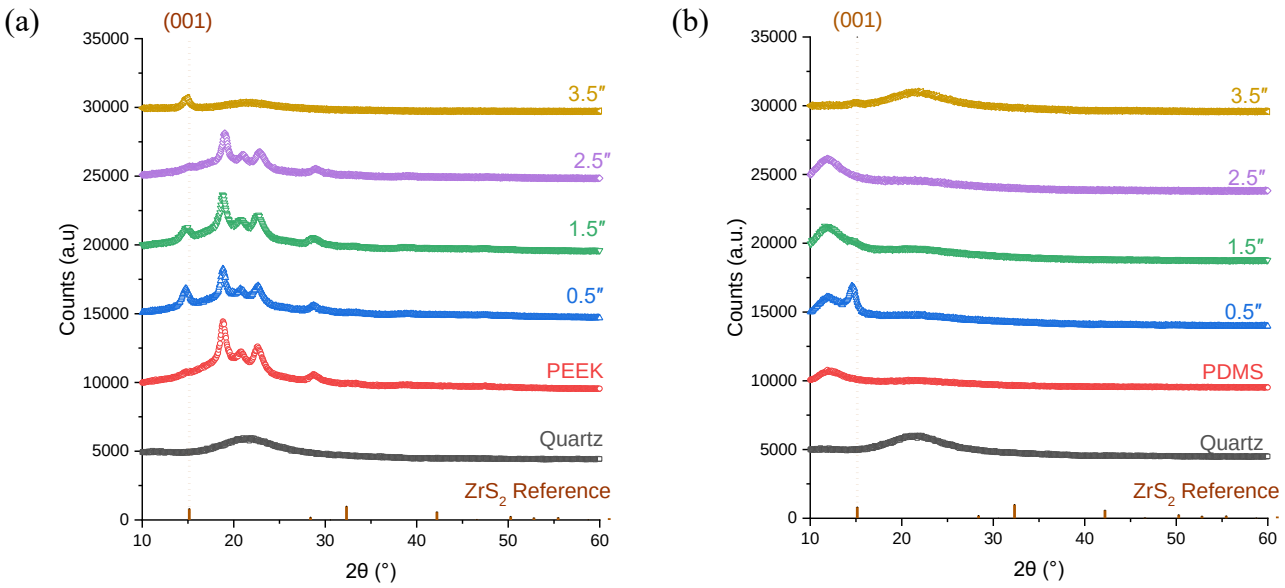

Figure 3.8. Diffractograms of ZrS_2 films deposited on PEEK (a) and 80 µm thick PDMS (substrates) placed 0.5″-2.5″ from the precursor inlets. Quartz substrates are placed 3.5″ from the precursor inlets. The ZrS_2 reference is COD 5910006.

The crystallinity of ZrS_2 films deposited on Kapton cannot be readily deconvoluted from diffractograms. As shown in Figure 3.9a, reflections from the Kapton substrate overlap with the expected ZrS_2 001 reflection at $2\theta = 15.1°$ and it is not clear if this peak is present in diffractograms. Therefore, to indirectly assess crystallinity, sample diffractograms are normalized to the most intense Kapton reflection at $2\theta = 22°$ and compared to the bare substrate. As shown in Figures 3.9b, 3.9c and 3.9d, the height of the reflection at $2\theta = 15°$ increases relative to those at $2\theta = 22$

and 26° on ZrS_2 films deposited on Kapton 0.5-2.5″ from the precursor inlets. As discussed in the following section, EDS and XPS data demonstrate deposition of stoichiometric ZrS_2 films on Kapton with limited impurities, which suggests that the feature increasing the height of the reflection at $2\theta = 15.1°$ is from the 001 reflection of ZrS_2. Operating on the assumption that this inference is true, the ZrS_2 film deposited on Kapton 0.5 and 1.5″ from the precursor inlets have comparable crystallinities, while the film deposited at 2.5″ is either weakly crystalline or amorphous. Finally, the crystallinity of the ZrS_2 film deposited on the quartz witness is higher than for depositions on PEEK and PDMS, but still lower than for depositions using on quartz substrates (Figures 2.21 and 3.10).

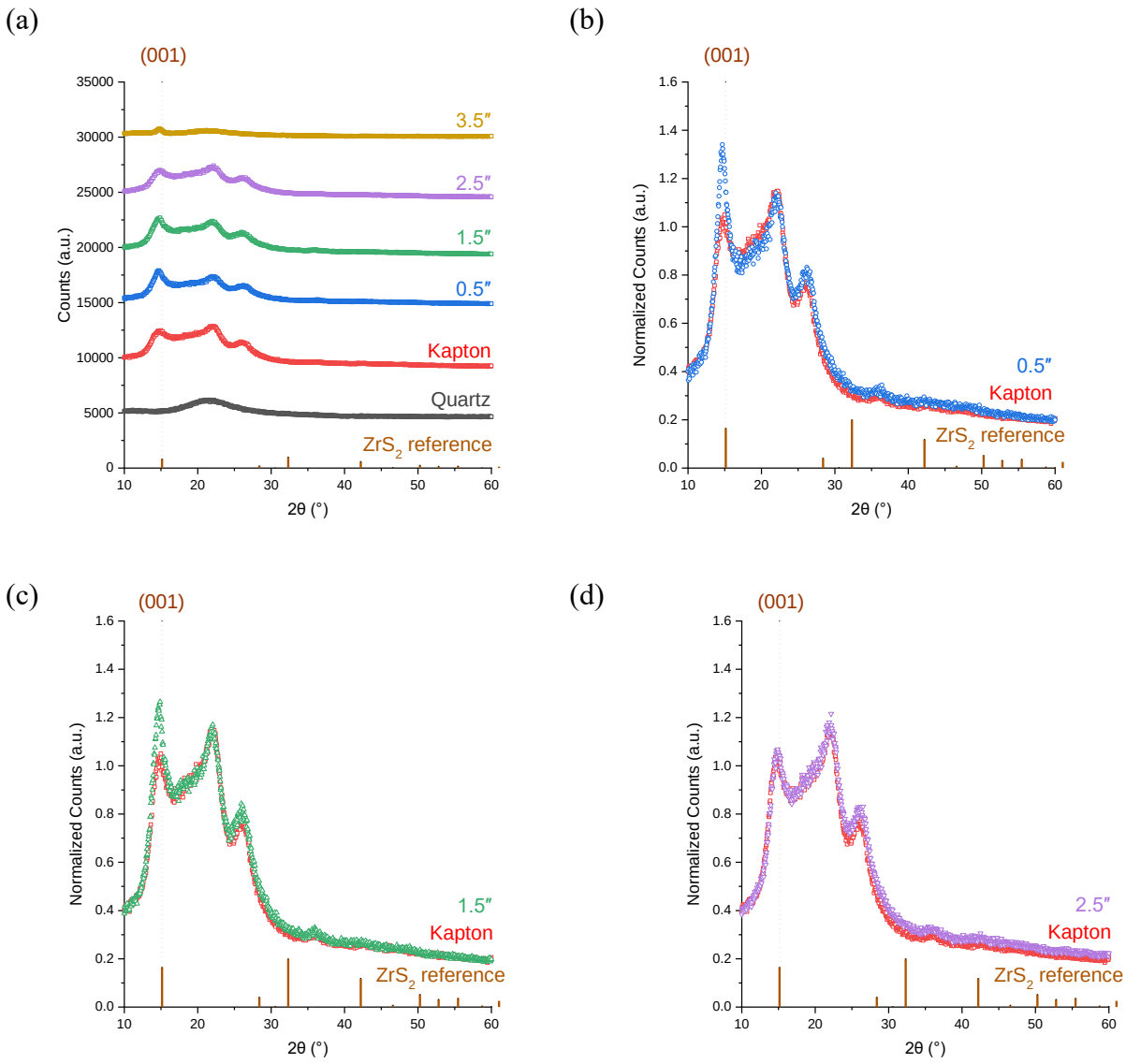

Figure 3.9. Diffractograms of ZrS_2 films deposited at 200 °C on Kapton substrates placed 0.5″ (a), 1.5″ (b) and 2.5″ (c) from the precursor inlets, and on a quartz substrate placed 3.5″ from the precursor inlets. (a) plots diffractograms of all films from the deposition without normalizing the data. (b), (c) and (d) are individual plots of ZrS_2 films deposited on Kapton 0.5, 1.5 and 2.5″ from the precursor inlets, respectively, that are normalized to the most intense reflection of the Kapton substrate. The ZrS_2 reference is COD 5910006.

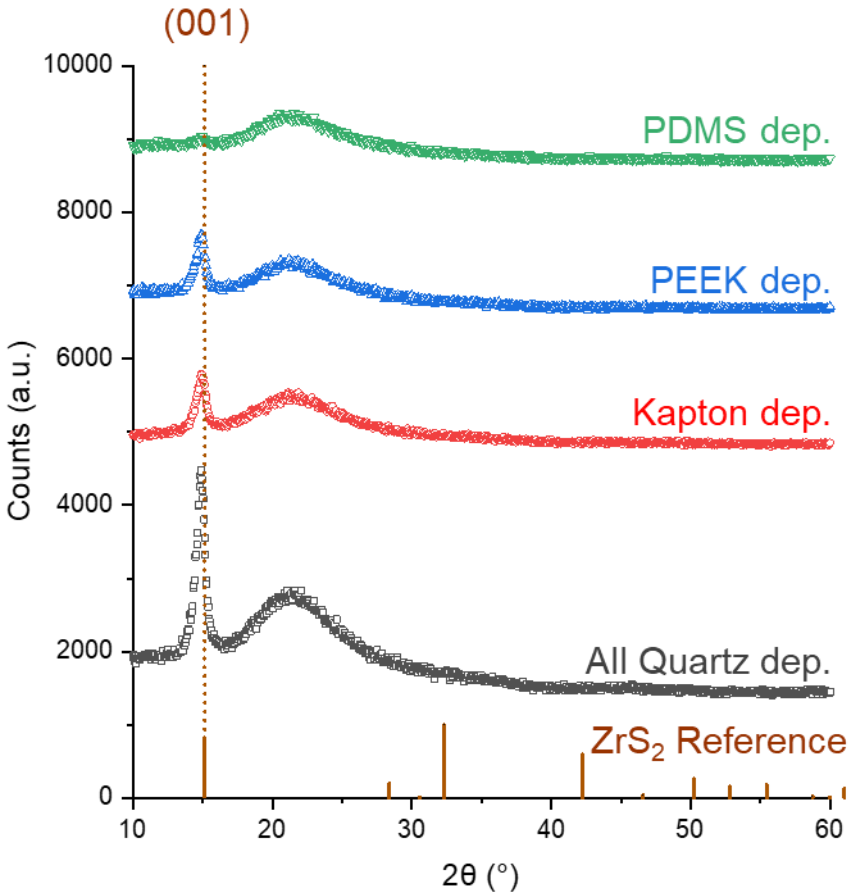

Figure 3.10. Diffractograms of ZrS_2 films deposited at 200 °C on quartz substrates placed 3.5″ from the precursor inlets with either all quartz substrates present or in depositions containing Kapton, Peek or PDMS substrates. The ZrS_2 reference is COD 5910006.

The crystallinity of ZrS_2 films increases down the reaction zone on PET substrates. Films deposited at the front of the reaction zone are amorphous, while those deposited 1.5″ and 2.5″ from the precursor inlets are weakly crystalline, with ZrS_2 001 reflections barely discernable in diffractograms (Figure 3.11). The reflection from the quartz witness sample at the rear of the reaction zone is most intense. As shown in figure (2.21), increasing crystallinity has previously been observed under the same deposition conditions on all quartz substrates, and demonstrates comparable growth of ZrS_2 on quartz and PET at 150 °C.

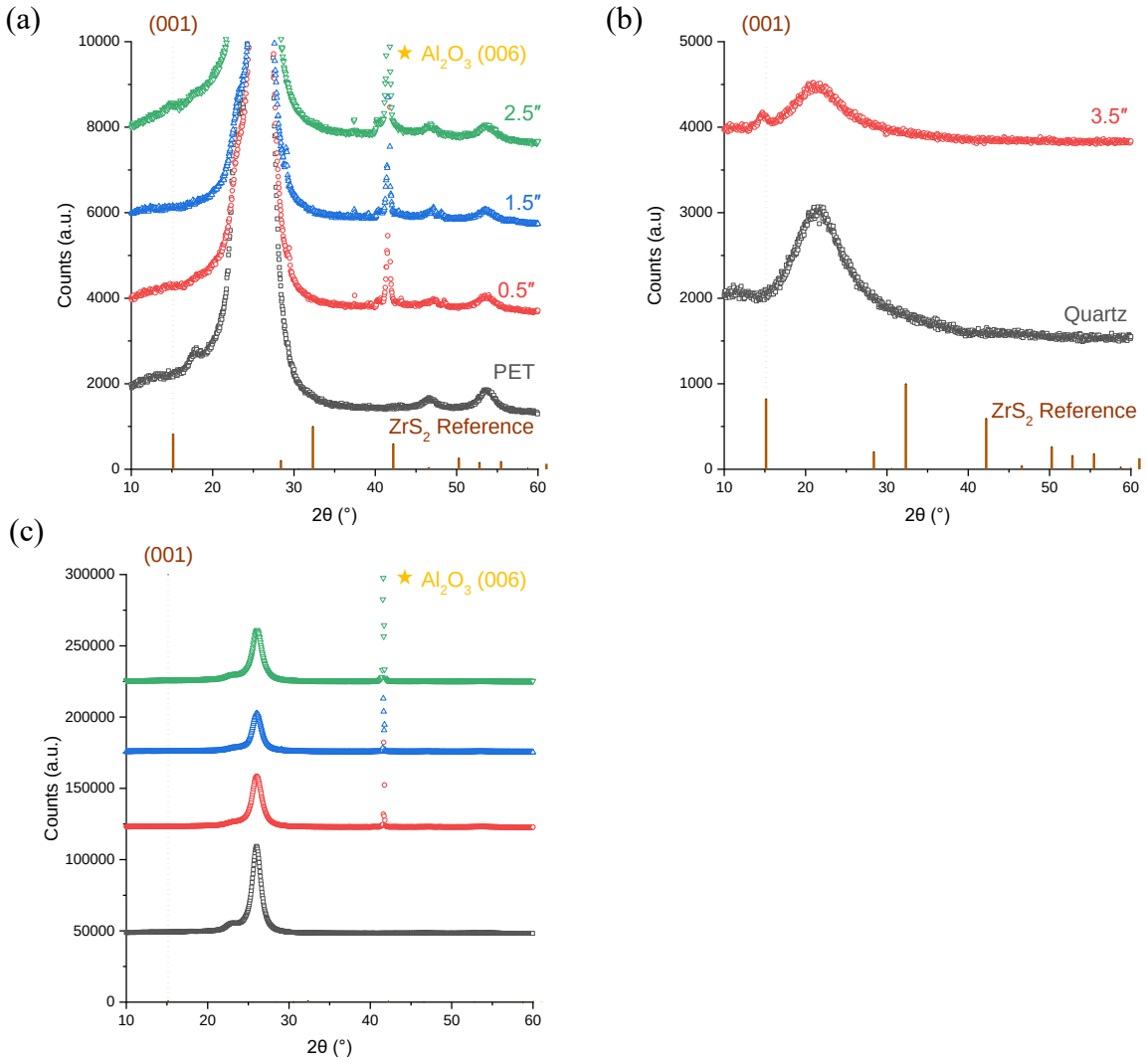

Figure 3.11. Diffractograms of ZrS_2 films deposited at 150 °C on PET substrates. Figure (a) shows diffractograms of the underlying PET substrate and films deposited 0.5″, 1.5″ and 2.5″ (c) from the precursor inlets. Figure (b) shows the diffractogram for a ZrS_2 film deposited 3.5″ from the precursor inlets in the same reaction, along with the underlying quartz substrate. Figure (c) is copy of figure (a) with the y-axis blown up to visualize the PET diffractions. The ZrS_2 reference is COD 5910006.

3.4.5. Composition and Purity

Stoichiometric ZrS_2 films with minimal impurity concentrations can be deposited on Kapton and PEEK substrates. The composition of ZrS_2 films on these substrates is compared to a single crystal in Figure 3.12 and Table 3.2 using EDS. While the zirconium content of single crystals and films is 38-39%, films on Kapton and PEEK are slightly sulfur deficient, with compositions of 56±1% and 58±1%, respectively. ZrS_2 single crystals have a sulfur composition of 60.7±0.5%. Sulfur deficiencies in films likely arises from increased oxygen content compared to single crystals; single crystals only have 1.0±0.1% oxygen and samples on Kapton and PEEK substrates have 6±1% and 2.5±0.8% oxygen, respectively. Analysis of film compositions by XPS also demonstrates relatively low oxygen incorporation, with samples deposited on Kapton and PEEK having oxygen contents of 3.8% and 4.2%, respectively, on the last depth profile (Figure 3.13, Table 3.3). No other impurities are detected in these films at the end of XPS depth profiles, with carbon and nitrogen content below the 1% limit of detection of our instrument. Like films deposited on quartz substrates, this suggests recipe 6 also affords minimal precursor incorporation at 200 °C during growth on Kapton and PEEK substrates (section **2.4.8**).

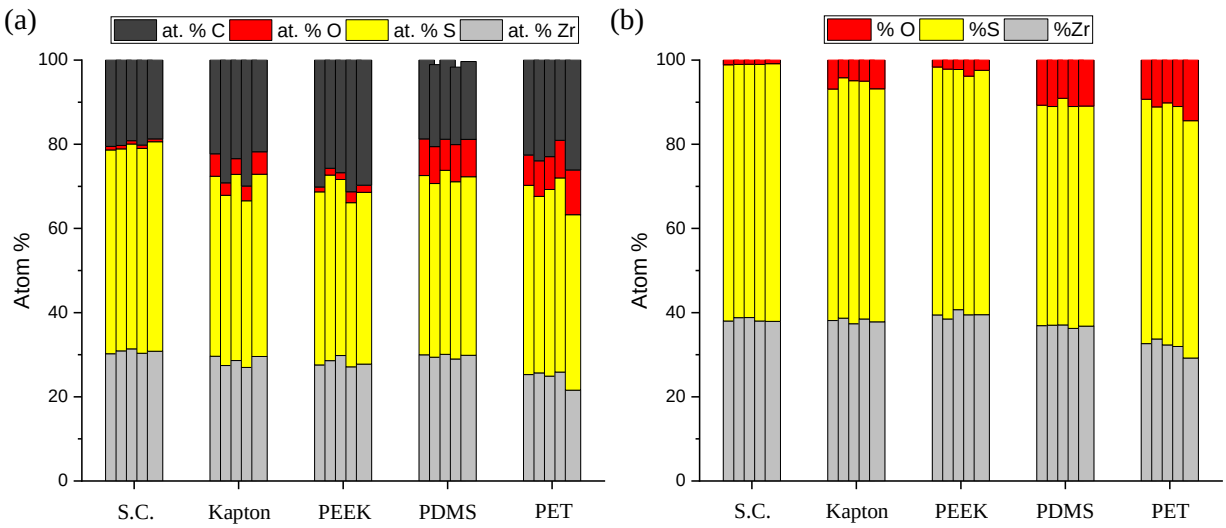

Figure 3.12. EDS of a ZrS_2 single crystal and films deposited at the front of the reaction zone (0.5″ from the precursor inlets) on Kapton, PEEK, PDMS and PET substrates. Figure (a) quantifies all elements and figure (b) removes carbon, which is overrepresented due to its high sensitivity factor.

Table 3.2. Average atom percent and S:Zr ratio determined by EDS on a ZrS_2 single crystal and films deposited on Kapton, PEEK, PDMS and PET substrates placed at the front of the reaction zone.

Substrate	% Zr	% S	% O	S:Zr
Single Crystal	38.3 ± 0.5	60.7 ± 0.5	1.0 ± 0.1	1.58 ± 0.3
Kapton	38.1 ± 0.3	56 ± 1	6 ± 1	1.48 ± 0.04
PEEK	39.5 ± 0.8	58 ± 1	2.5 ± 0.8	1.47 ± 0.05
PDMS	36.8 ± 0.3	52.6 ± 0.7	10.6 ± 0.8	1.43 ± 0.02
PET	32 ± 2	57 ± 1	11 ± 2	1.8 ± 0.1

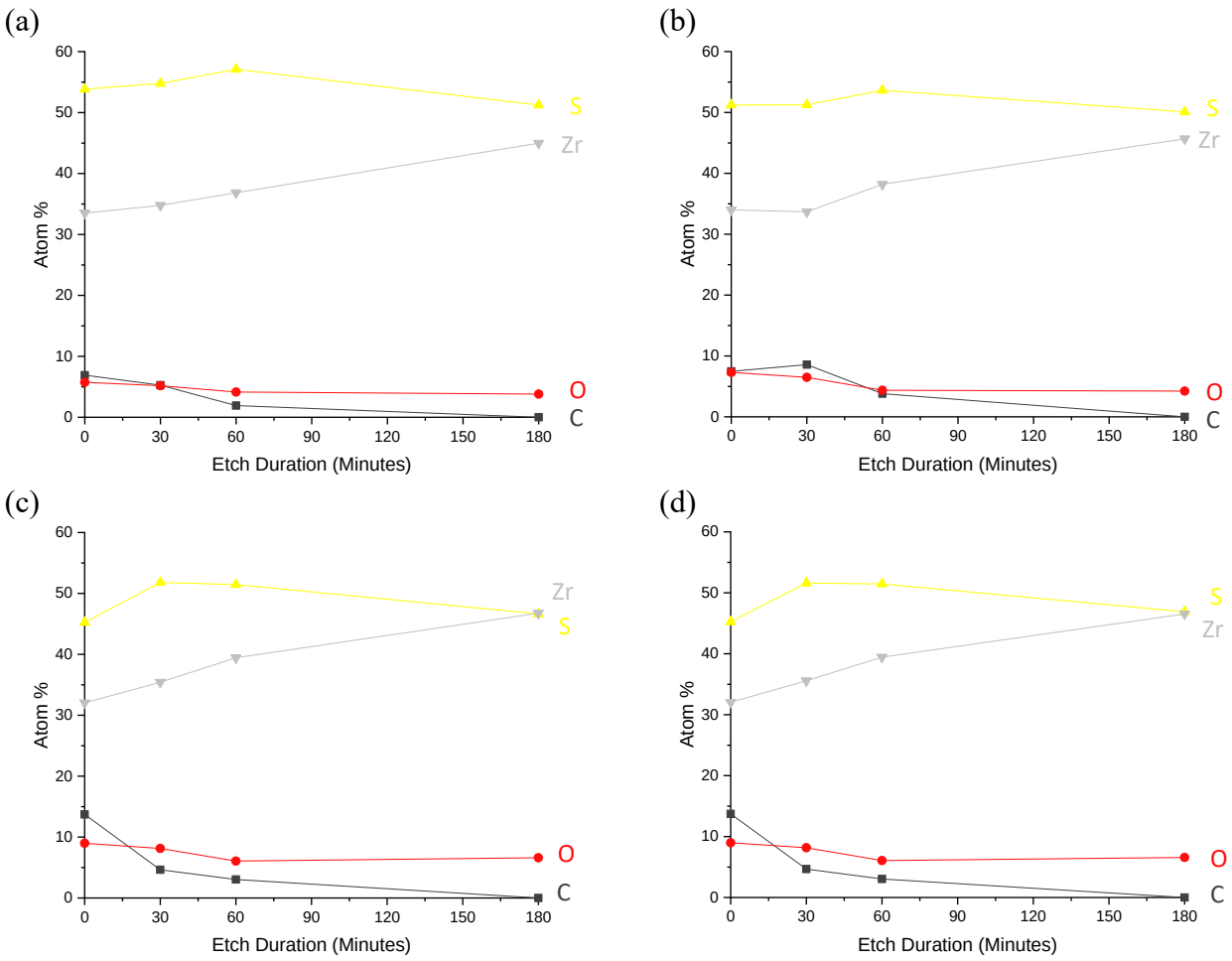

Figure 3.13. XPS depth profiles of ZrS_2 films deposited on (a) Kapton, (b) PEEK and (c) 80 µm thick PDMS substrates at 200 °C, and on PET (d) at 150 °C.

Table 3.3. Composition of ZrS_2 films determined by XPS on the last depth profile after sputtering for a total of 180 minutes.

Substrate	% Zr	% S	% O	% C	% N
Kapton	45.0	51.2	3.8	0.0	0.0
PEEK	45.7	50.1	4.2	0.0	0.0
PDMS	46.6	51.5	6.1	0.0	0.0
PET	46.5	46.9	6.6	0.0	0.0

Deposition of ZrS_2 films on 80 μm thick PDMS substrates affords oxygenated films, but with no detectable impurities arising from ligand incorporation. The composition of these films is compared to a single crystal in Figure 3.12 and Table 3.2 using EDS. While the zirconium and sulfur composition of a single crystal are 38.3±0.5 and 60.7±0.5%, respectively, on the frontmost film in the PDMS deposition these values are 36.8±0.3 and 52.6±0.7% (Figure 3.12 and Table 3.2). This sulfur deficiency arises from ca. 10% oxygen incorporation in the bulk of the film. Prior to this deposition, the rate of rise in the reactor was confirmed to be 0.5 mTorr/min, so it is unusual (at least for depositions on all quartz substrates) for the oxygen content in the bulk of the film to be >5%. Analysis of film composition by XPS also reveals elevated oxygen incorporation, with 6.1% detected on the last depth profile, which is ca. 50% higher than oxygen content in ZrS_2 films deposited on Kapton and PEEK substrates (Figure 3.13 and Table 3.3). Since there is also no detectable carbon or nitrogen on the final XPS depth profile of the ZrS_2 film on PDMS, oxygen associated with surface contamination does not account for the discrepancy in composition with films deposited on Kapton and PEEK. The source of excess oxygen in ZrS_2 films deposited on PDMS is not known at this time, but still may be related to outgassing from the polymer substrate or possibly due to lower air stability compared to films deposited on Kapton and PEEK substrates.

ZrS_2 films deposited on PET substrates also appear to suffer from high oxygen incorporation, and XPS depth profiling again shows limited impurity concentrations associated with ligand incorporation. By EDS, the composition of the frontmost film from this deposition is 32±2% Zr, 57±1% S, and 11±2% O (Figure 3.12, Table 3.2.) Since the ZrS_2 film analyzed on PET is ca. 500 nm, the origin of oxygen counts in EDS spectra cannot be confidently assigned to only the film. While quantifying carbon in our EDS spectra is usually not performed due to the high sensitivity factor of this element (in single crystals we observe ca. 20% C by EDS, but in XPS this element is below the limit of detection), in depositions on polymers carbon is useful for determining whether oxygen counts originate from the underlying substrate or within the ZrS_2 film. In the case of the frontmost sample on PET, the carbon composition is comparable to the baseline found for ZrS_2 single crystals (Figure 3.12) and does not offer a clear indication of whether high oxygen counts are from the underlying substrate. For comparison, see films deposited on PET substrates 1.5″ and 2.5″ from the reactor (Figure 3.14), where a clear increase in carbon and oxygen does suggest probing of the substrate. Depth profiles of ZrS_2 films on PET show 6.5% oxygen incorporation, which is ca. 50% higher than on Kapton and PEEK (Figure 3.13, Table 3.3). Like on quartz substrates in chapter 2, carbon and nitrogen impurities are below the 1% limit of detection of our instrument, suggesting minimal precursor ligand incorporation during film growth. However, this suggests that the additional oxygen seen by XPS is likely associated with oxygen incorporation in the ZrS_2 film. This may be due to increased outgassing of the polymer during deposition (water and oxygen can oxidize ZrS_2 to ZrO_2 during growth or possibly react with the Zr precursor to deposit ZrO_2) or due to a combination of lower stability in air and a slightly longer transfer time into the UHV chamber before XPS analysis.

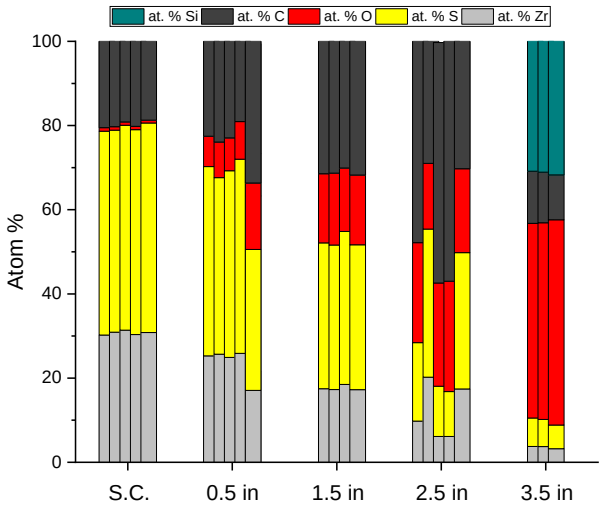

Figure 3.14. A bar graph comparing the composition of a ZrS_2 single crystal to films deposited at 150 °C on PET 0.5-2.5″ from the precursor inlets and a quartz substrate 3.5″ from the precursor inlets.

3.4.6. Electrical Properties

ZrS_2 films deposited at the front of the reaction zone on PEEK substrates have sheet resistances and resistivities typical for 200 °C reactions, but measurements are imprecise due to noise in voltage measurements. Although current readings were on the order of 10-100 nA and could be measured with relatively little noise on these samples, it was found that voltage measurements fluctuated in and out of the noise range of the voltmeter installed onto the four-point probe. The voltage readings were cross checked with a handheld voltmeter, which confirmed the issue was sample related and not due to failure of the installed voltmeter. To estimate sample sheet resistance, a phone camera was therefore used to record the simultaneous current and voltage measurements across samples, and then replayed to extract the data, giving a sheet resistance of $(5.4\pm3.9)\times10^6$ Ω/□. This falls with the range of sheet resistances of (4-8) × 10^6 Ω/□ measured on ZrS_2 films deposited on quartz substrates in the same location and under the same conditions.

Using these data and microscopy shown in Figure 3.4, the resistivity of ZrS_2 films on PEEK is estimated to be 865±619 Ω·cm. Although measurement error is rather large, these resistivities are comparable to ca. 950 Ω·cm resistivities measured on ZrS_2 films deposited on quartz substrates in the same location and under the same conditions (Figure 2.3.2). Current readings on four-point probe measurements were below the noise level of the ammeter on PEEK samples placed 1.5-2.5″ from the precursor inlets. The sheet resistance of the witness sample deposited on quartz was $(6.5\pm0.5)\times10^6$ Ω/□, but film thickness could not be measured by microscopy, so a precise resistivity value cannot be provided. Since the film is thinner than the frontmost sample on PEEK, the resistivity is likely several times lower than measured at the front of the reactor (Figures 2.19 and 2.32).

The resistivity of ZrS_2 films cannot be confidently estimated on Kapton substrates, and all samples deposited on or in the presence of PDMS and PET do not have measurable sheet resistances or resistivities. Like for samples deposited on PEEK substrates, ZrS_2 films deposited on Kapton have stable current readings on the order of 10-100 nA in four-point probe measurements, but voltage measurements suffer from worse noise levels. Indeed, using the same data extraction method as for samples on PEEK produces a current-voltage plot with an unacceptably low R^2 values (Figure 3.15), and the standard deviation of the sheet resistance calculated from these measurements is larger than the average value. The same is true of the sample 1.5″ from the precursor inlets, while current could not be measured on the sample 2.5″ from the precursor inlets. The sheet resistance of the quartz witness sample is $(5.4\pm1.5)\times10^6$ Ω/□, which is comparable to the witness sample from the deposition on PEEK. Current above the noise level of the ammeter could not be measured on any samples deposited on thick PDMS, thin PDMS and PET. The quartz witness samples from these depositions did not have measurable current,

suggesting the presence of PDMS and PET introduced species inhibiting conductivity downstream in the reactor. It is possible that current below the noise level in ZrS_2 samples on PET substrates is due to these samples not being thick enough, as the bubbler fill level was lower than for previous depositions at 200 °C (and the bubbler had to be refilled after the next two depositions).

(a)

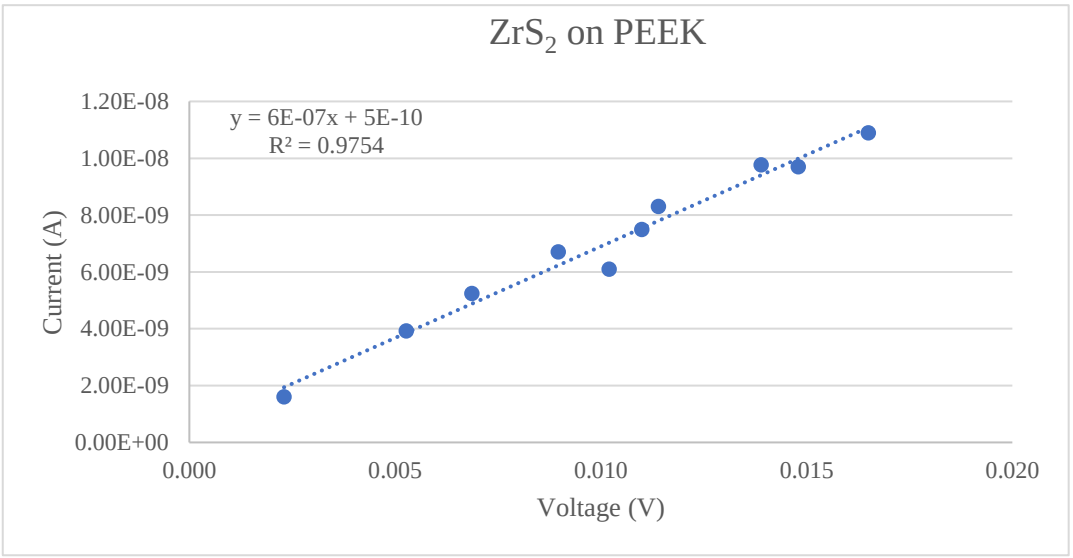

(b)

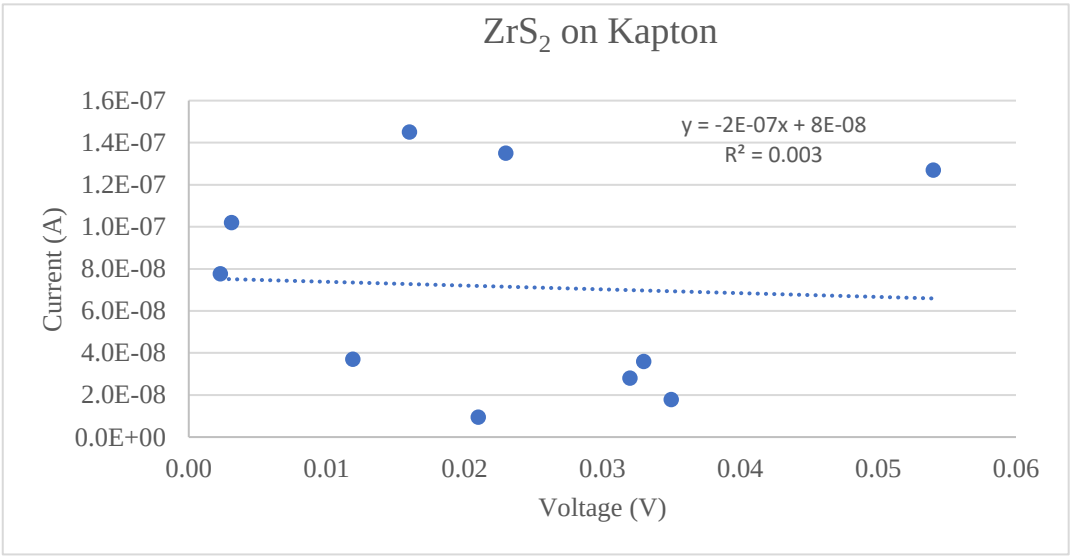

Figure 3.15. Current-voltage plots of four-point probe data collected on the frontmost sample deposited at 200 °C on (a) PEEK and (b) Kapton.

3.5. Conclusions

We have demonstrated direct deposition of ZrS_2 films onto several polymer substrates using low temperature CVD with $Zr(NMe_2)_4$ and H_2S as precursors. High quality, crystalline and continuous ZrS_2 films with good adhesion can be deposited on Kapton and PEEK substrates at 200 °C. These films contain minimal impurities and have comparable compositions to the stoichiometric material. Deposition of crystalline films is also possible on PMDS at 200 °C but film uniformity decreases with increasing distance from the precursor inlets. ZrS_2 films are not well adhered to PDMS substrates, which could allow for transfer to other surfaces. Film growth on PET substrates at 150 °C produces continuous and well adhered films with varying morphologies down the reaction zone. The films are amorphous and partially oxidized. Lowering growth temperatures and durations may afford deposition onto more thermally sensitive substrates.

3.6. References

1. Gao, W.; Ota, H.; Kiriya, D.; Takei, K.; Javey, A., Flexible Electronics toward Wearable Sensing. *Accounts of Chemical Research* **2019,** *52* (3), 523-533.

2. Baran, D.; Corzo, D.; Blazquez, G. T., Flexible Electronics: Status, Challenges and Opportunities. *Frontiers in Electronics* **2020,** *Volume 1 - 2020*.

3. Han, S.-T.; Peng, H.; Sun, Q.; Venkatesh, S.; Chung, K.-S.; Lau, S. C.; Zhou, Y.; Roy, V. A. L., An Overview of the Development of Flexible Sensors. *Advanced Materials* **2017,** *29* (33), 1700375.

4. Kim, S.; Quy, H. V.; Bark, C. W., Photovoltaic technologies for flexible solar cells: beyond silicon. *Materials Today Energy* **2021,** *19*, 100583.

5. Ramanujam, J.; Bishop, D. M.; Todorov, T. K.; Gunawan, O.; Rath, J.; Nekovei, R.; Artegiani, E.; Romeo, A., Flexible CIGS, CdTe and a-Si:H based thin film solar cells: A review. *Progress in Materials Science* **2020,** *110*, 100619.

6. Gao, L.; Chen, L.; Huang, S.; Chen, N.; Yang, G., Flexible and Highly Durable Perovskite Solar Cells with a Sandwiched Device Structure. *ACS Applied Materials & Interfaces* **2019,** *11* (19), 17475-17481.

7. Watson, S.; Bian, D.; Sahraei, N.; Winter, A. G.; Buonassisi, T.; Peters, I. M., Advantages of operation flexibility and load sizing for PV-powered system design. *Solar Energy* **2018,** *162*, 132-139.

8. Ostfeld, A. E.; Arias, A. C., Flexible photovoltaic power systems: integration opportunities, challenges and advances. *Flexible and Printed Electronics* **2017,** *2* (1), 013001.

9. Kim, S.; Holz, M.; Park, S.; Yoon, Y.; Cho, E.; Yi, J., Future Options for Lightweight Photovoltaic Modules in Electrical Passenger Cars. *Sustainability* **2021,** *13* (5), 2532.

10. Subudhi, P.; Punetha, D., Progress, challenges, and perspectives on polymer substrates for emerging flexible solar cells: A holistic panoramic review. *Progress in Photovoltaics: Research and Applications* **2023,** *31* (8), 753-789.

11. Katiyar, A. K.; Hoang, A. T.; Xu, D.; Hong, J.; Kim, B. J.; Ji, S.; Ahn, J.-H., 2D Materials in Flexible Electronics: Recent Advances and Future Prospectives. *Chemical Reviews* **2024,** *124* (2), 318-419.

12. Dong, T.; Simões, J.; Yang, Z., Flexible Photodetector Based on 2D Materials: Processing, Architectures, and Applications. *Advanced Materials Interfaces* **2020,** *7* (4), 1901657.

13. Nassiri Nazif, K.; Daus, A.; Hong, J.; Lee, N.; Vaziri, S.; Kumar, A.; Nitta, F.; Chen, M. E.; Kananian, S.; Islam, R.; Kim, K.-H.; Park, J.-H.; Poon, A. S. Y.; Brongersma, M. L.; Pop, E.; Saraswat, K. C., High-specific-power flexible transition metal dichalcogenide solar cells. *Nature Communications* **2021,** *12* (1), 7034.

14. Hoang, A. T.; Hu, L.; Kim, B. J.; Van, T. T. N.; Park, K. D.; Jeong, Y.; Lee, K.; Ji, S.; Hong, J.; Katiyar, A. K.; Shong, B.; Kim, K.; Im, S.; Chung, W. J.; Ahn, J.-H., Low-temperature growth of MoS_2 on polymer and thin glass substrates for flexible electronics. *Nature Nanotechnology* **2023,** *18* (12), 1439-1447.

15. McConney, M. E.; Glavin, N. R.; Juhl, A. T.; Check, M. H.; Durstock, M. F.; Voevodin, A. A.; Shelton, T. E.; Bultman, J. E.; Hu, J.; Jespersen, M. L.; Gupta, M. K.; Naguy, R. D.; Colborn, J. G.; Haque, A.; Hagerty, P. T.; Stevenson, R. E.; Muratore, C., Direct synthesis of ultra-thin large area transition metal dichalcogenides and their heterostructures on stretchable polymer surfaces. *Journal of Materials Research* **2016,** *31* (7), 967-974.

16. Ahn, C.; Lee, J.; Kim, H.-U.; Bark, H.; Jeon, M.; Ryu, G. H.; Lee, Z.; Yeom, G. Y.; Kim, K.; Jung, J.; Kim, Y.; Lee, C.; Kim, T., Low-Temperature Synthesis of Large-Scale

Molybdenum Disulfide Thin Films Directly on a Plastic Substrate Using Plasma-Enhanced Chemical Vapor Deposition. *Advanced Materials* **2015,** *27* (35), 5223-5229.

17. Mun, J.; Park, H.; Park, J.; Joung, D.; Lee, S.-K.; Leem, J.; Myoung, J.-M.; Park, J.; Jeong, S.-H.; Chegal, W.; Nam, S.; Kang, S.-W., High-Mobility MoS_2 Directly Grown on Polymer Substrate with Kinetics-Controlled Metal–Organic Chemical Vapor Deposition. *ACS Applied Electronic Materials* **2019,** *1* (4), 608-616.

18. Chavez, D.; Berube, A. D.; Davis, L. M., Zirconium disulfide single crystal, ZrS_2(0001), characterized by X-ray photoelectron spectroscopy. *Surface Science Spectra* **2025,** *32*, 014004.

19. Cole, P. Chemical Resistance Database. https://www.coleparmer.com/Chemical-Resistance (accessed May 2, 2025).

20. Castillo, L. D.; Moussessian, A.; McPherson, R.; Tan, Z.; Zhenwei, H.; Dean, R.; Johnson, R. W. In *Flexible electronic assemblies for space applications*, 2010 IEEE Aerospace Conference, 6-13 March 2010; 2010; pp 1-6.

21. Gouzman, I.; Grossman, E.; Verker, R.; Atar, N.; Bolker, A.; Eliaz, N., Advances in Polyimide-Based Materials for Space Applications. *Advanced Materials* **2019,** *31* (18), 1807738.

22. Melzer, M.; Mönch, J. I.; Makarov, D.; Zabila, Y.; Cañón Bermúdez, G. S.; Karnaushenko, D.; Baunack, S.; Bahr, F.; Yan, C.; Kaltenbrunner, M.; Schmidt, O. G., Wearable Magnetic Field Sensors for Flexible Electronics. *Advanced Materials* **2015,** *27* (7), 1274-1280.

23. Husain, Q. Z.; Corsino, D.; Catania, F.; Ishida, K.; Meister, T.; Ellinger, F.; Münzenrieder, N.; Cantarella, G., DC and AC Performance of InGaZnO Thin-Film Transistors on Flexible PEEK Substrate. *IEEE Transactions on Electron Devices* **2024,** *71* (10), 6073-6078.

24. Wang, Y.; Hu, Y., Optimization of flexibility and phase transformation characteristics of Al/Sb multilayer films on PEEK substrates. *Materials Science in Semiconductor Processing* **2025,** *188*, 109206.

25. Dahiya, R.; Gottardi, G.; Laidani, N., PDMS residues-free micro/macrostructures on flexible substrates. *Microelectronic Engineering* **2015,** *136*, 57-62.

26. Silicone (PDMS) Chemical Compatibility. https://tym.co.uk/pages/silicone-pdms-chemical-compatibility (accessed May 2, 2025).

27. Chemical Resistance Chart. http://m.topsflo.com/d/files/9_chemical-resistance.pdf (accessed May 2, 2025).

28. Li, L.; Han, L.; Hu, H.; Zhang, R., A review on polymers and their composites for flexible electronics. *Materials Advances* **2023,** *4* (3), 726-746.

Chapter 4. Thermal Evaporation and Annealing of Germanium(II) Sulfide Thin Films

4.1. Contributions

The work presented below is derived in part from a manuscript in progress. Preliminary experiments depositing (by thermal evaporation and solution deposition) and characterizing GeS films were performed by Professor Luke M. Davis, Dr. Lauren Hartle, Susan Schmidt, and Fengfan Zhu. Later, I deposited GeS films, and annealed GeS films in H_2S (under the supervision of Professor Luke M. Davis) and Ar atmospheres. Caroline Ding, Ben Kass-Mullet and David Palomares also deposited GeS films by thermal evaporation and annealed under Ar atmospheres. I performed the majority of microscopy on GeS films, although significant contributions were also provided by Ben Kass-Mullet, David Palomares, and several others. Although results are not shown here, Daniela Chavez did extensive work characterizing the composition and band positions of GeS single crystals and films using XPS, UPS and Kelvin probe. RBS experiments and simulations were performed by Dr. Hussein Hijazi at Rutgers University. Professor Luke M. Davis wrote some of the introductory text and project framing in this chapter and prepared several figures. This project is funded by Tufts University and the National Science Foundation (DMR-2224949).

4.2. Abstract

Deployment of cadmium telluride tandem photovoltaics could be expedited if top cells are deposited using the same capital and type of fabrication equipment for close space sublimation. Germanium(II) sulfide (GeS) is an attractive top cell candidate composed of Earth-abundant and non-toxic elements, and can be evaporated congruently at low temperatures of 300-400 °C.

However, there are few reports describing growth of continuous and crystalline GeS films suitable as photo-absorbers due to high crystallization temperatures. We identify re-evaporation of GeS and slow kinetics of crystallite nucleation as barriers to obtaining crystalline GeS by annealing amorphous precursor films. Several methods are demonstrated to increase the surface roughness or surface area of amorphous precursor films, which are shown to enhance the kinetics of nucleation and enable fabrication of continuous and crystalline GeS films. Annealing in H_2S is also explored as a method for enhancing nucleation kinetics, but results in oxidation of films before or during crystallization. The resistivity of films annealed in inert atmospheres is several orders higher than in some single crystals.

4.3. Introduction

Tandem photovoltaics based on cadmium telluride (CdTe) photo-absorbers may enable deployment of modules with increased power conversion efficiencies (PCEs). The addition of a wide bandgap top cell to current CdTe modules could afford PCE's beyond the Shockley-Queisser limit.[1] Such efficiencies have already been demonstrated by tandem photovoltaics based on similarly performing Si modules, with III-V on Si tandems achieving an impressive record PCE of 36.1%.[2] Although CdTe accounts for only 5% of photovoltaics modules deployed globally, this technology accounts for almost half of the United States production capacity.[3, 4] Development of new tandem modules based on existing CdTe technology would be transformative for domestic production of electricity.

If current manufacturing processes for CdTe are extended to top cells, it could enable rapid deployment of tandem modules. Existing industrial deposition methods for CdTe include close space sublimation (CSS) and chemical vapor transport (CVT, typically CSS enhanced by a carrier

gas), which use temperatures of 600-800 °C to achieve film growth rates as high as 10 μm/min.[5-7] To enable rapid deployment of CdTe tandem modules, we seek to identify and develop top cells evaporating similarly to CdTe. To reduce development costs, such absorbers should be deposited using the same fabrication equipment as for CdTe, which will require processing temperatures no greater than 600-800 °C. In searching for top-cell materials for CdTe modules, we focus on low toxicity, wide bandgaps, and high evaporability to enable facile deployment.

These requirements lead us to germanium(II) sulfide (GeS), a promising 2-D semiconductor containing earth abundant and non-toxic elements. GeS has closely spaced direct and indirect bandgaps in the 1.6-1.8 eV range, with an absorption coefficient $>10^4$ cm^{-1}.[8, 9] The carrier transport properties of GeS are also favorable, with reports of minority carrier mobilities of 86-90 $cm^2V^{-1}s^{-1}$,[10, 11] and photoexcited carrier lifetimes between 120-565 ps.[11-13] These properties have allowed for fabrication of photodetectors[11, 14-16] and recently for assembly of photovoltaics.[9, 14, 17, 18] The first reported GeS devices were reported in 2021, and maintain the record PCE of 1.36%.[9] Finally, GeS evaporates cleanly under vacuum at 300-400 °C as the molecular species,[19-21] and the vapor pressure has been reported as a function of temperature.[22] The evaporation behavior of GeS lends itself to convenient deposition by either CSS or CVT, and the former has been demonstrated recently.[9, 23] Amorphous GeS films were sublimed as early as the 1970's by Stanchev and Vodencharov.[24]

Despite the ease of evaporating GeS, there remain few modern reports of high quality, crystalline films.[9, 17, 18, 23, 25] Feng and coworkers first demonstrated polycrystalline GeS films by close space sublimation,[9] but a crystallization temperature of ≥375 °C and the high thermal expansion coefficient of GeS led to delamination of films. This issue was alleviated by using $MoSe_2$ as an interfacial layer between GeS and the Mo substrate. Zhang and coworkers reported a

low nucleation density of GeS crystallites during physical vapor transport depositions,[25] but found that the use of a pre-deposited amorphous GeS seed layer improved surface coverage. Attempts to deposit GeS films by chemical vapor deposition also afforded sparse crystallite coverage,[26] and although atomic layer deposition has demonstrated highly conformal and continuous GeS films,[27] the material was amorphous.

Annealing is promising strategy to crystallize as-deposited amorphous GeS layers but may be complicated by the high volatility of GeS. Hu and coworkers first reported annealing of amorphous GeS films deposited on FTO substrates by chemical bath deposition.[17] The GeS films were annealed under atmospheric pressure nitrogen for 5 minutes at 380 °C, and crystallized as highly oriented orthorhombic GeS, with only the 200 and 400 reflections present in diffractograms. SEM images showed continuous films with highly oriented, plate like grains. The only other report of annealing to obtain crystalline GeS films was by Drabavicius and coworkers, who deposited amorphous GeS films by thermal evaporation and annealed under Ar at a pressure of ca. 0.9 atmospheres for an unspecified amount of time. However, under these conditions films annealed at 370-390 °C were discontinuous and filled with voids, and films annealed at ≥400 °C partially or completely sublimed.[23] These results are perhaps unsurprising, considering that GeS and germanium(II) selenide (GeSe) have near identical vapor pressure curves at these temperatures,[19] and that films of the latter have been found to completely sublime after annealing at atmospheric pressure for only 30 minutes at 450 °C.[28] Accordingly, several reports of annealing GeSe films utilize durations of only 5 minutes,[17, 29, 30] and it is likely that annealing of GeS films may also require these short annealing durations to prevent complete film loss.[17]

Two-stage deposition is another method for obtaining crystalline GeS films. Zhang and coworkers initially attempted to grow crystalline GeS films by vapor transport deposition using an

Ar carrier gas at a pressure of 90 Pa and a substrate temperature of 380-420 °C, but found that these conditions resulted in sparse coverage of large crystallites.[25] However, when an amorphous seed layer of GeS was deposited first with a substrate temperature of 160 °C, subsequent growth using the original deposition conditions at 380-420 °C afforded nearly continuous films of crystalline GeS. It is noteworthy to demonstrate that during this procedure, the pre-deposited amorphous GeS layer is technically annealed under Ar and for 35-50 minutes, which is likely not possible without simultaneous growth of GeS due to re-sublimation of films. Besides this report and one other,[9] challenges and solutions for obtaining continuous, crystalline GeS films has not been addressed within the literature.

I hypothesized that annealing GeS films in H_2S atmospheres would enhance carrier transport properties relative to inert atmospheres. Such improvements have been demonstrated for the congener tin(II) sulfide (SnS). Typically, SnS films are treated with 2.5-4% H_2S at 400 °C,[31-33] although pure H_2S has also been utilized.[34] Annealing under both conditions facilitates substantial crystal grain growth,[31, 32, 34] and reduces recombination losses at boundaries.[31] H_2S is also believed to fill mid band gap sulfur vacancies in SnS that may act as recombination centers.[35] Compared to as deposited films, annealing SnS in 4% and 100 % H_2S at 400 °C increases the carrier concentration and decreases the resistivity several-fold, leading to increases of ca. 25% in short-circuit current density in photovoltaic devices.[31, 34] Indeed, some of the highest efficiency SnS photovoltaics are fabricated by using an H_2S annealing step.[31, 33]

In this work we identify nucleation, evaporation, and oxidation of GeS to GeS_2 as challenges to obtaining high quality crystalline GeS films when annealing under inert and H_2S containing atmospheres. We present seeding and surface roughening of films as methods for increasing defect site density and film nucleation kinetics when annealing under inert atmospheres,

and successfully balance the rates of nucleation, crystallization, and (re-)evaporation to provide good-quality films on a variety of substrates. Annealing experiments under H_2S atmospheres did not produce crystalline GeS films and resulted in partial oxidation to GeS_2 as the temperature and H_2S concentration increased. The resistivity of GeS films annealed in inert atmospheres is comparable to some reported values from single crystals, but several orders of magnitude higher than others.

4.4. Experimental

4.4.1. Deposition and Annealing of GeS Thin Films

Material: Germanium(II) sulfide, 99.99+% GeS (containing 1-5% elemental germanium) was purchased from Strem Chemical Co. (Newburyport, MA, USA). GeS powder was stored under 5-10 millitorr vacuum between depositions. Single crystals of GeS (>99.9995%, flux zone grown) were purchased from 2D Semiconductors USA (Scottsdale, AZ) and were analyzed by Rutherford Backscattering Spectrometry (RBS) and Energy Dispersive X-ray Spectroscopy (EDS).

Deposition apparatus: A 3.5-cm tall glass ring was placed inside a flat-bottomed, 50 mm inner diameter Schlenk drying chamber (Chemglass, AF-0556-02). GeS powder was placed within this ring and the substrate was placed face down on the ring. The chamber was evacuated to 5-10 mTorr and then heated with a hot plate, using an aluminum block (4″×3″×2″) placed on top to enhance uniformity of heating (Figure 4.1). To load the chamber, it was refilled with argon from a Schlenk line, and then the top removed. GeS was massed to 2.40-2.50 g, and then added carefully to the inside of the ring. The top of the ring was wiped free of debris with a Kimwipe. Substrates were cleaned as described below and placed upside down on top of the glass ring. The chamber

was then assembled, evacuated, and refilled with argon. The evacuate and refill cycle was repeated twice more, and then the chamber evacuated for deposition.

Figure 4.1. Photographs of deposition chamber set-up: (a) 50-mm Schlenk drying chamber on Al block on hot plate; (b) close-up of deposition chamber showing an inverted substrate supported by a 3.5-cm glass ring, with GeS powder loaded inside the glass ring; (c) Al foil wrapped around the block during a GeS film deposition—the GeS vapor can be seen as a brown gas.

Temperature calibration. At a hot plate set temperature of 460 °C, the temperature of the Al block, glass substrate, and chamber bottom were measured in air with a thermocouple as a function of time (Figure 4.2).

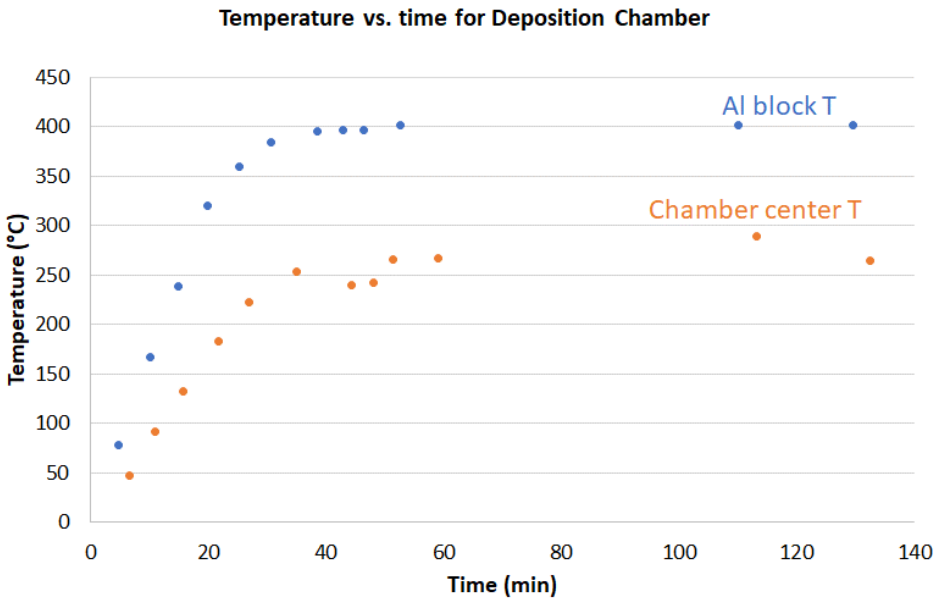

Figure 4.2. Temperature calibration for the deposition chamber with a hot plate set temperature of 460 °C. Blue dots represent the temperature of the Al block measured next to the bottom of the Schlenk drying chamber and orange dots represent the temperature of the center of the bottom of the Schlenk drying chamber (where GeS source powder is normally placed). Note that while depositions are performed under vacuum, the temperature calibration was performed at atmospheric pressure.

Sand-blasting substrates. Glass substrates were sand blasted using silica sand sprayed from a nozzle at 15 psi. The gun was kept 2-3″ from the substrate during the process and rastered across the surface at a rate of ca. 3 inches/second for 1–10 minutes to keep the surface roughness as even as possible.

Substrate cleaning: Samples were precleaned by scrubbing with Alconox detergent and rinsing with deionized water. Samples were then cleaned by rinsing with SEMI-grade acetone, SEMI-grade isopropanol, and blowing dry with compressed N_2**.** Finally, samples were exposed to UV/ozone (Ossila) immediately before deposition for 20 minutes. In instances where substrates were roughened using sand blasting, this cleaning procedure was performed afterwards.

4.4.2. H_2S Annealing

Annealing Chamber. As-deposited GeS samples were annealed at atmospheric pressure using mixtures of Ar and H_2S gas. Experiments were conducted in a fume hood inside of a 40-mm ID Schlenk drying chamber (Chemglass, AF-0556-01) with the same design as the deposition chamber used for GeS film deposition. However, to prevent damage to components from H_2S exposure, the drying chamber centering ring material was switched from Viton to a perfluoroelastomer (Chemglass Life Sciences, CG-309-226). The stopper valve was also replaced with a variant using perfluoroelastomer O-rings instead of Viton (Chemglass life sciences,CG-961-50). During annealing experiments, samples were placed on the bottom of the chamber, which was heated using the same hot plate and Al block set-up used for GeS depositions. Temperature calibrations for the chamber are shown in Figure 4.3 below.

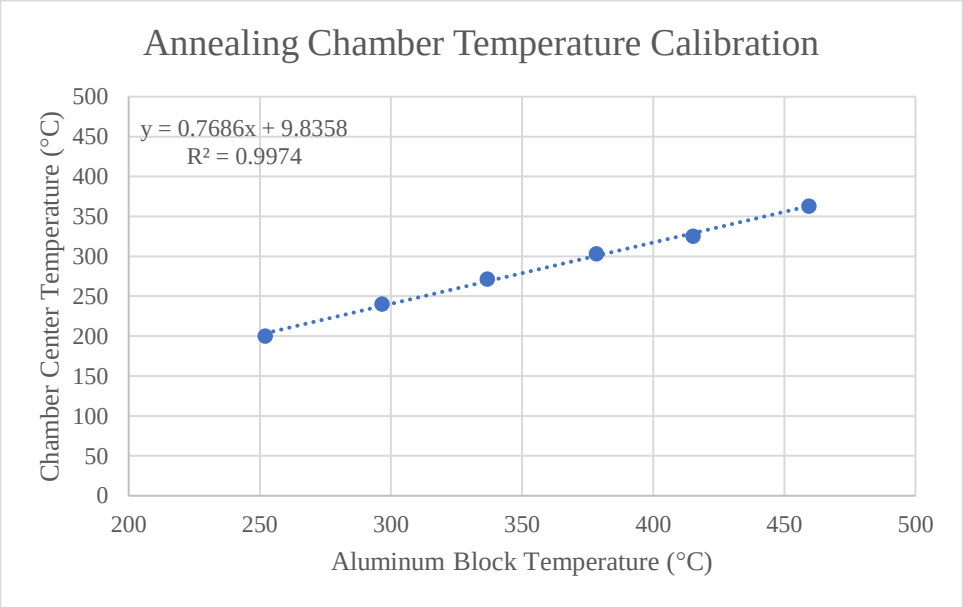

Figure 4.3. Temperature calibration of the annealing chamber set up. The temperature measured on the aluminum block is correlated to the temperature at the bottom center of the annealing chamber. The maximum temperature samples could reach was 355 °C.

Gas Delivery and Scrubbing System. To deliver mixtures of Ar and H_2S gas to the annealing chamber, a manifold was assembled using H_2S resistant components. A schematic of the manifold and annealing set up is shown if Figure 4.4. Ar gas is sourced from a gas cylinder outside of the fume hood and through a Schlenk line to a gas rotamer, while H_2S is supplied from a lecture bottle (Matheson, G1540275) inside of the fume hood to a separate gas rotamer. To prevent corrosion and leaks of H_2S, gas carrying lines are EPDM rubber, while tees and valves are glass, with the latter using perfluoroelastomer valves.[36] It is recommended that stainless-steel tees be used in place of glass, as it is difficult to fit stiff EPDM tubing over glass without risk of shattering the glass. Gas rotamers were constructed from glass, 316 stainless steel and use EPR seals (Matheson, E1EB401E200). A glass column chromatography tube (1.5″ OD, 18″ length) is used as the scrubber bed and filled with SULFURTRAP EX media (Chemical Product Industries, ST-EX-50-10). Ground glass joints on the scrubber bed were sealed using chemically resistant Krytox grease. The standard operating procedure for the H_2S annealing apparatus can be found in **Appendix 1**. It is advised that this setup only be operated in a highly ventilated area such as a fume hood.

.

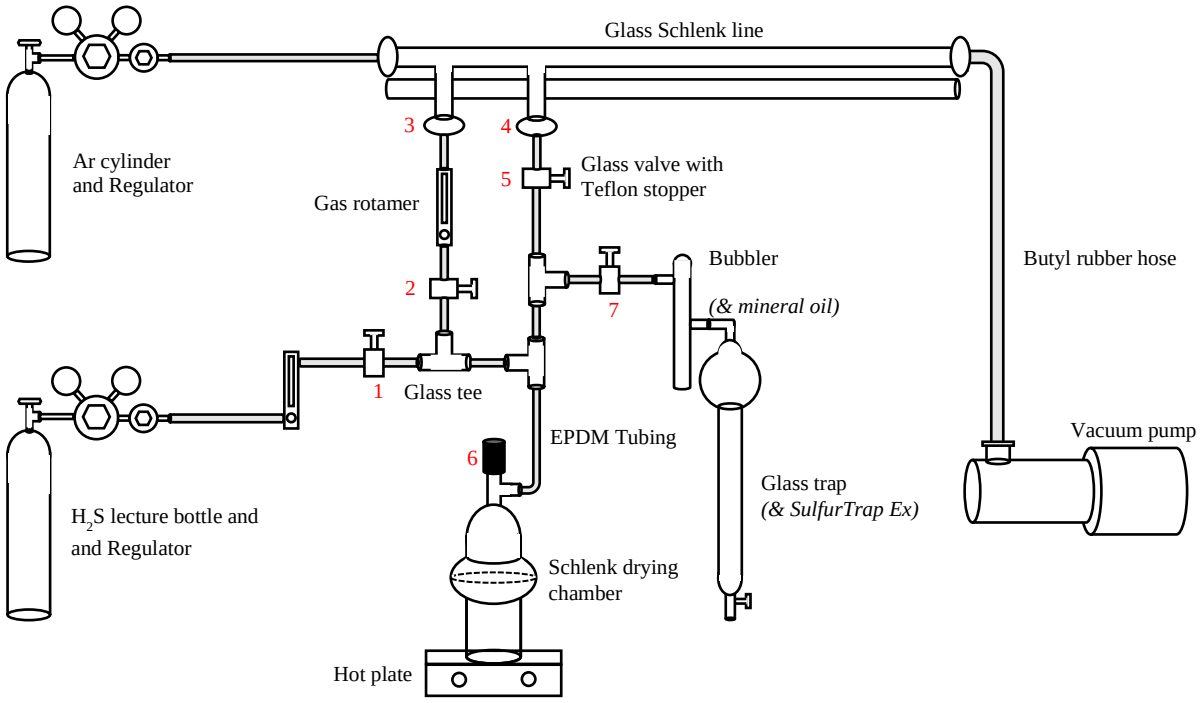

Figure 4.4. Schematic of the annealing chamber and gas manifold system used for H_2S annealing experiments. Valves mentioned in the standard operating procedure are numbered in red.

4.4.3. High Temperature Ar Annealing

Samples were annealed in a 1″ diameter and 39″ long quartz tube with heating provided by a Lindburg/Blue M mini-mite tube furnace. A schematic and photograph of the setup is provided in Figure 4.5. As-deposited GeS films were transferred from the deposition chamber and into the quartz tube outside of the heated zone of the tube furnace. When the tube furnace reached the set temperature of 375-425 °C, the quartz tube was slid horizontally to insert GeS films into the heated region. After GeS films were annealed for the set duration, typically 10 minutes, the quartz tube was slid horizontally to remove the samples from the heated zone and allow them to cool to room temperature. All annealing experiments were performed under atmospheric pressure using Argon

(Ar) gas supplied through a gas rotamer. The gas flow rate was initially set to 150 sccm for 2 hours to remove residual water and oxygen from the quartz tube and reduced to 10 sccm when GeS samples were inserted into the heated zone of the tube furnace. Note that while this work was performed in the open on a bench top, any annealing using H_2S should (1) be performed in a fume hood and (2) not utilize moving parts to prevent accidental cracking of the quartz tube.

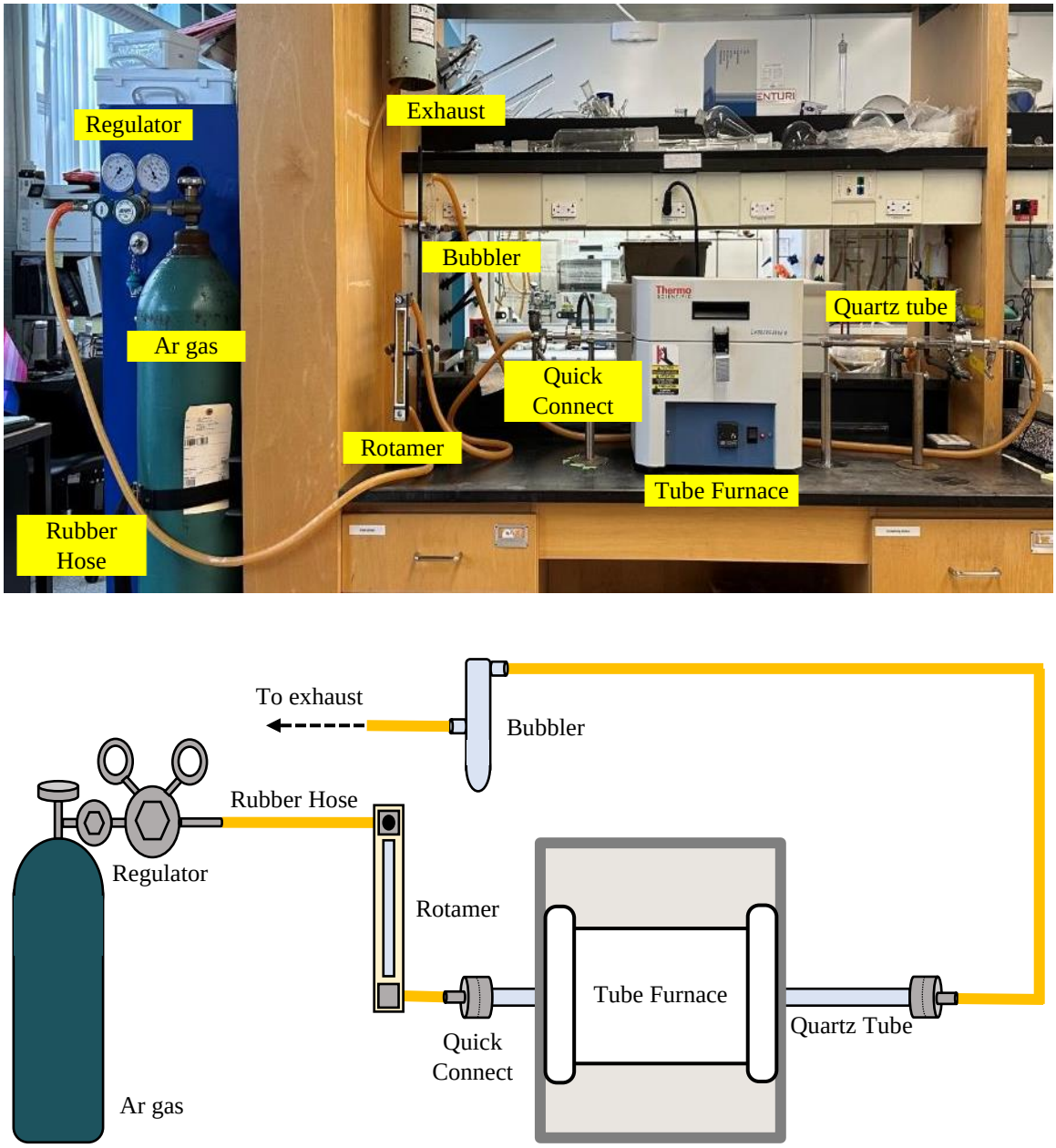

Figure 4.5. Schematic and photograph of annealing furnace.

4.4.4. Characterization of GeS Films and Single Crystals

Morphology of GeS films: The morphology of thin-film samples was examined by scanning electron microscopy (SEM) at Tufts University. An AMRAY 1845 FE-SEM, refurbished by SEMTech Solutions, was used for all microscopy.

Crystallinity of GeS films: Samples were analyzed by powder X-ray diffraction (pXRD) at the Harvard University. The routine θ-2θ scans were collected on a Bruker D2 Phaser with Bragg-Brentano geometry, and high-resolution XRD scans were collected on a Bruker D8 Discover using Göbel mirror/ACC2 geometry.

Composition of GeS crystals and films: Single crystals of were analyzed by Rutherford Backscattering Spectrometry (RBS) and Energy Dispersive X-ray Spectroscopy (EDS). RBS experiments and simulations were performed by Dr. Hussein Hijazi of the Rutgers University Laboratory for Surface Modification, Ion Scattering (RBS) Facility. A $^{4}He^{2+}$ ion beam energy of 2.0 MeV was used, with a spot size of 1 mm and an energy resolution of 18 keV. The detector was located 5 cm from the sample surface, on the same side as the beam but at an angle of 17° from the beam axis. EDS data were collected at Tufts using a Thermo Noran Series Six EDS with a Peltier-cooled silicon drift detector. The EDS detector is normal to the electron beam in our AMRAY 1845 FE-SEM, so the sample was tilted 20° towards the detector, at a working distance of 20-28 mm.

4.5. Results and Discussion

4.5.1. Deposition and characterization of amorphous GeS thin films

GeS thin films were deposited in a custom-built vacuum sublimation system described in the experimental section. The GeS source powder and substrate were heated to 253 ± 13 and 140 ± 2 °C, respectively, and the pressure was 5-10 mTorr. We grew GeS films on glass substrates for most annealing studies and for characterization of electrical and optical properties. Additional depositions were carried out briefly on zinc oxide (ZnO), gold (Au), indium tin oxide (ITO), c-plane sapphire (Al_2O_3), and quartz substrates. The as-deposited films were yellow to dark brown,

depending on thickness, and highly reflective. Films do not appear to degrade over months of storage in air, except during summer months with several consecutive days of high humidity.

The growth of GeS films becomes less reproducible with the number of depositions. Preliminary depositions of GeS were carried out on glass substrates to determine the growth rate of films. While the first few depositions suggest a linear growth rate of 60 nm/min (determined from scanning electron microscopy cross section images), growth becomes less controllable over time and typically increases with deposition duration. As shown in Figure 4.6, thickness for a set duration (70 minutes) tends to increase with the number of depositions, even with the mass of the GeS source powder refilled to the same value every few depositions. One hypothesis for increasing deposition rates is accumulation of GeS onto the glass ring sample holder, which resublimes during each new deposition. Alternatively, differences in substrate cleaning may impact the growth rate of films. Neither hypothesis was pursued further on glass substrates.

The growth rate of GeS films is highly dependent on the source temperature. As shown in Figure 4.6, Al block temperatures of 380 and 390 °C produce films of similar thicknesses for 80 minute depositions, but at 400 °C film thickness increases by 2-3×. Thus, fluctuations in temperature during longer depositions (>120 min) may account for deviation from expected thicknesses by several hundred nm. Despite our best efforts and depositing with Al block temperatures of ≤390 °C control of film thicknesses was typically limited to limited to 100's of nm on all substrates.

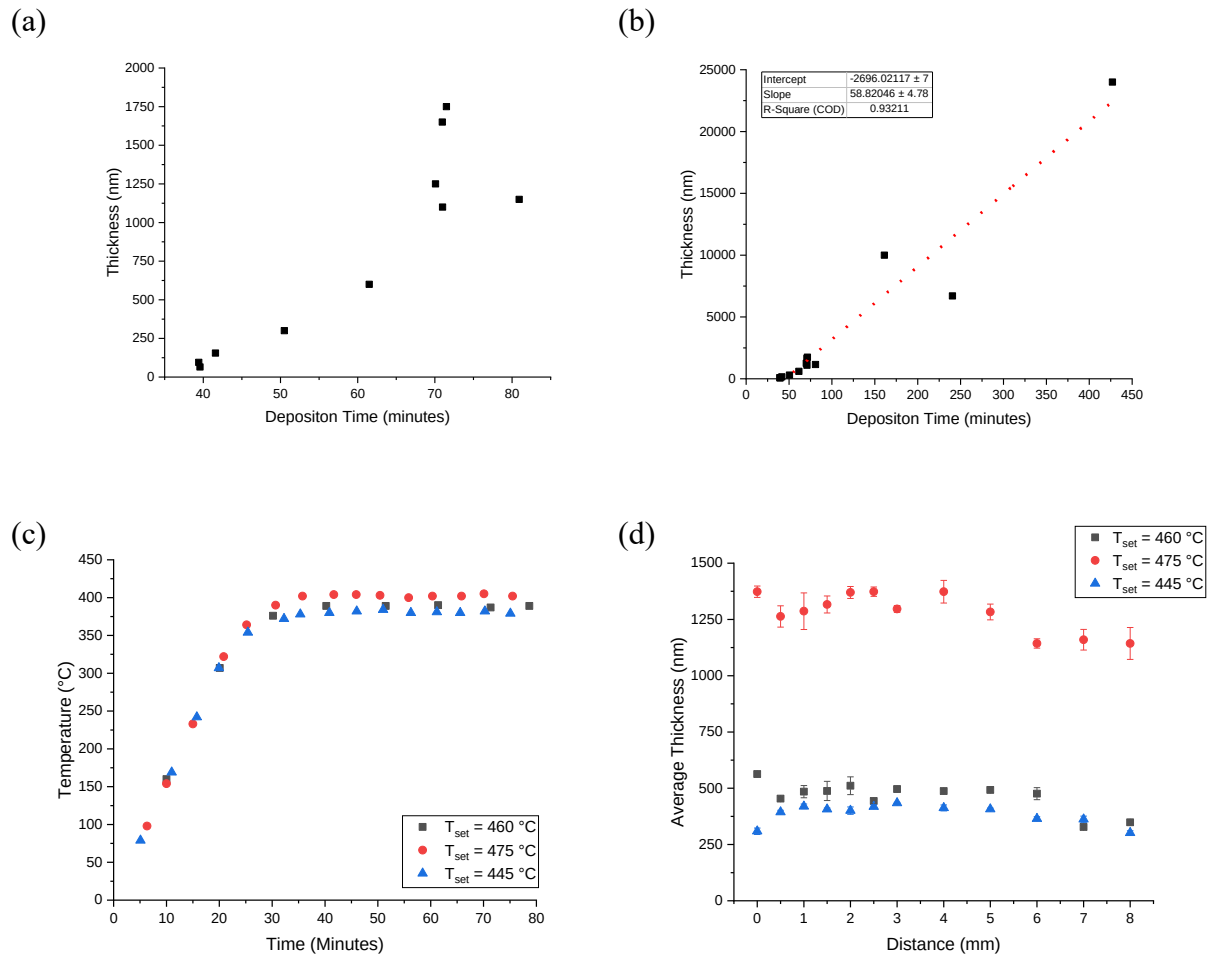

Figure 4.6. (a) Plot of film thickness (nm) vs. total deposition duration (minutes) for a series of GeS films. Close to linear growth is achieved at first, giving a growth rate of ca. 60 nm/min, but subsequent depositions for 70 minutes produced films with differences in thickness of >100 nm from the first film produced in the series. (b) A plot of film thickness (nm) vs. total deposition duration (minutes) that includes films deposited for over 150 minutes, with a trendline added to emphasize the variations (both over and under) the expected thickness based on growth rates observed in shorter depositions. (c) Plot of Al block temperature (°C) for 80 minute depositions with hot plate set temperatures of 445, 460 and 475 °C (blue, black and red dots, respectively). (d) Thickness profiles (distance measured from center of ring to the edge of deposition) of GeS films deposited in (c). The color scheme is the same as in figure (c).

Our as-deposited films contain stoichiometric GeS with minimal impurities. We first calibrated our energy-dispersive X-ray spectrometer (EDS) using Rutherford backscattering spectrometry (RBS) on a single crystal of GeS (Figure 4.7). Whereas RBS confirmed the single

crystal to be stoichiometric, EDS data for a crystal from the same batch suggests a Ge:S ratio of 1.25:1 (Table 4.1, Figure 4.7). This difference likely reflects matrix effects on the EDS sensitivity factors. Films deposited in our laboratory consistently have a Ge:S ratio of 1.2-1.3 on glass substrates and <1% oxygen incorporation (Table 4.1) The high carbon concentration in both single crystals and films is a result of the high sensitivity factor of this element. Analysis of GeS single crystals and films by Daniela Chavez shows carbon concentrations below 1%.

Table 4.1. Composition of GeS single crystal and film (on glass) measured by RBS and EDS

Method	At.% Ge	At.% S	At.% C	At.% O	Ge:S
RBS, sc	49.4	50.6	n.d.	n.d.	0.98:1
EDS, sc	46.4±0.2	37.1±0.4	16.5±0.9	n.d.	1.25:1
EDS, film	49.3±0.6	39.2±0.9	10.3±1.8	0.5±0.5	1.26:1

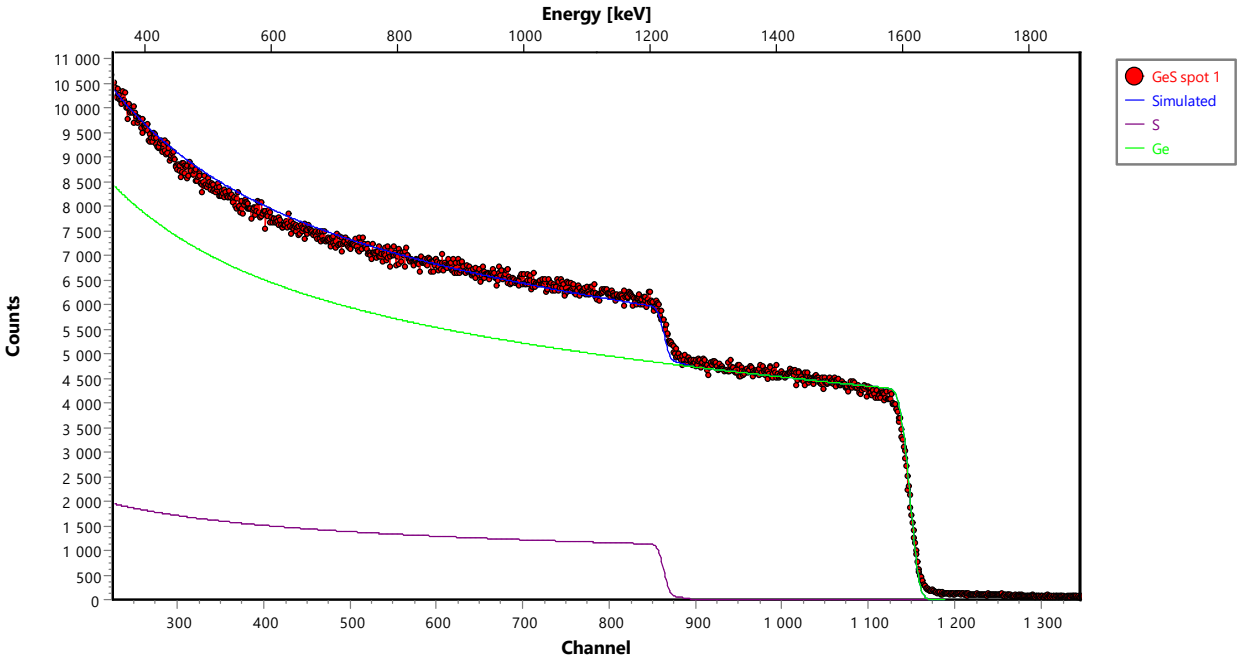

Figure 4.7. Composition of a GeS single crystal measured by Rutherford backscattering spectrometry. The single crystal of GeS was shipped overnight to Rutgers in a vial under argon, and RBS data were collected on two spots. RBS data and simulations for spot one is above. The composition measured at spot 1 was 49.4 at.% Ge, 50.6 at. % S; at spot 2, the composition was 48.7 at. % Ge, 51.3 at. % S. Simulations suggest that an oxygen surface layer thicker than ca. 5 nm would be observable as a peak around channel 500, and would shift the S shoulder (near channel 850) towards lower channel number. Therefore, the single crystal (specified to be >99.9995% pure) is stoichiometric (within 2 at. %) and free from detectable contamination (i.e., impurities are <1 at. %).

Powder X-ray diffraction (pXRD) and scanning electron microscopy (SEM) indicate that as-deposited GeS films are amorphous with smooth grains on the order of 10 nm. Figure 4.8 shows representative diffractograms and micrographs of as-deposited GeS films on glass, ITO and quartz substrates. These data demonstrate no substantial differences in crystallinity or morphology with substrate selection and corroborate reports of high crystallization temperatures required for thermal evaporation and annealing of GeS flims.[9, 17, 18, 25]

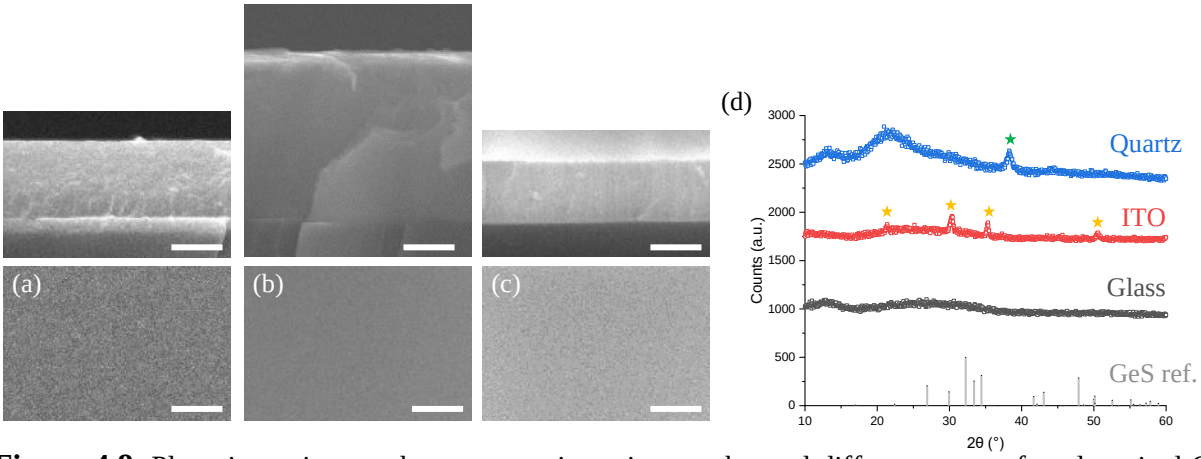

Figure 4.8. Plan view micrographs, cross section micrographs, and diffractograms of as-deposited GeS films on ITO, glass and quartz substrates. Figure (a) is a plan view (bottom) and cross section (top) image of GeS on ITO. Figures (b) and (c) are the same for GeS on glass and quartz, respectively. The scale bar in figures (a), (b) and (c) is 500 nm; at this magnification grains of the amorphous GeS films cannot be distinguished. Figure (d) shows diffractograms of the films as left; yellow stars indicate peaks from the ITO substrate and the green star on the quartz substrate is the 111 peak of Au sputtered onto the film. The GeS reference pattern (abbreviated as GeS ref.) is COD 1540751.

4.5.2. H_2S Annealing of GeS Films

Considerations for H_2S Annealing. GeS annealing experiments must be performed at atmospheric pressure to prevent re-sublimation of films. During preliminary studies at pressures of 5-10 mTorr, complete loss of GeS films was observed within 20-30 minutes of heating while attempting to reach annealing temperatures of >300 °C. This is consistent with deposition studies, where growth rates of ca. 60 nm/min are observed at only ca. 250 °C under the same pressure. Crystallization of GeS films was not observed by p-XRD at lower temperatures, so to access higher temperatures the rate of GeS sublimation must be reduced by increasing the pressure. Sublimation of GeS at these temperatures and pressures is not surprising given our deposition source temperature of ca. 250 °C and reports on the high volatility of the material.[19, 37]

Thermodynamic calculations suggest that dilute atmospheres of H_2S are necessary to prevent oxidation of GeS films during annealing. While annealing of GeS in H_2S could have similar benefits to those observed for SnS, there is a risk that GeS reacts with H_2S to form GeS_2.

Therefore, the thermodynamics of this reaction were investigated using FactWeb and FactSageEdu, which are free online versions of FactSage,[38] a thermodynamics database and calculations program. As shown in Figure 4.9, the Gibbs free energy (ΔG) is negative between 50-400 °C; the reaction of GeS and H_2S is spontaneous over the accessible range of temperatures in the annealing chamber. As the temperature is increased, the reaction becomes less favorable, with ΔG trending to less negative values and the equilibrium constant (K_{eq}) decreasing several orders of magnitude. Equilibrium between GeS and H_2S was also explored by using FactSageEdu to generate a temperature vs. partial pressure of H_2S phase diagram for GeS. The total pressure of the system is set to 1 atmosphere to reflect conditions in the annealing chamber setup. As shown in Figure 4.10, increasing the partial pressure of H_2S leads to oxidation of GeS to GeS_2 between ca. 0-800 °C. Color-coded isotherms at annealing temperatures of interest are added to the phase diagram to estimate the maximum partial pressure of H_2S over GeS before formation of GeS_2. This phase diagram suggests that when annealing a GeS film in H_2S at 200 °C, the partial pressure of H_2S should be kept below 10^{-4} atmospheres, or 76 millitorr, to prevent formation of GeS_2. At 400 °C the maximum partial pressure increases to 10^{-2} atmospheres, or 7.6 Torr.

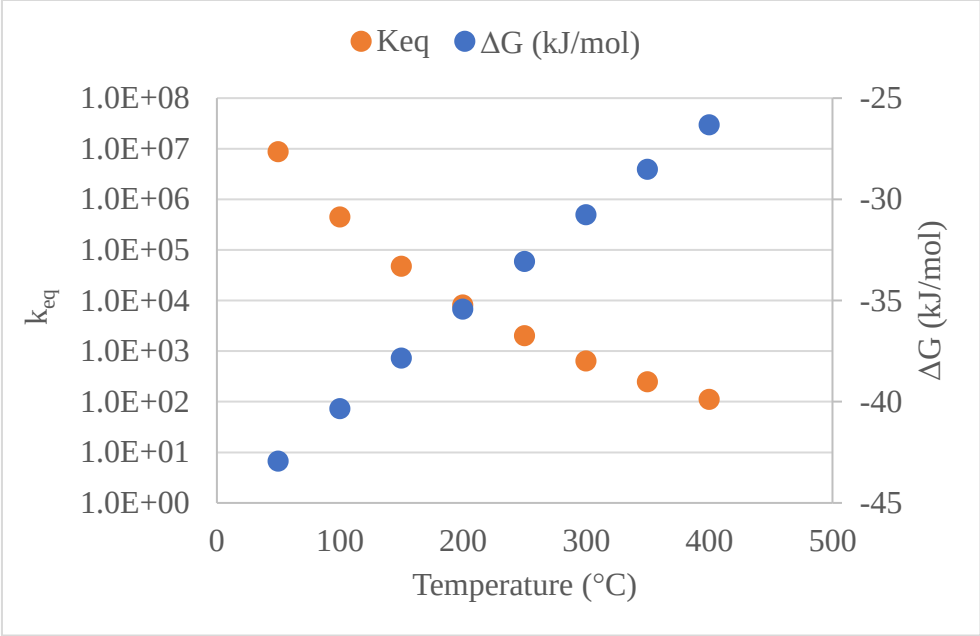

Figure 4.9. Thermodynamic calculations for the reaction GeS + H_2S → GeS_2 + H_2. Blue dots represent the value of ΔG and are referenced to the y-axis at right. Orange dots represent the value of k_{eq} and are referenced to the y-axis at right.

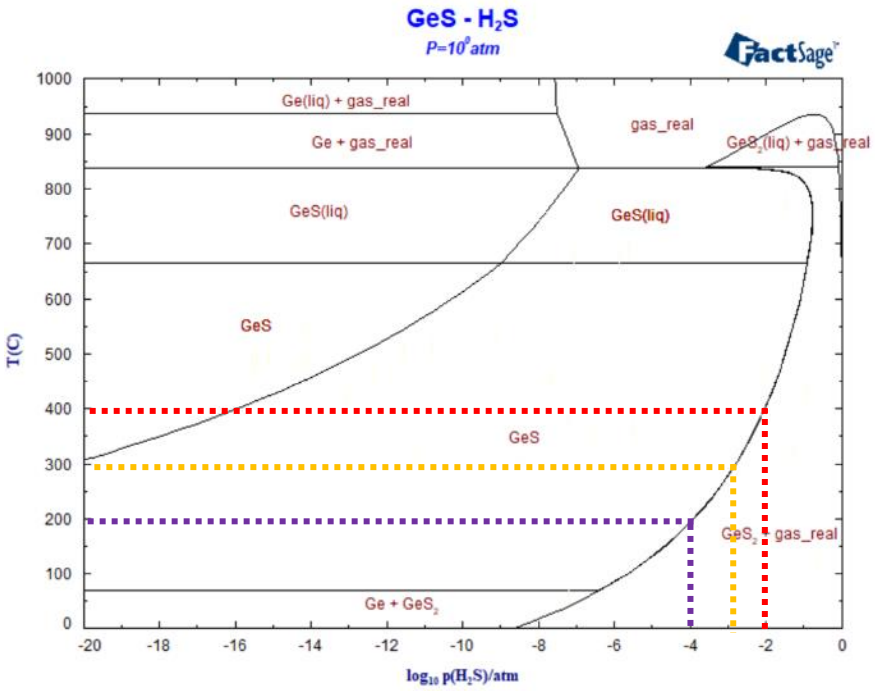

Figure 4.10. A temperature (T) vs. partial pressure of H_2S (P_{H2S}) phase diagram of GeS generated using FactSage. The maximum partial pressure of H_2S over GeS before formation of GeS_2 is approximated by adding isotherms at 200 (purple lines), 300 (orange lines) and 400 °C (red) lines to the plot and extrapolating to the x-axis values.

Annealing in Dilute H_2S Mixtures. Annealing GeS in dilute mixtures of H_2S and Ar at 355 °C does not result in significant changes to film morphology nor composition. For these experiments, films were annealed for 30 minutes at temperature in 0, 2.5, and 50% H_2S mixtures. Analysis by SEM shows that post-annealed films have smooth surfaces with roughly spherical grains ca. 50 nm in diameter. These morphologies are mostly indistinguishable from as-deposited films. The exception is found in anneals using 50% H_2S (Figure 4.11), where sparse regions of film appear elevated from the rest of the surface and contain platelets several microns across. These features are hypothesized to be crystalline GeS, as the Ge:S ratio by EDS is 1.2-1.3 and matches that of unannealed films. The Ge:S ratio on remainder of this sample, and samples annealed in 0 and 2.5% H_2S are also 1.2-1.3 (Table 1), and suggest little to no conversion of GeS to GeS_2 occurs under these conditions.

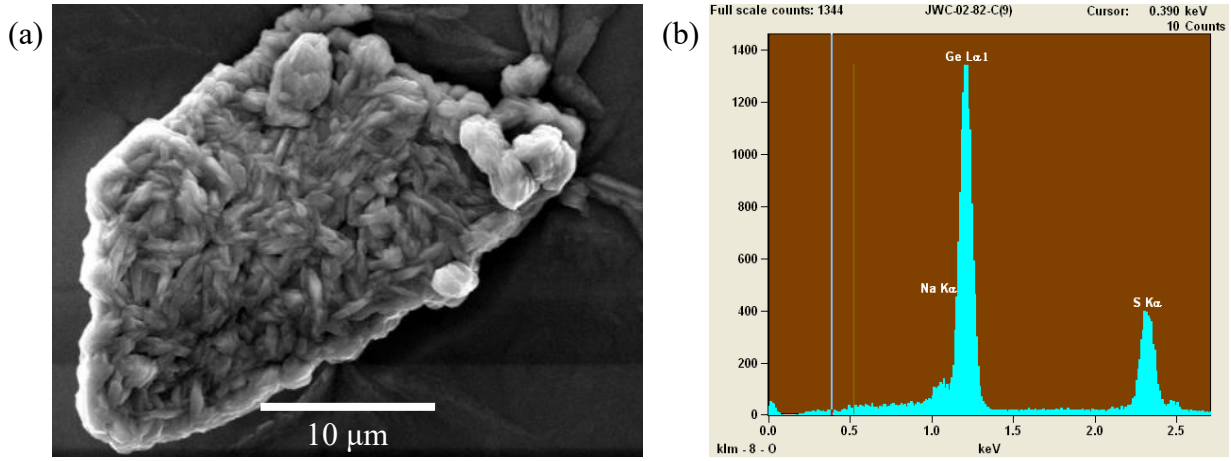

Figure 4.11. Microscopy and EDS of a GeS film annealed at 355 °C for ca. 30 minutes in 50% H_2S. Figure (a) is micrograph believed of a feature believe to be crystalline GeS. Figure (b) is an EDS spectrum of this features and has a Ge:S ratio of 1.3 with no detectable oxygen.

Annealing in 100% H_2S. Careful selection of annealing temperatures and duration is required to suppress oxidation of GeS to GeS_2 when using 100% H_2S. When the concentration of H_2S is increased from 50% to 100% for a 30 minute anneal at 355 °C, the Ge:S ratio does not

change for films with thicknesses of ca. 1000 nm. However, when film thickness decreases to < 600 nm or annealing duration increases to >70 min, the Ge:S ratio is found to decrease to as low as 0.6 (Table 4.2). If the annealing temperature is decreased to 320 or 275 °C, the Ge:S ratio does not decrease on anneals of ca. 30 minutes. But, when annealing for ca. 2 hours at 320 °C partial oxidation is observed as a gradient of compositions across the film; the Ge:S ratio decreases with decreasing film thickness (Figure 4.12). Overall, these results suggest kinetics, rather than thermodynamics, dominate the rate of oxidation of GeS in our H_2S annealing set up.

Table 4.2. Compilation of conditions used for GeS annealing experiments under H_2S atmospheres. The thicknesses, Ge:S ratio, and locations of any features appearing crystalline are provided. Note that the annealing duration specifies the time at the set temperature and does not include heat up and cool down times.

Sample Name	% H_2S	Film Thickness (nm)	Annealing Temperature °C	Annealing Duration (min)	Ge:S By EDS	Location of Crystallites
JWC-2-82-B	0	---	355	30	1.3	None
JWC-2-82-C	2.5	---	355	30	1.3	None
JWC-2-82-D	50	---	355	30	1.2	Sparse signs of nucleation
JWC-2-87-B	100	---	320	30	1.2–1.3	Ring mark, film corner
JWC-2-91-B	100	1000-1100	320	28	1.2–1.3	Ring mark
JWC-2-90-C	100	---	355	73	0.6	Entire film
JWC-2-91-C	100	600-750	355	28	0.6–1.1	Ring mark, film corner
JWC-2-107-A	100	600-1200	355	35	0.6–1.3	Ring mark, film corner
JWC-2-107-B	100	1100-1300	320	70	0.6–1.3	None
JWC-2-107-C	100	900-1300	320	115	0.8–1.3	Ring mark
JWC-2-127-B	100	200-350	355	26	0.6	Entire film

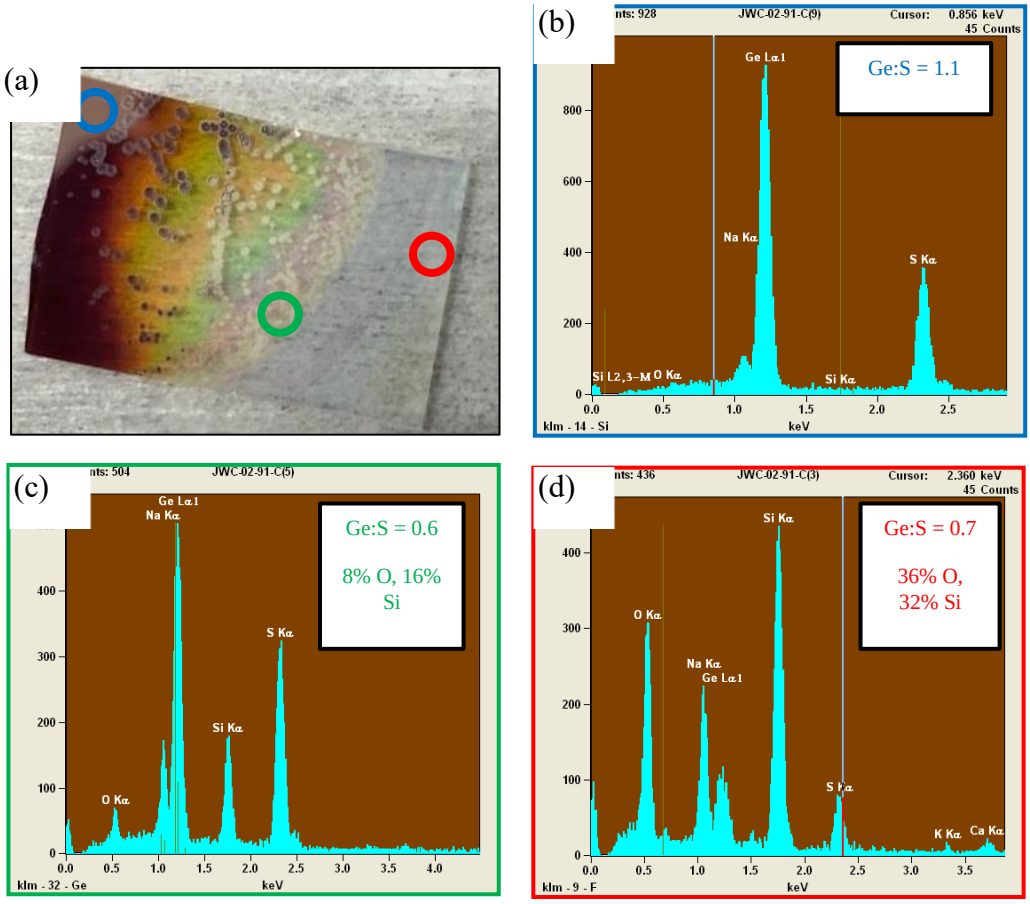

Figure 4.12. EDS of a 600-750 nm thick GeS film annealed for 28 minutes at 350 °C under 100% H_2S. Figure (a) is a photograph of the sample, with locations used for EDS circled in different colors. Figures (b), (c) and (d) are EDS spectra taken in the light blue, green and red regions, respectively. Across the sample the Ge:S ratio decreases from 1.3 to 0.6.

Localized changes to film morphology appear when annealing in 100% H_2S, but limited p-XRD data is available to confirm if these features are crystalline GeS. At all temperatures surveyed when annealing in 100% H_2S, changes in morphology are observed on or directly next to the ring mark left by the sample holder during deposition. In this region, thin elongated platelets with dimensions on the order of 10 microns are visible (Figure 4.13). EDS in these regions is complicated by high oxygen counts and silicon counts from the underlying substrate, but preliminary data show Ge:S ratios of <0.8. When the annealing temperature is increased to 355

°C, sand dollar shaped features can be seen on the sample surface by eye on samples annealed for <30 minutes (Figure 4.14). These features are similar in size and density to those seen on GeS films annealed at ≥375 °C under Ar atmospheres, where crystalline films are obtained (Figure 4.14). However, instead of the large platelets regularly found on these islands in high temperature Ar annealing, microscopy reveals the sand dollar features on H_2S annealed films are pits with no visible features (i.e., crystallites). It is hypothesized that annealing in 100% H_2S at 355 °C initially enables crystallization of GeS, but these crystallites are then partially oxidized, as suggested by Ge:S ratios of 0.6-0.8 in in these regions (and a change in color from brown to white or colorless). To determine if any of the features observed by SEM are crystalline GeS, films annealed for 25-30 minutes at 275, 320 and 355 °C were analyzed by p-XRD. As shown in Figure 4.15, films annealed at 275 and 320 °C remain amorphous, while films annealed at 355 °C have a moderate intensity diffraction at 2θ of 15.5°. This peak does not match known diffractions known for GeS or GeS_2, and an identity could not be assessed from one weak diffraction.

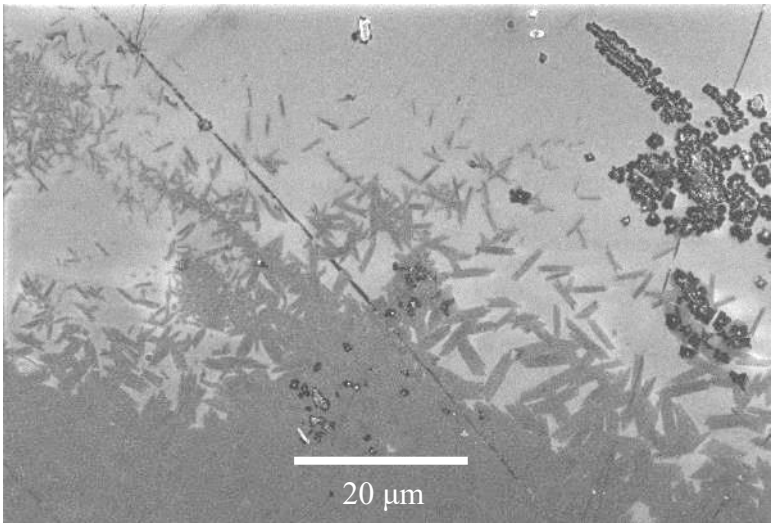

Figure 4.13. Representative micrograph of platelets observed near the ring mark of GeS films annealed under 100% H_2S.

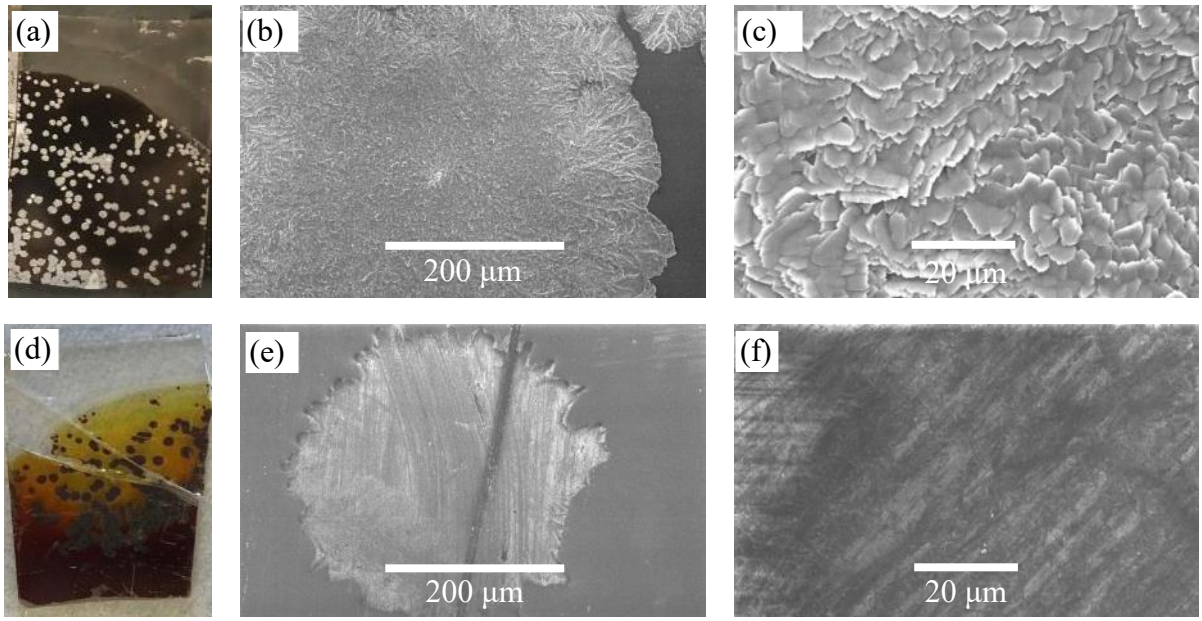

Figure 4.14. Comparison of sand dollar features on GeS films annealed at 400 °C under Ar and 355 °C under 100% H_2S. Figures (a) and (d) are photographs of GeS films annealed at 400 °C for 10 minutes under Ar and 30 minutes at 355 °C under 100% H_2S, respectively. Figures (b) and (c) are micrographs showing the presence of platelets in sand dollar shaped features seen in figure (a). Figures (e) and (f) are micrographs showing the absence of platelets in sand dollar shaped features seen in figure (b).

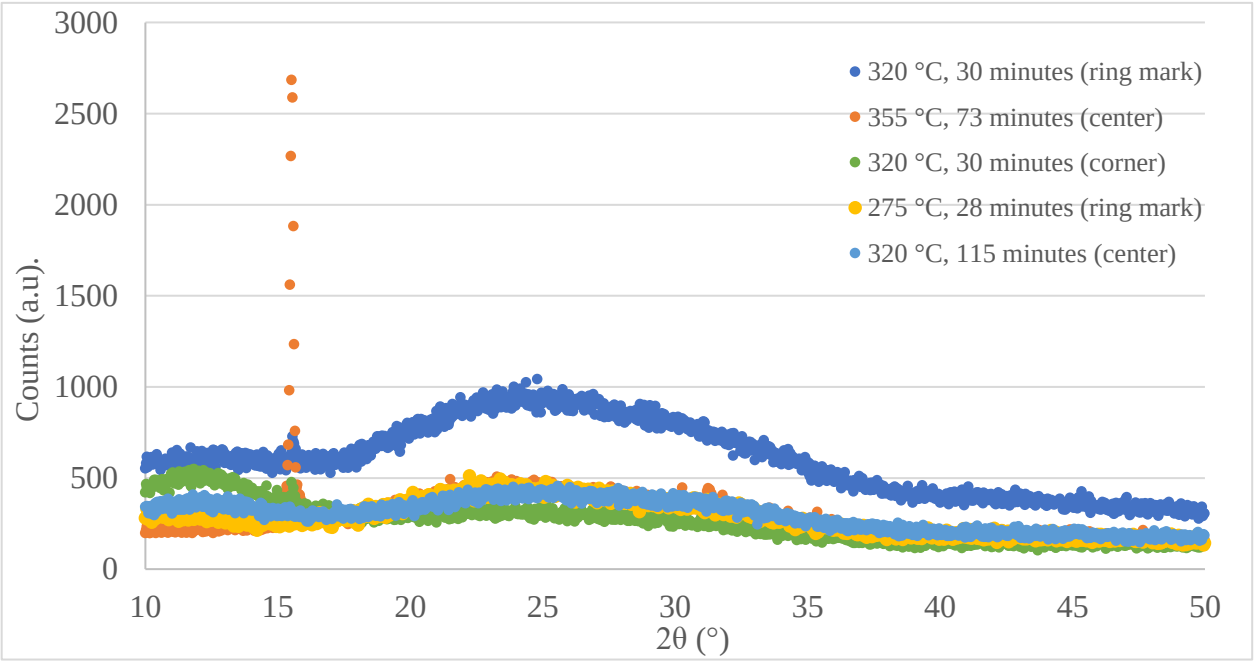

Figure 4.15. Diffractograms of GeS films annealed under 100% H_2S at 275, 320 and 355 °C. Locations of each measurement are specified in the legend.

Annealing of GeS under H_2S atmospheres did not yield crystalline films, but significant parameter space exists to expand these studies. Initially, annealing was attempted under Ar and either 2 or 50% H_2S at 355 °C, but this did not lead to widespread changes to film morphology or crystallinity. When the concentration of H_2S was increased to 100%, changes to morphology were observed, however these were likely associated with formation of GeS_2. It was found that under 100% H_2S the extent of oxidation increased with both annealing temperature and duration. As shown in figure 4.16, few annealing experiments were carried out for durations for more than 30 minutes or with dilute H_2S mixtures. Based on the appearance of (presumably) GeS crystallites at 355 °C when annealing for 30 minutes in 50% H_2S (Figure 4.11a), and that longer growth/annealing times enables more complete coverage of GeS films obtained by two stage vapor transport depositon,[25] annealing for longer periods under dilute H_2S mixtures may lead to full crystallization of GeS films. These experiments could be performed in the apparatus described in **4.4.2** or the CVD reactor used to deposit ZrS_2 (see section **2.3.1**), although there remains the risk of GeS films re-subliming. Also shown in Figure 4.16 are conditions screened at higher temperatures in the following section. It is predicted that annealing for >30 minutes at these temperatures (>400 °C) will result in significant or complete loss of films.

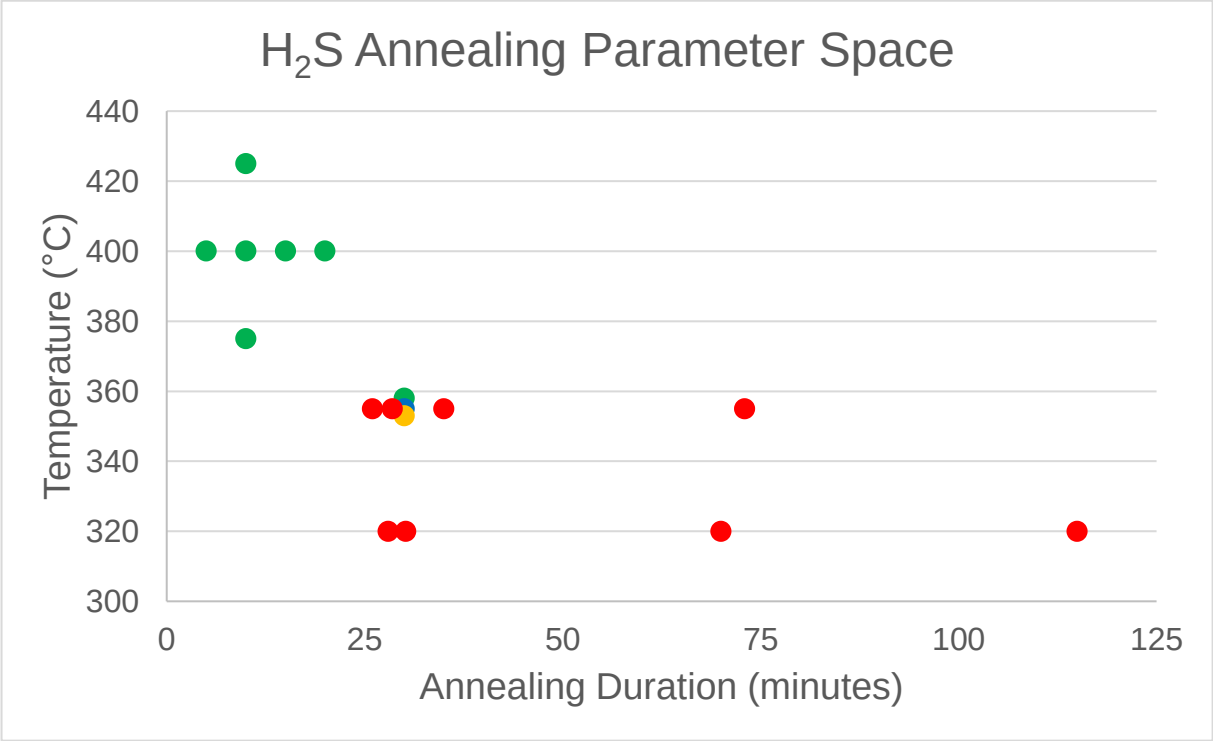

Figure 4.16. Plot of the deposition parameter space accessed by GeS annealing experiments. Green dots represent 100% Ar atmospheres (including conditions screened in the following section), the blue dot represents a 2.5% H_2S atmosphere, the yellow dot represents a 50% H_2S atmosphere and red dots represent 100% H_2S atmospheres.

4.5.3. High Temperature Ar Annealing

Preliminary annealing studies of GeS films. To prevent oxidation and resublimation of GeS at elevated temperatures required for crystallization,[9] we chose to anneal films under atmospheric pressure using a quartz tube based annealing system described in Figure 4.5. Under the protective flow of argon gas, films were inserted into the heated zone of a tube furnace for 10 minutes at temperatures of 375-425 °C. We adopted this procedure after finding that leaving films in the heated zone of the furnace while heating to the set temperature or cooling to room temperature resulted in complete loss of films ≤1 um thick by re-sublimation of GeS. Similarly,

annealing under vacuum of 5-10 mTorr was not possible as films completely evaporated before reaching substrate temperatures of 300 °C.

Post annealed GeS films remain the stoichiometric material and are crystalline, but have heterogeneous morphologies. Analysis of film composition by EDS (Figure 4.17) confirms that the Ge:S ratio remains near 1.25 when GeS films are annealed on ITO; this is also true of films annealed on glass and metal (Pt, Au and Ni) substrates. Diffractograms reveals that the post-annealed films deposited on glass and ITO are highly oriented orthorhombic GeS, with major diffractions from the 200 and 400 planes, and additional diffractions attributed to orthorhombic GeS detectable on films ≥1 μm thick (Figure 4.18). Annealing to fabricate highly oriented orthorhombic GeS films and GeSe films has been reported previously,[17, 23, 28-30] and produced homogeneous morphologies. However, by visual inspection we find that our films have scattered silver islands on the order of 100-1000 μm in diameter. As demonstrated on ITO substrates in Figure 4.19, the size and density of these islands does not appear to be correlated to film thickness or annealing temperature, although islands tend to be larger and more disperse on glass substrates compared to ITO (Figures 4.18 and 4.19).

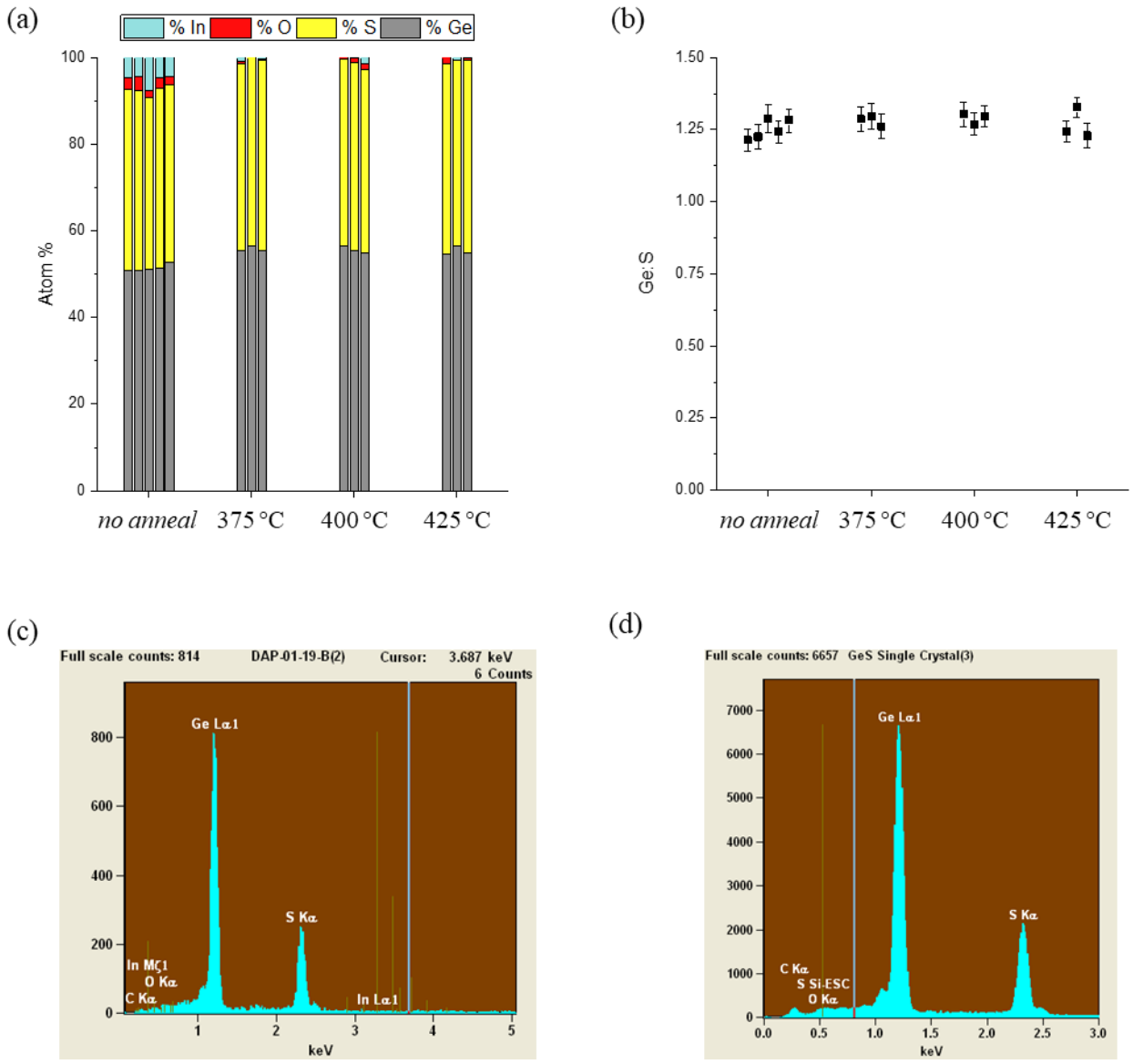

Figure 4.17. (a) Bar graph of the composition of an unannealed GeS film on an ITO substrate compared to pieces of the same filmed annealed at 375, 400 and 425 °C. (b) A scatter plot of the Ge:S ratio of data shown in figure (a). Figures (c) and (d) are EDS spectra of a GeS film annealed on ITO at 375 °C and a GeS single crystal, respectively.

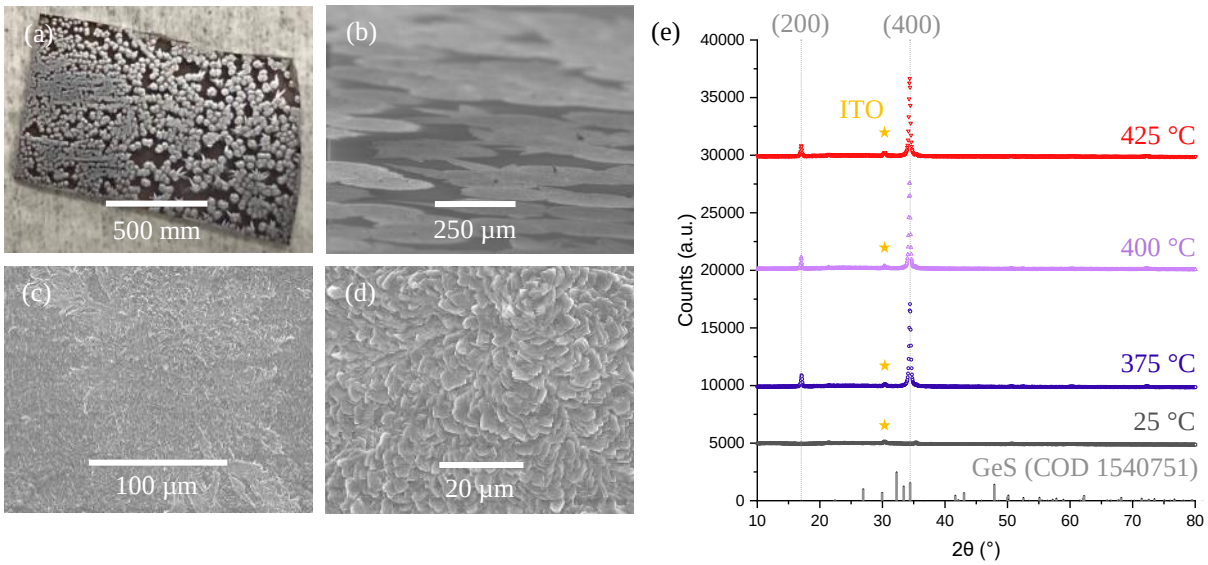

Figure 4.18. Photographs, micrographs and p-XRD of GeS films annealed at 400 °C on a glass substrate. Figure (a) is a photograph showing silver islands on the GeS surface, while figure (b) shows the same using a tilted cross section micrograph. Figure (c) is a micrograph showing dendritic like growths hypothesized to be initial sites of nucleation on silver islands. Figure (d) is a second micrograph that reveals the morphology of the islands is comprised of platelets several microns across. Figure (e) shows powder X-ray diffractograms of an 850 nm thick GeS film on ITO annealed at various temperatures. Yellow stars denote peaks from the ITO substrate.

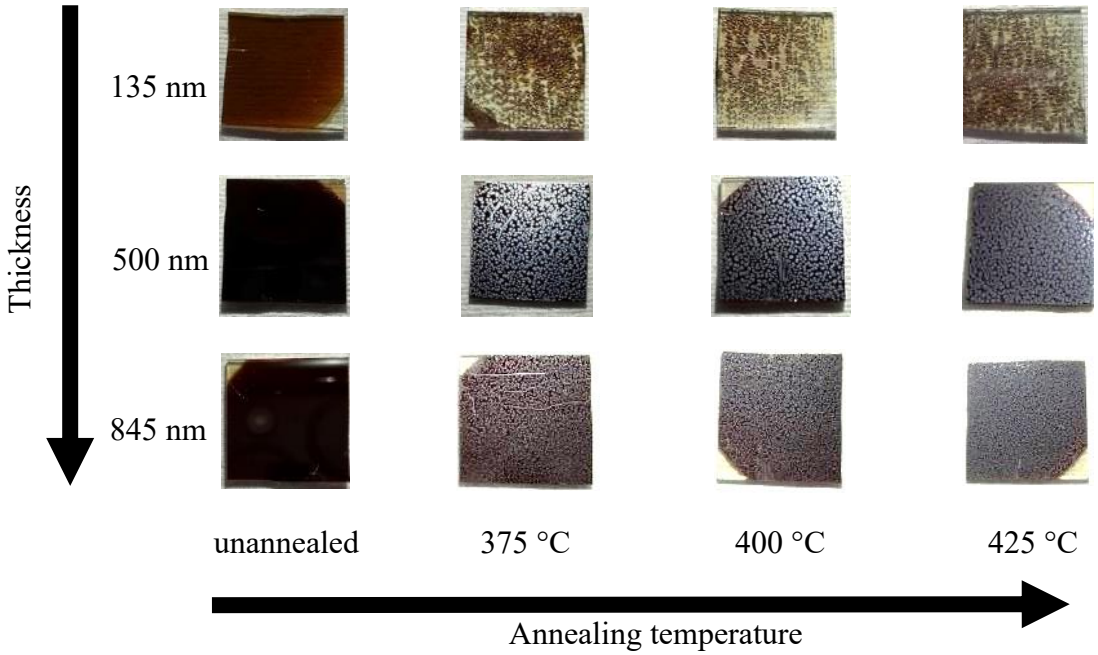

Figure 4.19. Annealing grids of GeS deposited on ITO substrates.

We further investigated the silver islands using SEM and found they were composed of 1-5 μm diameter platelets. On films ≥1 μm thick and annealed at 400 or 425 °C, a portion of the platelets would reach >10 μm in one lateral dimension. Platelet length and density appear to increase with temperature, with films annealed at 425 °C having regions covered in forests of rods. The center of the islands tend to have the largest size crystallites and appear to be the site of initial crystallization. We also found that the islands are often raised several microns above the rest of the film surface (Figure 4.18). On quartz substrates this led to delamination of films ≥1 μm thick, so we did not pursue additional studies. Between the silver spots we do not observe any large platelets and these regions have no observable features. We note that the morphology of our annealed GeS films is quite similar to films obtained by Zhang and coworkers using vapor transport deposition,[25] and also suffer from discontinuities in crystalline material.

Controlling surface roughness to enhance nucleation kinetics. To increase the continuity of crystalline GeS films we searched for methods to improve kinetics of nucleation. Our preliminary annealing studies suggest that the kinetics of GeS crystal growth are quite high, as we observed crystallites extending several hundred microns from nucleation sites on silver islands. Comparatively, the kinetics of nucleation of GeS are quite slow, leading to formation of isolated islands of crystalline material. To obtain continuous crystalline GeS films with homogenous morphology, we sought a method for fusing the silver islands together. Zhang and co-workers resolved this issue by depositing for longer and allowing island size to increase,[25] but we can't afford significant increases in annealing time and must balance the kinetics of GeS sublimation to prevent film loss.

In preliminary annealing studies we observed that GeS crystallites would form along imperfections or scratch marks, and utilized surface roughening to increase the kinetics of crystallite nucleation. We initially attempted roughening films using the back of a metal spatula, but then moved to fine grit sandpaper as this would not generate scratches as deep. As shown in Figure 4.20, when we purposefully scratched the entire GeS surface with sandpaper prior to annealing, we observed a significant increase in the coverage of silver crystallites. We hypothesized that the high surface area to volume ratio of the scratched GeS film and resulting debris on the surface increased the number of defect sites encouraging nucleation to occur. However, due to uneven crystallization (likely arising from uneven roughening by hand) and occasional exposure of the underlying substrate, we sought an alternative method to increase the surface area without damage to amorphous precursor film.

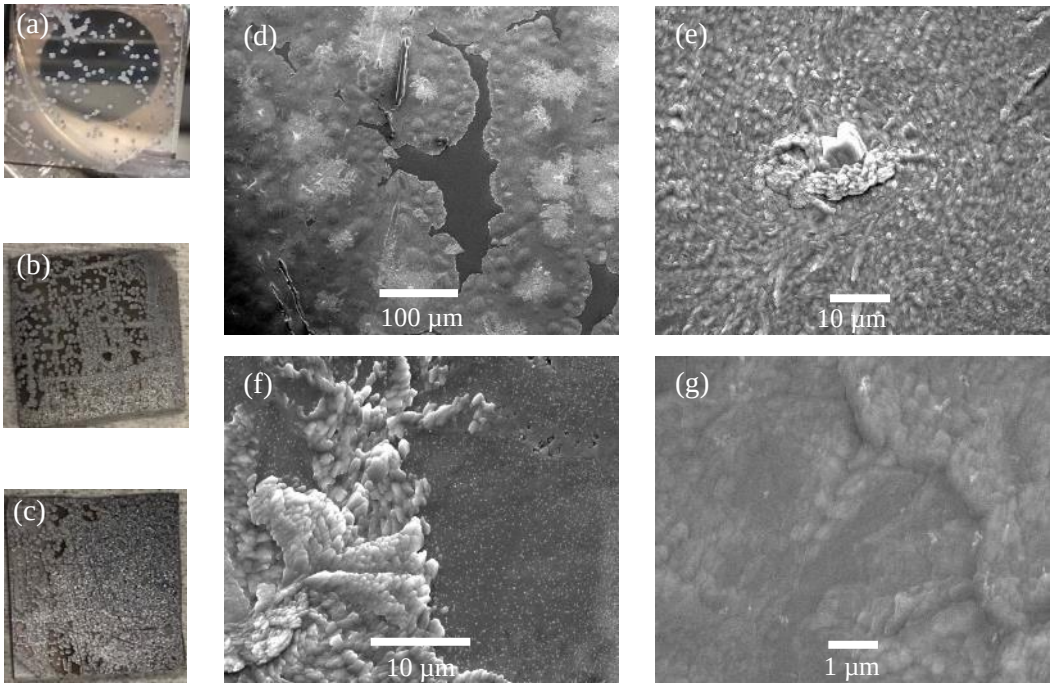

Figure 4.20. Photographs and micrographs of post annealed GeS samples on ITO after the scratching treatment. Photographs (a) shows a GeS film annealed at 400 °C for 10 minutes with no surface treatment and photographs (b) and (c) show samples annealed under the same conditions, but with light and heavy scratching, respectively. Micrographs (d)-(g) were taken on the sample shown in figure (c). Micrograph (d) shows that most GeS islands are more interconnected than on the sample in figure (a), but that gaps remain. Micrograph (e) is zoomed in on a nucleation center on a GeS island. Micrograph (f) shows the edge of an island, where large plate like grains abruptly stop. Micrograph (g) shows that the flat area surrounding plates on islands shown in figure (f) are comprised of smoother and flatter grains.

To avoid damage to the film surface from scratching while maximizing available surface area, we opted to use crystalline GeS powder. As shown in Figure 4.21, we covered the surface of amorphous GeS films with the same crystalline powder used for deposition and annealed at 375-425 °C for 10 minutes using our previously described recipe. SEM images show that the resulting films have near complete closure between crystalline islands and an increased density of nucleation zones (Figure 4.22) Compared to untreated GeS films, the seeded annealed films have flatter and

smaller grains, and do not have large plate like crystallites protruding from the surface. Unfortunately, using a GeS seed layer results in source powder debris remaining on the surface, which we found could only be partially removed using scotch tape. We therefore looked for alternative methods to increase the defect density of our amorphous GeS films.

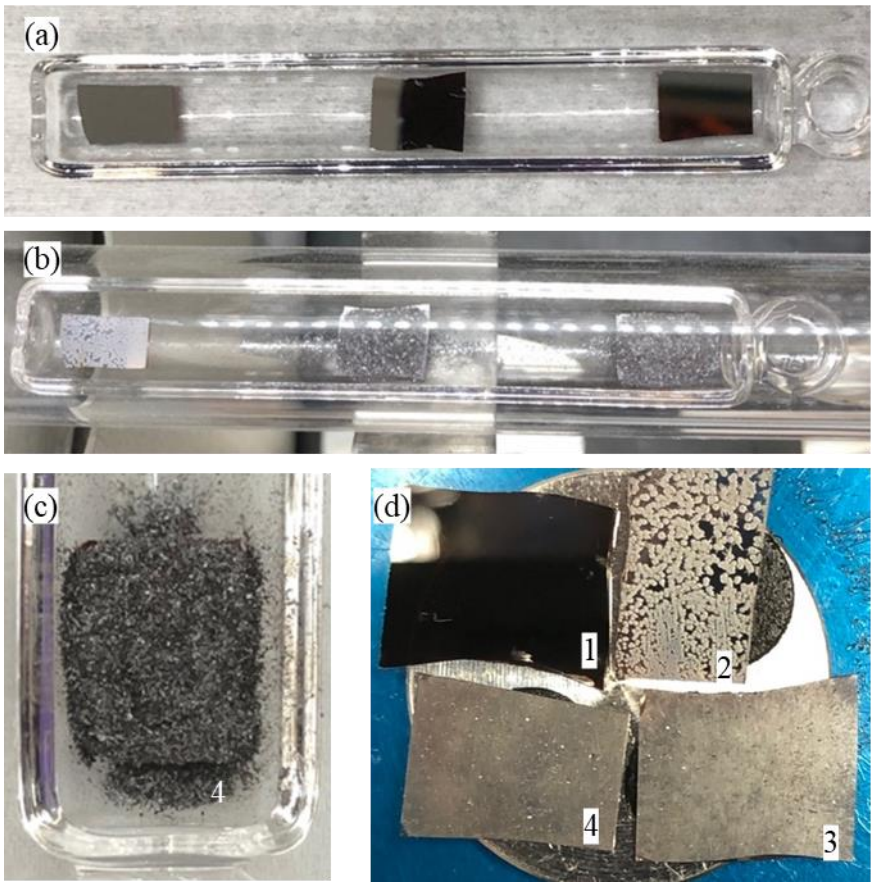

Figure 4.21. Photographs of the set up for seed annealing of GeS samples and comparison of surface coverage on post-annealed samples. Image (a) shows films loaded into a quartz boat before annealing, (b) shows samples after annealing with GeS source powder still on the sample surface, (c) shows sample 4 coated with a GeS seed layer and (d) shows post annealed films on an SEM stub. In figure (d), sample (1) was not annealed, sample 2 was annealed with no seed layer and samples (3) and (4) were annealed with thin and thick coatings of crystalline GeS seed layers, respectively

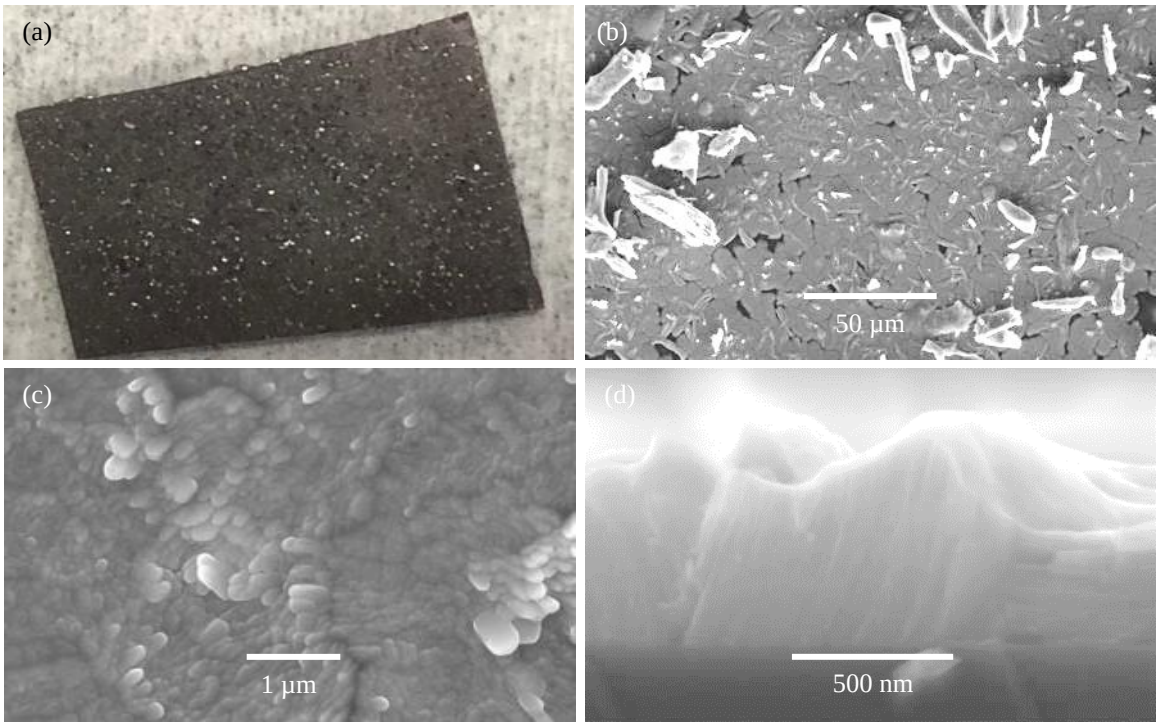

Figure 4.22. Photographs and micrographs of GeS films annealed at 400 °C on a glass substrate using a seed layer. Figure (a) is a photograph showing that the post annealed film has a silver and shiny appearance across the whole substrate, rather than the formation of islands. Figure (b) is a low magnification micrograph of the sample showing elimination of islands and nearly full film closure. The large chunks of material strewn above the surface is residue from the seed layer. Figure (c) is a micrograph taken at higher magnification to reveal that the morphology of the seed-layer annealed film is comprised of platelets on the order of 100 nm across. Figure (d) is a cross section micrograph of the film and demonstrates the 2-D nature of our films; layers of GeS crystallites are visualized.

To increase the defect density of amorphous GeS films, we used sandblasting to roughen the surface of glass substrates prior to deposition. For this series of experiments, we deposited films ca. 2 µm thick. As shown in Figure 4.23, sand blasting substrates results in shallow depressions in the surface of the GeS films that increase in coverage as the duration of sand blasting was increased from 1 to 10 minutes. Amorphous GeS films conformally deposit on the roughened regions of the substrate, with the same grain size seen in untreated glass substrates. The roughened

amorphous GeS films were then annealed for 10 minutes at 375-425 °C using the same recipe as for preliminary studies on untreated glass substrates.

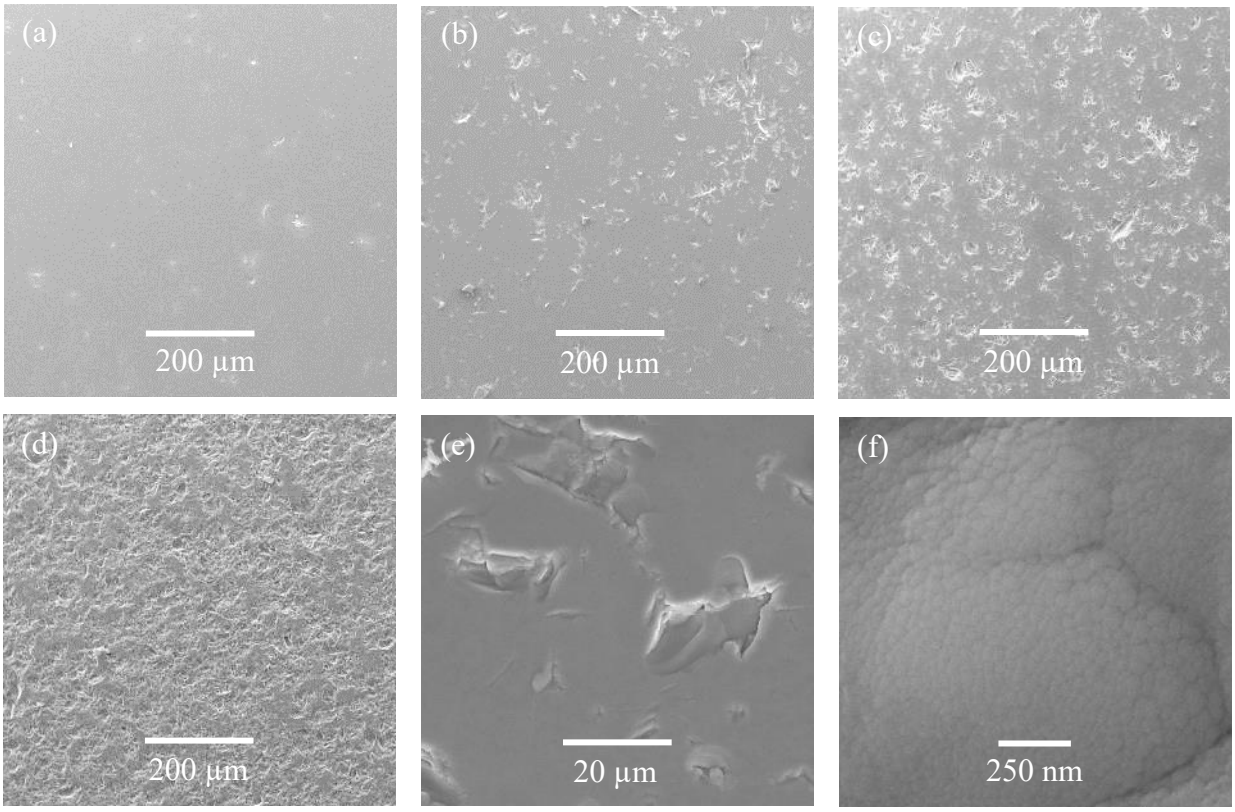

Figure 4.23. Micrographs of as-deposited GeS samples on sand-blasted glass substrates. Figures (a), (b), (c), and (d) are low magnification images of GeS deposited on glass substrates sand-blasted for 1, 3, 5, and 10 minutes, respectively. Surface roughness of the samples increases with sand-blasting duration. Figure (e) reveals that the roughness from sandblasting is due to the formation of pits in the GeS surface. Figure (f) is a representative high magnification micrograph of the sample (both around and in the pitted features) showing smooth morphology and flat grains typical of as-deposited GeS films.

Sand blasted substrates allow for fabrication of continuous films of crystalline GeS. By visual inspection, we found that our sandblasting treatment prevented any obvious formation of isolated silver islands, which exclude any possibility for fully continuous films. Using SEM, we found that films with a sandblasting treatment of 1 minute still had islands of crystalline material,

albeit with significantly smaller gaps of <100 µm, but in films sandblasted treated for 3, 5 and 10 minutes we could prevent growth of isolated islands. The morphology of our films is comprised of compact grains lying mostly parallel to the substrate, similar to films annealed using a seed layer. Like films of similar thicknesses annealed on untreated substrates, increasing the temperature from 375 °C to 400-425 °C resulted in the formation of long platelets of GeS protruding from the sample surface. However, we found that the growth of the platelets could be suppressed by increasing the sandblasting duration. As shown in Figure 4.24, by using 10 minutes of sandblasting treatment we prevented growth of enlarged platelets at 400 °C and significantly reduced their size at 425 °C. Additional images comparing the morphology of sand blasted and annealed GeS films are available in figures 4.24-4.30.

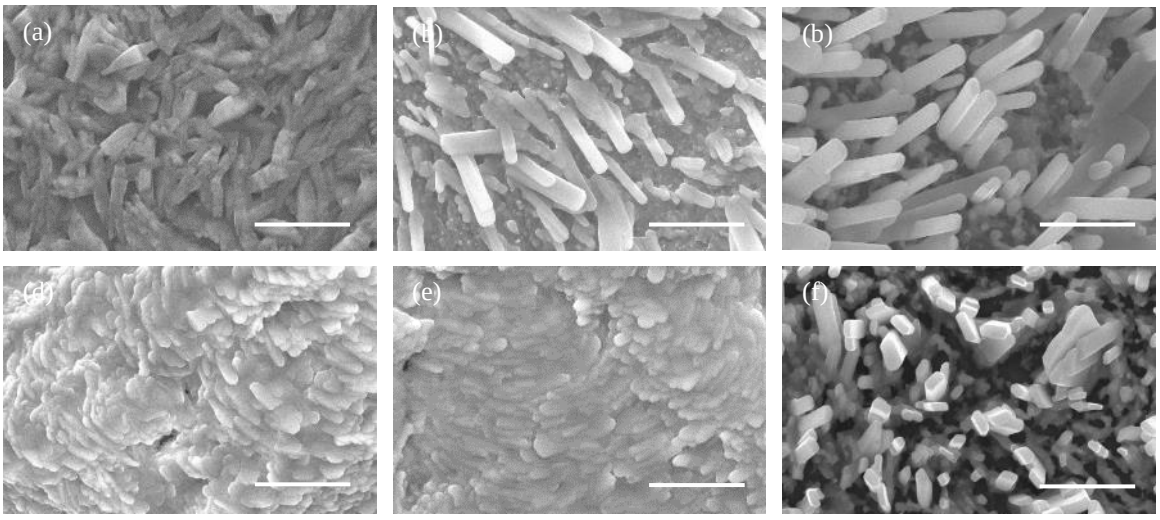

Figure 4.24. Plan view micrographs of GeS films annealed on a glass substrate sandblasted for 3 minutes at 375 (a), 400 (b) and 425 °C (c), and for 10 minutes at 375 (d), 400 (e) and 425 °C (f). The scale bar for all images is 5 µm.

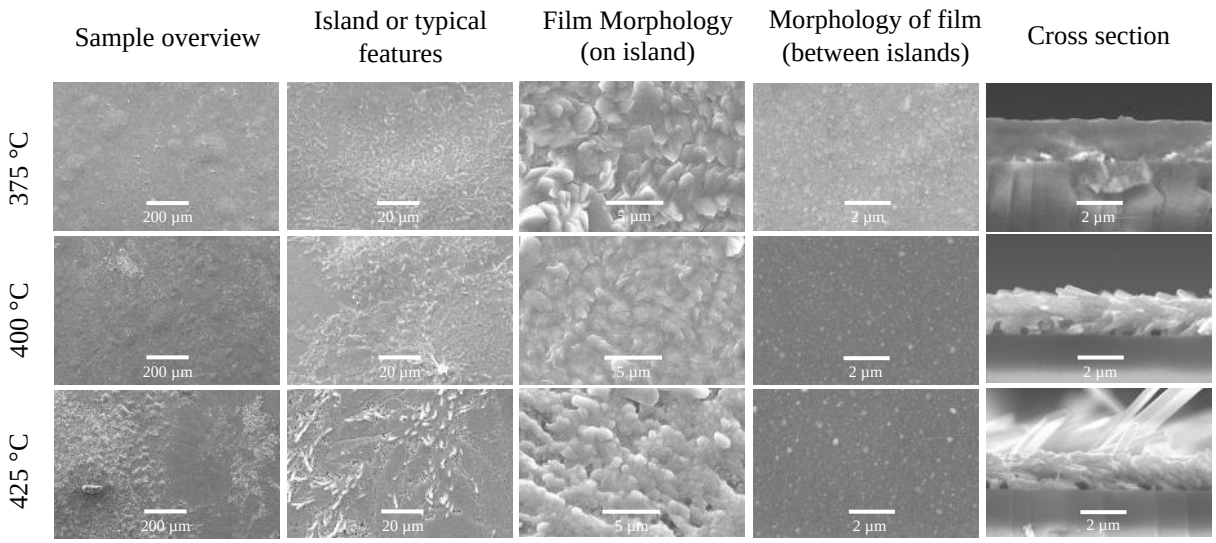

Figure 4.25. Micrographs of GeS samples annealed 375, 400 and 425 °C on glass substrates without sandblasting the underlying substrate or using a seed layer. The films have islands comprised of platelets of crystalline GeS and are surrounded by material that does not appear crystalline. At an annealing temperature of 425 °C, elongated platelets are seen protruding from islands.

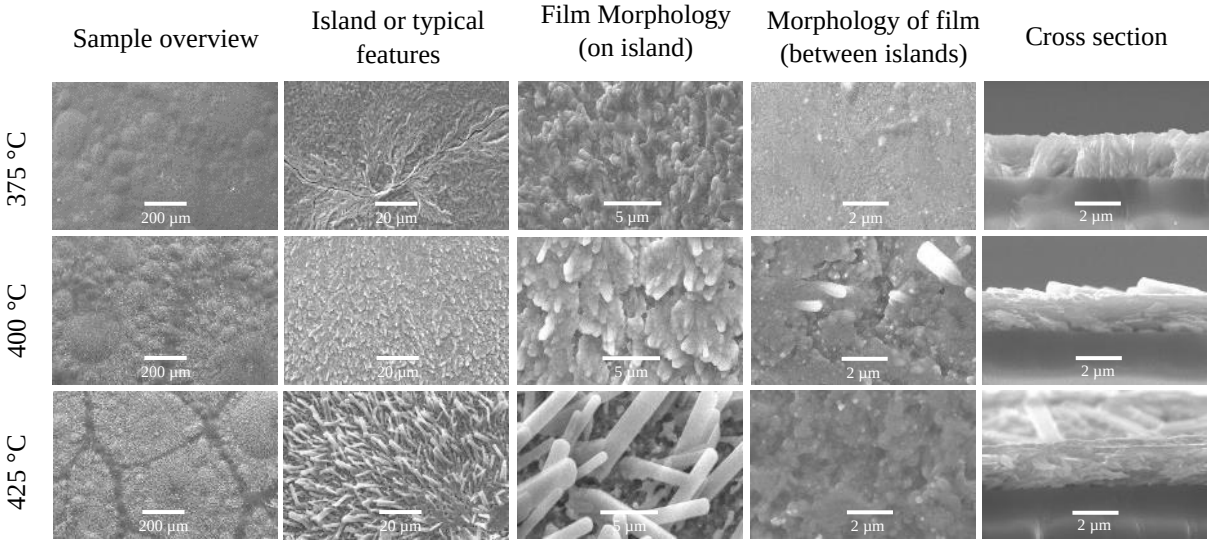

Figure 4.26. Micrographs of GeS samples annealed 375, 400 and 425 °C on glass substrates after 1 minute of sandblasting treatment. Although islands of separated crystallites remain, the gap between these islands is smaller compared to untreated substrates. Additionally, the region between islands appears to have crystallites at annealing temperatures of 400 and 425 °C. As with untreated substrates, elongated platelets appear at annealing temperatures of 400 and 425 °C, with greater density at 425 °C.

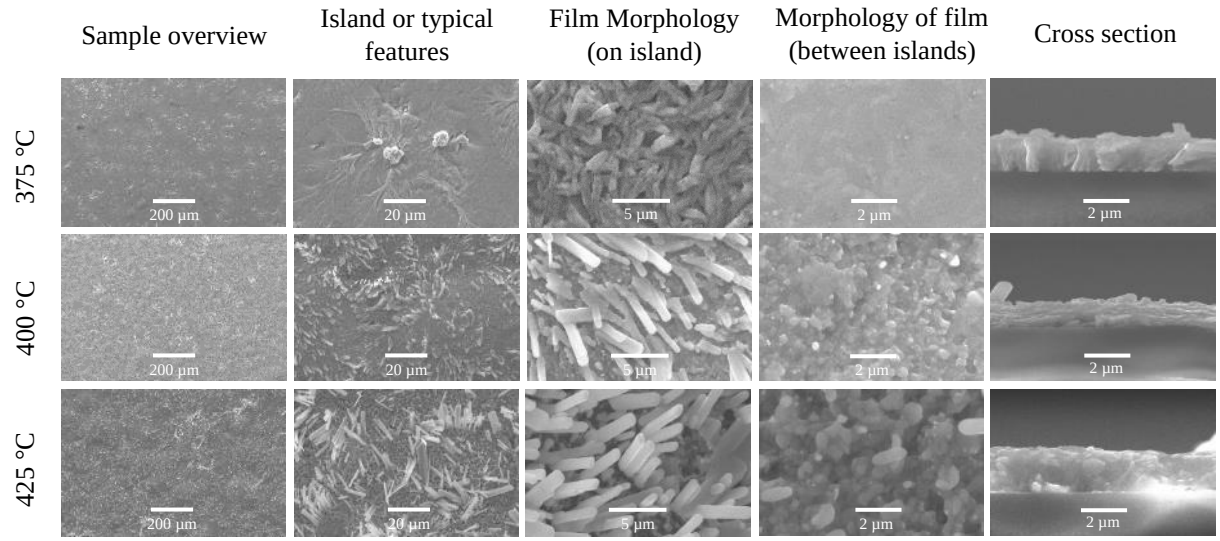

Figure 4.27. Micrographs of GeS samples annealed 375, 400 and 425 °C on glass substrates after 3 minutes of sandblasting treatment. Islands of separated crystalline material have been eliminated and a mixture of rounded and elongated platelets are observed. Outside of nucleation centers on films annealed at 375 °C it is less clear if crystallites are present. On films annealed at 400 and 425 °C the films are a mix of rounded and elongated platelets, with the higher temperature affording larger elongated platelets.

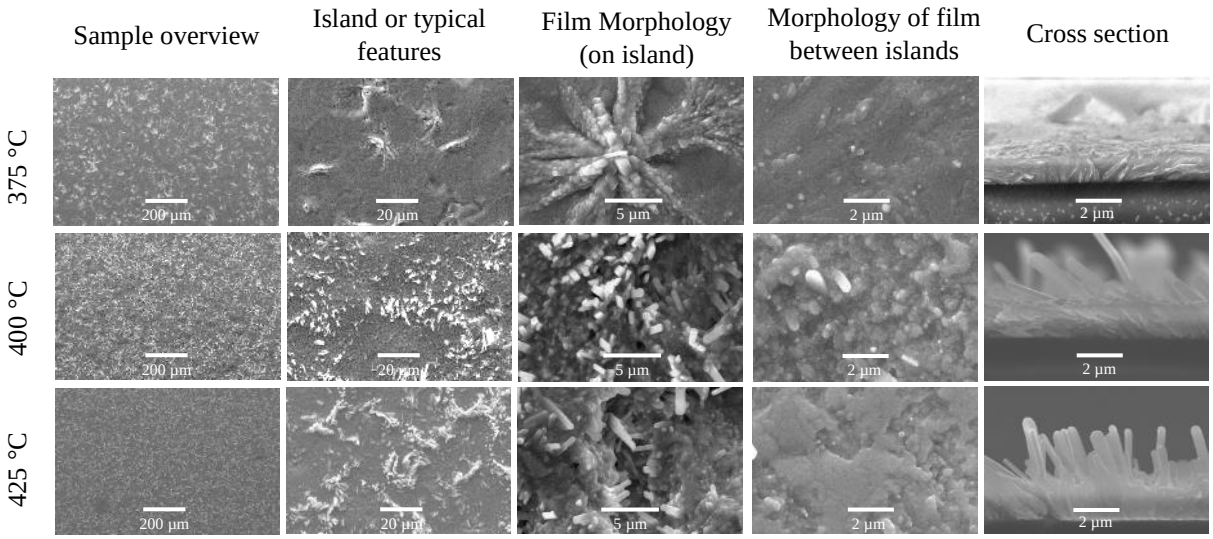

Figure 4.28. Micrographs of GeS samples annealed 375, 400 and 425 °C on glass substrates after 5 minutes of sandblasting treatment. Islands of separated crystalline material are eliminated and at all temperatures regions with continuous crystallites are observed. On films annealed at 375 °C this consists of nucleation zones and flat crystallites while at 400 and 425 °C a mixture of rounded and elongated platelets is observed. The density and lengths of elongated crystallites is markedly shorter than for films annealed on substrates 0, 1, or 3 minutes of sandblasting.

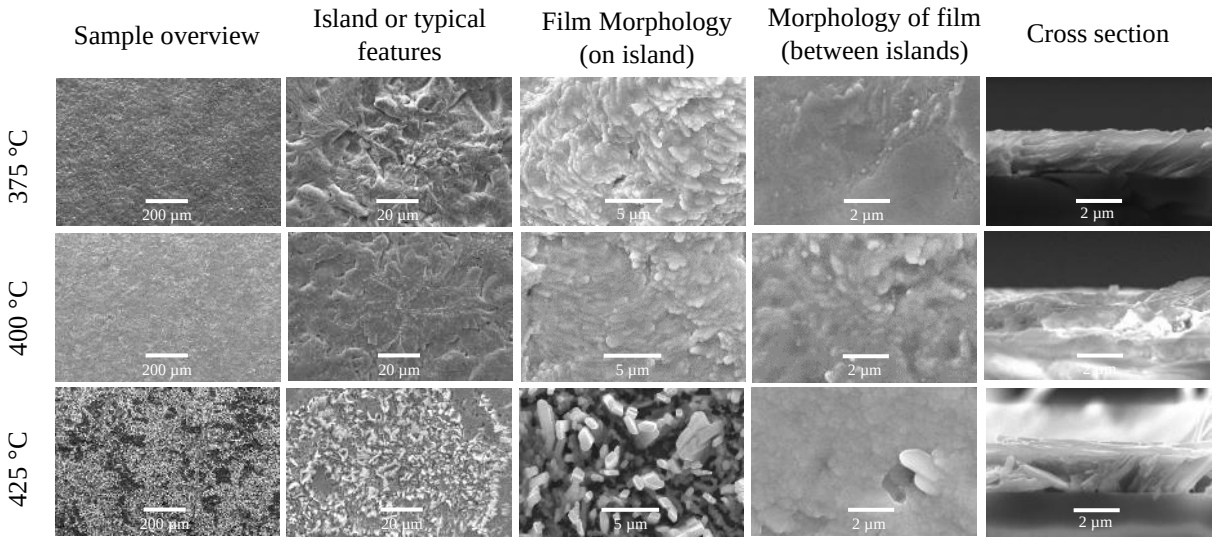

Figure 4.29. Micrographs of GeS samples annealed 375, 400 and 425 °C on glass substrates after 10 minutes of sandblasting treatment. Islands of separated crystalline material are eliminated and at all temperatures regions with continuous crystallites are observed. On films annealed at 375 and 400 °C this consists of nucleation zones and flat crystallites. At 425 °C a mixture of flat crystallites and elongated platelets are observed, with the latter having shorter lengths compare to films annealed on substrates sandblasted for 0, 1, 3, or 5 minutes.

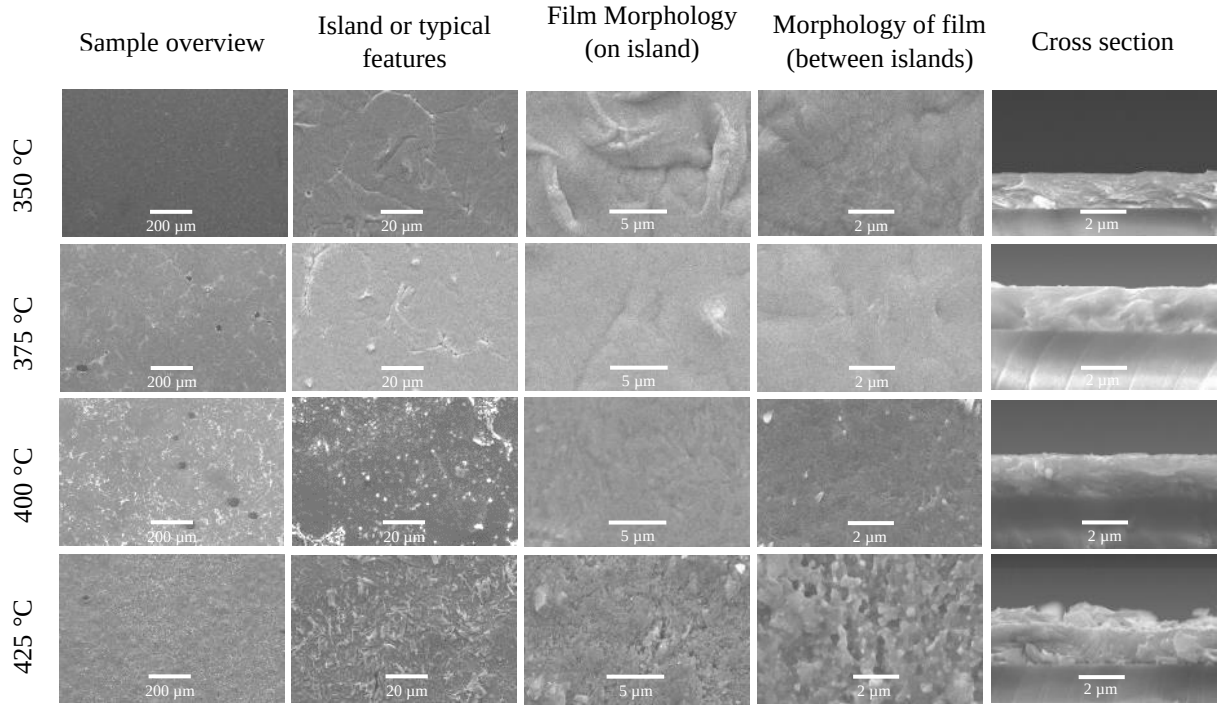

Figure 4.30. Micrographs of GeS samples annealed 375, 400 and 425 °C on glass substrates with a seed layer. Islands of separated crystalline material are eliminated and at all temperatures regions with continuous crystallites are observed. On films annealed at 350, 375 and 400 °C flat crystallites are observed, while at 425 °C a mixture of flat crystallites and elongated platelets are present. Pinholes are present on all samples after removal of the seed layer reside using scotch tape, followed by rinsing with semi-grade acetone and isopropanol, and then drying with nitrogen gas.

Analysis by p-XRD confirms that all films annealed on sandblasted substrates are orthorhombic GeS with preferential orientation in the (400) plane. As for films annealed on untreated substrates, several minor diffractions also attributed to orthorhombic GeS are observed. In films annealed at 375 °C, the intensity of these additional peaks decreases with sandblasting duration, while the intensity of these new peaks remains mostly constant with sandblasting duration in films annealed at 400 and 425 °C. For all annealing temperatures, we find that the intensity of the 400 peak decreases as the sand blasting treatment duration is increased (Figure 4.31). Across each sandblasting duration, the intensity of the 400 peak does not change with

annealing temperature. These findings suggest that annealing at 375-400 °C produces films with similar crystallinity in the (400) plane and that surface roughness influences film crystallinity more strongly than annealing temperature.

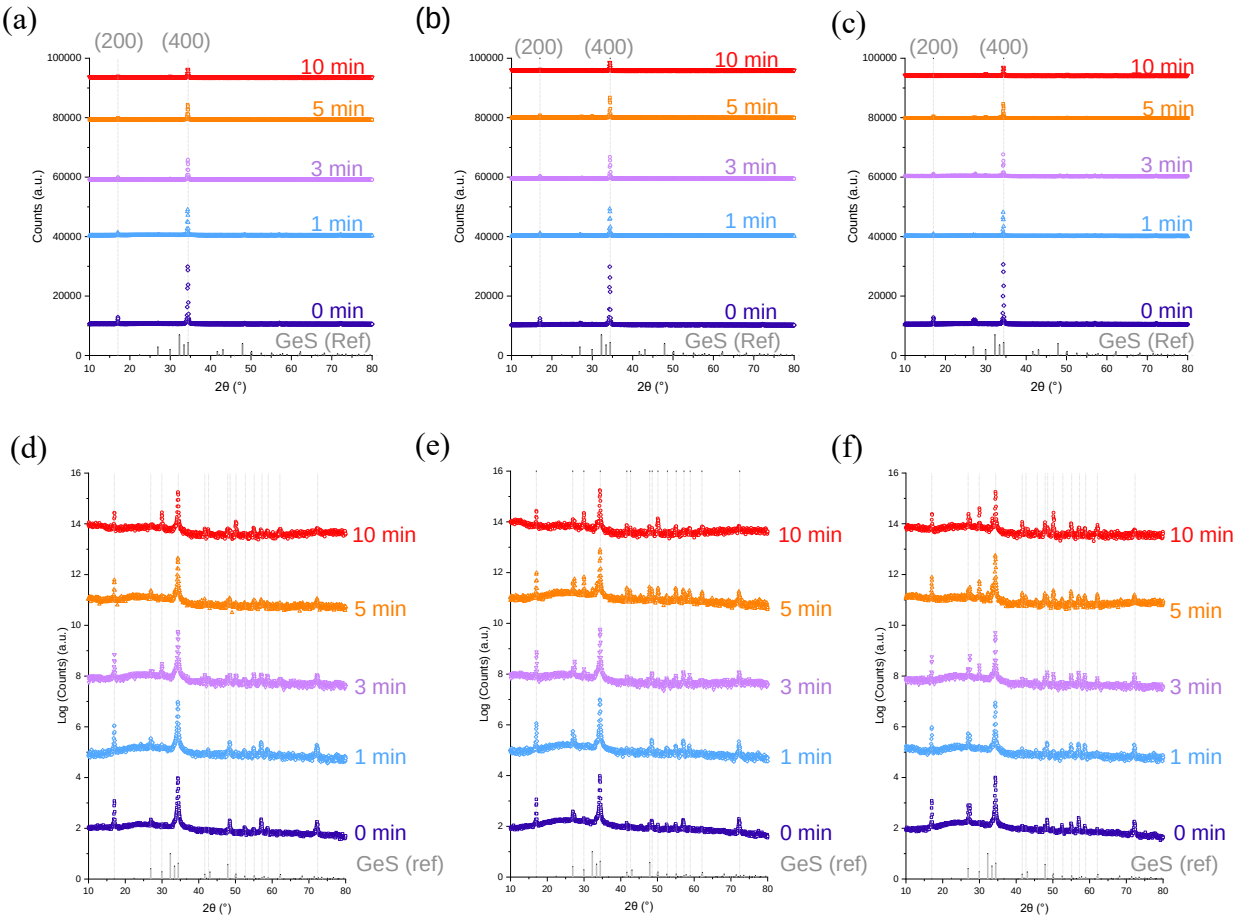

Figure 4.31. Diffractograms of GeS films annealed at temperatures of 375 (a,d), 400 (b,e) and 425 °C (c,f) on sandblasted substrates roughened for 0-10 minutes at temperatures. Log plot diffractograms are shown below the standard diffractograms to visualize minor reflections. The GeS reference (GeS ref) is COD (1540751).

4.5.4. Electrical Properties of GeS Films

To assess the electrical properties of GeS films annealed on sandblasted glass substrates, we used photoexcited Van der Pauw measurements. The sheet resistance of samples annealed at 375 °C was measured in dark (0 suns), 1 sun and 4 suns illumination by Daniela Chavez. Then, by

using cross section micrographs to determine film thicknesses, the resistivity of GeS films was calculated. Due to complex surface morphologies comprised of elongated platelets on films annealed at 400 and 425 °C, these samples are excluded from measurements since film thicknesses are non-trivial and cannot be confidently used for resistivity calculations.

Sheet resistance measurements demonstrate GeS films are photoconductive and have resistivities similar to some GeS single crystals. As shown in Figure 4.32, the sheet resistance of GeS films measured in the dark is between 10^{10}-10^{11} Ω/□ and decreases an order of magnitude to 10^{9}-10^{10} Ω/□ under photoexcitation. The corresponding resistivities in dark and under photoexcitation are 10^{6}-10^{7} Ω·cm and 10^{5}-10^{6} Ω·cm, respectively. There is no clear trend between surface roughening duration and resistivity other than substrates roughened for 10 minutes consistently having the lowest resistivity. Data for unannealed witness samples is not shown, but current readings were below the limit of detection on the solar simulator, indicating a resistivity of at least 10^{11} Ω·cm. Together, these measurements demonstrate that annealing improves the electrical transport properties of GeS films and that these samples are photoconductive. The resistivity of our films is large compared to some reports of GeS single crystals, with resistivities of 10^{2}-10^{3} Ω·cm[39], but comparable to others with resistivities between 10^{6}-10^{7} Ω·cm.[40, 41]

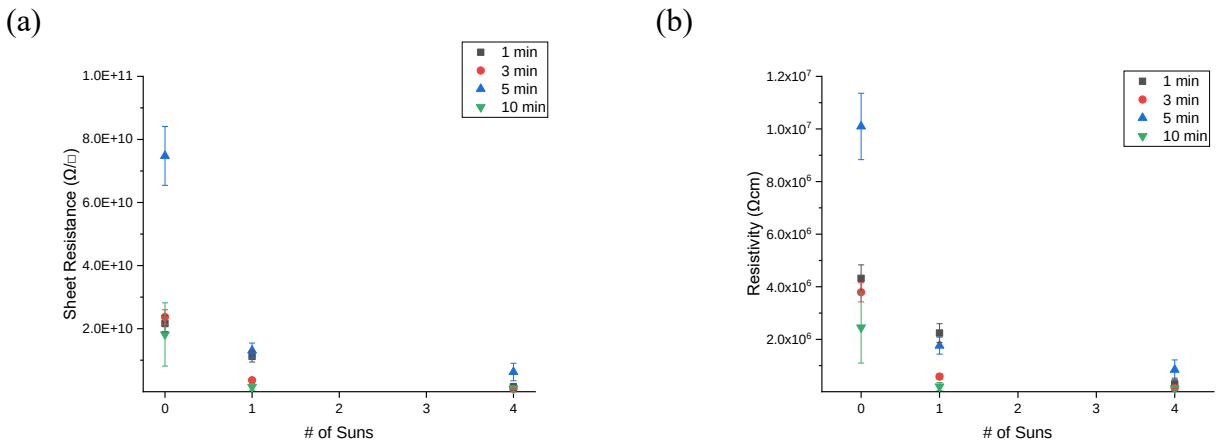

Figure 4.32 Sheet resistance (a) and resistivity (b) versus solar flux for GeS films annealed at 375 °C on glass substrates sand blasted for 1, 3, 5 and 10 minutes.

4.6. Conclusions

We have demonstrated seeding and substrate roughening strategies for balancing the kinetics of evaporation and nucleation during annealing of GeS films. Stoichiometric GeS films can be prepared through a simple thermal evaporation method, and while annealing under H_2S results in partial oxidation to GeS_2, annealing under Ar atmospheres results in no change to film composition. Films annealed at 375-425°C under Ar are highly oriented with good crystallinity, and a variety of morphologies can be achieved by controlling roughness of the underlying substrate. Crystallizing GeS films improves the carrier transport properties and allows us to demonstrate the material is photoactive using resistivity measurements. The presence of elongated platelets in many films and relatively high resistivity may remain barriers to assembling GeS photovoltaics.

4.7. References

1. Polman, A.; Knight, M.; Garnett, E. C.; Ehrler, B.; Sinke, W. C., Photovoltaic materials: Present efficiencies and future challenges. *Science* **2016,** *352* (6283), aad4424.

2. Best Research-Cell Efficiency Chart. https://www.nrel.gov/pv/cell-efficiency.html (accessed April 28, 2025).

3. Feldman, D.; Margolis, R. *Q4 2019/Q1 2020 Solar Industry Update*; United States, 2020.

4. McGott, D., Cadmium Telluride Solar Cells: From Fundamental Science to Commercial Applications. 2023.

5. Miller, C. A.; Peters, I. M.; Zaveri, S. *Thin Film CdTe Photovoltaics and the U.S. Energy Transition in 2020*; QESST Engineering Research Center: 2020.

6. McCandless, B. E.; Sites, J. R., Cadmium Telluride Solar Cells. In *Handbook of Photovoltaic Science and Engineering*, 2003; pp 617-662.

7. Amin, N.; Rahman, K. S., Close-Spaced Sublimation (CSS): A Low-Cost, High-Yield Deposition System for Cadmium Telluride (CdTe) Thin Film Solar Cells. 2017; pp 361-379.

8. Malone, B. D.; Kaxiras, E., Quasiparticle band structures and interface physics of SnS and GeS. *Physical Review B* **2013,** *87* (24), 245312.

9. Feng, M.; Liu, S.; Hu, L.; Wu, J.; Liu, X.; Xue, D. J.; Hu, J.-S.; Wan, L.-J., Interfacial Strain Engineering in Wide-Bandgap GeS Thin Films for Photovoltaics. *Journal of the American Chemical Society* **2021,** *143*, 9664-9671.

10. Stanchev, A.; Vodenicharov, C., Photoconductivity kinetics of germanium monosulphide thin films. *Thin Solid Films* **1976,** *38* (1), 67-72.

11. Fan, X.; Su, L.; Zhang, F.; Huang, D.; Sang, D. K.; Chen, Y.; Li, Y.; Liu, F.; Li, J.; Zhang, H.; Xie, H., Layer-Dependent Properties of Ultrathin GeS Nanosheets and Application in UV–Vis Photodetectors. *ACS Applied Materials & Interfaces* **2019,** *11* (50), 47197-47206.

12. Khanmohammadi, S.; Tran, C.; Amini, H.; Colin-Ulloa, E.; Ekuma, C.; Koski, K. J.; Titova, L. V. In *Engineering ultrafast carrier dynamics in GeS: nanostructuring and small molecule intercalation*, 2022 47th International Conference on Infrared, Millimeter and Terahertz Waves (IRMMW-THz), 28 Aug.-2 Sept. 2022; 2022; pp 1-2.

13. Kushnir, K.; Shi, T.; Damian, L.; Anilao, A.; Koski, K. J.; Titova, L. V. In *Zero-Valent Au, Cu, and Sn Intercalation into GeS Nanoribbons: Tailoring Ultrafast Photoconductive Response*, Ultrafast Phenomena and Nanophotonics XXIV, 2020; p 17.

14. Hsueh, H.-C.; Li, J.-X.; Ho, C.-H., Polarization Photoelectric Conversion in Layered GeS. *Advanced Optical Materials* **2018,** *6* (4), 1701194.

15. Lan, C.; Li, C.; Yin, Y.; Guo, H.; Wang, S., Synthesis of single-crystalline GeS nanoribbons for high sensitivity visible-light photodetectors. *Journal of Materials Chemistry C* **2015,** *3* (31), 8074-8079.

16. Ulaganathan, R. K.; Lu, Y.-Y.; Kuo, C.-J.; Tamalampudi, S. R.; Sankar, R.; Boopathi, K. M.; Anand, A.; Yadav, K.; Mathew, R. J.; Liu, C.-R.; Chou, F. C.; Chen, Y.-T., High photosensitivity and broad spectral response of multi-layered germanium sulfide transistors. *Nanoscale* **2016,** *8* (4), 2284-2292.

17. Hu, L.; Feng, M.; Wang, X.; Liu, S.; Wu, J.; Yan, B.; Lu, W.; Wang, F.; Hu, J.-S.; Xue, D.-J., Solution-processed Ge(II)-based chalcogenide thin films with tunable bandgaps for photovoltaics. *Chemical Science* **2022**.

18. Ribeiro, T. C. Science and technology of solar cells based on SnS, SnS_2 and GeS. Doctoral dissertation, Universidade Federal de Minas Gerais, 2023.

19. Lu, W.; Fang, Y.; Li, Z.; Li, S.; Liu, S.; Feng, M.; Xue, D.-J.; Hu, J.-S., Investigation of the sublimation mechanism of GeSe and GeS. *Chemical Communications* **2021,** *57* (87), 11461-11464.

20. Ross, L.; Bourgon, M., Thermal analysis of germanium(II) sulfide. *Canadian Journal of Chemistry* **2011,** *46*, 2464-2468.

21. Sutter, E.; Sutter, P., 1D Wires of 2D Layered Materials: Germanium Sulfide Nanowires as Efficient Light Emitters. *ACS Applied Nano Materials* **2018,** *1* (3), 1042-1049.

22. Shimazaki, E.-i.; Wada, T., Vapor Pressure of Germanium Monosulfide. *Bulletin of the Chemical Society of Japan* **2006,** *29* (3), 294-296.

23. Drabavičius, A.; Pakštas, V.; Jasiūnas, R.; Koltsov, M.; Talaikis, M.; Naujokaitis, A.; Spalatu, N.; Kondrotas, R.; Gulbinas, V.; Franckevičius, M., Synthesis and characterization of polycrystalline GeS thin films for optoelectronic applications. *Materials Science in Semiconductor Processing* **2025,** *188*, 109193.

24. Stanchev, A.; Vodenicharov, C., Kinetics of Vacuum Deposition of GeS Films. *physica status solidi (a)* **1975,** *27* (2), 615-619.

25. Zhang, Q.; Matsumura, R.; Fukata, N., Synthesis of Large-Area GeS Thin Films with the Assistance of Pre-deposited Amorphous Nanostructured GeS Films: Implications for Electronic and Optoelectronic Applications. *ACS Applied Nano Materials* **2023,** *6* (8), 6920-6928.

26. Robinson, F.; Sethi, V.; de Groot, C. H. K.; Hector, A. L.; Huang, R.; Reid, G., Low-Pressure CVD of GeE (E = Te, Se, S) Thin Films from Alkylgermanium Chalcogenolate

Precursors and Effect of Deposition Temperature on the Thermoelectric Performance of GeTe. *ACS Applied Materials & Interfaces* **2021,** *13* (40), 47773-47783.

27. Kim, S. B.; Sinsermsuksakul, P.; Hock, A. S.; Pike, R. D.; Gordon, R. G., Synthesis of N-Heterocyclic Stannylene (Sn(II)) and Germylene (Ge(II)) and a Sn(II) Amidinate and Their Application as Precursors for Atomic Layer Deposition. *Chemistry of Materials* **2014,** *26* (10), 3065-3073.

28. Chen, B.; Ruan, Y.; Li, J.; Wang, W.; Liu, X.; Cai, H.; Yao, L.; Zhang, J.-M.; Chen, S.; Chen, G., Highly oriented GeSe thin film: self-assembly growth via the sandwiching post-annealing treatment and its solar cell performance. *Nanoscale* **2019,** *11* (9), 3968-3978.

29. Liu, S.-C.; Yang, Y.; Zhang, X.; Huang, L.-B.; Sun, J.-K.; Guan, B.; Li, X.; Xue, D.-J.; Hu, J.-S., Tuning the Optical Absorption Property of GeSe Thin Films by Annealing Treatment. *physica status solidi (RRL) – Rapid Research Letters* **2018,** *12* (12), 1800370.

30. Zi, W.; Mu, F.; Lu, X.; Cao, Y.; Xie, Y.; Fang, L.; Cheng, N.; Zhao, Z.; Xiao, Z., Post-annealing treatment of a-GeSe thin films for photovoltaic application. *Solar Energy* **2020,** *199*, 837-843.

31. Sinsermsuksakul, P.; Sun, L.; Lee, S. W.; Park, H. H.; Kim, S. B.; Yang, C.; Gordon, R. G., Overcoming Efficiency Limitations of SnS-Based Solar Cells. *Advanced Energy Materials* **2014,** *4* (15), 1400496.

32. Steinmann, V.; Jaramillo, R.; Hartman, K.; Chakraborty, R.; Brandt, R. E.; Poindexter, J. R.; Lee, Y. S.; Sun, L.; Polizzotti, A.; Park, H. H.; Gordon, R. G.; Buonassisi, T., 3.88% Efficient Tin Sulfide Solar Cells using Congruent Thermal Evaporation. *Advanced Materials* **2014,** *26* (44), 7488-7492.

33. Kim, S. B.; Zhao, X.; Davis, L. M.; Jayaraman, A.; Yang, C.; Gordon, R. G., Atomic Layer Deposition of Tin Monosulfide Using Vapor from Liquid Bis(N,N′-diisopropylformamidinato)tin(II) and H2S. *ACS Applied Materials & Interfaces* **2019,** *11* (49), 45892-45902.

34. Park, H. H.; Heasley, R.; Sun, L.; Steinmann, V.; Jaramillo, R.; Hartman, K.; Chakraborty, R.; Sinsermsuksakul, P.; Chua, D.; Buonassisi, T.; Gordon, R. G., Co-optimization of SnS absorber and Zn(O,S) buffer materials for improved solar cells. *Progress in Photovoltaics: Research and Applications* **2015,** *23* (7), 901-908.

35. Polizzotti, A.; Faghaninia, A.; Poindexter, J. R.; Nienhaus, L.; Steinmann, V.; Hoye, R. L. Z.; Felten, A.; Deyine, A.; Mangan, N. M.; Correa-Baena, J. P.; Shin, S. S.; Jaffer, S.; Bawendi, M. G.; Lo, C.; Buonassisi, T., Improving the Carrier Lifetime of Tin Sulfide via Prediction and Mitigation of Harmful Point Defects. *The Journal of Physical Chemistry Letters* **2017,** *8* (15), 3661-3667.

36. Dasgupta, N. P.; Mack, J. F.; Langston, M. C.; Bousetta, A.; Prinz, F. B., Design of an atomic layer deposition reactor for hydrogen sulfide compatibility. *Review of Scientific Instruments* **2010,** *81* (4), 044102.

37. Hirayama, C., Thermodynamic Properties of Solid Monoxides, Monosulfides, Monoselenides, and Monotellurides of Ge, Sn, and Pb. *Journal of Chemical & Engineering Data* **1964,** *9* (1), 65-68.

38. Bale, C. W.; Chartrand, P.; Decterov, S. A.; Eriksson, G.; Hack, K.; Jung, I. H.; Kang, Y. B.; Melançon, J.; Pelton, A. D.; Robelin, C.; Petersen, S., FactSage Thermochemical Software and Databases. *Calphad* **2002,** *26* (2), 189-228.

39. Bletskan, D.; Glukhov, K.; Kabatsii, V., Influence of cation vacancies and Bi impurity on the electronic structure and photoelectric properties of orthorhombic GeS. *Journal of Optoelectronics and Advanced Materials* **2019,** *21*, 629-640.

40. Solanki, G. K.; Patel, D. B.; Unadkat, S.; Agarwal, M. K., Synthesis and characterization of germanium monosulphide (GeS) single crystals grown using different transporting agents. *Pramana* **2010,** *74* (5), 813-825.

41. van den Dries, J. G. A. M.; Lieth, R. M. A., Growth rate and some electrical properties of GeS single crystals. *physica status solidi (a)* **1971,** *5* (3), K171-K174.

Appendix 1: Standard Operating Procedures

Performing a CVD Reaction. The following procedure is used to deposit ZrS_2 films in the CVD reactor. A safety buddy should be standing nearby when starting and stopping a deposition and if the operator needs to access items inside the walk-in fume hood during a deposition. The H_2S detector should be turned on and left in the fume hood by any components the user is accessing to check for the presence of H_2S.

First the CVD reactor is vented to insert substrates. Prior to venting, the valve directly upstream of the H_2S MFC is closed (otherwise 1-2 ppm H2S leaks through), and it should be ensured that the bubbler valves are also closed (these should only be open when running a deposition). The Ar purging MFC is then set to 100 sccm, the butterfly valve isolating the vacuum pump is closed, and the clamp securing the KF25 blank access door to the reactor is removed. The venting process takes ca. 4-5 minutes, after which the sample door will either fall off or can be removed with little to no effort (regardless, the operator should wait with their hand in front of the door, so it does not fall to the ground – this typically occurs at ca. 400 Torr, as the pressure gauge is calibrated to N_2/air and not Ar). The sample tray is then removed from the reaction zone using a copper wire. The sample tray is placed on a cleanroom matte in front of the CVD reactor and substrates are placed onto the front portion using tweezers. The tray is then carefully picked up using clean gloved hands and inserted into the KF cross, with a copper wire used to push the tray further back into the reaction zone. The KF25 blank access door and its clamp are then reinstalled and the butterfly valve isolating from vacuum is opened.

The CVD reactor is then baked out. The Ar purging MFC flowrate remains at 100 sccm and the bellows valve in front of the H_2S MFC is opened. The tube furnace is baked out at a temperature of 400 °C for 2 hours. During this time, the stainless-steel lines are heated to 110 °C

using heating tapes controlled by the Flexotherm temperature controller box, while the downstream quick connect flange, KF25 cross, and KF25 bellows hose are heated to 45 °C using heating tapes. The upstream KF25 quick connection is heated to 60 °C. After the bakeout, the lid of the tube furnace is propped open using an Al block and cooled to the deposition setpoint temperature. The H_2S carrying line heated tapes are turned off and the heating tapes on the $Zr(NMe_2)_4$ carrying line are changed to their setpoint temperatures and allowed to cool (the heating tape on the line is set to 43 °C and the heating tape on the quick connect flange to KF25 adapter and KF25 blank feedthrough and tubes is set to 58 °C). During this time, the heated jacket for the bubbler is set to the desired temperature.

Prior to a deposition, the rate of rise in the CVD reactor is checked to confirm it is ≤1 mTorr/min. Once the setpoint temperatures of the heated lines and tube furnace are reached, the Ar purging MFC is turned off and the bellows valves in front of the Ar purging MFC and H_2S MFC are closed, followed by the butterfly valve isolating the reaction zone from vacuum. The pressure is then monitored over the course of 2-3 minutes. Provided the rate of rise is acceptable, the butterfly valve is reopened, and the bellows valves are opened in front of both the Ar purging and H_2S MFCs. Note that the Ar purging MFC should not be plugged in before opening the bellows valve directly downstream of it, as this introduces a pocket of higher-pressure gas, which when released can cause the substrates to be blown out of place on the sample tray.

To start a deposition, MFCs are adjusted to the desired setpoints, and precursors are introduced to the reaction zone. First, a butterfly valve isolating the pressure gauge is closed to protect the gauge from exposure to H_2S. The flow rate of the Ar purging MFC is then increased to the desired setpoint (typically 200 sccm). Next, H_2S is introduced to the reaction zone by sequentially opening valves, starting with the lecture bottle main valve, followed by the valve on

the H_2S lecture bottle regulator, and then the VCR bellows valves on either side of the H_2S purifier. Before each valve is opened, all connections upstream must be checked with the H_2S detector. The H_2S MFC is then turned on and the flowrate is adjusted. Note that at low flowrate settings (1-5 sccm), it often takes a minute for H_2S to start flowing (it is likely that the MFC needs to be recalibrated). Next, $Zr(NMe_2)_4$ is introduced into the reaction zone by plugging in the MFC controlling the bubbler carrier gas and simultaneously opening the valves immediately upstream and downstream of the bubbler. The carrier gas flowrate may be adjusted before or after opening the bellows valves on either side of the bubbler.

To stop a deposition, the sequence used to start the reaction is run in reverse. First, the valves installed on the $Zr(NMe_2)_4$ bubbler are simultaneously closed, and the carrier gas MFC is turned off. This order should be maintained to prevent back streaming of H_2S into the bubbler. The bubbler heated jacket and heated tapes on the $Zr(NMe_2)_4$ carrying line are then turned off. Next, the H_2S MFC is turned off, followed by closing valves sequentially from downstream to upstream at the H_2S lecture bottle. During this step, breakthrough of H_2S at the vacuum pump is checked by sampling the exhaust. Finally, the furnace is set to 20 °C and propped open with an aluminum block to speed the cooling process Once the temperature of the furnace reaches ≤30 °C, the Ar purge gas flow rate is decreased to 10 sccm and the butterfly valve isolating the pressure gauge is opened. When not in use or to store samples, the CVD reactor is kept at these conditions (room temperature, active vacuum with 10 sccm of Ar flowing).

Replacing the Scrubber on the CVD Reactor. To prevent breakthrough of H_2S while using the CVD reactor, the SULFURTRAP EX scrubbing media must be routinely changed. Breakthrough once occurred after flowing ca. 3 L of H_2S through ca. 800 g of scrubbing agent,

suggesting that each gram of media added can scrub ca. 3.75 mL of H_2S. However, a large margin of safety is preferred, so afterwards the scrubber was changed after only flowing 2.5 L. When molecular sieves are added to the foreline trap, the total volume of H_2S that can be scrubbed decreases proportionally to the reduction in mass of the SULFURTRAP EX media (i.e., when 600 g of media is loaded, it must be replaced after flowing ca. 1.8 L of H_2S).

To replace the SULFURTRAP EX media, the CVD reactor should first be partially refilled with Ar and isolated from vacuum. First, the butterfly valve isolating the reaction zone from vacuum is closed. The Ar purging MFC is then turned on and gas is flowed until the pressure in the reactor reaches 10-15 Torr. The Ar purging MFC should then be turned off and valves downstream of both the Ar purging MFC and H_2S MFC should be closed so the pressure in the reaction zone does not rise.

The downstream half of the CVD reactor is then vented so that the foreline trap can be removed. For the following steps, the H_2S detector should be on and a safety buddy should be standing nearby. Open the bottom sash of the walk-in fume hood and turn off the vacuum pump. Then, removed the KF 25 clamp on the upstream side of the foreline trap and break the connection, which will vent downstream half of the CVD reactor. Finally, break the downstream connection on the foreline trap and remove it from the fume hood so that the scrubbing agent can be replaced. Note: use the H_2S detector to check for any H_2S gas in the foreline trap or pump oil (none should ever be detected unless breakthrough otherwise occurs during regular operation of the CVD reactor.

Next, the old SULFURTRAP EX MEDIA is removed. Open the foreline trap and pour out the used scrubbing media into a solid waste container. Remove the Buna-N centering ring and also the metal mesh at the bottom of the foreline trap. Rinse the inside of the foreline trap with acetone

and isopropanol to remove dust and residue from the previously installed scrubbing agent. It may be necessary to use a clean room matte and long tweezers to wipe the inside. After rinsing, dry the foreline trap using nitrogen gas. Next, clean the Buna-N O-ring using hexane (to remove the grease), followed by acetone, isopropanol and drying with nitrogen gas. Use a foam applicator to remove residue from the Buna-N O-ring and any residue in the groove of the foreline trap where it sits.

New SULFURTRAP EX media and molecular sieves can now be added to the foreline trap. Both scrubbing agents should be baked overnight in a vacuum oven at >250 °C to remove water and added to the foreline trap while hot. First, reassemble the foreline trap by replacing the metal mesh at the bottom and then adding the Buna-N O-ring and outer clamp. The Buna-N O-ring should be coated with Krytox grease to reduce corrosion from H_2S and improve the seal. Using a funnel, pour the baked SULFURTRAP EX media into the foreline trap (ca. 600 g) followed by molecular sieves (ca. 200 mL). Both the beakers containing the baked scrubber and the foreline trap will be hot to the touch, so heat resistant gloves should be worn.

Once the scrubbing agents are added to the foreline trap, it is brought back to the CVD reactor and reinstalled. Once the KF 25 clamps are replaced, turn on the vacuum pump and evacuate the downstream half of the CVD reactor (the butterfly valve is still closed) Note: if dust from the SULFURTRAP EX media is seen in the vacuum pump connection where the foreline trap is installed, use a foam applicator wetted with isopropanol to remove it. During this time, all EPDM O-rings downstream of the vacuum isolation butterfly valve should also be replaced. The vacuum pump oil should be replaced too. This step should be done in the walk-in fume hood with a safety present nearby and the H_2S detector on person.

Finally, the foreline trap and downstream half of the CVD reactor exposed to atmosphere are baked. Using the Omega temperature control boxes, set the heating tape on the foreline trap to 100 °C and the KF25 bellows hose to 110 °C. After baking out these components for 1 hour, turn off the heating tape on the foreline trap and continue to bake the KF25 bellows hose until the foreline trap has reached room temperature. The heating tape on the KF25 bellows hose is then turned off and the butterfly valve isolating the upstream half of the CVD reactor can be re-opened. This step is usually proceeded by a baking out the reactor as normal.

Baking out the CVD Reactor. Before each new CVD reaction, the quartz tube must be replaced, and the CVD reactor must be baked out afterwards to remove water introduced to the system by this step. A safety buddy should be present when removing a previously used tube, as ZrS_2 deposited on the walls may hydrolyze and produce small amounts of H_2S gas (the gas can be smelled but is below 1 ppm in concentration and cannot be detected using the H_2S detector).

First, the old quartz tube is removed from the CVD reactor by refilling the system with Ar. The valve directly downstream of the H_2S MFC is closed, while the valve in front of the Ar purging MFC is opened and gas is flowed at 100 sccm. The butterfly valve isolating the upstream side of the reactor to vacuum is then closed and the KF25 clamp on the sample access door is removed. The CVD reactor will then reach atmospheric pressure in ca. 5 minute, causing the sample door to fall off (the operator should wait with their hand in front of the door, so it does not fall to the ground – this typically occurs at ca. 400 Torr, as the pressure gauge is calibrated to N_2/air and not Ar). Using a copper wire, remove the sample tray from the CVD reactor. Finally, undo the KF25 connections on the KF25 to quick connect adapters and remove the quartz tube with the KF 25 quick connect adapters still installed.

The old quartz tube is then moved to another hood to remove the KF25 quick connect adapters and prepare to be cleaned. With hands (or septa) covering both ends of the quick connect flanges, transfer the quartz tube from the CVD hood to another hood. Remove the quick connect flanges, clean any residue off them using SEMI-Grade isopropanol, and then replace the EPDM O-rings. Place a septum at the bottom of the quartz tube and secure it with either a worm clamp or copper wire, and then fill it with 2 molar HCl to etch away the ZrS_2 deposited on the walls. The etch step typically takes a few hours. This step should be done with a safety buddy present and the H_2S detector on hand, as initially a few ppm of H_2S is generated.

Next, a new quartz tube is installed onto the CVD reactor. The quartz tube should first be cleaned using the base bath and acid bath, and cleaned again using SEMI-grade acetone and SEMI-grade isopropanol rinses. After drying the quartz tube with nitrogen, it should be baked out in the glassware oven to remove some of the absorbed water (this step should be finished before the old quartz tube is removed so that the time the CVD reactor is exposed to air is minimized to only a few minutes). The KF25 quick connect flanges are reinstalled onto the quartz tube while it is still hot (the user should allow the quartz tube to cool off for ca. 5 minutes before handling it) and the quartz tube is replaced on the CVD reactor. The KF25 centering O-rings used on the KF25 quick connect adapters should be replaced with new EPDM O-rings at this time. Typically, other KF25 centering O-rings are not replaced as often, but at a minimum are changed if the rate of rise appears to be higher than normal after bakeouts or on the same day the scrubbing agents in the foreline trap are replaced. After returning the sample tray to the quartz tube and reinstalling the sample door, the CVD reactor can now be brought back under vacuum. Finally, the CVD reactor should be baked out as described above.

Operating the GeS Deposition Chamber. The following procedure is used to deposit GeS using the Schlenk drying chamber shown in figure 4.1. Experiments are performed inside the fume hood, with a safety buddy present when evacuating glassware before starting the deposition and when removing the Schlenk drying chamber from the heat source at the end of the deposition.

First, the GeS source powder is weighed and adjusted. Using the key connected to the Schlenk drying chamber, refill the system to atmospheric pressure using Ar. The top of the Schlenk drying chamber is then removed and the bottom half is unclamped and placed on the fume hood floor. Remove the glass sample holder ring using long metal tweezers and then pour the GeS powder in the Schlenk drying chamber into a tared weigh boat. Record the mass of the GeS powder and add new powder as necessary to keep the mass between 1.4-1.5 g. Wipe the insides of the Schlenk drying chamber with a kimi wipe to remove any GeS dust and then place the glass sample holder ring back in the center of the bottom half of the Schlenk drying chamber. Carefully pour the GeS powder back into the area enclosed by the sample holder ring. If the GeS is uneven, lightly tap the bottom and sides of the Schlenk drying chamber to move the GeS powder around. Finally, use a kimi wipe to remove any GeS debris from the top of the glass sample holder ring. Re-clamp the bottom half of the Schlenk drying chamber.

Next, position the hot plate set up and load a sample. With the bottom of the Schlenk drying chamber clamped into place, slide the hot plate/Al block set up underneath and adjust the height of the lab jack so that the Al block is flush with the bottom of the Schlenk drying chamber. The clamp can be loosened slightly to assist in keeping the chamber bottom in good thermal contact. Load the substrate into the Schlenk drying chamber by using tweezers to lower it onto the glass sample holder ring. Replace the top half of the Schlenk drying chamber and adjust the position of

the hot plate and assembled Schlenk drying chamber so that there is not torque from the rubber hose used to connect to the Schlenk line (otherwise the Schlenk drying chamber may fall over).

The Schlenk drying chamber is then evacuated several times in preparation for a deposition. Using the Schlenk line, bring the Schlenk drying chamber to a vacuum of ≤10 mTorr and then refill to atmospheric pressure with Ar. Provided the Schlenk drying chamber can reach the desired pressure (there are no obvious external leaks), fill the liquid nitrogen trap to lower the base pressure of the Schlenk drying chamber to ca. 5 mTorr. Repeat the refilling process an addition two times, and then evacuate the Schlenk drying chamber for the fourth and final time. Once a pressure of 5-10 mTorr is reached, set the hot plate temperature to 450 °C (or the desired temperature.) The deposition is now underway and can be tracked by recording the time and temperature of the Al block.

After the deposition has run for the desired time, it may be stopped, and samples retrieved. To do so, the hot plate is turned off and the lab jack supporting the hot plate is lowered so that the Al block is no longer in contact with the Schlenk drying chamber bottom. Be sure the Schlenk drying chamber is secure before lowering the lab jack. Once the Schlenk drying chamber reaches room temperature, use the Schlenk line to refill it with Ar, remove the top half, and retrieve samples using tweezers. When not using the Schlenk drying chamber, place it under active vacuum using the Schlenk line.

Operating the H_2S Annealing Chamber. The following procedure is used to introduce H_2S to the Schlenk drying chamber for annealing experiments. Experiments are performed with a safety buddy present and a H_2S detector on person. When operating inside the fume hood with flowing H_2S, the emergency exhaust is turned on.

First, the annealing chamber is evacuated three times and refilled with argon to remove atmosphere and contaminants. Vacuum and argon are supplied from the Schlenk line to the annealing chamber through valves 4, 5 and 6, while valves 1, 2 and 7 are closed. The chamber is then evacuated a fourth time and valve 6 is closed.

The manifold is then vented to atmosphere while keeping the annealing chamber under vacuum. With valves 1, 2, 6 and 7 closed, argon is introduced through valves 4 and 5. Valves 4 and 5 are then closed and valve 7 is opened. The system is now at atmospheric pressure and newly introduced gases must pass through the scrubbing bed.

Next, the ratio and flowrates of Ar and H_2S are set using as rotamers. Ar is introduced to the system by opening valves 2 and 3, then setting the desired flowrate. To flow H_2S into the manifold, the lecture bottle is opened, followed by the regulator needle valve and valve 1. Before each valve is opened, the connection upstream is leak checked using the H_2S detector. The H_2S flow rate is then set with using a rotamer.

Finally, the annealing chamber is refilled with the desired Ar/H_2S mixture and heating is started. With Ar and H_2S flowing through the reactor bed (at rates set in the previous step), valve 6 is slowly opened to refill the annealing chamber from vacuum; the mineral oil bubbler prevents back streaming of atmosphere into the reaction zone. Valve 6 is then leak checked using the H_2S detector. Provided no H_2S is detected from any point in the annealing set up, the hot plate is turned on and the annealing process is started.

To stop the annealing process, H_2S gas is turned off and the system is cooled to room temperature. First, the hot plate is turned off, followed by closing the H_2S lecture bottle. Once the H_2S gas rotamer reads 0 sccm and the headspace between the bottle and regulator is emptied, valve 1 is closed. When the system reaches room temperature and the manifold has been purged with Ar

for 2 hours, the annealing chamber is opened. This step is done with a safety buddy present, the H_2S detector on person, and the hood sashes open as little as possible with the emergency exhaust on. When H_2S (typically 20-30 ppm after opening the Schlenk drying chamber) is no longer detected in the fume hood, samples can be retrieved for analysis.

Operating the High Temperature Ar Annealing Furnace. The following procedure is used to anneal GeS films using the tube furnace setup shown in figure 4.5. A safety buddy should be present when sliding the quartz tube to move samples in and out of the heated zone during an annealing experiment.

First samples are inserted into the quartz tube. Set the rotamer Ar flowrate to 100 sccm and remove the downstream quick connect flange from the quartz tube. Using tweezers, place samples into the quartz tube and then push them down the quartz tube into the desired position using either long tweezers or a copper wire. Replace the downstream quick connect flange.

Then the quartz tube is purged with Ar gas to ensure water and oxygen are removed. Typically, 150 sccm Ar is flowed for 2 hours for this procedure. Flowing for 30 minutes has also been demonstrated to prevent oxygen incorporation during annealing.

Next, samples are annealed at the desired temperature. With samples outside of the heated zone (not heated by coils or covered by insulation of the tube furnace), set the furnace temperature to the desired set point, and reduce the Ar flowrate to 10 sccm on the rotamer. Once the temperature has reached the setpoint, carefully slide the quartz tube so that samples are inserted into the heated zone of the tube furnace. After annealing for the set amount of time, slide the quartz tube back to its original position. It is often helpful to lower the quartz tube supports on each side, and then

hover the quartz tube in place while sliding into position. The supports can be re-installed after the quartz tube is moved into position.

Finally, samples are cooled to room temperature and retrieved. To cool the tube furnace down faster, an Al block is used to prop the lid open. The Ar gas flowrate is then increased to 50 sccm using the rotamer (otherwise the bubbler may backfill as the temperature cools down.) When the tube furnace and samples have cooled to <40°C, the downstream quick connect flange can be removed and samples can be retrieved using tweezers. When the tube furnace annealing set up is not in use, 10 sccm Ar is flowed through the quartz tube to keep water and oxygen out.

Operating the Vapor Transport Deposition Reactor. The following procedure is used to deposit CuBr films in the vapor transport deposition reactor. A safety buddy should be in the room during the deposition.

First, the source powder and samples are loaded into the quartz tube. The quartz tube reaction zone is isolated from vacuum by closing the butterfly valve on the KF25 tee and then the Ar gas flowrate is set to 100 sccm on the rotamer to refill the quartz tube. Be sure to remove the KF25 clamp from the sample door/pressure gauge before beginning to refill with Ar. Once the system is vented, user tweezers to insert a boat holding the desired amount of CuBr powder (typically 0.5-0.75 g) and then slide the boat into position using either long tweezers or a copper wire. Substrates are then placed on the stainless-steel sample holder and slid into place. Finally, replace the sample door/pressure gauge and open the butterfly valve on the KF25 tee to reintroduce vacuum.

Next a deposition is run. Substrates are first heated by inputting the desired temperature on the Omega temperature controller for the heated tape wrapped on the exposed quartz tube on the

outlet side (for CuBr depositions this is typically not used.) Once the temperature of the heated tape has reached the setpoint value, increase the Ar gas flowrate to 150 sccm using the rotamer and set the temperature to 350 °C on the tube furnace. After the deposition has run for the desired amount of time, turn off the Omega temperature controller for the heated tape, set the tube furnace temperature to 20 or 25 °C, and prop open the tube furnace lid to speed up the cooldown process.

Finally, samples are retrieved. The reactor should be refilled to atmospheric pressure using the same procedure described above to insert samples. The sample tray is removed and sampled are recovered using tweezers. In the case that a bakeout is required, remove the CuBr powder source boat and store it under Ar or vacuum elsewhere (typically a spare Schlenk drying chamber.)

The reactor should be periodically baked out to remove internal leaks of water. The reactor is typically baked out for 2 hours by flowing 100 sccm Ar under active vacuum while heating the tube furnace to 400 °C, and exposed quartz tube on the outlet side and KF25 tee to 110 °C (using the heating tape). After a bakeout, the rate of rise of the reactor should be ca. 5 mTorr/min. When not in use, the reactor should be kept under active vacuum and 10 sccm of Ar should be flowed through the rotamer as a protective gas.

Appendix 2: Deposition of Copper(I) Bromide Thin Films for Fabrication of Zirconium(IV) Sulfide Photovoltaics

Contributions

The work presented below is derived from a manuscript in progress. I deposited ZrS_2 and CuBr thin films and characterized them using scanning electron microscopy, energy dispersive X-ray spectroscopy and four-point probe. Daniela Chavez and I sputtered metal contacts to complete devices and etched to make contact to the underlying substrate. Photovoltaic devices were tested by Daniela Chavez. Professor Luke M. Davis supervised the project. Some text included herein was written by Professor Luke M. Davis and Dr. Lauren Hartle. This project is funded by Tufts University and the National Science Foundation (DMR-2224949).

Experimental

Materials. Copper(I) bromide (99.99%) was purchased from Strem chemical Co., and used without further purification. For preliminary depositions of copper(I) bromide (CuBr) films by thermal evaporation, 98% pure powder was used.

Thermal Evaporation of CuBr Films. Thermal evaporation of CuBr films was performed using the same set up as for deposition of GeS films (Figure 4.1), but with two modifications. First, the 50 mm Schlenk drying chamber was replaced with the 40 mm Schlenk drying chamber used for annealing GeS films in H_2S, and second, the glass sample holder ring was replaced with a glass beaker of approximately the same height. The mass of CuBr loaded into the beaker varied across several depositions, but was typically 0.75-1.25 g. The hot plate setpoint temperature was either 500 or 550 °C temperature, which gives a predicted CuBr source temperature of ca. 320 or 350 °C (Figure 4.3.). The actual source temperatures are likely lower since thermal insulation is provided

by the bottom of the beaker holding the CuBr source powder. The deposition duration was typically 45-55 minutes in total and the deposition procedure was the same as for GeS films (**Appendix 1**).

Physical Vapor Transport of CuBr Films. Physical vapor transport of CuBr films was performed using the apparatus detailed in figure A2.1 below. The deposition procedure is described in **Appendix 1.** For depositions of CuBr, between 0.5-0.75 g of source powder was loaded into a quartz boat, which was kept under active vacuum between depositions. The CuBr source powder temperature was heated to 350 °C and an Ar carrier gas flow rate of 150 sccm was used. Depositions were carried out for ca. 30 minutes in total (including time for the temperature to ramp up to the setpoint). The substrate temperature varied with proximity from the heated zone of the tube furnace; films inside the insulated zone (but not heated by the coils) were ca. 175 °C while those outside the insulation dropped off in temperature to ca. 40 °C over the span of 2-3 inches. Films deposited <100 °C were used to fabricate photovoltaic devices (those at the front of the reaction zone were often over 1000 nm thick).

(a)

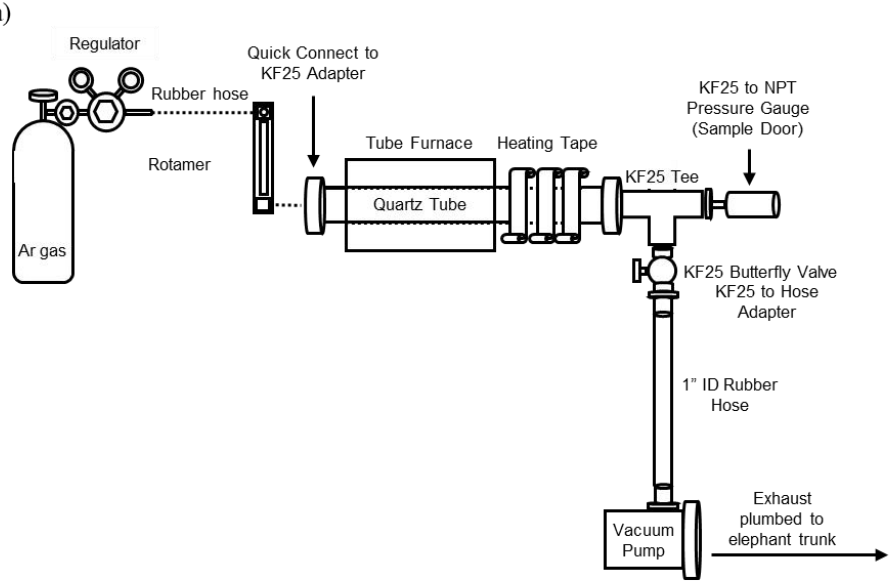

(b)

(c)

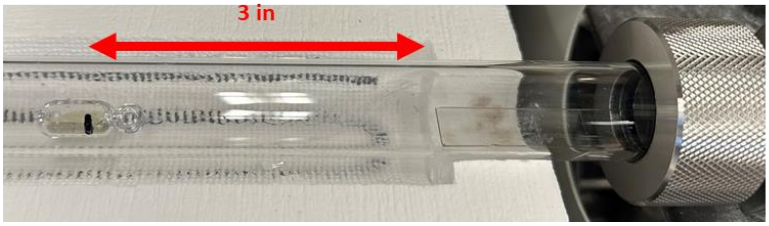

Figure A2.1. A schematic (a) and photograph (b) of the vapor transport apparatus used to deposit CuBr films. (c) a photograph of a source boat and substrate loaded into the reactor. The boat is placed 3 in from the wall of insulation and substrates are placed back-to back starting 3 in from the center of the source boat.

Fabricating ZrS_2 photovoltaics. Devices were fabricated over the course of one day by first depositing ZrS_2 films onto either FTO or ITO substrates at 200 °C using recipe 6 (Table 2.1). Immediately after venting the ZrS_2 samples deposited onto FTO substrates, they were loaded into either the Schlenk drying chamber or into the vapor transport reactor for deposition of CuBr. Samples deposited onto ITO substrates (for Schottky devices) were kept in the reactor while CuBr films were being deposited. The devices were finished by sputtering coating Au/Ti (200 nm/10 nm) contacts at the Tufts University Micro and Nano Fabrication Facility. An NSC3000 DC sputter tool with a base pressure of ca. 5×10^6 Torr was used to deposit the contacts. Finally, CuBr and ZrS_2 layers were etched to make contact with the FTO or ITO substrates using acetonitrile and 2 molar hydrochloric acid, respectively. The etchants were applied using foam applicators.

Photovoltaic Device Measurements. The ZrS_2 photovoltaic devices were tested using a Newport-Oriel M-92192 solar simulator with a Keithley 2440-5A source meter under simulated AM-1.5G filtered light of 1.08 suns. A 1600 W xenon arc lamp was filtered with 0.1, 0.1, 0.5, and 0.04 neutral density filters. Indium pads were applied to the metal contacts on devices, and Signatone SE-BCB Be-Cu probe tips were used to contact the In pads.

Selecting CuBr as a Hole Transport Layer

To assemble photovoltaics from n-type ZrS_2 absorber layers, a p-type hole transport layer is required. We selected CuBr, which is transparent to visible light with a band gap of 3 eV,[42] and has favorable carrier transport properties such as a mobility of 7-9.5 $cm^2V^{-1}s^{-1}$ and carrier concentration on the order of 10^{17} cm^{-3}.[42, 43] Importantly, continuous CuBr can be deposited by thermal evaporation,[42, 44] and the vapor pressure is known as a function of temperature.[45, 46] Finally, the band positions of ZrS_2[47-51] and CuBr[42, 52] are both reported, and are reasonably well-matched.

A band diagram of selected layers for our ZrS_2 photovoltaics is shown below in Figure A2.2 and the values of band positions are listed in Table A2.2.

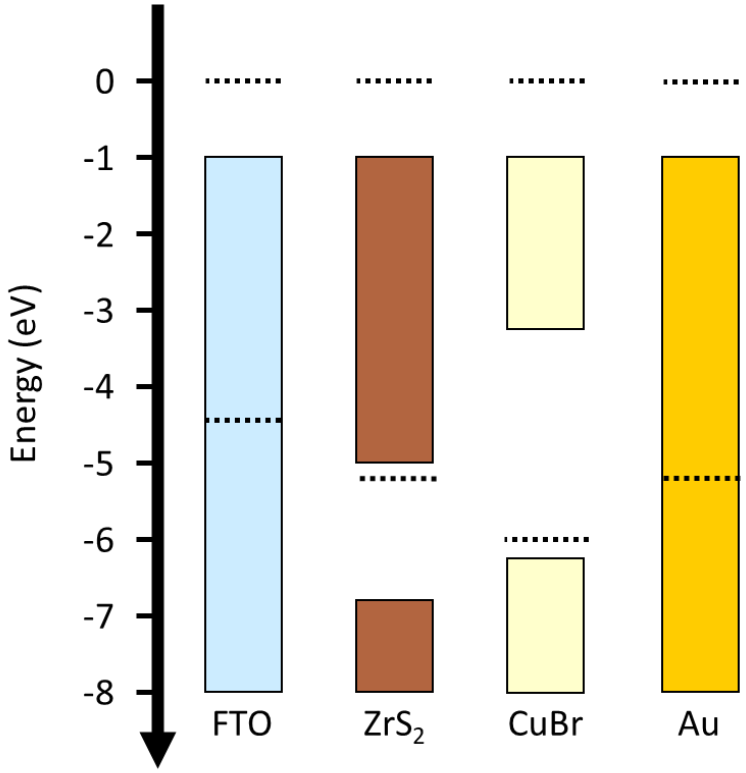

Figure A2.2. Energy band positions of ZrS_2, CuBr and metal contacts for proposed photovoltaic devices.

Table A2.2. Energy band positions of ZrS_2 and CuBr

Layer	Valence Band Maximum (eV)	Fermi Level (eV)	Band Gap (eV)	References
ZrS_2	-6.8	-5.2	1.7 – 1.8	6, 7, 8, 9, 10
CuBr	-6.26	-6.0	2.9 – 3.0	1, 11

Preliminary Results

CuBr Thermal Evaporation and Vapor Transport Deposition. Preliminary depositions of CuBr films on glass substrates using both thermal evaporation and vapor transport deposition produce mostly continuous films with few cracks between grains. Grain sizes are typically on the order of several hundred nm on films deposited by thermal evaporation, while grain size varies based on location and temperature in the vapor transport deposition reactor (Figures A2.3) For films placed inside of the insulated zone of the tube furnace, grains have diameters near 1 μm, while those placed outside of the insulated zone have grains diameters of ca. 100 nm. There is limited crystallography data collected on films deposited by both thermal evaporation and vapor transport deposition. The sheet resistance of CuBr films deposited by thermal evaporation is ca. 10^4-10^5 Ω/□.

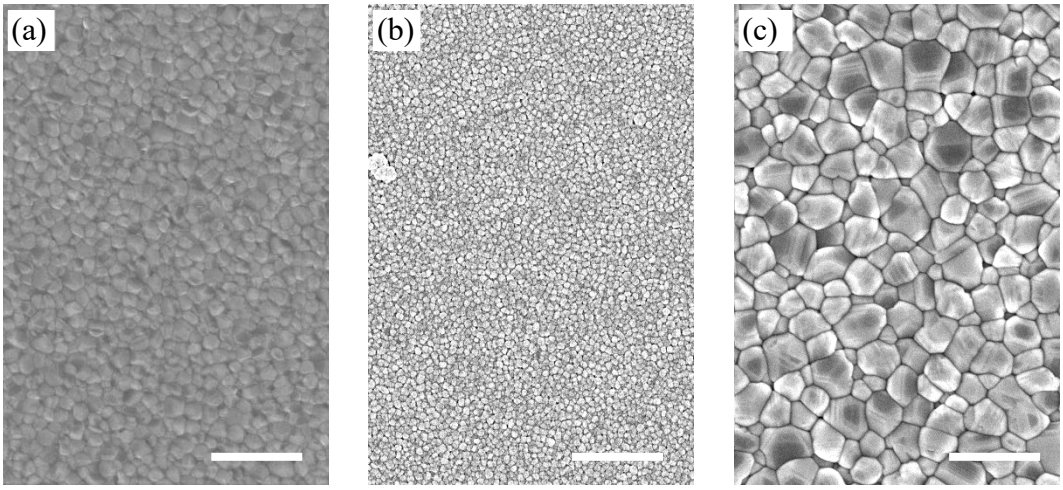

Figure A2.3. Plan view micrographs of CuBr films deposited on glass substrates using (a) thermal evaporation and (b,c) vapor transport deposition. (b) shows the morphology of a CuBr film placed in the rear of the deposition zone (ca. 40 °C) and (c) shows the morphology of a CuBr film placed at the front of the reaction zone (ca. 175 °C). The scale bar is 2 μm.

The morphology of CuBr films deposited by thermal evaporation and physical vapor transport onto ZrS_2 is found to depend on the age of substrate. As shown in Figure A2.4, thermal evaporation of CuBr films on ZrS_2 samples stored under Ar for several weeks have morphologies comparable to films deposited onto glass substrates, with few gaps between grains. When CuBr is thermally evaporated onto ZrS_2 films deposited the same day when fabricating devices, CuBr morphology is either discontinuous or shows secondary growths. Often CuBr films deposited on ZrS_2 for devices become cloudy over the course of several hours. Similar results are observed using physical vapor transport, with depositions of CuBr on glass and ZrS_2 films stored over 1-2 weeks having comparable morphologies and well defined grains. However, when CuBr is deposited onto fresh ZrS_2 films by chemical vapor transport, grain sizes are smaller or crystallites are not apparent. For both thermal evaporation and vapor transport deposition, it seems that the condition of the ZrS_2 substrate impacts growth. One hypothesis for this discrepancy is that storage of ZrS_2 films in the CVD reactor over several weeks resulted in the formation of a surface oxide (ZrO_2), which modifies the growth behavior of CuBr. Additionally, in the absence of ZrO_2, a chemical reaction between ZrS_2 and CuBr could proceed more rapidly, leading to deterioration of the CuBr layer. Data is not available to substantiate either of these claims.

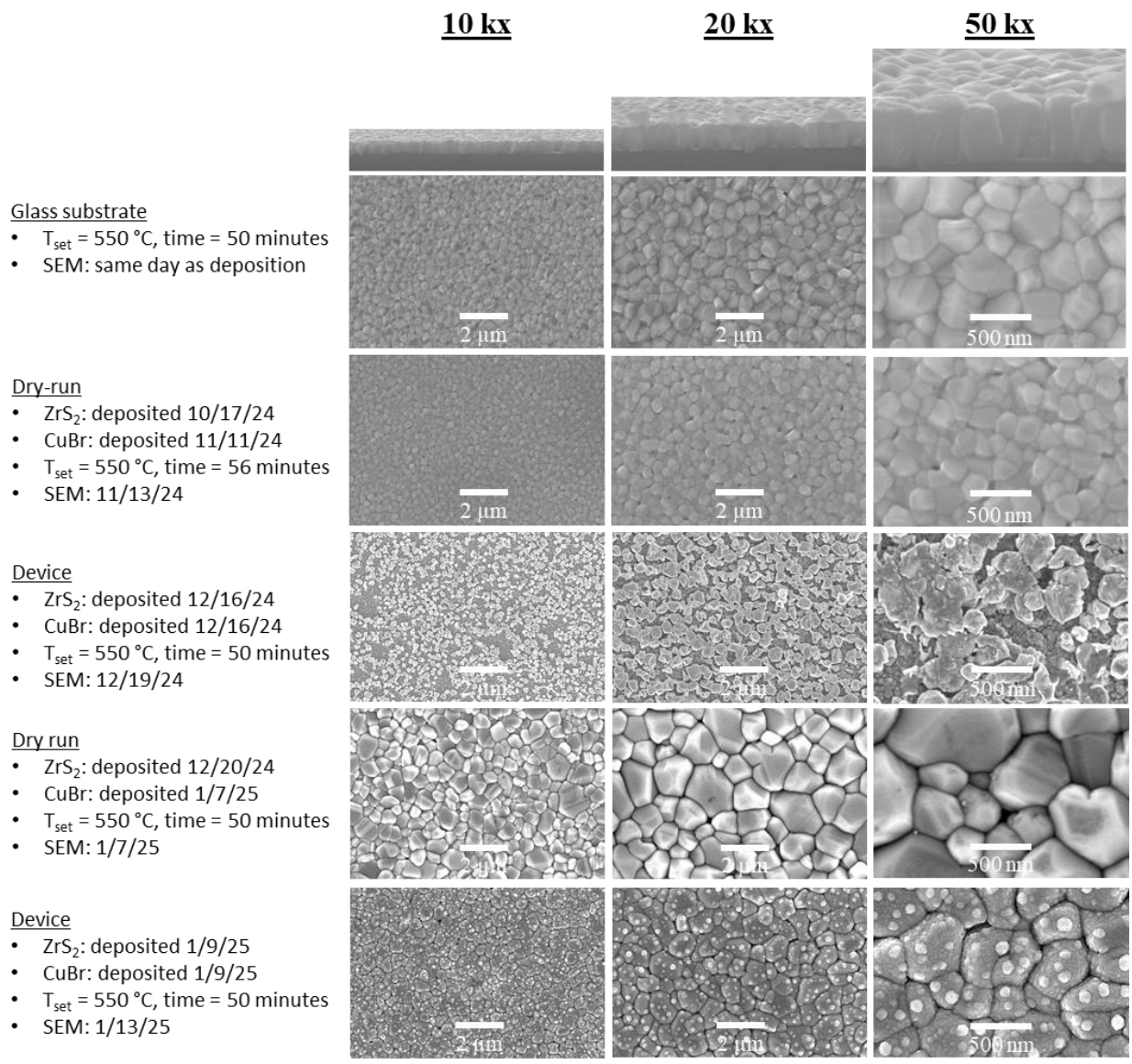

Figure A2.4. Micrographs of CuBr films deposited on various ZrS_2 substrates using thermal evaporation.

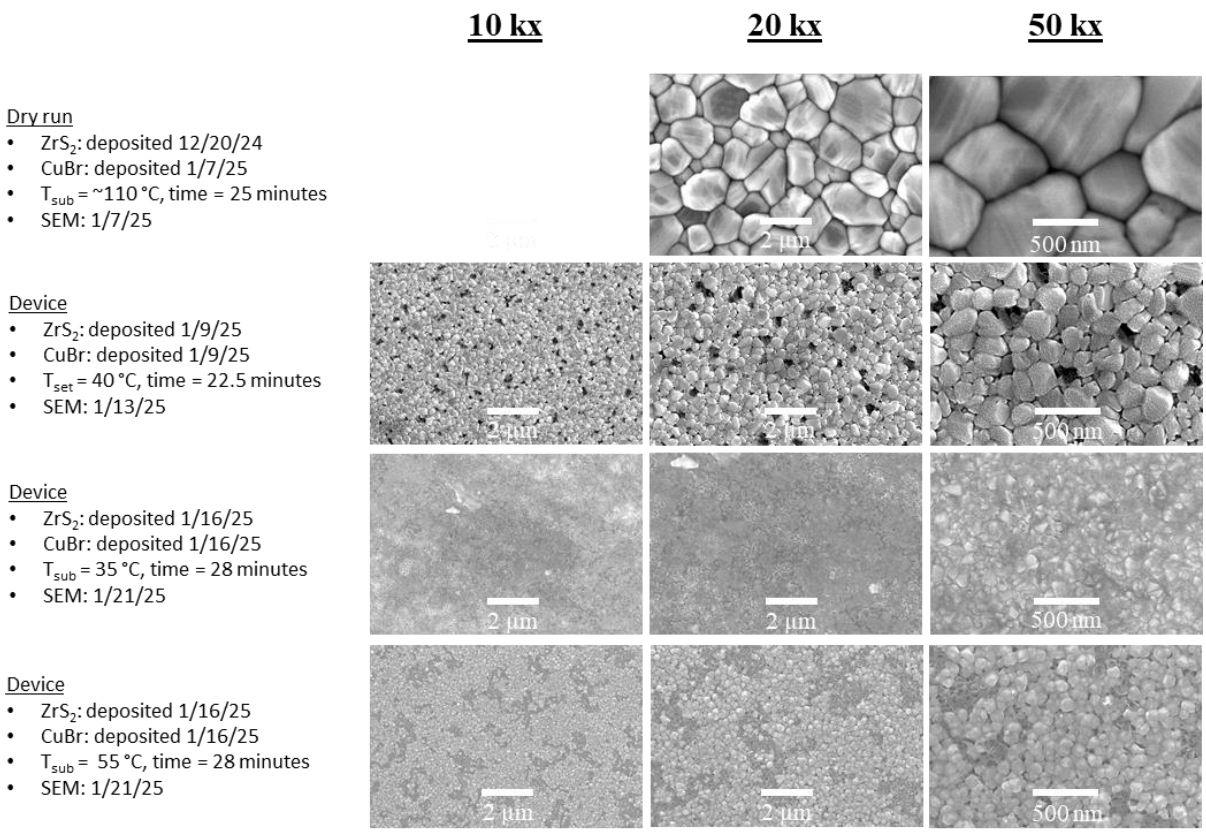

Figure A2.5. Micrographs of CuBr films deposited on various ZrS_2 substrates using physical vapor transport.

Photovoltaic Devices: Attempts to fabricate ZrS_2 photovoltaics were complicated by poor adhesion between layers. Applying In pads to the Au contacts often resulted in what appeared to be delamination of the Au contacts, and led to shorts in devices. After devices were tested, a Scotch tape test was used to determine where adhesion between layers was failing. Using a combination of SEM and EDS, we found that failure primarily occurred between the ZrS_2 and CuBr layers, as analysis of the substrate after the Scotch tape test shows little to no CuBr, which was instead found on the Scotch tape. Poor adhesion between ZrS_2 and CuBr may be related to cloudiness observed in the CuBr layer after a few hours of deposition on to ZrS_2. Careful placement probe tips by Daniela Chavez did allow for measurements of devices, which are briefly discussed here.

ZrS_2 photovoltaic devices utilizing CuBr show good diode behavior in the dark, but photocurrent is low. The best three devices we assembled are shown in Figure A2.6. Dark curves for these devices show they behave as diodes and have take off voltages of ca. 0.25 V. The series resistance is below 100 Ω. However, light curves show these devices have low photocurrent densities, ca. 0.05 $mAcm^{-2}$, affording efficiencies below 0.01% (the champion device had a PCE of 0.007%). Open circuit voltages were typically below 0.1 V, although in one instance this value was as high as 0.15 V. I hypothesize that the small grain size of our ZrS_2 films is partially responsible for the low photocurrent in our devices, as the large number of grain boundaries could produce trap states reducing the number of carriers extracted from the device. Further measurements of ZrS_2 carrier properties (such as carrier lifetime and diffusion lengths) will be necessary to assess this hypothesis. Poor adhesion between the ZrS_2 and CuBr layers, and possible reactions between these layers are likely impacting device performance as well. Finally, ZrS_2 Schottky devices assembled using ITO substrates are shorted.

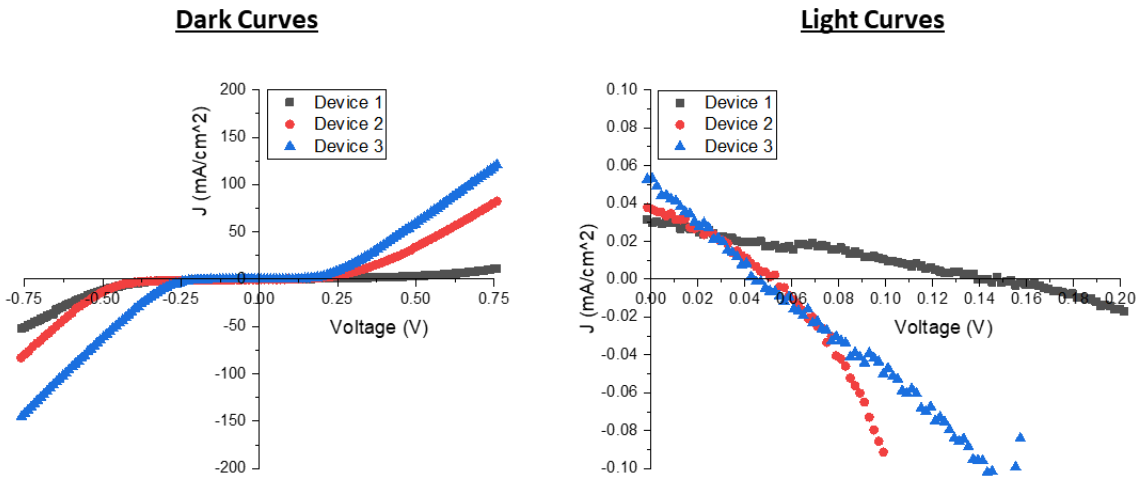

Figure A2.6. J-V curves of FTO:ZrS_2:CuBr:Au/Ti devices measured in the dark and under 1 sun.

References

1. Xia, B.; Zhang, L.; Tian, D.; He, S.; Cao, N.; Xie, G.; Zhang, D.; Chu, X.; Zhao, F., A self-powered p-CuBr/n-Si heterojunction photodetector based on vacuum thermally evaporated high-quality CuBr films. *Journal of Materials Chemistry C* **2024,** *12* (3), 1012-1019.

2. Chang, C. M.; Davis, L. M.; Spear, E. K.; Gordon, R. G., Chemical Vapor Deposition of Transparent, p-Type Cuprous Bromide Thin Films. *Chemistry of Materials* **2021,** *33* (4), 1426-1434.

3. Yamada, N.; Tanida, Y.; Murata, H.; Kondo, T.; Yoshida, S., Wide-Range-Tunable p-Type Conductivity of Transparent CuI1−Br Alloy. *Advanced Functional Materials* **2020,** *30* (34), 2003096.

4. Shelton, R. A. J., Vapour pressures of the solid copper (I) halides. *Transactions of the Faraday Society* **1961,** *57* (0), 2113-2118.

5. Iizuka, A.; Shibata, E.; Sato, M.; Onodera, N.; Nakamura, T., Vapor pressure measurements of CuBr and ZnBr2 by the Knudsen effusion method and their vapor species identification. *Thermochimica Acta* **2014,** *593*, 1-6.

6. Gong, C.; Zhang, H.; Wang, W.; Colombo, L.; Wallace, R. M.; Cho, K., Band alignment of two-dimensional transition metal dichalcogenides: Application in tunnel field effect transistors. *Applied Physics Letters* **2013,** *103* (5).

7. Guo, Y.; Robertson, J., Band engineering in transition metal dichalcogenides: Stacked versus lateral heterostructures. *Applied Physics Letters* **2016,** *108* (23).

8. Moustafa, M.; Zandt, T.; Janowitz, C.; Manzke, R., Growth and band gap determination of the ZrS_xSe_{2-x} single crystal series. *Physical Review B* **2009,** *80* (3), 035206.

9. Moustafa, M.; Wasnick, A.; Janowitz, C.; Manzke, R., Temperature shift of the absorption edge and Urbach tail of ZrS_xSe_{2-x} single crystals. *Physical Review B* **2017,** *95* (24), 245207.

10. Huang, J.; Tian, Y.; Cheng, Y.; Li, X.; Zhang, S.; Jiang, J.; Chen, J.; Wang, G.; Li, J.; Yin, Z.; Zhang, X., Large-area epitaxial growth of 2D $ZrS_{2(1-x)}Se_{2x}$ semiconductor alloys with fully tunable compositions and bandgaps for optoelectronics. *Science China Materials* **2023,** *66* (5), 1870-1878.

11. Rajani, K. V.; Daniels, S.; Rahman, M.; Cowley, A.; McNally, P. J., Deposition of earth-abundant p-type CuBr films with high hole conductivity and realization of p-CuBr/n-Si heterojunction solar cell. *Materials Letters* **2013,** *111*, 63-66.